

# Control of coherent transport by the interplay of confinement and magnetic fields in open quantum billiards

**Dissertation**

zur Erlangung des Doktorgrades

des Fachbereichs Physik

der Universität Hamburg

vorgelegt von

**Christian V. Morfonios**

aus Rhodos

Hamburg

2014







Gutachter der Dissertation:	Prof. Dr. Peter Schmelcher Prof. Dr. Fotios K. Diakonos
Gutachter der Disputation:	Prof. Dr. Peter Schmelcher Prof. Dr. Andreas Hemmerich
Datum der Disputation:	19.11.2014
Vorsitzende des Prüfungsausschusses:	Prof. Dr. Caren Hagner
Vorsitzende des Promotionsausschusses:	Prof. Dr. Daniela Pfannkuche
Dekan der Fakultät für Mathematik, Informatik und Naturwissenschaften:	Prof. Dr. Heinrich Graener

# Zusammenfassung

---

In dieser Arbeit wird der kohärente Quantentransport von Elektronen durch zweidimensionale mesoskopische Strukturen in Abhängigkeit des Wechselspiels zwischen der einschränkenden Geometrie und dem Einfluss angewandter Magnetfelder untersucht mit dem Ziel, die Leitfähigkeit zu kontrollieren. Umfangreiche Untersuchungen des Magnetotransports in einem hoch aufgelösten parametrischen Raum werden mittels eines Rechenverfahrens durchgeführt, das multiterminale Strukturen willkürlicher Geometrie und Topologie behandelt. Die Methode basiert auf der modularen Zusammensetzung elektronischer Propagatoren von inter- oder intra-verbundenen Subsystemen und schafft somit eine große Flexibilität in den Systemanordnungen sowie hohe Recheneffizienz. Leitfähigkeitskontrolle wird zuerst für elongierte Quantenbilliards und -reihen dargestellt, die eingeschränkte Zustände von quasi-entarteten, an den Leitungen stark gekoppelten Zuständen geometrisch abtrennen. Ein schwaches Magnetfeld bestimmt hier den Strom durch Phasenmodulation interferierender Zustände. Weiter wird gezeigt, wie Weichwand-Potentiale für ein effizientes und robustes Schalten der Leitfähigkeit genutzt werden können, indem energiepersistente, kollimierte oder magnetisch gebeugte Elektronenbahnen von Fano-Resonanzen im tiefen Quantenregime isoliert werden. In einer multiterminalen Konfiguration ermöglicht die leitende und fokussierende Eigenschaft gekrümmter Grenzsektionen einen magnetisch kontrollierten, direktionalen Transport wo eingehende Elektronenwellen exklusiv an ausgewählte Ausgänge strömen und dabei einen Strom-Kreuzschalter schaffen. Zusammen mit einer umfassenden Analyse der charakteristischen Transportmerkmale und räumlichen Verteilungen von Streuzuständen demonstrieren die Ergebnisse einen geometrisch unterstützten Aufbau von Kontrollelementen magnetischer Leitfähigkeit in dem Regime der linearen Antwort.

## Abstract

---

In this thesis the coherent quantum transport of electrons through two-dimensional mesoscopic structures is explored in dependence of the interplay between the confining geometry and the impact of applied magnetic fields, aiming at conductance controllability. Extensive magnetotransport investigations in a highly resolved parameter space are performed with a developed computational technique which treats multiterminal structures of arbitrary geometry and topology. The method relies on the modular assembly of the electronic propagators of subsystems which are inter- or intra-connected, thereby providing large flexibility in system setups combined with high efficiency in computation. Conductance control is first demonstrated for elongated quantum billiards and arrays thereof which geometrically separate confined states from quasi-degenerate states coupled strongly to the attached leads. A weak magnetic field here tunes the current by phase modulation of interfering states. It is further shown how soft-wall potentials can be employed for efficient and robust conductance switching by isolating energy persistent collimated or magnetically deflected electron paths from Fano resonances in the deep quantum regime. In a multiterminal configuration, the guiding and focusing property of curved boundary sections enables magnetically controlled directional transport with input electron waves flowing exclusively to selected outputs, thereby realizing a current cross-junction. Together with a comprehensive analysis of characteristic transport features and spatial distributions of scattering states, the results demonstrate the geometrically assisted design of magnetoconductance control elements in the linear response regime.



*To my family*



# Table of Contents

---

<b>0</b>	<b>Introduction</b>	<b>1</b>
0.1	Electron waves at the nanoscale . . . . .	1
0.2	Open quantum billiards . . . . .	2
0.3	Taming wave propagation in the deep quantum regime . . . . .	4
0.4	The necessity of efficient computational techniques . . . . .	6
0.5	Outline of the thesis . . . . .	6
<b>1</b>	<b>Electrons in mesoscopic low-dimensional systems</b>	<b>9</b>
1.1	Two-dimensional electron systems . . . . .	9
1.1.1	Band structure and effective mass . . . . .	9
1.1.2	Heterojunctions and band engineering . . . . .	10
1.1.3	Modulation doping and band diagram . . . . .	12
1.2	Coherent transport devices . . . . .	13
1.2.1	Shaping the 2DES . . . . .	14
1.2.2	Mesoscopic length scales . . . . .	15
1.2.3	Approximations to the Hamiltonian . . . . .	17
1.3	Magnetoelectric subbands and transport channels . . . . .	18
1.4	Density of states . . . . .	22
<b>2</b>	<b>Coherent electronic transport: Landauer-Büttiker formalism</b>	<b>25</b>
2.1	Leads and reservoirs . . . . .	25
2.2	Scattering matrix and transmission function . . . . .	26
2.2.1	Lead eigenmodes . . . . .	26
2.2.2	Transmission amplitudes and coefficients . . . . .	27
2.2.3	Connected scatterers . . . . .	30
2.2.4	Two-terminal system . . . . .	32
2.3	Two-terminal Landauer formula . . . . .	32
2.3.1	General case of coherent transport . . . . .	33
2.3.2	Linear response regime . . . . .	34
2.3.3	Transmission as conductance . . . . .	36
2.4	Multiterminal conductance . . . . .	37
2.4.1	Current from scattering states . . . . .	37
2.4.2	Conductance matrix . . . . .	38
2.4.3	Current and (fictitious) voltage probes . . . . .	39

<b>3</b>	<b>Stationary scattering in planar confining geometries</b>	<b>41</b>
3.1	In-plane Hamiltonian . . . . .	41
3.2	Greenian formulation of scattering . . . . .	42
3.2.1	Green functions . . . . .	42
3.2.2	Scattering matrix from Greenian . . . . .	46
3.2.3	Elements of formal scattering theory . . . . .	51
3.3	Non-Hermitian approach to scattering . . . . .	54
3.3.1	Decomposition of configuration space . . . . .	54
3.3.2	Effective scattering Hamiltonian for finite system . . . . .	56
3.3.3	Connection to electronic transport . . . . .	60
3.4	Multi-state interference effects . . . . .	64
3.4.1	Fano interference . . . . .	64
3.4.2	Aharonov-Bohm oscillations . . . . .	67
3.5	Scattering in locally symmetric structures . . . . .	70
3.5.1	Local symmetry induced invariants . . . . .	70
3.5.2	Generalized parity and Bloch theorems . . . . .	72
3.5.3	Types of locally symmetric potentials . . . . .	73
<b>4</b>	<b>Computational quantum transport in multiterminal and multiply connected structures</b>	<b>75</b>
4.1	Computational schemes for quantum transport . . . . .	75
4.2	From operators to matrices . . . . .	77
4.2.1	Grid discretization and tight-binding Hamiltonian . . . . .	77
4.2.2	Dispersion relation . . . . .	81
4.3	Scattering via spatial decomposition . . . . .	82
4.3.1	Truncation of the Hamiltonian . . . . .	82
4.3.2	Open system propagator . . . . .	85
4.4	Computation of the propagator . . . . .	89
4.4.1	Block-partitioning of the Hamiltonian . . . . .	89
4.4.2	Standard recursive Green function method . . . . .	92
4.4.3	Reordered block-Gaussian elimination scheme . . . . .	92
4.5	Extended RGF for multiply connected structures . . . . .	96
4.5.1	Modular partitioning . . . . .	96
4.5.2	Inter-connection . . . . .	98
4.5.3	Intra-connection . . . . .	100
4.5.4	Computational efficiency and considerations . . . . .	101
4.6	Transport through multiterminal and multiply connected billiard systems . . . . .	102
4.6.1	Single three-terminal elliptic billiard . . . . .	102
4.6.2	Transmission and localization patterns in a looped multiterminal structure . . . . .	105
<b>5</b>	<b>Magnetoconductance switching by phase modulation in arrays of oval quantum billiards</b>	<b>111</b>
5.1	System setup, approximations and computational approach . . . . .	111
5.2	Single oval billiard: transmission suppression . . . . .	114
5.3	Quantum dot array: composite states and transmission bands . . . . .	118
5.4	Conductance switching . . . . .	123

---

5.5	The impact of impurities . . . . .	126
5.6	Summary and conclusions . . . . .	128
<b>6</b>	<b>Current control in soft-wall electron billiards: energy-persistent scattering in the deep quantum regime</b>	<b>129</b>
6.1	Persistent switching via geometric rescaling at low energies . . . . .	129
6.2	Decoupling of resonances and controllable finite-temperature conductance . . . . .	131
6.3	Closed billiard eigenspectrum . . . . .	134
6.4	Switching between collimated and backscattered wave propagation . . . . .	136
6.5	Conductance switching in soft-wall billiard arrays . . . . .	139
6.6	Billiard geometry and soft-wall potential variations . . . . .	141
6.7	Summary and conclusions . . . . .	143
<b>7</b>	<b>Directional transport in multiterminal focusing quantum billiards</b>	<b>145</b>
7.1	From two-terminal to multiterminal conductance control . . . . .	145
7.2	Setup and computational approach . . . . .	147
7.3	Symmetries of the transmission coefficients . . . . .	149
7.4	Transmission spectra at zero magnetic field . . . . .	150
7.5	Geometry dependent mean transmission . . . . .	152
7.6	Transmission in a magnetic field . . . . .	156
7.7	Bent coupled wires . . . . .	160
7.8	Directed conductance . . . . .	162
7.9	Summary and conclusions . . . . .	164
<b>8</b>	<b>Summary, conclusions, and perspectives</b>	<b>167</b>
<b>A</b>	<b>Green functions of leads</b>	<b>171</b>
A.1	Green function of an infinite Q1D wire . . . . .	171
A.2	Interface Green function of a semi-infinite Q1D wire . . . . .	173
<b>B</b>	<b>Block-matrix inversion and Schur complement</b>	<b>175</b>
B.1	Inversion by block-Gaussian elimination . . . . .	175
B.2	Application to block-partitioned lattice Hamiltonian . . . . .	177
<b>C</b>	<b>Inter- and intra-connection of modules</b>	<b>179</b>
C.1	Inter-connection between two modules . . . . .	179
C.2	Intra-connection of a module . . . . .	181
<b>D</b>	<b>Gauge transformation of the Greenian</b>	<b>185</b>
D.1	Gauge transformation between two different axial gauges . . . . .	185
D.2	Gauge transformation for the inter-connection of two modules . . . . .	186
<b>E</b>	<b>Natural units</b>	<b>189</b>
	<b>Bibliography</b>	<b>191</b>

---



---

# Introduction

---

*All knowledge degenerates into probability.*

— David Hume

A Treatise of Human Nature, 1738

When writing that “all knowledge degenerates into probability”, 18th century philosopher David Hume could barely have anticipated to what literal extent this statement would be carried two centuries later with the establishment of quantum theory in the description of nature. The claim as such, expanded beyond its original context as the epitome of empiricism, indeed applies to what has become the standard concept by which the realm of the microscopic is approached. Regardless of its interpretation as a fundament of nature or as an emergence of still obscure origin, it is the inherent probability of events which remains deterministically accessible at scales where particles reveal their wavy self—even if empirical ability to sense physical phenomena has been pushed to extreme accuracy. The probabilistic character of a system’s behavior immediately brings the question of its controllability into a very specific dichotomy: Absolute certainty about a property prior to its measurement is achieved only by forcing the associated probability to the limit of zero or unity.

## 0.1 Electron waves at the nanoscale

Although ubiquitously desirable in science, controllable system response is of particular relevance in the field of electronic transport in fabricated semiconductor nanostructures. Here, the property to be controlled is the electronic flow between the electrodes attached to an effectively two-dimensional region of nanoscale confinement. Such devices are usually electrostatically defined by nanoscale patterned metallic gates on top of a semiconductor heterostructure junction where electrons have been restricted to move forming an effectively two-dimensional free electron system. The size of a typical device is large enough to treat the surrounding crystal lattice as continuous, but small enough for the quantum features of the transported electrons to become important or even dominate the system response. In this mesoscopic regime, where the electronic De Broglie wavelength is comparable to the size of the confinement, the system can be treated in the framework of scattering theory, as applied to waves propagating coherently within given geometrical constraints provided that inelastic processes are suppressed. Probability in transport accordingly enters in the form of transition rates from ingoing to outgoing waves in the presence of multiple electrode terminals. This identification of transmission probabilities as the essential component of electronic conductance is due to the pioneering work of Landauer [1] and Büttiker [2] and has since become a successful conceptual and technical basis in treating quantum coherent

transport as well as modeling decoherence processes [3,4]. Vanishing and maximal current flow between two terminals is here translated to a transmission probability of zero and unity, respectively, at the Fermi energy of the incoming electrons. Given the underlying theoretical description of transport, the challenge posed here is to identify, understand and ultimately manipulate the mechanisms which may enable its controllability.

Though simple and in many ways intuitive, the Landauer-Büttiker picture of mesoscopic transport was far from obvious when proposed, owing to the non-equilibrium situation of current flow as well as the complications added by many-body interactions in actual experimental settings. An important test of the theory was the experimental confirmation of the quantized conductance in narrow quasi-one-dimensional channels by Whareem *et al.* in 1988 [5], repeated and refined later in shorter nanoscale constriction (so-called quantum point contacts) [6]. Relying on the simple geometry of these systems and the ballistic transport achieved, transmission is mediated by practically decoupled channels leading to characteristic plateaus in the measured conductance. Regarding current control, in such a setting the charge flow current can be switched on and off by tuning the gates defining the quantum point contacts. This requires, however, a real-time gate operation on local scale to alter the electrostatic confinement of the device and is further subject to geometrical restrictions in applying the gate voltages. Moreover, deviations from the ideal plateaus is generally caused by imperfections such as impurity scattering [7], and the observed quantization steps may also break down depending on the confining potential configuration [8]. As shown already in Refs. [5,6], another possibility to control the current is to apply a global magnetic field which successively depopulates the magnetoelectric subbands. The practical disadvantage is here that a very high field strength is needed to raising the Landau subbands through the Fermi level. Apart from these considerations, it clear that the suppression of current is here forced essentially by imposing electrostatic or magnetic energy barriers on the electron flow. An alternative route to nanoelectronic current control is to exploit the wave dynamics in the device determined by weaker magnetic fields in combination with a confinement potential which in general couples individual scattering states.

## 0.2 Open quantum billiards

Prominent candidate elements for such a type of conductance control are so called open electron ‘billiards’ [9–15]. As the name suggests, these are two-dimensional structures which confine ballistically moving particles within a region of space of certain geometry, with openings along their boundary through which the particle can escape. In their classical version, the dynamics of a point particle is defined by the shape of the boundary, and so the phase space of trajectories in billiards have served as a paradigm in studying nonlinear dynamics and chaos [16]. Such constructs would be of little relevance to electronic transport devices if it were not for the immense technological progress in nanoscale fabrication techniques over the last few decades: Nowadays, electrons can be restricted with very high accuracy to move along a two-dimensional semiconductor interface [17], and the confinement potential defining an electron billiard can be patterned to almost arbitrary profile and well below the electronic mean free path and coherence length [18–21]. In other words, the idealized billiard potential can practically be drawn directly in the laboratory.

Quantum billiards, in which moving point particles are replaced by waves, have thereby been used to model nanoscale transport devices and set the grounds for the theoretical description and experimental investigation of coherent transport in the mesoscopic regime. They are also widely known as effectively zero-dimensional quantum ‘dots’ (or even ‘artificial atoms’ [22]), though we will mostly use the term ‘billiard’ which emphasizes their spatial

extent in the form of 2D cavities. It should be pointed out that, in the absence of magnetic fields and inelastic processes, the stationary scattering framework is formally equivalent for matter and light waves; many aspects of transmission are therefore investigated in microwave billiards rather than electron billiards, since the experimental setup is incomparably easier to construct and free from the inherent imperfections of solid state. Motivated by its classical counterpart, this unified quantum billiard model provides a unique platform to explore the quantum-to-classical crossover in the form of quasi-bound states [23] and wave function scars [24–26], the role of integrability in transmission statistics [27, 28] and shot noise [29] as well as signatures of quantum chaos [16, 30–32]. At higher energies the relation of wave patterns to classical trajectories and the resulting transmission spectra are explained successfully using semiclassical techniques [32–34] which provide valuable insight into the dynamics taking place. Billiard systems are also convenient for the study of the ubiquitous phenomenon of Fano interference [35, 36], because of its clear connection to geometrically defined quasi-bound states [11] whose coupling to the leads can vary the spectral width from isolated Fano peaks [37–42] to the overlapping regime [14, 43, 44]. In the latter case the effect of resonance trapping [45–48] can be induced where the widths of Fano resonances bifurcate [48] as a function of system parameters, meaning that lineshapes of vanishing width can be superimposed on broader resonances. In the opposite extreme, broad resonances overlap and the interference of the associated strongly lead-coupled states in general lead to a highly irregular transmission profile in varying energy.

A promising aspect of electron billiards with respect to conductance control is the drastic modification of their transport properties by an externally applied magnetic field [49–55], and they therefore dominate the intense investigation of coherent magnetotransport in the mesoscopic regime, where quantum interference meets and overlaps with the notion of oriented paths. Aharonov-Bohm (AB) interference [56] at weak magnetic fields is generalized from its occurrence in ring-shaped devices [57–59] to billiard setups [60, 61] where the interference of spatially extended states at the lead openings give rise to multimode transmission oscillations in varying field strength. The combination of quantum dots or wires with ring geometries into hybrid structures has been used to study the intricate interplay between Fano and AB interference [62–66]. At intermediate field strengths the electronic dynamics is dominated by the Lorentz deflection which becomes particularly important in the case of multiterminal structures [67–69] where the Onsager reciprocity relations [70] take effect [2]. For strong magnetic fields, where well spaced Landau levels occupy the bulk, transport is mediated by edge states [50, 71] localized at the billiard boundary and multi-terminal transmission is determined by the device topology and remains largely unaffected by the potential landscape caused, e. g. by impurities. An early manifestation of edge state transport was the quantum Hall effect [72, 73], an extraordinary example of precision in conductance quantization. Since edge states are essentially of one-dimensional nature, their interference may lead to well defined AB oscillations in structures where they are caused to couple among each other, as by diffraction at sharp lead openings [50]. The above three regimes of magnetotransport are in general not separated but combine depending on the confining geometry and the lead attachment which may lead to enhanced irregularities in the conductance profile. The above magnetically related phenomena acquire an additional twist when the electronic spin is taken into account, and ‘spintronics’ has developed into a field of its own [74]. However, the small Zeeman splitting in weak magnetic fields does not alter the overall conductance much at finite temperatures; Spin-orbit coupling is also relatively weak in conventional semiconductors like GaAs and is usually neglected for transport of conduction band electrons [75].

Assembling individual dots into linear arrays via coupling QPCs gives rise to new fea-

tures such as the precursor of bands in the transmission spectra [76] and magnetically induced Bragg scattering [77], resonant transmission and reflection [51] and the formation of coupling-induced bipartite states [78], depending on the type and strength of coupling [79]. Lateral arrays of dots or antidots (closed areas expelling instead of confining electrons) lead to even more complex band structures [80, 81] and interesting properties in the presence of magnetic fields such as alternative versions of the quantum Hall effect [82] modulated by AB interference [83]. Connected dots also reveal the importance of electron-electron interactions in the observed response [84–88] which may lead to Coulomb blockade [89, 90] of electron transport for sufficiently isolated dots. For strongly lead-coupled systems interactions are otherwise widely treated on a mean field level through self-consistent calculations [91, 92]. Together with the finite potential of the gates defining the device, they lead to an effective softening of the electron billiard boundaries [93] which is taken into account in more realistic simulations [8, 94]. The dynamics within soft-wall billiards may correspondingly show pronounced differences with respect to the hard-wall counterpart, such as stabilization of particular trajectories [51, 95], suppression (quenching) of the Hall resistance [94] and enhanced occurrence of sharp Fano resonances [12].

### 0.3 Taming wave propagation in the deep quantum regime

From the above—by no means exhaustive—listing of theoretical and experimental progress in the field of quantum transport it becomes clear that a large diversity of phenomena are available with a remarkable impact on the transmission in billiard systems. It is plausible to think of these effects as a toolkit to control conductance in nanostructures: Once the corresponding mechanism in each case is understood and verified, it can in principle be used to manipulate the transport behavior under given circumstances. In most cases, however, the findings show a non-trivial energy dependence of transmittivity as a result of the complex nature of wave propagation. Indeed, a statistical treatment of generic transport devices reveals the manifestation of *universal* conductance fluctuations [96], both in varying Fermi energy and applied magnetic field, as a result of elastic impurity scattering at low temperatures. Another consequence of wave interference in disordered structures is the phenomenon of weak localization [97, 98] which is lifted by a magnetic field. In fact, localization effects [99–102] and conductance fluctuations [10, 30] are also present in a large variety of ballistic open quantum dot systems. Such universal characteristics are well described in the framework of random matrix theory (RMT) [103, 104] and by semiclassical methods [32, 104] where a distinction between symmetry classes and integrability is concluded.

In view of this inherent irregularity of conductance characteristics for generic systems, the quest for transport controllability inevitably finds its way to the exploitation of *non-universal* properties based on specific device design. This is in accordance with the fact that, apart from the generic effect of disorder and chaotic scattering, sample-specific properties are largely determined by the system geometry and the placement of attached leads. An illuminating example is the use of Fano interference in structures with certain geometrical features as a current switching mechanism [66, 105], tunable by a magnetic field [62, 106] or by a controllable coupling to continuum [42] or resonant [39] states. Indeed, an isolated Fano resonance lineshape reaches the two desired limits of zero and unit transmission in a single-channel scattering setting. Resonant control of transport has also been proposed in terms of cascading of transmitting or reflecting states in billiard arrays [51, 77]. Nevertheless, resonant effects are in general sensitive to energy variations and prone to attenuation by imperfections in the setup. Moreover, they are eventually washed away from the conductance profile due to thermal contribution of neighboring states around the Fermi level at finite temperatures.

With respect to multiterminal conductance control, there have been proposals utilizing window-coupled quantum waveguides as an electronic directional coupler [107–111], also by use of magnetic fields [112–115], or three-terminal junctions [116]. For example, in Ref. [114] the electronic flow can be altered by modifying the window opening and thereby changing the coupling of the scattered wave to the outputs, and then switched by a magnetic field. Again, however, such setups are based on resonant-like features or show strongly fluctuating transmission, and in general feature a relatively small directivity. In Ref. [109] the operation is performed on ingoing Gaussian wave packets and thus of little applicability [114] in a stationary picture of transport. Moreover, the magnetic fields used must typically be strong enough to force the electrons into the edge states regime [112, 114, 115] or raise magnetic barriers [113].

A remarkable demonstration of transport control is given in a recent work by Rotter *et al.* [117] where incoming waves can be completely transmitted to the output terminal following exclusively classical trajectories. These non-universal states have definite Wigner-Smith delay times and are accessed as exceptional points in parameter space away from RMT predictions. Their incoming momentum components are determined via a systematic protocol and belong to relatively high channels in the attached leads in order to resolve classical phase space. Since the constructed waves behave like particles (with the deterministic destiny to escape through the input or output lead), the transmission equals zero or unity. Although the approach could be envisaged as a means of beam-like classical wave propagation [117], its application to electronic devices is questionable since it would demand the selective population of reservoir-coupled channels.

In the present work, the aim is to reach the same limits of zero and unity in non-resonant transmission, though in the deep quantum regime, that is, in the ground transversal mode of the attached leads, at electronic wavelengths comparable to the geometrical characteristics of the transport device. The states at such low energy are in general spatially extended, only occasionally resembling classical counterparts, and the challenge is to suppress the otherwise ubiquitous current fluctuations mentioned above. We investigate the possibility to achieve a smooth background transmission spectrum in appropriately designed billiard setups and its magnetically induced switching between zero and one.

As outlined below, efficient magnetic control of coherent transport in the linear response regime and at low temperatures is demonstrated numerically and analyzed by means of different underlying mechanisms. For a linear array of hard-wall elongated billiards we exploit the geometry to induce destructive interference between quasi-degenerate states which are phase-modulated by a weak field into maximal transmission, in a broad energy range. A soft-wall potential is then used in a similar geometry to create energetically persistent collimated or backscattered motion. Here the deflecting property of the field is combined with the decoupling of quasi-bound states from the leads, resulting in totally suppressed conductance over the whole first channel at zero field which is switched to its maximal value by turning on the field. The challenge of efficient conductance control is increased in multiterminal devices since scattering states in general couple to all leads and thereby for any lead pair the other leads act like sinks for the probability flux. Here, efficient directional conductance is demonstrated for a four-terminal setup through the selective coupling of scattering states to different lead pairs at zero field and their switching by weak or strong fields. Transport control is in total achieved by simple means utilizing the interplay of the effect of the magnetic field with the specific geometry and potential design of the system. In all cases a relative robustness of the switching effect against small variations in the confining potential is shown, certifying the functionality of the devices as nanoelectronic circuit elements.

## 0.4 The necessity of efficient computational techniques

The pursuit of conductance controllability in terms of non-universal mechanisms as described above is tightly connected to the ability of performing extensive investigations of device setups in highly resolved parameter space of with varying potential configurations, input energy and applied magnetic field strength. In particular, the needed flexibility in geometry variations and lead positioning renders necessary the use of equally flexible as well as powerful numerical techniques to arrive at the quantities of interest. A particular computational technique which has been established as a standard in quantum transport simulations due to its conceptual simplicity and numerical robustness is the recursive Green function (RGF) method [118]. Based on the Green function approach to scattering in confined geometries, it used a recursion scheme to compute the relevant part of the single-particle propagator from an effective tight-binding Hamiltonian where the effect of the leads attached to the device (open boundary conditions) is accounted for by non-Hermitian self-energy matrices. Since its first formulation more than three decades ago [97, 119, 120], it has been refined and extended in various ways depending on the physical situation at hand, as briefly reviewed below in Chap. 4. A particular advantage is the possibility to perform the recursion on the level of subsystems of a composite structure by effectively solving a matrix Dyson equation [121], thereby reducing significantly the computational cost—especially when the system can be decomposed into partly repeated sections, as is the case for the billiard systems studied here. Rotter *et al.* [50, 122] specialized this technique to the case of connected modules of simple (analytically solvable) regular geometries, thereby achieving transport calculations at very high energies and field strengths. Another version of remarkable flexibility is the ‘knitting’ algorithm by Kazymyrenko *et al.* [123] where, conversely, single sites are added one by one to build the complete device structure. We here develop an extended RGF scheme which combines these two approaches by connecting multiterminal modules, though of arbitrary form, into composite structures of arbitrary topology, with a block-reordered version of the standard RGF at the core computing the single-module propagators. This enables the rapid investigation of large diversity of device structures with continuously varying geometry parameters in highly resolved energy and field variation, making the method tailor-made for system optimization with respect to transport controllability.

## 0.5 Outline of the thesis

Each chapter of the thesis starts with an introductory passage which motivates its content and provides its main highlights. In brief, the structure and content of the chapters are as follows:

Chapters 1, 2, and 3 provide a relatively self-contained account on the theory of coherent electronic transport in mesoscopic systems, adapted to the needs of the present work and discussed in the context of quantum billiards. The presentation follows a top-down order:

**Chapter 1** introduces the basic principles of nanoscale semiconductor structures and the circumstances under which two-dimensional open electron billiards are realized, within the approximations used in following applications.

**Chapter 2** reviews the Landauer-Büttiker picture of transport where conductance is deduced from transmission, clarifying the concept of electron reservoirs and the connection of multiterminal devices to wave scattering.

**Chapter 3** presents the Green function formalism pertaining to the scattering matrix and

other quantities relevant to transport, with emphasis on the considerations applicable to lead-coupled systems. It closes with a discussion of the main interference effects encountered in the setups to be studied as well as a brief presentation of the newly developed theory of scattering in locally symmetric systems.

**Chapter 4** is devoted to the numerical computation of the Green function within a tight-binding effective Hamiltonian approach. We here develop an extended version of the recursive Green function (RGF) technique which enables the assembly of multiply connected composite structures from given subsystems, with arbitrarily positioned multiple leads. It is based on a block-Gaussian elimination scheme for solving the matrix Dyson associated with the inter- and intra-connection of subsystems. The subsystem propagators are found using a block-reordered RGF method which enables a selective computation of local quantities (state and current densities) in addition to global ones (transmission). In combination, the two methods provide a powerful tool to study structures of arbitrary geometry and topology with high flexibility.

**Chapter 5** explores the magnetotransport through arrays of two-terminal oval-shaped quantum billiards and demonstrates their functionality as a conductance switch in the linear response regime. The effect relies on a systematic suppression of the field-free transmission due to destructive interference of lead-coupled states, which is lifted by a weak phase-modulating field. Resonances in the coupled-dot system, whose splitting saturates into banded spectra for large dot number, are analyzed in terms of characteristic local density distributions. Present already for a single quantum dot, the conductance switching ratio is drastically enhanced for a double-dot system and proves robust against remote impurity disorder at low temperatures.

**Chapter 6** shows how the use of soft-wall boundaries in elongated billiards can be combined with orbital magnetism to achieve efficient current control in varying Fermi energy. The underlying mechanism is the energy persistent backscattering of magnetically deflected states which are geometrically rescaled by the soft walls, in combination with the collimation of forward propagation at zero field. In this manner, the omnipresent conductance fluctuations at low energies are suppressed in favor of a smooth and tunable transport due to the complete decoupling of quasi-bound states from the leads. The robustness of the switching functionality is certified by variations in the shape and potential profile of the billiard.

**Chapter 7** takes a challenging step to investigate the possibility of magnetoconductance control in multiterminal electronic devices. A semi-elliptic four-terminal billiard is here chosen, where the key property is the separation of scattering states which are strongly coupled to different pairs of leads in the field-free case. The transmitted electrons are thereby mediated by rotator and librator modes which are guided and focused by the convex boundary, respectively. By tuning the magnetic field strength, the ingoing electron waves are then directed to selected leads via extended Lorenz-deflected states or edge states. The device thus functions as a unique, magnetically operated, directional current junction.

**Chapter 8** summarizes the results of the thesis, concludes on the presented aspects of current control in mesoscopic devices and points at open perspectives.



---

# Electrons in low-dimensional mesoscopic systems

---

In this chapter the basic principles of nanoscale semiconductor structures are presented along with the circumstances under which quantum effects dominate the properties of current-carrying electrons. Within this mesoscopic regime, the concept of an ‘open electron billiard’ is introduced as a prototype, idealized nanoelectronic transport device in which quantum coherence is maintained. Under the associated approximations to the system Hamiltonian, we finally analyze the characteristics of quantum states resulting from low-dimensional confinement.

## 1.1 Two-dimensional electron systems

The constriction of freely moving electrons to a plane, and their further confinement into desired geometric structures at the nanoscale, provide a unique platform for the theoretical investigation and experimental observation of quantum effects. We now briefly outline the basic ingredients which enable the realization of such systems at the interface between semiconductor crystals. We make brief use of capitalized notation  $\mathbf{R} = (x, y, z) \equiv (\mathbf{r}, z)$  and  $\mathbf{R} = (k_x, k_y, k_z) \equiv (\mathbf{k}, k_z)$  for three-dimensional vectors, before separating out the planar vectors  $\mathbf{r}$  and  $\mathbf{k}$  of the actual 2D transport system.

### 1.1.1 Band structure and effective mass

The dynamics of electrons within solids is governed by their interaction with the atoms of the crystal lattice and with all other electrons, and the determination of their spectral properties and response to external forces constitute a complicated quantum many-body problem. The essential electronic behavior is, however, successfully described in using effective potentials in a single-particle picture. In the presence of the periodic crystal potential  $V_{\text{cr}}(\mathbf{R})$  in a solid, electrons occupy Bloch eigenstates

$$\Psi_{\mathbf{K}}(\mathbf{R}) = e^{i\mathbf{K}\cdot\mathbf{R}} u_{\mathbf{K}}(\mathbf{R}), \quad (1.1)$$

labeled by the crystal momentum  $\hbar\mathbf{K}$ , where  $u_{\mathbf{K}}(\mathbf{R})$  follows the periodicity of  $V_{\text{cr}}$ . The corresponding energy levels arrange into bands  $E_n(\mathbf{K})$ , the form of the  $n$ -th band in a certain direction  $\mathbf{K}$  being determined by the type of atoms in the solid and their structure within the unit cell of the lattice. For intrinsic semiconductors, the chemical potential  $\mu$  lies within the gap between the top  $E_V$  of a (set of) fully populated valence band(s) and the bottom  $E_C$  of a (set of) empty conduction band(s), so that there are no free charge carriers at low temperatures. Free carriers are provided by doping the crystal with donor (acceptor) impurities

which yield available states within the gap close to  $E_C$  ( $E_V$ ) and can thereby excite electrons (holes) into the principal minimum (maximum) of the conduction (valence) band. A ‘gas’ of electrons (or holes) is thus created, with motion along wave vectors around the Fermi surface in the Brillouin zone. In Fig. 1.1 (a) the band structure of the semiconductor GaAs is shown together with its Brillouin zone (resulting from its zincblende crystal structure), with focus on the direct primary band gap.

In the vicinity of a local band extremum ( $E_n^0, \mathbf{K}^0$ ), the dispersion relation can be described by a quadratic form

$$E_n(\mathbf{K}) = E_n^0 + \frac{\hbar^2}{2} \sum_{ij} M_{ij}^{-1} (k_i - k_i^0)(k_j - k_j^0), \quad (1.2)$$

where  $M$  is the (inertial) effective mass tensor,

$$M_{ij} = \hbar^2 \left[ \frac{\partial^2 E_n(\mathbf{K})}{\partial k_i \partial k_j} \right]^{-1} = \hbar^2 \left[ \frac{\partial v_j}{\partial k_i} \right]^{-1}, \quad (1.3)$$

defined by equating the rate of change in crystal momentum with externally acting forces  $F$ , and comparing to the change in the group velocity  $\mathbf{V} = (v_x, v_y, v_z) = \nabla_{\mathbf{K}} E_n(\mathbf{K}) / \hbar$ ,

$$\mathbf{F} = \frac{d}{dt} \hbar \mathbf{K} \Leftrightarrow \frac{d}{dt} v_i = \sum_j M_{ij}^{-1} F_j, \quad (1.4)$$

in analogy to semiclassical dynamics [124]. For a semiconductor with a direct gap between  $E_V$  and  $E_C$  at the center point  $\Gamma$  ( $\mathbf{K} = \mathbf{0}$ ) of the Brillouin zone, such as GaAs (see Fig. 1.1 (a)), the dispersion around the principal minimum of the conduction band is parabolic with an isotropic, diagonal effective mass  $M_{ij} = m^* \delta_{ij}$ ,

$$E(\mathbf{K}) = E_C + \frac{\hbar^2}{2m^*} K^2 \quad (1.5)$$

(we now drop the band index  $n$ , since we will focus exclusively on the conduction band). Thus, the electron gas forming at just above  $E_C$  effectively consists of particles moving freely on a spherical equienergetic surface, just like they would in free space, but with a (typically smaller) mass  $m^* \neq m_e$  determined by the curvature of the dispersion  $E(\mathbf{K})$  at the band minimum. The corresponding electron dynamics under the impact of, e.g., impurities, charge accumulation, or externally applied voltages, can therefore effectively be described by a potential term  $V(\mathbf{R})$  in a single-particle Hamiltonian, where the effect of the crystal potential  $V_{\text{cr}}(\mathbf{R})$  has been incorporated through the mass tensor  $M$ .

### 1.1.2 Heterojunctions and band engineering

To further manipulate the behavior of the freely moving conduction band electrons (or valence band holes), different semiconducting crystals can be combined to form heterostructures with typically planar interfaces, or ‘junctions’, between materials of altering composition. The band structure of such inhomogeneous systems, and primarily the band edges  $E_C$  and  $E_V$  relevant for the effectively free motion, become spatially dependent in the direction where the material changes, or direction of ‘growth’ of the heterostructure, which we will take to be the  $z$ -axis. The aim of this ‘band engineering’ is to design desirable and controllable charge carrier properties by combining layers of suitable material parameters and thickness, and appropriately doped with donor or acceptor impurities. More specifically, the 3D motion of the effectively free electrons can be restricted to the 2D plane defined by a heterojunction along the  $z$ -axis between materials with different band gaps. We now describe the formation of such a 2D electron system (2DES) in a GaAs/AlGaAs heterostructure.

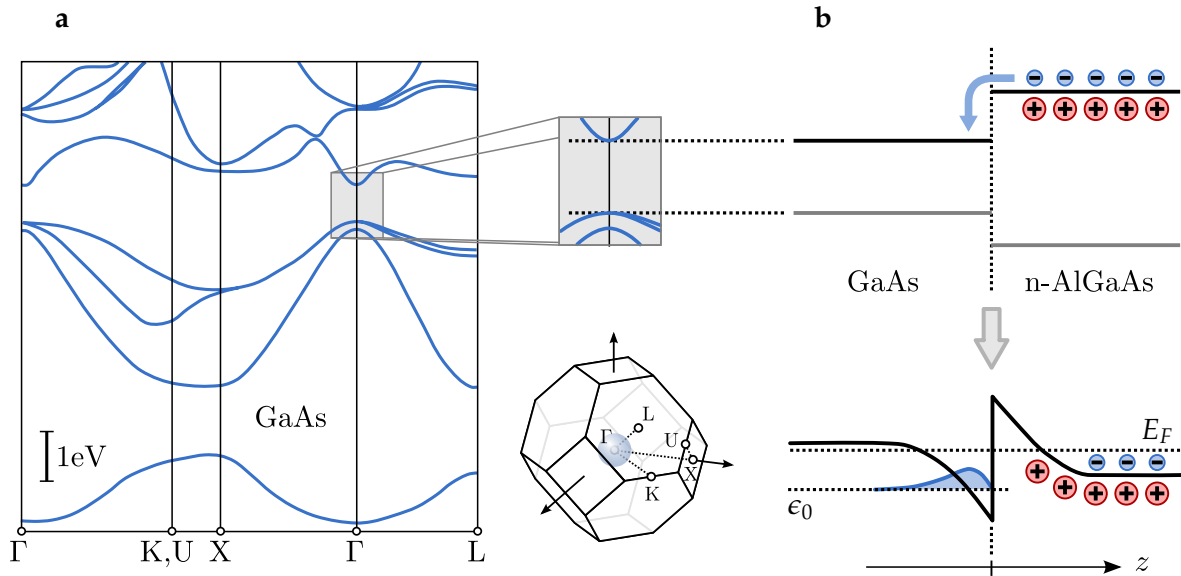


**Figure 1.1:** (a) Band structure of GaAs along the directions in  $K$ -space indicated on the Brillouin zone shown in the lower inset (reproduced from Ref. [125]). The upper inset shows the (direct) band gap between the approximately parabolic conduction and valence bands for electrons with energies close to the band gap edges, with a spherical Fermi surface at the center of the Brillouin zone (lower inset). (b) Upon contact with  $n$ -doped AlGaAs (upper panel) with ionized donors (+), which has a larger band gap aligned with that of GaAs, conduction electrons (-) from the  $n$ -AlGaAs diffuse into the GaAs, and a charge accumulation at the interface induces an electrostatic potential which bends the band edges downwards along  $z$  (lower panel). When the chemical potential (dashed line) on both sides equilibrates, the conduction band edge develops a quantum well on the GaAs side due to the band edge discontinuity across the heterojunction. If the well supports bound states (ground state density shown), then a 2DEG along the  $(x, y)$ -interface can form for Fermi energies within the well.

The most commonly used methods to grow a heterostructure are molecular beam epitaxy (MBE) and metal-organic chemical vapor deposition (MOCVD), by which high quality interfaces with minimal roughness and imperfections can be fabricated [75], of great importance for controllable electron transport along heterojunctions. In MBE, beams containing the heterostructure constituents (here Ga, As and Al, as well as a potential donor dopant Si) at tunable concentration impinge on a substrate in ultrahigh vacuum. In MOCVD, the constituents are carried by hydrogen in gaseous form and consecutively deposited on a heated substrate by chemical reaction. In order to avoid structural defects at the heterojunctions arising from a mismatch in the lattice spacing between the grown materials, constituents are suitably chosen so that the resulting compound crystals will have similar lattice constant.<sup>1</sup> Moreover, in order to form a 2DES at a heterojunction, the contacted materials should optimally have aligned band gaps with relatively small conduction band edge difference, which in turn requires similar electron affinity, the energy needed for an electron at  $E_C$  to escape from the crystal [75]. These requirements are fulfilled for the growth of  $\text{Al}_x\text{Ga}_{1-x}\text{As}$  on a GaAs substrate, where a mixing portion  $x = 0.3$  retains the direct band gap of GaAs and induces a conduction band edge difference  $\Delta E_C = 0.33 \text{ eV}$ . The difference in band gap and edge energies for the separate materials—or connected over a heterojunction, but be-

<sup>1</sup> The strong effect of mechanical strain resulting from lattice constant mismatch between the materials of a heterostructure can in fact also be used as an advantage in terms of flexibility in fabrication, larger  $\Delta E_C$  or increased mobility (smaller effective mass  $m^*$ ), but are not as widely as the standard GaAs/AlGaAs setting we focus on here.

fore thermally equilibrating—is schematically shown in the upper panel of Fig. 1.1(b) for an AlGaAs layer grown on top of GaAs.

To introduce free charge carriers to the system, the AlGaAs layer is doped with donor impurities (typically Si), which ionize to release electrons into the conduction band minimum and thereby elevate the local chemical potential [124]. The donor-doped material is denoted n-AlGaAs, and the simplified process resulting in a 2DES, sketched in Fig. 1.1 (b), is as follows [75]. When the n-AlGaAs layer brought into contact with the GaAs substrate through the growth procedure, the conduction band edge becomes a function of the depth,  $E_C(z)$ , where we set  $z = 0$  at the heterojunction. Part of the ionized donor electrons now diffuse across the junction into the GaAs region. There they lose part of their kinetic energy, as dictated by the discontinuity  $\Delta E_C$  in the band edge between the materials, which prevents them from returning to the n-AlGaAs layer. The system therefore equilibrates, with aligned chemical potential, into an accumulation of electrons at the heterojunction, resulting in an electrostatic potential barrier which suppresses further diffusion of electrons into the GaAs and bends  $E_C(z)$  across the band edge discontinuity.

Finally, a narrow potential well of approximately triangular profile, which we separately denote as  $V_J(z)$ , has formed over a small width  $w_J$  across the heterojunction. Within this junction well, motion along the  $z$ -axis is quantized into (a finite number of) energy levels  $\epsilon_n$ , measured from the bottom  $E_C(z = 0) \equiv E_C^0$  of the well, with corresponding (bound) wave functions  $\zeta_n(z)$ . In the narrow well these levels will have relatively large energy spacing, so that, at sufficiently low temperature, the electrons occupy only the lowest level  $\epsilon_0$ , with a nodeless wave function  $\zeta_0(z)$ . They are thus restricted to a small vertical width at the interface but can move freely, with their effective mass  $m^*$ , in the  $x$ - and  $y$ -directions, thus constituting a 2D free electron gas. Since the transversally confining potential separates out, the single-electron wave function can generally be written as

$$\Psi(\mathbf{R}) = e^{i\mathbf{k}\cdot\mathbf{r}}\zeta_0(z), \quad (1.6)$$

and the 3D free-electron-like dispersion in Eq. (1.5) accordingly reduces to a 2D version,

$$E(\mathbf{k}) = E_C^0 + \epsilon_0 + \frac{\hbar^2}{2m^*}k^2, \quad (1.7)$$

which, in practice, will be offset to the ground level of the junction well,  $E_C^0 + \epsilon_0 \equiv 0$ .

### 1.1.3 Modulation doping and band diagram

The above procedure of doping a region in the heterostructure while populating another region with the provided charge carriers is called ‘remote doping’. Although the donor impurities in the n-AlGaAs layer provide the free electrons in the spatially separated 2DES, the positively charged ions left back still form a disordered potential landscape in the plane of the 2DES which causes (in general undesired) random elastic scattering effects. Therefore, in practice an additional, undoped AlGaAs layer (a ‘spacer’) is grown between the GaAs and n-AlGaAs layers, which separates the donor impurity ions further from the 2DES (see Fig. 1.2). With this so called ‘modulation doping’, the properties charge carriers in the 2DES can be adjusted according to the needs and purpose of the setup. A thick spacer reduces the density of electrons in the 2DES, but at the same time increases their mobility, the latter being of higher importance for the lateral (i.e., within the  $xy$ -plane) electronic transport we will concentrate on.

The electrostatic Coulomb potential of each donor impurity ion in the plane of the 2DES is now weakened by the presence of the spacer, and further screened by the electrons themselves. For a spacer thickness  $d$ , the effective potential that an electron feels at 3D distance

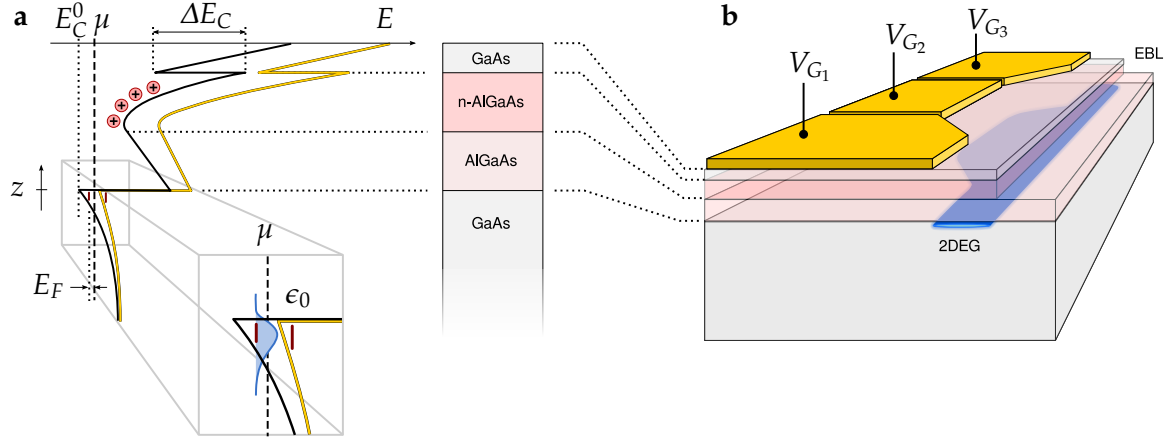


**Figure 1.2:** (a) Band diagram  $E_C(z)$  (black line) of a heterostructure consisting of a GaAs substrate on top of which an undoped AlGaAs spacer layer, a doped n-AlGaAs layer and a GaAs cap are grown, with band edge discontinuity  $\Delta E_C$  between GaAs and AlGaAs. (b) Section of a nanoelectronic device defined (on the left) by top gate voltages  $V_{G_{1,2,3}}$  applied to independent cap electrodes. For sufficiently negative voltages, the band diagram in (a) is modified (yellow line) locally below the top gates such that the Fermi level  $\mu$  lies below the ground energy level  $\epsilon_0$  of the heterojunction well at  $z = 0$ . The 2DEG is thus depleted below the top gates leading to an effective confinement potential defining the device. As shown on the right, confinement can alternatively be achieved by etching away material (e.g., by electron-beam lithography) from the heterostructure, with depletion being caused by highly occupied surface states (see text).

$R_{\text{imp}} = \sqrt{r_{\text{imp}}^2 + d^2}$  from a pointlike impurity can be modeled by [75]

$$V_{\text{scr}}(R_{\text{imp}}) = \frac{A(d)}{R_{\text{imp}}^3} = \frac{e^2}{4\pi\epsilon_0\epsilon_b} \frac{q_{\text{TF}}(1 + q_{\text{TF}}d)}{q_{\text{TF}}^3} \frac{1}{(r_{\text{imp}}^2 + d^2)^{\frac{3}{2}}}, \quad (1.8)$$

where  $\epsilon_b$  denotes the relative permittivity of the material. The Thomas-Fermi screening wave number  $q_{\text{TF}}$  is, for the low temperatures we will consider, approximated by  $q_{\text{TF}} \approx 2/a_B$ , where  $a_B$  is the effective Bohr radius. Typical values for a GaAs semiconductor are  $\epsilon_b = 13.8$  and  $a_B = 9.8$  nm.

Above the doped n-AlGaAs layer, the heterostructure is typically further equipped with an undoped ‘cap’ layer (GaAs in Fig. 1.2) which shields the donor charges from the sample surface, on top of which metallic gates at tunable voltage may be positioned. The band edge  $E_C(z)$ , which has bended upwards along  $z$  in the doped layer due to the accumulation of positive charges, develops a discontinuity at the interface to the cap, much like the one at  $z = 0$ ; see Fig. 1.2 (a). This well is, however, empty of occupying electrons, since it lies above the Fermi level  $\mu$  in the present configuration. The chemical potential  $\mu_G$  at the metal gate on the surface of the heterostructure is usually ‘pinned’ by partly occupied surface states below the conduction band edge, and  $\mu = \mu_G + eV_G$  can be controlled by an applied gate bias voltage  $V_G$  (note that the electron charge is set to  $q_e = -e < 0$ ). Besides the above general characteristics, the exact form of the band diagram sketched in Fig. 1.2 (a) requires a full self-consistent determination of the electrostatic potential building up and the associated charge density, with the layer thicknesses and dopant concentration as inputs [75].

## 1.2 Coherent transport devices

Having established a simple picture of effectively free electronic motion at heterostructure interfaces, we now briefly describe how 2D transport devices can be designed and under

what circumstances quantum effects can be observed in such setups. These conditions will provide the basis for the modeling of electronic transport in the following chapters.

### 1.2.1 Shaping the 2DES

Once a 2DES has formed at the heterojunction between two semiconductors, as described above, the effectively free 2D electrons can be further restricted into areas of desirable shape. As will be seen in Chaps. 5, 6 and 7, the particular form of the confinement of the electron gas in the  $xy$ -plane, in combination with an externally applied magnetic field, may lead to interesting quantum transport effects and enable their controllability. Two common experimental techniques to create confinement patterns into a 2DES are biased top gates and chemical etching [126].

By assembling a metallic gate on top of the cap layer of the heterostructure, the Fermi energy at the 2DES, and in turn its electronic density, can be adjusted by application of a bias voltage on the gate, as alluded to previously. Thus, if the bias is such that the Fermi level lies sufficiently below the lowest quantized level of the transversal well,  $\mu < \epsilon_0$ , then at low temperature the level remains unpopulated and the 2DES becomes depleted under the gate. A top gate with a particular geometry or even different top gates next to each other can then be used to deplete the electron gas and thereby give it a desirable shape by adjusting the gate bias. This approach is schematically shown on the left side of Fig. 1.2, where  $\mu > \epsilon_0$  (populated 2DES) is assumed for zero gate bias (or absence of gate), while the electron gas is depleted below some negative threshold voltage. In a simplified picture one can think of a spatially dependent well ground level  $\epsilon_0(\mathbf{r})$ , whose difference from the Fermi level  $\epsilon_0$  defines an effective potential  $V(\mathbf{r})$  which confines 2DES in the  $xy$ -plane. Note, however, that the gate voltage does not only shift the  $\epsilon_0$  alone (and thus the Fermi energy), but also modifies the band diagram of the heterostructure in total. Moreover, the depletion profile of the 2DES does not follow exactly that of the gate(s) on top, but depends on the thickness of the intervening layers and on the applied bias. In other words, the lateral shape of confining potential  $V(\mathbf{r})$  will be smoothed with respect to the top gates and characterized by some boundary softness, that is, a gradual rather than stepwise variation under the top gate edges.

Instead of depleting the 2DES via gate voltages, the in-plane motion of electrons can alternatively be restricted by ‘cutting away’ parts of the heterostructure material itself, as shown in Fig. 1.2. This is done by lithographically marking (e.g., by electron-beam lithography) a desired pattern on a layer of material which can afterwards be removed by wet or dry chemical etching (that is, dissolving the material in solution or in a plasma). In this way, patterned devices can be grown where vertical sidewalls restrict the 2DES. If the all layers are cut down to the substrate, then the 2DES is physically terminated at the sidewall and further depleted by surface states. For some materials (e.g., GaAs), such surface states can be so highly occupied that only the cap layer needs to be etched, with the 2DES then depleted similarly to the case of a negative top gate bias. In fact, also the top gates deposited onto a grown heterostructure are generally patterned by etching. An advantage of using top gates is the ability to vary the effective confining potential  $V(\mathbf{r})$  during an experiment by tuning their bias voltage. On the other hand, etched heterostructures can provide sharper confinement and thus a more precise definition of the device geometry.

To serve as a transport device, the 2D confinement leaves two or more openings, usually in the form of narrow constrictions called ‘quantum point contacts’, to areas connected to metallic electrodes (the terminals), between which a charge current can flow. In a two-terminal setup, e.g., the current flows from a ‘source’ to a ‘drain’ side gate under an applied voltage difference  $V_{SD}$  (see Fig. 1.2 (b)). If the confinement forms a straight segment of

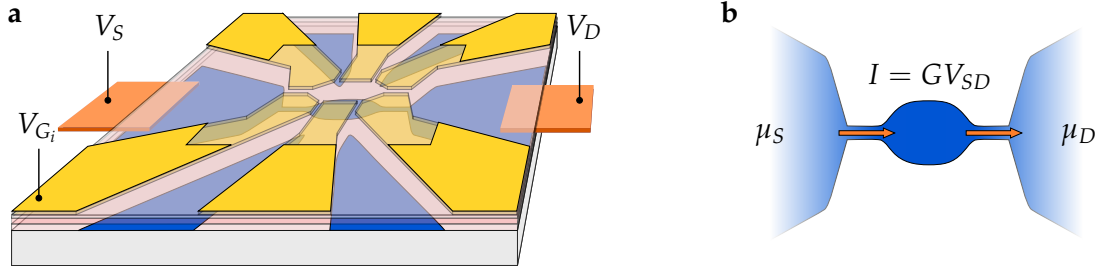


**Figure 1.3:** (a) Two-terminal transport device defined by top gate electrodes with tunable voltages  $V_{G_{i=1,\dots,6}}$  which confine the 2DEG at a heterojunction underneath. A source electrode at voltage  $V_S$  and a drain electrode at voltage  $V_D$  are attached to the part of the 2DEG extending into the device region at the center. (b) The device is theoretically treated as an open system connected to electrodes at chemical potentials  $\mu_{S,D} = eV_{S,D}$ . The current  $I = GV_{SD} = G(V_S - V_D)$  flowing through the device, where  $G$  its conductance, is determined in the Landauer-Büttiker theory of transport developed in Chap. 2.

constant width, along which the (in-plane) transversal potential profile does not vary, the system is referred to as a quasi-1D ‘quantum wire’ and is of particular conceptual importance in transport theory, as we will see in the following. Further confining the 2DES in all directions creates a quasi-0D ‘quantum dot’ of controllable geometry, whose quasi-bound levels typically mediate resonant transport, and also multiply connected (ring-shaped) systems can be formed which provide spatially separated pathways for the electronic motion. Finally, elements such as the above can be connected into arrays and lattices, adding to the plethora of transport structures which can be fabricated.

### 1.2.2 Mesoscopic length scales

With the fabrication techniques described above, the 2DES can be confined to regions of size as small as tenths of nanometers, and so the created devices are called ‘nanoelectronic’. At such system sizes, electronic behavior can thus no longer be described by assigning macroscopic material (bulk) properties; at the same time, the devices are formed over lengths considerably larger than the material lattice constant and cannot be treated at the microscopic level of isolated atoms or molecules. They therefore belong to an intermediate, *mesoscopic* regime, where quantum effects drastically enter the description of electronic transport. Two length scales of fundamental importance for the transport properties of a mesoscopic system are the elastic and inelastic mean free paths of electrons.

The *elastic mean free path*

$$l_e = v_F \tau_e \quad (1.9)$$

is the average length an electron travels at Fermi velocity  $v_F = \hbar k_F / m^* = \sqrt{2E_F / m^*}$  before being elastically scattered, e.g., by a (static) potential of (remote) impurities, within a scattering time  $\tau_e$ . The latter can be found from the mobility  $\mu = e\tau_e / m^*$  of a sample, which in turn depends on the charge density of the 2D electron gas at a particular heterojunction, and yields the diffusion constant  $D = v_F^2 \tau_e / d = v_F l_e / d$  in  $d$  dimensions. Irrespective of its strength, static potential disorder does not break the phase coherence of the electronic wave function, leading to sample-specific (reproducible) quantum interference effects. It imposes, however, limitations on the controllability of transport in a designed confinement potential, since the randomly (though coherently) scattered waves lead to substantial quantum

fluctuations in measured quantities as system parameters are varied, such as the so-called universal conductance fluctuations [118].

The *inelastic mean free path*

$$l_{in} = v_F \tau_\phi \quad (1.10)$$

is the length an electron travels during the phase-breaking time  $\tau_\phi$ , the mean time between consecutive dephasing events, without being elastically scattered, and can be combined with  $l_e$  into the phase coherence (Thouless) length

$$l_\phi = \sqrt{D\tau_\phi} = \sqrt{l_{in}l_e}. \quad (1.11)$$

Such are the inelastic scattering of electrons with lattice phonons or with other electrons, upon which the phase coherence of the scattered electron is lost, other processes which entangle the electronic states with the environment, or even scattering in an applied time-dependent potential which in general also breaks coherence.<sup>2</sup> The inelastic and phase coherence lengths are thus not universally determined for a (doped) material, but depend basically on the properties of a particular setup. They also decrease with increasing temperature, usually being of the order of a few  $\mu\text{m}$  at about 1 Kelvin, but can also be made larger in a high-mobility 2DES (e.g.,  $l_{in} = 5\mu\text{m}$  and  $l_\phi = 1.62\mu\text{m}$  at a GaAs/AlGaAs heterojunction with mobility  $\mu = 10^5\text{cm}^2/\text{Vs}$  [118]).

For a typical mesoscopic semiconductor, the characteristic length scales are typically related as

$$l_e < l_\phi < l_{in} \quad (1.12)$$

at low temperatures [128].

If the size  $L$  (the maximal lateral length) of mesoscopic device designed on a heterostructure is smaller than the phase coherence length (or inelastic mean free path),  $L < l_\phi$  ( $l_{in}$ ), then the wave function in a single electron picture remains coherent during scattering within the confining potential  $V(\mathbf{r})$ . This gives rise to observable interference phenomena and thereby a manifestation of the quantum mechanical nature of electronic transport. With the fabrication techniques outlined above (modulation-doped heterostructures), mesoscopic transport systems can be realized where also the remote impurity potential becomes negligible in the plane of the 2DES, so that also the elastic mean free path exceeds the system size even at small Fermi wavelength  $\lambda_F = 2\pi/k_F$ . Under such circumstances we thus have

$$\lambda < L < l_e, l_\phi \quad (1.13)$$

and transport is said to be *ballistic* [128], with the electron waves in the 2DES scattered only by the boundaries of the confining potential (and not in the bulk of the device). This is the regime we will consider primarily here, with an investigation of the impact of disorder in Chap. 5.

The potential used to simulate such ballistic transport devices is usually chosen uniform (zero) within a 2D region of certain geometry, and the model systems are coined *open quantum billiards*, in resemblance of particle billiards used to study classical dynamics. In this spirit, treating the same system quantum mechanically has established evidence of a quantum-to-classical ‘crossover’ [23, 27, 29] as well as signatures of ‘quantum chaos’ [16, 32, 129]. Regarding electronic transport, the basic experimental probes of quantum interference effects are the shape of the billiard (and the confining potential in general), the positions of the terminal openings, the Fermi energy, and an externally applied magnetic field [128], all of which affect the relative phases between propagating waves in the system.

---

<sup>2</sup> Note that each type of inelastic scattering is generally characterized by a different dephasing time depending on the circumstances, with  $\tau_\phi$  determined from an average inelastic scattering rate [127].

### 1.2.3 Approximations to the Hamiltonian

The effective mass approximation, described above, remains valid if the 3D single-electron envelope [130, 131] wave function  $\Psi(\mathbf{R})$  varies slowly over length scales of the size of the unit lattice cell(s) of the heterostructure. For a heterostructure grown in the  $z$ -direction with diagonal mass tensor  $M$  and spherical Fermi surface (as is the simple case for an [Al]GaAs heterostructure), the conduction band electrons are then described by a time-independent Schrödinger equation

$$\mathcal{H}_{\text{eff}}\Psi(\mathbf{R}) = E \Psi(\mathbf{R}), \quad (1.14)$$

governed by the effective single-particle Hamiltonian

$$\mathcal{H}_{\text{eff}} = \frac{1}{2m^*} \left[ \frac{\hbar}{i} \nabla_{\mathbf{r}} + e\mathbf{A}(\mathbf{r}) \right]^2 + \frac{1}{2} \frac{\hbar}{i} \frac{\partial}{\partial z} \frac{1}{m^*(z)} \frac{\hbar}{i} \frac{\partial}{\partial z} + V_{\text{eff}}(\mathbf{R}), \quad (1.15)$$

where a magnetic vector potential  $\mathbf{A}(\mathbf{r})$  has been included through the (in-plane) minimal-coupling [132] canonical momentum

$$\mathbf{p} = \boldsymbol{\pi} + q_e \mathbf{A} = \boldsymbol{\pi} - e\mathbf{A} = \frac{\hbar}{i} \nabla_{\mathbf{r}}, \quad (1.16)$$

( $\boldsymbol{\pi} = \mathbf{p} + e\mathbf{A} \equiv m\mathbf{v}$  being the kinetic momentum), to produce a perpendicular magnetic field

$$\mathbf{B} = \nabla \times \mathbf{A} \perp \mathbf{r} = (x, y). \quad (1.17)$$

The effective mass is assumed to change only along the direction of growth ( $z$ ) of the different materials, acquiring the value  $m^*(z \leq 0) \equiv m_0^*$  in the layer just below the heterojunction (where the 2DES forms) with the corresponding kinetic operator allowing for current conservation along  $z$  [118].

The effective 3D potential

$$V_{\text{eff}}(\mathbf{R}) = E_C(z) + V_{\text{imp}}(\mathbf{R}) + V_{\text{dev}}(\mathbf{R}) + V_{\text{int}}(\mathbf{R}) \quad (1.18)$$

is here taken to include:

- (i) the conduction band edge profile  $E_C(z)$  resulting from the sample growth,
- (ii) the total potential  $V_{\text{imp}}(\mathbf{R})$  produced by any donor (or acceptor) impurity distribution (screened in the region of the 2DES),
- (iii) the effective potential  $V_{\text{dev}}(\mathbf{R})$  induced by metallic gates or surface charges at etched edges of the transport device, used to confine the 2DES, and
- (iv) a contribution  $V_{\text{int}}(\mathbf{R})$  from many-body interactions, as approximated by a self-consistent Hartree potential or by density-functional theory [118].

In the vicinity  $0 \leq z \leq w_J$  of the 2DES at the heterojunction, we assume the total effective potential to acquire a separable form for motion in the junction plane and normal to it,

$$V_{\text{eff}}(\mathbf{r}, w_J \leq z \leq 0) = V_J(z) + V(\mathbf{r}), \quad (1.19)$$

where  $V_J(z)$  is the (approximately triangular) junction potential well trapping the 2DES and  $V(\mathbf{r})$  is the lateral potential defining the 2D transport device setup.

Since we will primarily be studying the impact of the quantum billiard *geometry* at low energies, we will further mostly assume billiards with ‘hard walls’, that is, a very steep

lateral potential change in  $V_{\text{dev}}(\mathbf{r}, w_J \leq z \leq 0)$  at the confining boundaries. The impact, and advantages, of a ‘soft wall’ boundary will be investigated in Chap. 6. Experimentally, current technology indeed allows for the fabrication of very sharp nanoelectronic device patterns, with potential slope of several meV/nm [18–20], which can be tuned by additional gates [18, 19].

To include the coupling of the electron spin, represented by the Pauli matrix vector  $\sigma$ , to the magnetic field, a Zeeman term

$$\mathcal{H}_\sigma = g_L \mu_B \sigma \cdot \mathbf{B} \quad (1.20)$$

should be included, where  $g_L$  is the effective Landé factor of the material [130, 133] and  $\mu_B = e\hbar/2mc$  is the Bohr magneton, which shifts the energy levels of spin-up and spin-down electrons (the  $z$ -component in the perpendicular field) by  $\pm \frac{1}{2} g_L \mu_B B$ . Spin also couples to the orbital motion of the electrons, which further shifts the energy bands and lifts band degeneracies in the presence of inversion asymmetry in the (crystal or confining) potential, even for  $\mathbf{B} = \mathbf{0}$ . Spin-orbit coupling is therefore particularly relevant for the splitting of heavy and light hole bands and thus for the impact of excitons on the optical properties of low-dimensional heterostructures near band gaps [75]. For a 2DES in the  $xy$ -plane, spin-orbit interaction is usually described by a Rashba Hamiltonian [134]

$$\mathcal{H}_{\text{SO}} = \alpha(\sigma \times \mathbf{k}) \cdot \hat{\mathbf{z}}, \quad (1.21)$$

where the coupling constant  $\alpha$  depends on the heterostructure details [130]. The effect can be tuned by external gates [135] and thus be used to study spin-dependent transport [136–140]. Here, we will restrict ourselves to ‘spinless electrons’, thus neglecting the Zeeman splitting and spin-orbit coupling terms in the Hamiltonian, which can be justified for not too strong magnetic fields and highly symmetric structures with adjustable 2DES density [139], respectively. Even in cases where this does not apply, however, the impact of spin coupling is of secondary relevance to the particular aspects of transport controllability to be studied in Chaps. 5–7: Specifically, our aim will be to control *smooth* (background) variations of transport in varying Fermi energy, so that fine shifts (spin-dependent or not) of resonant features are not expected to affect qualitatively the overall behavior.

### 1.3 Magnetoelectric subbands and transport channels

For energies within junction well,  $E < V_J(-w_J)$ , the effective Schrödinger equation 1.14 for the 2DES in a static setup simplifies to

$$\left\{ \frac{1}{2m_0^*} \left[ \frac{\hbar}{i} \nabla_{\mathbf{r}} + e\mathbf{A}(\mathbf{r}) \right]^2 + V(\mathbf{r}) - \frac{\hbar^2}{2m_0^*} \frac{\partial^2}{\partial z^2} + V_J(z) \right\} \Psi(\mathbf{R}) = E \Psi(\mathbf{R}), \quad (1.22)$$

now with a single effective mass  $m_0^*$  and with a separable solution of the form

$$\Psi(\mathbf{R}) = \psi(\mathbf{r}) \zeta_n(z), \quad (1.23)$$

where  $\zeta_n(z)$  is the  $n$ -th bound state wave function in the junction well corresponding to the energy level  $\epsilon_n$ , and  $\psi(\mathbf{r})$  is the *scattering wave function* of the lateral open transport system (open billiard) with continuous in-plane wave vector  $\mathbf{k}$ .

Approximating the junction by a triangular well (see Fig. 1.2(a)), that is, a linear potential ( $V_J(z < 0) \propto -z$ ) emerging from a hard wall ( $V_J(z = 0) \rightarrow \infty$ ), the transversal solutions are given by Airy functions [75, 141], sketched in Fig. 1.4(b). These vanish at the  $z = 0$  interface

and are, with increasing energy, increasingly localized towards the substrate bulk (more negative  $z$ ), into which they decay exponentially. In absence of the ‘device’ potential and for weak impurity scattering at the 2DES plane, we can set  $V(\mathbf{r}) = 0$  in Eq. (1.19) to obtain, at zero magnetic field, free-electron plane wave solutions  $\psi(\mathbf{r}) = e^{i\mathbf{r}\cdot\mathbf{k}}$  for the in-plane motion. The energy is then given by

$$E = E_{n,k} = \epsilon_n + \frac{\hbar^2}{2m_0^*} k^2, \quad (\text{Q2D}) \quad (1.24)$$

where  $\epsilon_n$  are the Airy eigenenergies [141], whose level spacing reduces as energy increases since the well widens (note that the energy is here offset to the band edge minimum,  $E_C^0 \equiv 0$ ). With a given (Fermi) energy  $E$ , an electron can now move in *subbands* corresponding to the transversal energies with  $\epsilon_n < E$ , with in-plane momentum magnitude  $\hbar k = \sqrt{2m_0^*(E - \epsilon_n)}$  in the  $n$ -th subband. The higher the transversal subband occupied, the lower the available kinetic energy for in-plane motion. Since the junction well can be made relatively narrow, its levels lie enough apart that only the first subband is occupied at low temperature and Fermi energy,  $\epsilon_0 < E < \epsilon_1$ , and we arrive at the previous Eqs. (1.6) and (1.7).

In a similar manner, if the 2DES is further confined into a quantum wire (as described in Sec. 1.2.1), say, along the  $x$ -axis, motion is quantized also laterally in the  $y$ -direction. Considering a steep confining potential  $V(\mathbf{r}) = V_w(x, y)$  in Eq. (1.22), we will assume, for simplicity, an ideal quantum wire with hard walls separated by a width  $w$ ,

$$V_w(x, y) = V_w^0 \theta\left(|y| - \frac{w}{2}\right) = \begin{cases} 0, & |y| < \frac{w}{2} \text{ (inside the wire)} \\ V_w^0, & |y| \geq \frac{w}{2} \text{ (otherwise)} \end{cases}, \quad V_w^0 \rightarrow \infty \quad (1.25)$$

where  $\theta$  is the unit step (Heaviside) function. As explained later in Sec. 2.1, the infinite extent of the wire in each longitudinal ( $\pm x$ ) direction represents the connection of the transport device to an electrode.

Under the boundary conditions imposed by this wire potential (vanishing wave function at the planes  $y = \pm w/2$ ), the in-plane part of the total wave function can now be written

$$\psi(x, y) = \chi_m(y) e^{ik_x x} \equiv \Phi(x, y), \quad (1.26)$$

where

$$\chi_m(y) = \sqrt{\frac{2}{w}} \times \begin{cases} \cos(k_{y,m} y), & m \text{ odd,} \\ \sin(k_{y,m} y), & m \text{ even,} \end{cases} \quad k_{y,m} = \frac{m\pi}{w} \quad (1.27)$$

are the transversal *modes* of the quantum wire (in analogy to the modes of the electromagnetic field in a light waveguide) with eigenenergies

$$E_m = \frac{\hbar^2}{2m_0^*} k_{y,m}^2 = \frac{m^2 \pi^2 \hbar^2}{2m_0^* w^2}, \quad m = 1, 2, \dots \quad (1.28)$$

whose level spacing now increases with  $m$ . For the total energy we thus have

$$E = E_{n,m,k_x} = \epsilon_n + E_m + \frac{\hbar^2}{2m_0^*} k_x^2, \quad (\text{Q1D}) \quad (1.29)$$

so that, for each subband  $n$  of the heterojunction well, we now have motion along the wire in parabolic subbands  $m$  with longitudinal momentum  $\hbar k_x = \sqrt{2m_0^*(E - E_m - \epsilon_n)}$ , as shown in Fig. 1.4. Considering the width of the wire to be larger than that of the heterojunction,  $w > w_J$ , we can assume that the level spacing of the lowest levels is smaller for the wire

confinement, so that the energy can cover a number  $N$  of multiple wire-subbands within the first junction-subband,  $\epsilon_0 < E_1 < E_2 < \dots < E_N < \epsilon_1$ .

The quantization of the 3D effectively-free-electron momentum into heterojunction and QW subbands is schematically shown in Fig. 1.4. While the confinement at the heterojunction plane allows for the formation of the 2DES, the motion in the subbands of the QW confinement provides the origin of *transport channels* and the associated quantization of conductance in mesoscopic structures, as will be shown in Chap. 2.

### Landau levels

For a homogeneous field  $B$  normal to the  $xy$ -plane, the vector potential can be chosen to be of the form

$$A(x, y) = (\nu - 1)By \hat{x} + \nu Bx \hat{y}, \quad (1.30)$$

where  $\nu = 0$  or  $1$  yields the Landau gauges  $A = (-By, 0, 0)$  or  $(0, Bx, 0)$  and  $\nu = 1/2$  yields the symmetric gauge  $A = (-By/2, Bx/2, 0)$ . Setting  $\nu = 0$ , the stationary Schrödinger equation for  $\psi(\mathbf{r})$  becomes

$$\left\{ \frac{\hbar^2}{2m_0^*} \frac{\partial^2}{\partial y^2} + \frac{1}{2} m_0^* \omega_c^2 [y - y_c]^2 + V(x, y) \right\} \psi(x, y) = E\psi(x, y), \quad (1.31)$$

where  $\omega_c = eB/m_0^*$  is the classical cyclotron frequency and

$$y_c = -\frac{p_x}{q_e B} = \frac{\hbar}{ieB} \frac{\partial}{\partial x}. \quad (1.32)$$

In the absence of confinement,  $V(x, y) = 0$ , the Hamiltonian commutes with  $p_x$  and thus has eigensolutions of the form

$$\psi(x, y) = \chi_l(y) e^{ik_x x}, \quad (1.33)$$

where the  $\chi_l(y)$  are now the eigenfunctions (a Gaussian function times Hermite polynomials) of a harmonic oscillator shifted by  $y_c = \hbar k_x / eB$ , which in turn is the (conserved) center ordinate of a classical cyclotron orbit [71]. Consequently, the states arrange into infinitely degenerate *Landau levels* with eigenenergies

$$E_l = \left( l - \frac{1}{2} \right) \hbar \omega_c, \quad l = 1, 2, \dots \quad (1.34)$$

yielding zero group velocity, with the corresponding classical cyclotron radii being  $r_l = v/\omega_c = \sqrt{2m_0^* E_l} / eB$ . The magnetic length  $\ell_m = r_0 = \sqrt{\hbar / eB}$  is the radius of a disk enclosing the magnetic flux quantum  $\phi_0 = h/e$ , and the degeneracy of the ground Landau level is counted by the number of such disks resulting in flux density  $B$  for a given area of the 2DES.

### Edge states

In the presence of a QW confinement along the  $x$ -axis,  $V(\mathbf{r}) = V(y)$ , the longitudinal momentum  $\hbar k_x$  (and thus the cyclotron center ordinate  $y_c$ ) is still conserved under the chosen gauge  $\nu = 0$  in Eq. (1.30), but the degeneracy of the Landau levels is lifted and Q1D *magnetoelectric* subbands form. This is seen analytically [142, 143] for a harmonic confinement potential  $V(y) = m_0^* \omega^2 y^2 / 2$ , which can be combined with the magnetic one into an oscillator potential with hybrid frequency  $\tilde{\omega} = \sqrt{\omega^2 + \omega_c^2}$ , such that a continuous term is added to the total energy [118],

$$E = E_{n,l,k_x} = \epsilon_n + \tilde{E}_l + \frac{\hbar^2}{2\tilde{m}^*} k_x^2, \quad l = 1, 2, \dots, \quad (1.35)$$

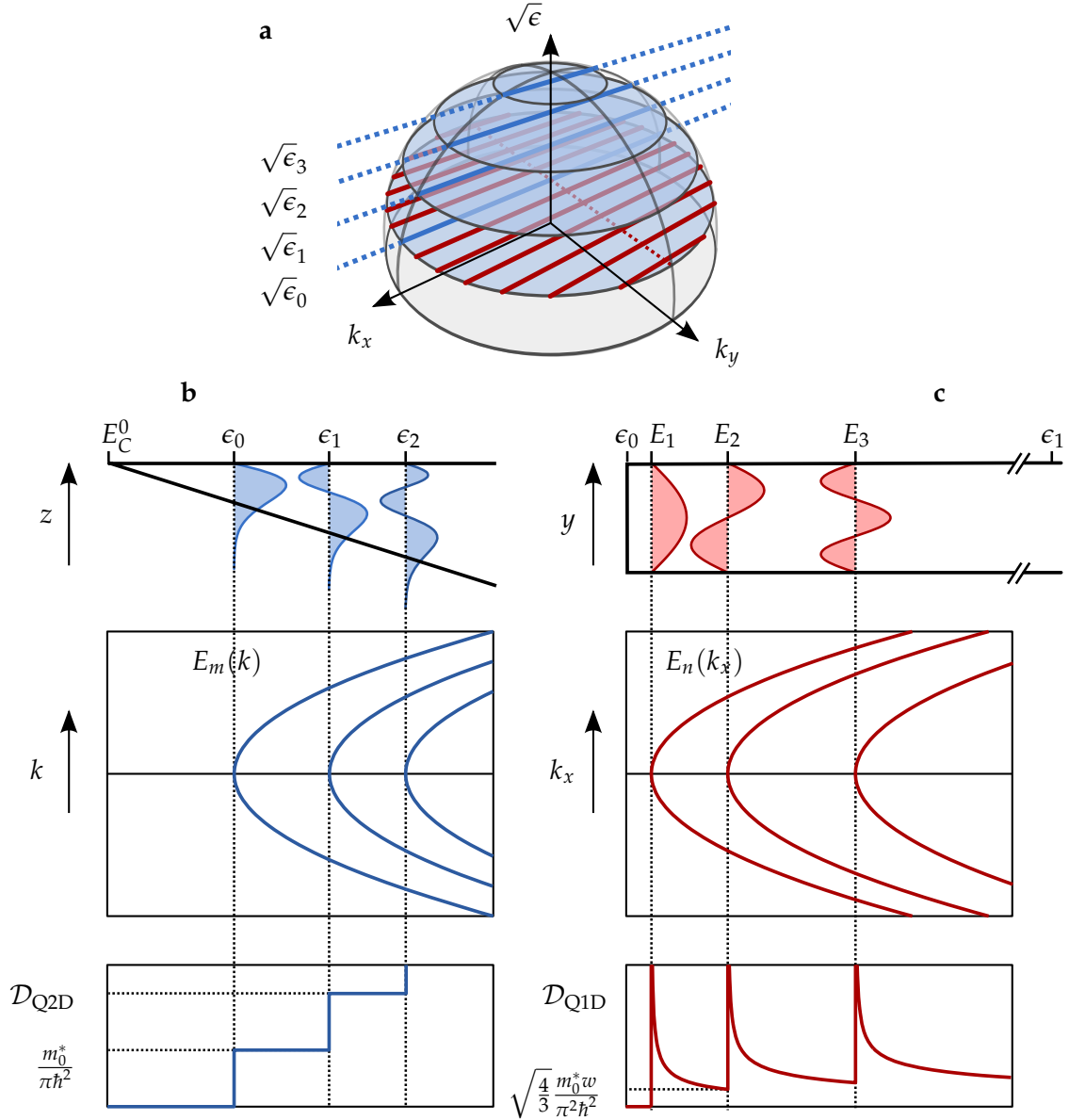


**Figure 1.4:** Energy quantization into subbands. (a) Energy (blue lines) and momentum (red lines) quantization for simultaneous confinement in a triangular junction well  $V_J(z)$  and a square quantum wire well  $V_w(y)$ , respectively. For a given energy, the motion of a state in the first level  $\epsilon_0$  of  $V_J(z)$  is further quantized in the  $y$ -direction, with allowed values of  $k$  along the red lines. (b) Energy levels and wavefunctions of  $V_J(z)$  (top), corresponding subbands of in-plane motion (middle) and density of states (bottom). (c) Energy levels and wavefunctions of  $V_w(y)$  (top), corresponding subbands of motion along  $x$  (middle) and density of states (bottom), where the shown energy range is assumed to lie within the first subband of the  $z$ -confinement.

in similarity to Eq. (1.29) but with magnetically defined band thresholds through  $\tilde{E}_l = (l - 1/2)\hbar\tilde{\omega}$ , and with rescaled effective mass  $\tilde{m}^* = m_0^*(\tilde{\omega}/\omega)^2$  and cyclotron center ordinate  $\tilde{y}_c = y_c\omega_c/\tilde{\omega}$ . Note that, for a given field strength  $B$  and energy  $E$ , states with larger  $|k_x|$  are transversally localized (as approximated by their cyclotron center ordinate) closer the edges of the wire, with positive (negative) group velocity  $v_{n,l} = \hbar k_x / \tilde{m}^* = \pm [2(E - \epsilon_n - \tilde{E}_l) / \tilde{m}^*]^{1/2}$  at the upper (lower) border, since  $y_c \propto k_x$ .

These *edge states* are more clearly visualized in association to their classical counterparts in a hard-wall QW potential, Eq. (1.25), where reflection is specular at the bound-

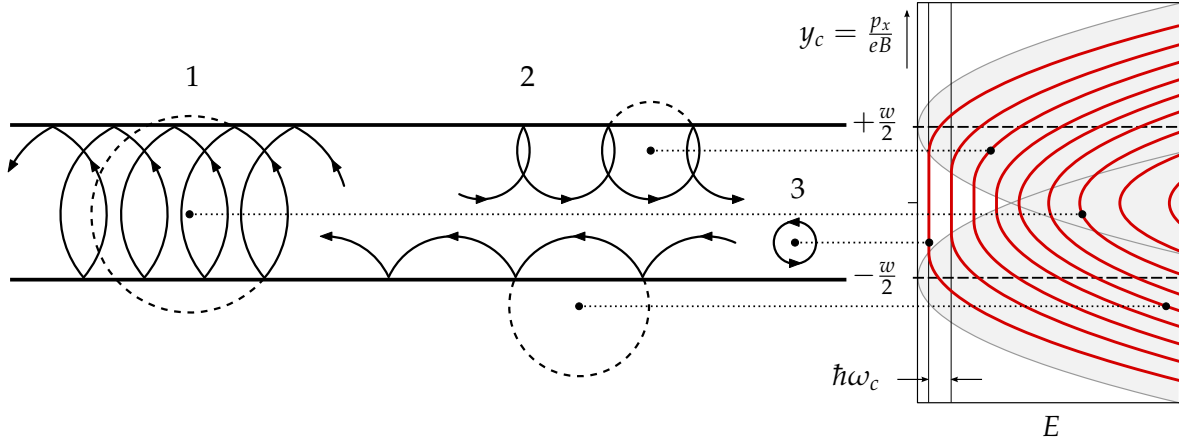


**Figure 1.5:** Energy dispersion with magnetoelectric subbands for a hard-wall quantum wire of width  $w$  in a magnetic field corresponding to cyclotron frequency  $\omega_c$  (right), and selected traversing (1), skipping (2) and cyclotron (3) classical trajectories with guiding centers  $y_c = p_x / eB$  corresponding to points in the dispersion subbands. Right- and left-moving skipping orbits (corresponding to edge states) lie within the upper and lower parabolas  $2m_0^*E = [eB(y_c \mp w/2)]^2$  [71], with cyclotron orbits between them and traversing orbits in their overlap.

aries. The dispersion can here be found numerically [118] and is sketched in Fig. 1.5 for a relatively strong field together with characteristic classical trajectories. The bands are no longer parabolic: The lower the band, the more it tends to flatten in the bulk (around the axis) of the wire, so that these states have vanishing group velocity. Closer to the wire edges, the bands bend upwards and the associated states thus propagate in opposite  $x$ -directions on opposite edges. Edge states correspond to classical *skipping* orbits with  $w/2 - |y_c| < r_l < w/2 + |y_c|$ , bulk-confined states (with no contribution to transport) to *cyclotron* orbits with  $r_l < w/2 - |y_c|$ , and transversally extended states to *traversing* trajectories with  $r_l > w/2 + |y_c|$ .

## 1.4 Density of states

Apart from the reduction and controllability of scattering processes in the 2DES (compared to 3D systems), its lower dimensionality also simplifies the observation and description of quantum effects in electron transport due to its modified density of states (DOS). The DOS in energy,  $\mathcal{N}(E)$ , is a simple property characterized by the dimensionality of a system, and provides information about the distribution of states, even when details of the states themselves and their energy levels are unknown. It is determined by the number of states  $\mathcal{N}(E)dE$  available in the energy interval from  $E$  to  $E + dE$ , and can thus be generally defined as a sum

$$\mathcal{N}(E) = \sum_n \delta(E - E_n) \quad (1.36)$$

on the levels  $E_n$  of any system, which is converted to an integral for (quasi-) continuous spectra. In the case of a band structure  $E_n(\mathbf{K})$ , the sum runs over all crystal momenta  $\hbar\mathbf{K}$  and all bands  $n$  as well as eventual band and spin degeneracies.

To obtain the DOS per unit volume,  $\mathcal{D}(E)$ , states can be counted first in  $d$ -dimensional  $\mathbf{K}$ -space, the wave vectors being quantized by imposed (periodic) boundary conditions on a box, and then transformed to a DOS in energy through the system's dispersion relation. This gives a density  $\mathcal{D}_d(\mathbf{K}) = 2/(2\pi)^d$  per unit (length) <sup>$d$</sup>  in  $\mathbf{K}$ -space, where the factor 2 accounts

for electronic spin degeneracy. For a ‘truly’ free-electron dispersion relation  $E = \frac{\hbar^2}{2m^*} \sum_{i=1}^d k_i^2$ , the DOS in energy  $E \geq 0$  per unit volume becomes [75]

$$\mathcal{D}_1(E) = \frac{1}{\pi\hbar} \sqrt{\frac{2m^*}{E}}, \quad \mathcal{D}_2(E) = \frac{m^*}{\pi\hbar^2}, \quad \mathcal{D}_3(E) = \frac{m^*}{\pi^2\hbar^3} \sqrt{2m^*E} \quad (1.37)$$

for  $d = 1, 2, 3$  dimensions, respectively. Here, the  $1/\sqrt{E}$  divergence of the 1D density as well as the constancy of the 2D density are to be noted, which have important implications for the theory of transport to be developed. A common feature in all dimensions is that the density increases with the effective mass  $m^*$ .

For the confined Q1D and Q2D systems discussed previously, the dimensional characteristics in Eq. (1.37) are repeated in each subband. Inserting the corresponding dispersions, Eqs. (1.29), (1.24), into the defining Eq. (1.36) and integrating over the wave vectors (times 2 for spin, and accounting for both positive and negative  $k_x$  in Q1D), we obtain, respectively,

$$\mathcal{D}_{\text{Q1D}}(E) = \frac{m_0^*}{\pi\hbar^2} \sqrt{\frac{2\hbar^2}{m_0^*}} \sum_{n,m} \frac{\theta(E - \epsilon_n - E_m)}{\sqrt{E - \epsilon_n - E_m}}, \quad \mathcal{D}_{\text{Q2D}}(E) = \frac{m_0^*}{\pi\hbar^2} \sum_n \theta(E - \epsilon_n). \quad (1.38)$$

The density thus increases stepwise for each populated subband of the unconfined 2DES, and with subband threshold divergencies (which are attenuated under more realistic conditions) for the ideal QW confinement.

In the presence of a magnetic field, the unconfined 2DES of (piecewise) constant DOS condenses into the discrete Landau levels, each level  $l$  populated by all states between  $E_l \pm \hbar\omega_c/2$ , so that the Fermi level is discontinuously (for an ideal 2DES) pinned to the successive lower Landau levels with increasing field  $B$  to keep the number of electrons constant [75]. In the Q1D confinement, the density behaves like  $\mathcal{D}_{\text{Q1D}}(E)$  above, though with magnetoelectric subband thresholds.

### Charge density

The density of electrons in energy and space of a system at chemical potential  $\mu$  is obtained by multiplying the DOS with the probability density for an electron to occupy a state of energy  $E$  at temperature  $\Theta$ , given by the Fermi-Dirac distribution (or occupation) function,

$$f(E; \mu, \Theta) = \left[ 1 + \exp\left(\frac{E - \mu}{k_B\Theta}\right) \right]^{-1}, \quad (1.39)$$

where  $k_B$  is Boltzmann’s constant. Integrated over all available energies, the spatial electronic density for a homogeneous system (with a spatially invariant  $\mathcal{D}$ ) is thus defined as

$$n(\mu) = \int_E dE \mathcal{D}(E) f(E; \mu, \Theta), \quad (1.40)$$

where, for the conduction electrons relevant here, the lower limit of integration is set to the bottom  $E_C$  of the conduction band. In the case of a 2DEG, we insert  $\mathcal{D}_{\text{Q2D}}$  into Eq. (1.40) to obtain

$$n_{\text{Q2D}}(\mu) = \sum_n n_n(\mu) = \frac{m_0^*}{\pi\hbar^2} k_B\Theta \sum_i \ln \left[ 1 + \exp\left(\frac{\mu - \epsilon_i}{k_B\Theta}\right) \right], \quad (1.41)$$

where  $n_n$  is the charge carrier density in the  $n$ -th subband of the heterojunction confinement and energies are offset to  $E_C$ .

In the limit of zero temperature, the Fermi-Dirac distribution approaches a step function at  $\mu$ ,

$$f(E; \mu, \Theta \rightarrow 0) \rightarrow \theta(\mu - E), \quad (1.42)$$

meaning that, at very low temperatures, only states close to the Fermi level can contribute to dynamical phenomena such as transport, since all other states are either completely empty or completely occupied, and the electron gas is referred to as ‘degenerate’. The electron density is then practically given by integrating up to  $\mu$  in Eq. (1.40), or, alternatively, taking the limit  $\Theta \rightarrow 0$  in Eq. (1.41), which yields

$$n_{\text{Q2D}}(\mu) = \sum_i n_i(\mu)|_{\Theta \rightarrow 0} = \frac{m_0^*}{\pi \hbar^2} \sum_i (\mu - \epsilon_i) \theta(\mu - \epsilon_i). \quad (1.43)$$

Further, in the so called ‘quantum limit’ of low electronic energy, to which we will restrict ourselves here, only the first subband  $i = 1$  is populated, which yields a density directly proportional to the Fermi energy  $E_F = \mu - \epsilon_1$ ,

$$n_{\text{Q2D}} = n_{2\text{D}} = n_1(\mu, \Theta \rightarrow 0) = \frac{m_0^*}{\pi \hbar^2} E_F = \frac{k_F^2}{2\pi}, \quad (1.44)$$

that is, the 2D density  $2/(2\pi)^2$  in  $k$ -space times the area  $\pi k_F^2$  of the Fermi surface (a circle in 2D). Note here that, since the electron density normally does not vary with temperature [75], Eq. (1.41) for the first subband ( $i = 1$ ) can be divided by Eq. (1.44) to give a temperature dependence of the chemical potential,

$$\mu(\Theta) = \epsilon_1 + \ln \left[ \exp \left( \frac{\Theta_F}{\Theta} \right) - 1 \right], \quad (1.45)$$

where  $\Theta_F = E_F/k_B$  is the Fermi temperature, so that  $E_F \equiv \mu(\Theta) - \epsilon_1$ . This dependence of  $\mu$  is negligible, however, for the low temperatures  $\Theta \ll \Theta_F$  which establish the degenerate 2DEG.

---

# Coherent electronic transport: Landauer-Büttiker formalism

---

Having described the transverse quantization of motion into subbands in low-dimensional mesoscopic systems, we will now see how these are utilized to describe coherent transport through devices like quantum billiards within the effective independent-electron picture. This is done within the Landauer-Büttiker theory of transport in multiterminal structures, which relates the scattering matrix of the system to its electrical conductance. After presenting the general framework, we focus on the linear response regime of transport.

## 2.1 Leads and reservoirs

In order to cause the electrons of a 2DES to flow through a designed transport device, a bias voltage  $V_{SD}$  is applied between a source and a drain electrode attached to it through metallic contacts. The contacts are typically attached to regions of the 2DES which extend spatially beyond the mean free path and, more importantly, the coherence length of the electrons, and connected to the actively coherent (and ballistic) region of the device—in our case a quantum billiard structure—via constrictions in the form of quantum point contacts, the *terminals*. Any phase relation between distant points during scattering within the device is thus completely lost upon exiting through one of the device terminals, and the contacts are thus said to be ‘decohering’. Since inelastic scattering takes place in the contact regions, energy can be redistributed among the charge carriers, allowing for dissipation of the power generated by a flowing current.

In the state of current flow, the total system is not in equilibrium, and therefore no true Fermi level can be assigned to it. However, if the applied bias voltage  $V_{SD}$  is small enough, the system is not driven strongly out of equilibrium, and local quasi-Fermi levels [75]  $\mu_S$  and  $\mu_D$  can be assigned to the source and drain reservoirs, respectively, energetically separated by the potential energy due to the bias,

$$\mu_S - \mu_D = eV_{SD}. \quad (2.1)$$

Recall that we define the electron charge as  $q_e = -e < 0$ , so that a positive voltage on the drain lowers the electronic energy by  $-eV$ . The quasi-Fermi levels themselves depend on the local charge concentration and on the temperature  $\Theta$ , but for the weak deviations from equilibrium and low temperatures we will be considering, it is commonly assumed that the electrons provided by each reservoir for transport through the device are distributed according to a corresponding Fermi-Dirac occupation function,

$$f_p(E; \Theta) \equiv f(E; \mu_p, \Theta), \quad p = S, D. \quad (2.2)$$

Electrons that arrive at or emerge from the terminals are thus statistically distributed in the Fermi sea of available electronic levels. Therefore, the contact regions can be thought of as electron *reservoirs* releasing or accepting electrons without practically affecting the local chemical potentials  $\mu_p$ . Electrons entering a contact region from the side of the device through the connecting terminal cannot be *coherently* re-entered (backscattered) into the device, but are rather absorbed by the Fermi sea in the reservoir. For an individual electron, the situation would be equivalent if the terminal were connected to a still perfectly coherent contact, but in the form of a ideal quantum wire extending to infinity, a semi-infinite *lead*. The connection of a general multiterminal transport device to electron reservoirs can therefore be represented by attaching an equal number of such semi-infinite leads, each lead  $p$  lying at a Fermi level  $\mu_p$ , as shown in Fig. 2.1 (a), with energies occupied according to  $f_p(E; \Theta)$ . In dependence of the width of the terminal constriction  $w_p$ , the representing lead supports propagation in corresponding (magneto)electric subbands  $E_m^{(p)}(k_x)$ , where the  $x$ -axis is locally aligned along each lead.

## 2.2 Scattering matrix and transmission function

With leads representing the connection to electron reservoirs, which in turn correspond to the attached (biased) electrodes, the open 2D cavity of the transport device alone can now be treated as a scattering system: Electron waves incident in one of the leads enter the cavity, scatter off the 2D confining potential and are transmitted into other leads or reflected into the same lead, as shown in Fig. 2.1 (b).

### 2.2.1 Lead eigenmodes

Supplying each lead  $p$  with an in-plane coordinate system  $(x_p, y_p)$ , in the asymptotic region  $x_p \rightarrow \infty$  of the  $p$ -th lead the scattering wave function  $\psi(\mathbf{r})$  at energy  $E$  can be written as

$$\psi(x_p, y_p) = \sum_{m=1}^{N_p} \sum_{s=+,-} a_{m,s}^{(p)} \Phi_{m,s}^{(p)}(x_p, y_p), \quad x_p \rightarrow \infty \quad (2.3)$$

with the lead eigenfunctions now defined as

$$\Phi_{m,s}^{(p)}(x_p, y_p) = \frac{\varphi_m^{(p)}(y_p)}{\sqrt{v_m^{(p)}}} e^{is k_{x,m}^{(p)} x_p}, \quad s = +, - \quad (2.4)$$

where  $v_m^{(p)} = \hbar k_{x,m}^{(p)} / m_e$  (we will denote the in-plane effective mass by  $m_e$  from here on) is the longitudinal velocity in the  $m$ -th channel of the lead with transverse wave function  $\varphi_m^{(p)}$ , and the sign  $s = + (-)$  denotes propagation outwards (inwards) within the lead.

The lead eigenstates are now flux normalized [144, 145] with respect to the longitudinal motion along  $x_p$ ,

$$\langle \Phi_{n,s'}^{(q)}(E') | \Phi_{m,s}^{(p)}(E) \rangle = \delta_{qp} \delta_{nm} \delta_{s's} \delta(E' - E), \quad (2.5)$$

so that the probability current carried by a mode with unit amplitude is simply

$$\hat{\mathbf{j}}_{m,s}^{(p)} = s \hat{\mathbf{x}}_p, \quad (2.6)$$

independent of the channel momentum  $\hbar k_{x,m}^{(p)}$ .

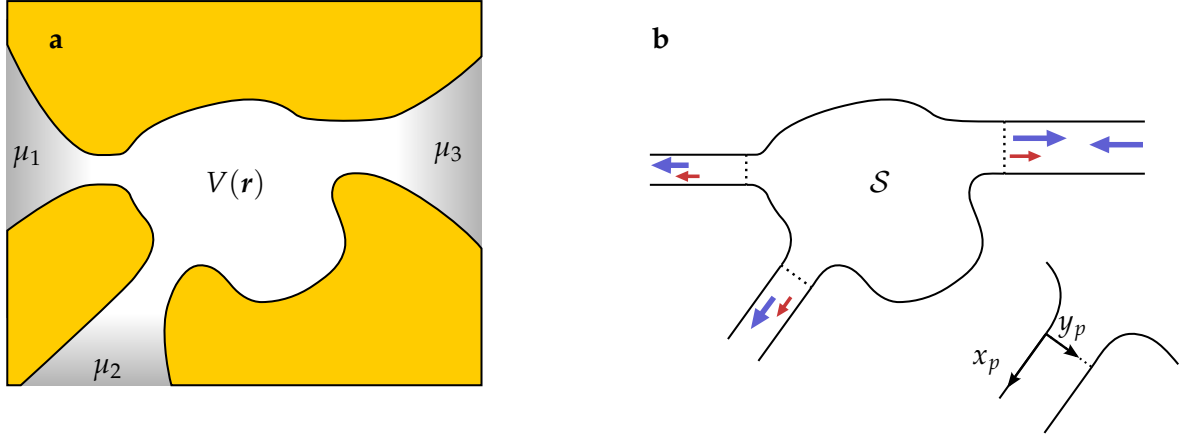


**Figure 2.1:** Sketch of a three-terminal transport device. (a) The gate-induced confinement potential separates the 2DEG in the device region from electrodes at local quasi-Fermi levels  $\mu_{1,2,3}$ , which correspond to decohering electron reservoirs. (b) The device is modeled by a quantum billiard attached (at the dotted lines) to straight semi-infinite leads of widths corresponding to the constrictions in the device. An incoming wave (here from lead 3) is scattered via the  $S$ -matrix of the system outwards into all channels of all leads.

For simplicity, we will assume ‘flat’ leads of widths  $w_p$  with zero (infinite) potential inside (outside), as described by the ideal QW potential (1.25) along  $x = x_p$ , so that the corresponding transversal wave functions  $\varphi_m^{(p)}(y_p)$  and energy levels  $E_m^{(p)}$  are given by Eqs. (1.27) and (1.28). The modes  $m$  are summed up to the total number of *open* channels in the lead

$$N_p(E) = \sum_m \theta(E - E_m^{(p)}) = \text{int} [\tilde{k}_p(E)], \quad (2.7)$$

where the scaled momentum  $\tilde{k}_p = w_p k / \pi$  (for the flat leads considered) serves as a continuous channel number for lead  $p$ . Note here that the energy is offset to the zero-point energy of the Q2D confinement of the 2DES above the conduction band minimum at  $z = 0$ , that is, we set  $\epsilon_0 \equiv 0$  in Eq. (1.29). Higher channels with  $m > N_p$  are *closed* for propagation since the longitudinal wavenumber in that case becomes imaginary,  $k_{x,m}^{(p)} = \pm i|\kappa_{x,m}^{(p)}|$ ; the corresponding (physically allowed) solutions, called *evanescent* modes, decay exponentially as  $x_p \rightarrow \infty$  and are therefore not included in the asymptotic expansion (2.3).

### 2.2.2 Transmission amplitudes and coefficients

It is the linearity of the (effective) Schrödinger equation that allows for its general solution to be written in the form of the superposition (2.3), and the amplitudes  $a_{m,s}^{(p)}$ , which will generally vary among different leads and modes, are thus linearly interrelated in the basis  $\{|\Phi_{m,s}^{(p)}\rangle\}$  of the eigenchannels. In a transport setting, it is natural to treat the electrons coming out from the device at a given energy  $E$  as the response of the system to those injected, on which one usually has an experimental handle. Accordingly, the amplitudes of outwards scattered states  $|\Phi_{m,+}^{(p)}\rangle$  in all leads  $p = 1, 2, \dots, N_L$  are expressed as a linear combination of the ingoing ones  $|\Phi_{m,-}^{(p)}\rangle$  through a square *scattering matrix*  $\mathcal{S}$  of dimension  $N_S = \sum_{p=1}^{N_L} N_p$ ,

$$\vec{a}_+(E) = \mathcal{S}(E)\vec{a}_-(E), \quad (2.8)$$

where the  $N_S \times 1$  column ‘vectors’  $\vec{a}_\pm$  collect all in- and outgoing amplitudes,

$$\vec{a}_s = \begin{pmatrix} \mathbf{a}_s^{(1)} \\ \mathbf{a}_s^{(2)} \\ \vdots \\ \mathbf{a}_s^{(N_L)} \end{pmatrix}, \quad \mathbf{a}_s^{(p)} = \begin{pmatrix} a_{1,s}^{(p)} \\ a_{2,s}^{(p)} \\ \vdots \\ a_{N_p,s}^{(p)} \end{pmatrix}, \quad s = +, -. \quad (2.9)$$

Denoting by  $|\psi_{n,+}^{(p)}\rangle$  the *scattering state* with *ingoing* wave only in mode  $n$  of lead  $p$  and scattered outgoing waves in all leads and modes, and by  $|\psi_{n,-}^{(p)}\rangle$  the *time reversed* state, with *outgoing* wave only in mode  $n$  of lead  $p$  and ingoing in all leads and modes, the (energetically ‘on-shell’) scattering matrix ( $S$ -matrix) elements can be expressed as the projection [128]

$$\langle \psi_{n,-}^{(q)}(E') | \psi_{m,+}^{(p)}(E) \rangle = \mathcal{S}_{qp}^{nm} \delta(E' - E), \quad (2.10)$$

and the asymptotic ( $x_q \rightarrow \infty$ ) wave function in lead  $q$  of a scattering state  $|\psi_{m,s}^{(p)}\rangle$  at energy  $E$  is

$$\psi_{m,s}^{(p)}(x_q, y_q) = \delta_{qp} \Phi_{m,-s}^{(q)}(x_q, y_q) + \sum_{n=1}^{N_q} \mathcal{S}_{qp}^{nm} \Phi_{n,s}^{(q)}(x_q, y_q), \quad s = +, -. \quad (2.11)$$

In other words,  $\mathcal{S}_{qp}^{nm}$  represents the probability amplitude to scatter from ingoing mode  $m$  in lead  $p$  into outgoing mode  $n$  in lead  $q$  at a given energy  $E$ . This becomes evident in terms of the probability flux

$$\mathbf{j}^{(p)} = \sum_{n=1}^{N_p} (\mathbf{j}_{n,+}^{(p)} + \mathbf{j}_{n,-}^{(p)}) = \sum_{n=1}^{N_p} (|a_{n,+}^{(p)}|^2 - |a_{n,-}^{(p)}|^2) \hat{\mathbf{x}}_p, \quad (2.12)$$

of the asymptotic state (2.3): The probability of an ingoing flux in (lead,mode)=  $(p, m)$  to transmit into (lead,mode)=  $(q, n)$  is given by the *partial transmission coefficient*

$$T_{qp}^{nm} = \frac{|\mathbf{j}_{n,+}^q|}{|\mathbf{j}_{m,-}^p|} = \frac{|a_{n,+}^q|^2}{|a_{m,-}^p|^2} = |\mathcal{S}_{qp}^{nm}|^2. \quad (2.13)$$

The total transmission coefficient, or *transmission function*  $T_{qp}(E)$ , from lead  $p$  to lead  $q$  is obtained by summing over all channels,

$$T_{qp} \equiv \sum_n \sum_m T_{qp}^{nm} = \text{Tr}[\mathcal{S}_{qp}^\dagger \mathcal{S}_{qp}], \quad (2.14)$$

where  $\mathcal{S}_{qp}$  is the sub-matrix of  $\mathcal{S}$  connecting the mode amplitudes of leads  $p$  and  $q$ .

## Unitarity

Each of the two sets of scattering states  $\{|\psi_{m,s}^{(p)}\rangle\}$  with  $s = +, -$  (the ‘physical’ one with outgoing scattered waves,  $s = +$ , being more closely connected to experiment), forms a complete orthonormal basis [144, 146, 147], and are therefore connected by a unitary transformation. The connection is given by Eq. (2.10), which means that the total  $S$ -matrix is *unitary*,

$$\mathcal{S}^\dagger \mathcal{S} = \mathcal{I}_{N_S}. \quad (2.15)$$

This is also seen from a more physical perspective in terms of the probability flux through the system. Indeed, unitarity of  $\mathcal{S}$  ensures the conservation flux, as seen directly from

Eq. (2.8): The total ingoing flux is given by  $\|\vec{a}_-\|^2 = \vec{a}_-^\dagger \vec{a}_-$ , and this norm is preserved under the transformation,

$$\sum_p \sum_n |j_{n,+}^q| = \|\vec{a}_+\|^2 = \mathcal{S}^\dagger \mathcal{S} \|\vec{a}_-\|^2 = \|\vec{a}_-\|^2 = \sum_q \sum_n |j_{n,-}^q|, \quad (2.16)$$

only if Eq. (2.15) holds, so that the outgoing flux equals the ingoing one.

Choosing a particular mode  $m$  in a lead  $p$ , the unitarity of  $\mathcal{S}$  implies that its partial transmission coefficients to all modes in all leads, but also *conversely*, the coefficients from all leads and modes to the chosen one, will add to unity,

$$\sum_q \sum_n T_{qp}^{nm} = \sum_q \sum_n T_{pq}^{mn} = 1 \quad \forall m, p. \quad (2.17)$$

Summing over all open channels  $m = 1, 2, \dots, N_p$  in lead  $p$  (assuming that  $N_p \leq N_q$ ), this leads to the *sum rule*

$$\sum_q T_{qp}(E) = \sum_q T_{pq}(E) = N_p(E) \quad (2.18)$$

for the transmission functions of a multiterminal setup at energy  $E$ .

## Symmetry

In the absence of a magnetic field and assuming a real, static potential, the Hamiltonian of the system is time-reversal invariant, that is, it commutes with the anti-unitary operator  $\mathcal{T}$  of time reversal. In a stationary picture, and disregarding the electron spin, the operation of  $\mathcal{T}$  reduces to complex conjugation [148]. With application of  $\mathcal{T}$  on an asymptotic scattering state, we can use Eq. (2.10) to get [149]

$$\mathcal{S}_{qp}^{nm} = \langle \psi_{n,-}^{(q)} | \psi_{m,+}^{(p)} \rangle = \langle \mathcal{T} \psi_{n,-}^{(q)} | \mathcal{T} \psi_{m,+}^{(p)} \rangle^* = \langle \psi_{m,-}^{(p)} | \psi_{n,+}^{(q)} \rangle = \mathcal{S}_{pq}^{mn}, \quad (2.19)$$

meaning that the  $S$ -matrix is, apart from unitary, also symmetric,

$$\mathcal{S}^\top = \mathcal{S}. \quad (2.20)$$

To see this from the amplitudes in Eq. (2.8), we notice that, if the Hamiltonian obeys time reversal invariance, then the complex conjugate of a scattering state solution with asymptotics (2.3) will be a solution of the same Schrödinger equation at the same energy. Its (modified) in- and outgoing asymptotic amplitudes will thereby be connected by the same  $S$ -matrix, yielding (by use of Eq. (2.8))

$$\vec{a}_-^* = \mathcal{S} \vec{a}_+^* \Rightarrow \vec{a}_+ = [\mathcal{S}^*]^{-1} \vec{a}_- \Rightarrow \mathcal{S}^* \mathcal{S} = \mathcal{I}, \quad (2.21)$$

which, combined with Eq. (2.15), leads to the symmetry of  $\mathcal{S}$ , Eq. (2.20).

Time-reversal invariance is broken in the presence of an external magnetic field  $\mathbf{B}$ , since the Hamiltonian (in general) becomes complex by the coupling of the magnetic vector potential with the momentum operator; this breaking is evident classically, where the Lorentz force deflects oppositely moving charges in opposite directions. However, one can aptly argue that, since any magnetic field is itself produced by moving charges, its direction would also be reversed under time reversal. Thus, following the considerations leading to Eq. (2.21), we now have  $\mathcal{S}^*(-\mathbf{B})\mathcal{S}(\mathbf{B}) = \mathcal{I}$ , which, since the unitarity condition still applies,  $\mathcal{S}^\dagger(\mathbf{B})\mathcal{S}(\mathbf{B}) = \mathcal{I}$ , leads to the *reciprocity* relation

$$\mathcal{S}_{qp}^{nm}(\mathbf{B}) = \mathcal{S}_{pq}^{mn}(-\mathbf{B}) \quad (2.22)$$

for the  $S$ -matrix [2,150], which is related to the principle of microscopic reversibility [151]. In fact, relation (2.22) follows directly from the Schrödinger equation (1.22) by considering the scattering eigenstates in Eq. (2.10): the complex conjugate of a state  $|\psi_{m,s}^{(p)}\rangle$  is an eigenstate of the same Hamiltonian at the same energy but with the vector potential (and thereby also the magnetic field) reversed, that is  $A \rightarrow -A$  in Eq. (1.22).

### 2.2.3 Connected scatterers

We now consider the case where two scatterers  $S_1$  and  $S_2$ , described by the  $S$ -matrices  $\mathcal{S}^{(1)}$  and  $\mathcal{S}^{(2)}$ , respectively, are connected through a number of leads, such that each connection lead of  $S_1$  is prolonged into a connection lead of  $S_2$  of equal width (in other words, no additional scattering is caused *within* the connected leads). This is illustrated in Fig. 2.2 for a single connection lead. To find the total  $S$ -matrix of the connected system in terms of  $\mathcal{S}^{(1)}$  and  $\mathcal{S}^{(2)}$ , we regroup the lead amplitudes, in- and outgoing ( $s = \pm$ ), of the *total* system of both scatterers before being connected into those in the lead(s) to be connected,  $\vec{a}^c$ , and those in the leads that remain unconnected,  $\vec{a}^u$ , and partition the total (unconnected)  $S$ -matrix  $\mathcal{S}^\circ$  accordingly,

$$\vec{a}_+ = \mathcal{S}^\circ \vec{a}_- ; \quad \vec{a}_s = \begin{pmatrix} \vec{a}_s^u \\ \vec{a}_s^c \end{pmatrix}, \quad \mathcal{S}^\circ = \begin{pmatrix} \mathcal{S}_{uu}^\circ & \mathcal{S}_{uc}^\circ \\ \mathcal{S}_{cu}^\circ & \mathcal{S}_{cc}^\circ \end{pmatrix}, \quad s = +, -. \quad (2.23)$$

The  $u$ - and  $c$ -blocks of the total  $S$ -matrix of the unconnected system are in turn block-diagonal in the two scatterers, connecting only ingoing to outgoing amplitudes of the same scatterer 1 or 2,

$$\vec{a}_s^l = \begin{pmatrix} \vec{a}_{s,1}^l \\ \vec{a}_{s,2}^l \end{pmatrix}, \quad \mathcal{S}_{kl}^\circ = \begin{pmatrix} \mathcal{S}_{kl}^{(1)} & 0 \\ 0 & \mathcal{S}_{kl}^{(2)} \end{pmatrix}, \quad k, l = u, c. \quad (2.24)$$

When the scatterers are connected, the outgoing amplitudes  $\vec{a}_{+,1}^c$  of  $S_1$  are coupled to the ingoing amplitudes  $\vec{a}_{-,2}^c$  of  $S_2$ , and similarly  $\vec{a}_{-,1}^c$  to  $\vec{a}_{+,2}^c$ , by a connection matrix  $\mathcal{C}$  which is block-antidiagonal in the scatterers,

$$\vec{a}_+^c = \mathcal{C} \vec{a}_-^c ; \quad \mathcal{C} = \begin{pmatrix} 0 & \mathcal{C}_{12} \\ \mathcal{C}_{12}^\dagger & 0 \end{pmatrix} = \mathcal{C}^{-1}, \quad \mathcal{C}_{12} = \text{diag} \left( e^{i\delta_n^{(p)}} \right), \quad (2.25)$$

where the block  $\mathcal{C}_{12}$  is a diagonal matrix (for appropriate numbering of the connection leads  $p$ ) containing phase shifts for each channel  $n$  which depend on the length of the connection lead(s), the longitudinal channel momenta, as well as on any applied magnetic vector potential.

Inserting the connection condition (2.25) into Eq. (2.23) yields a system of equations,

$$\begin{pmatrix} \vec{a}_+^u \\ \mathcal{C} \vec{a}_-^c \end{pmatrix} = \begin{pmatrix} \mathcal{S}_{uu}^\circ & \mathcal{S}_{uc}^\circ \\ \mathcal{S}_{cu}^\circ & \mathcal{S}_{cc}^\circ \end{pmatrix} \begin{pmatrix} \vec{a}_-^u \\ \vec{a}_-^c \end{pmatrix}, \quad (2.26)$$

from which the amplitudes  $\vec{a}_-^c$  in the connected lead(s) can be eliminated, in order to directly relate the amplitudes  $\vec{a}_\pm^u$  in the unconnected leads. We finally obtain

$$\vec{a}_+^u = \mathcal{S}_{uu} \vec{a}_-^u, \quad (2.27)$$

where

$$\mathcal{S}_{uu} = \mathcal{S}_{uu}^\circ + \mathcal{S}_{uc}^\circ [\mathcal{C} - \mathcal{S}_{cc}^\circ]^{-1} \mathcal{S}_{cu}^\circ = \mathcal{S}_{uu}^\circ + \mathcal{S}_{uc}^\circ \mathcal{R} \mathcal{S}_{cu}^\circ \quad (2.28)$$

is the desired  $S$ -matrix of the connected system, of the dimension of the unconnected part of  $\mathcal{S}^\circ$ . We see that the connection between the scatterers acts as a ‘perturbation’ on the

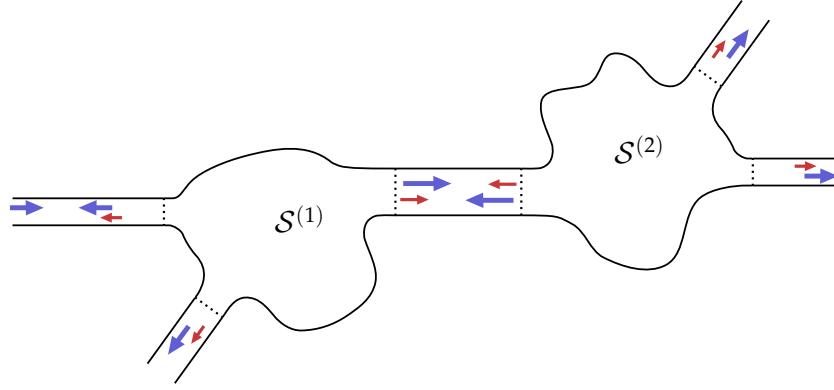


**Figure 2.2:** Two three-terminal scatterers with individual scattering matrices  $\mathcal{S}^{(1)}$  and  $\mathcal{S}^{(2)}$  connected via single lead. An incoming wave in one of the unconnected (outer) leads is scattered via the total scattering matrix  $\mathcal{S}_{uu}$  of Eq. (2.28) into all unconnected leads, with multiple reflections taking place within the connected (inner) lead.

original  $S$ -matrix, by contributing additional scattering ‘paths’ for incoming waves: They can either scatter directly to the outgoing leads, as represented by  $\mathcal{S}_{uu}^{\circ}$ , or they can scatter to the connection leads (through  $\mathcal{S}_{uc}^{\circ}$ ), where they are multiply reflected (as expressed by  $\mathcal{S}_{cc}^{\circ}$ ), to finally be scattered back to the outgoing leads (through  $\mathcal{S}_{ca}$ ). The multiple reflection in the connection region is more intuitively illustrated by writing the matrix  $\mathcal{R}$  in Eq. (2.28) in its power series representation (recall that  $\mathcal{C}^2 = \mathcal{I}$ ),

$$\mathcal{R} = [\mathcal{C} - \mathcal{S}_{cc}^{\circ}]^{-1} = \mathcal{C}[\mathcal{I} - \mathcal{S}_{cc}^{\circ}\mathcal{C}]^{-1} = \mathcal{C} \left\{ \mathcal{I} + \sum_{n=1}^{\infty} [\mathcal{S}_{cc}^{\circ}\mathcal{C}]^n \right\}, \quad (2.29)$$

where successive terms contribute scattering ‘paths’ with increasing number of reflections within the connection, picking up the channel phases of  $\mathcal{C}$  upon each reflection.

The general form (2.28) for connected scatterers will be encountered once more when we treat the complete (as opposed to asymptotic) scattering problem computationally in Chap. 4 (and in particular Sec. 4.5), with the  $S$ -matrix replaced by the resolvent (Green function) of the Hamiltonian. It should be noted here that the connected  $S$ -matrix (2.28) is approximative, since the individual matrices  $\mathcal{S}^{(1)}$  and  $\mathcal{S}^{(2)}$  have been defined here asymptotically, for open channels only. For short enough connection leads, evanescent modes of closed channels decaying from one scatterer can still have substantial amplitude when reaching the other scatterer and ‘leak’ into it, thereby contributing to the scattering and in the connected system. Moreover, evanescent modes from two scatterers decaying into a common connecting lead can ‘interfere’ into a contribution to the total current.<sup>1</sup>

<sup>1</sup> Consider, for example, an open (1) and a closed (2) channel in a lead segment (along  $x$  and around  $x = 0$ ) connecting two scatterers, where the wave function can be written as

$$\psi = \psi_1 + \psi_2; \quad \psi_1 = \chi_1(ae^{ikx} + be^{-ikx}), \quad \psi_2 = \chi_2(ce^{-\kappa x} + de^{\kappa x}), \quad k, \kappa > 0,$$

$\chi_1$  and  $\chi_2$  being the corresponding orthonormal transversal modes. The exponentially increasing part is here physical because of the finite extent of the segment, and originates from the state decaying into it from the right. In contrast to the probability density, where the counterpropagating waves interfere while the decaying modes do not, the total current density consists of an *incoherent* sum of the propagating mode currents and a *coherent* combination  $2\text{Im}(cd^*)\kappa$  from the decaying modes,

$$j \propto (|a| - |b|)k + (cd^* - d^*c)i\kappa,$$

which separate upon the  $y$ -integration over the orthonormal transversal wave functions. Thus, unless  $cd^*$  happens to be real, there is a contribution to transport from the closed channels between the scatterers.

As becomes clear in Sec. 3.2.2,  $S$ -matrix can be generalized naturally to include evanescent modes [14, 128] from the projection of the system's propagator (Green function) onto eigenstates of closed channels. We will not make explicit use of this version here, but treat connected scatterers directly and uniformly within the Green function approach, Sec. 4.5. In this framework the total  $S$ -matrix, and thus (multiterminal) transmission function, will be determined for an arbitrary device potential.

### 2.2.4 Two-terminal system

For a device with  $N_L = 2$  leads, which we take to be identical supporting equal number of open channels  $N_1 = N_2 = N(E)$  at a given energy  $E$ , the lead state amplitudes  $\vec{a}_\pm$  are connected by the unitary and symmetric two-terminal  $S$ -matrix

$$\mathcal{S} = \begin{pmatrix} \mathcal{S}_{11} & \mathcal{S}_{12} \\ \mathcal{S}_{21} & \mathcal{S}_{22} \end{pmatrix} = \begin{pmatrix} r & t \\ t & r' \end{pmatrix}, \quad (2.30)$$

partitioned into four  $N \times N$  matrices containing the transmission amplitudes ( $t$ ) to scatter between the modes of different leads and reflection amplitudes to scatter from the modes of lead 1 ( $r$ ) or lead 2 ( $r'$ ) back to the same lead. Due to the unitarity of  $\mathcal{S}$  (conservation of probability flux), Eq. (2.15), the transmission function (2.14),

$$T(E) = T_{12}(E) = T_{21}(E) = \text{Tr}[t^\dagger(E)t(E)], \quad (2.31)$$

adds up with the total reflection to the number of open channels,

$$T(E) + R(E) = N(E), \quad (2.32)$$

where  $R = T_{11} = T_{22} = \text{Tr}[r^\dagger r] = \text{Tr}[(r')^\dagger r']$ .

In the presence of a magnetic field, the reciprocity relation (2.22) for two attached leads together with the unitarity condition (2.32) leads to a total transmission from lead 1 to lead 2

$$T_{21}(\mathbf{B}) = N - T_{11}(\mathbf{B}) = N - T_{11}(-\mathbf{B}) = T_{21}(-\mathbf{B}) = T_{12}(\mathbf{B}), \quad (2.33)$$

that is, equal to the transmission from 2 to 1. In a two-terminal setup the symmetry of the transmission coefficient in Eq. (2.31) is thus *preserved* even when a magnetic field breaks time-reversal invariance and thereby also the symmetry of the  $S$ -matrix. Alternatively, transmission is independent of the sign (direction along a fixed axis) of the field, regardless of the geometrical symmetry of the confining potential.

This symmetry might seem counterintuitive in terms of the classical dynamics of a charged particle deflected by a magnetic field within an arbitrary confinement (asymmetric with respect to the two lead positions), since the (ballistic) trajectories would in general be completely different for opposite fields. However, note that each *reflected* trajectory (returning to the incoming lead) coincides with a time-reversed reflected trajectory at opposite field [152]. Baring in mind that  $R$  expresses a *probability* of reflection, it corresponds to a sum over all possible reflected trajectories in the classical counterpart (supplied with phases in a semiclassical treatment), thus yielding the symmetry of  $R$  (and of  $T$  by particle conservation) in  $B$ -field. Further, the two-terminal magnetic symmetry of transmission relies on the (coherent) single-particle picture employed, and is generally broken by the effects of many-body interactions [152].

## 2.3 Two-terminal Landauer formula

We now derive the relation between electrical current and transmission for two electrodes connected to the device, and examine the cases of low temperature and applied bias.

### 2.3.1 General case of coherent transport

Considering a two-terminal setup, the electronic current  $I$  flowing through the device under a small (positive) bias voltage  $V_{SD}$  applied between source and drain contacts will be equal, due to charge conservation, to the net current  $I_S$  traversing the source terminal of the device. This will in turn consist of the net current  $I_{\text{in}}$  flowing inwards from the source terminal to the device, minus the current  $I_{\text{out}}$  flowing outwards from the device to the source terminal and originating from the drain contact,

$$I = I_S = I_{\text{in}} - I_{\text{out}}. \quad (2.34)$$

We here assume that the voltage drop  $V_{SD}$  is measured at the contacts between which the current  $I$  flows (a two-terminal measurement), and further, that no scattering occurs between the contacts and the terminals, so that the leads attached to the device lie at the chemical potentials (quasi-Fermi levels)  $\mu_S$  and  $\mu_D$  of the source and drain reservoirs.

The ingoing current per unit energy consists of the electrons in all open channels  $m = 1, 2, \dots, N_S(E)$  of the Q1D source lead with partial (per channel and direction) state densities  $D_{\text{Q1D},m}^S(E)$  and occupation weight  $f_S(E)$  (given in Eq. (1.39)) which move *inwards* (thus 1/2 of the total states) with velocities  $v_m^S(E)$  *without* being reflected into the lead (with probability  $R^{mm}$  into channel  $m$ ). Since the electrons originate from the thermalizing (decohering) contacts, each contribution is added *incoherently*, and integration over energy gives

$$I_{\text{in}} = e \int_0^\infty dE f_S(E) \sum_{m=1}^{N_S} D_{\text{Q1D},m}^S(E) v_m^S(E) \left( 1 - \sum_{n=1}^{N_S} R_{SS}^{nm}(E) \right), \quad (2.35)$$

where the sign of the charge  $-e$  is dropped with the convention that the direction of current is opposite to the motion of electrons. For brevity, the lower limit of integration is set to 0, though only energies  $E > E_C^0 + \epsilon_0$  (above the ground state of the junction confinement) contribute. Similarly, the outgoing current is given by the states  $m$  of the drain lead transmitted to the source (with probability  $T^{nm}$  into channel  $n$ ),

$$I_{\text{out}} = e \int_0^\infty dE f_D(E) \sum_{m=1}^{N_D} D_{\text{Q1D},m}^D(E) v_m^D(E) \sum_{n=1}^{N_S} T_{SD}^{nm}(E), \quad (2.36)$$

where  $E_{N_S}^S \geq E_{N_D}^D$  has been assumed for the highest channel thresholds (so that all drain channels are open for transmission into the source lead).

These expressions simplify significantly by noticing that the product of the partial DOS (including spin degeneracy) with the channel velocity in a Q1D is an *invariant* (see Eqs. (1.38) and (1.29), with energy offset at  $E_C^0 + \epsilon_0$ ),

$$D_{\text{Q1D},m}^p(E) v_m^p = \frac{m_e}{\pi \hbar^2} \sqrt{\frac{\hbar^2}{2m_e(E - E_m)}} \frac{\hbar k_{x,m}}{m_e} = \frac{1}{\pi \hbar} \quad \forall m, \quad p = S, D \quad (2.37)$$

independent of the details of the leads such as type of Q1D confinement, material etc. [124, 153]. Taking into account also the two-terminal transmission symmetry  $T_{SD} = T_{DS} \equiv T$  and the unitarity condition  $T + R = N_S$ , the total current acquires the form

$$I = \frac{e}{\pi \hbar} \int_0^\infty dE T(E) [f(E; \mu_S, \Theta) - f(E; \mu_D, \Theta)], \quad (2.38)$$

in dependence of the bias through the difference  $\mu_S - \mu_D = eV_{SD}$  in local Fermi levels entering the distributions  $f_{S,D}$ . Equation (2.38) is a Q1D form of the Tsu-Esaki formula originally applied for tunneling, but is more commonly referred to as the Landauer formula after its use in (planar) mesoscopic nanostructures.

### Low temperature limit

At very low temperatures, the Fermi-Dirac occupation function can be approximated by step functions for each lead,

$$f(E; \mu_p, \Theta \rightarrow 0) \rightarrow \theta(\mu_p - E), \quad p = S, D, \quad (2.39)$$

so that only electrons from the reservoirs with energies within the sharp interval  $\mu_D < E < \mu_S$  contribute effectively to the charge flow, since all states below  $\mu_D$  in the source lead are occupied. The current then takes the form

$$I = \frac{e}{\pi\hbar} \int_{\mu_D}^{\mu_S} dE T(E), \quad (2.40)$$

a simple integral of the transmission function profile over the finite energy interval equal to the applied bias,  $\Delta E = eV_{SD}$ . If the bias is strong enough to push the quasi-Fermi level in the drain lead below  $E_C^0 + \epsilon_0$  (the lowest available level of the heterojunction confinement above the bottom of the conduction band), then no states are available in the source lead for the electrons from the drain to occupy, so that only electrons from the source above  $E_C^0 + \epsilon_0$  contribute.

In general, the charge carrier density in the source and drain contact regions will depend on the transmission of the device, since the latter determines the portion of electrons on either side of the scatterer during transport: Considering the case of a single channel,  $N_S = N_D = 1$ , the density on the source (drain) side will be weighted by  $(1 + R)f_{S(D)} + Tf_{D(S)}$ , respectively [118]. This will in turn modify the ‘local equilibrium’ quasi-Fermi levels of the leads in the immediate vicinity of the scatterer on the source and drain side to  $\mu'_S$  and  $\mu'_D$ , respectively, which will lie less far apart than  $\mu_S$  and  $\mu_D$ . In the present low temperature limit, step functions can replace the Fermi-Dirac distributions (now with the new levels  $\mu'_{S,D}$ ), and the potential drop across the scatterer can be simply approximated by [118]

$$\mu'_S - \mu'_D = (1 - T)(\mu_S - \mu_D) \quad (2.41)$$

for sufficiently small bias voltage.

### 2.3.2 Linear response regime

For very small bias,  $\mu_S - \mu_D = eV_{SD} \rightarrow 0$ , though still at finite temperature, the Fermi functions can be expanded in series around the equilibrium chemical potential taken to be the average  $\mu = (\mu_D + \mu_S)/2$ . To first order in  $V$ , the difference in Eq.(2.38) can be approximated as [75]

$$f(E; \mu_S, \Theta) - f(E; \mu_D, \Theta) = f\left(E; \mu + e\frac{V_{SD}}{2}, \Theta\right) - f\left(E; \mu - e\frac{V_{SD}}{2}, \Theta\right) \quad (2.42)$$

$$\approx eV_{SD} F_\Theta(E - \mu), \quad V_{SD} \rightarrow 0 \quad (2.43)$$

where

$$F_\Theta(E) \equiv \left. \frac{\partial f(E; \mu, \Theta)}{\partial \mu} \right|_{\mu=0} = - \left. \frac{\partial f(E'; \mu, \Theta)}{\partial E'} \right|_{E'=E+\mu} = \frac{1}{4k_B\Theta} \operatorname{sech}^2\left(\frac{E}{2k_B\Theta}\right) \quad (2.44)$$

is the *thermal broadening* function [127]. The current then becomes *proportional* to the small applied bias at given temperature and chemical potential,

$$I_{\text{lin}} = G(\mu, \Theta)V_{SD}, \quad (2.45)$$

with the proportionality factor  $G(\mu, \Theta)$  being the *conductance function* given by the convolution of the transmission function with the thermal broadening function in energy,

$$G(\mu, \Theta) = G_0 (T \circ F_\Theta)(\mu) = G_0 \int_0^\infty dE T(E) F_\Theta(\mu - E, \Theta), \quad (2.46)$$

using the fact that  $F_\Theta(E)$  is even in  $E$ , where

$$G_0 = \frac{e^2}{\pi\hbar} = 2 \frac{e^2}{h} \quad (2.47)$$

is the *conductance quantum* for spin-degenerate electronic transport (for each spin component alone, or for ‘‘spinless’’ electrons, the factor 2 is absent). When Eq. (2.45) applies, the transport is said to be in ‘linear response’, with the charge flow determined by the *equilibrium* properties of the system (such as  $\mu$  and  $\Theta$ ), and it is this regime we will address in Chaps. 5, 6 and 7.

The (shifted) thermal broadening function  $F_\Theta(\mu - E)$  (also known as the Fermi-Dirac probability density function [153]) is peaked symmetrically at  $E = \mu$ , it is normalized to unity,  $\int_{-\infty}^{+\infty} dE F_\Theta = 1$ , and its full width at half maximum is proportional to  $k_B\Theta$ . It is plotted (scaled by its maximum  $4k_B\Theta$ ) in Fig. 2.3 together with its effect on the transmission profile of a type of quantum billiard device studied later in Chap. 5, producing conductance profiles in varying Fermi energy  $E_F = \mu - E_C^0 - \epsilon_0$  at different temperatures. It is clear that  $F_\Theta$  has a smearing effect on the transmission function, increasingly washing away detailed features in  $T(E_F)$  as  $\Theta$  is raised; the transmission is said to be ‘thermally averaged’ around a given value of  $E_F$ .

The conductance function (2.46) can be used to write the general expression for the current for finite bias and temperature, Eq. (2.38), as [127, 153]

$$I = \frac{1}{e} \int_{\mu_D}^{\mu_S} d\epsilon G(\epsilon, \Theta), \quad (2.48)$$

where  $\mu$  in Eq. (2.46) is now treated just as a variable of integration  $\epsilon$ . This shows that linear response of the current to the applied voltage can be established even at *finite* bias (that is, *not* restricted to the limit  $V_{SD} \rightarrow 0$ , as in Eq. (2.42)), under the condition that  $G(\epsilon, \Theta)$  is constant in energy within the interval  $\mu_D < \epsilon < \mu_S$ , which leads again to the linear  $I$ - $V$ -relation, Eq. (2.45).

The smoothness of  $G(\epsilon, \Theta)$  depends on the profile of the transmission function  $T(E)$ , in combination with the smearing effect of the thermal averaging in Eq. (2.46). Due to impurity scattering, with mean free path smaller than then coherence length,  $l_e < l_\phi$  in a mesoscopic system (see Sec. 1.2.2),  $T(E)$  typically varies rapidly as a result of multiple interference of scattered waves. Even in the absence of elastic disorder, realized, e.g., by a thick spacer layer (see Fig. 1.2), multiple scattering at the boundaries within an electron billiard usually leads to a strongly fluctuating transmission function. Therefore, linear response at a given temperature  $\Theta$  is retained only for a bias far below the thermal width,  $eV_{SD} = \mu_S - \mu_D \ll k_B\Theta$ , so that any variation in  $T(E)$  has been smeared out by the thermal average in  $G(\epsilon, \Theta)$ . The challenge to maintain linear response in a coherent transport device over larger bias (even larger than the thermal width) thus relies on the elimination of random strong fluctuations in the transmission, despite multiple wave interference. This consists in (i) depleting resonance widths to a minimum, since narrow resonant features are smeared out already by a small thermal width, and (ii) keeping the overall (background) transmission profile smooth. In fact, this twofold task will constitute a central aim in Chaps. 5, 6 and 7, where the strategy will be to use the *shape* of the electron billiard (including confinement potential and lead positioning) to decouple resonant states from a *magnetically controlled* transmission background.

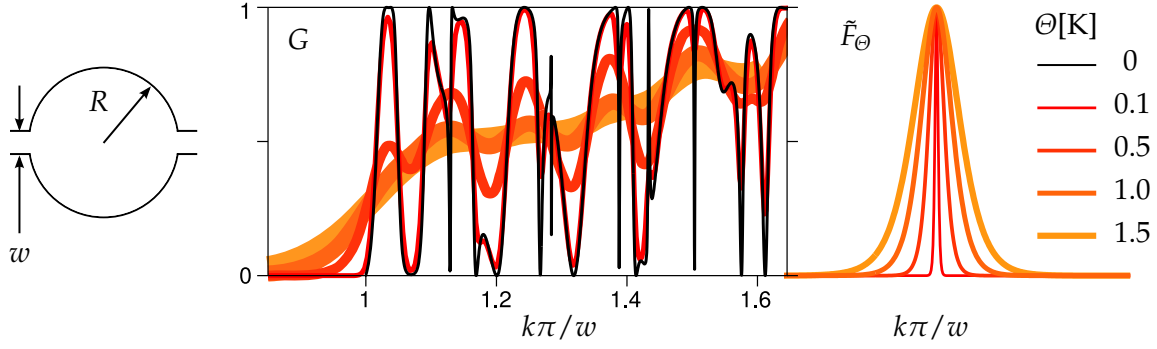


**Figure 2.3:** Conductance  $G/G_0$  of a circular hard-wall billiard of radius  $R = 220\text{nm}$  with two symmetrically attached leads of width  $w = 0.3R$ , at temperatures  $\Theta = 0$  (black), 0.1, 0.5, 1.0, 1.5 K (red to orange), as a function of dimensionless total momentum (channel number)  $k\pi/w$ . The scaled thermal broadening function  $\tilde{F}_\Theta = \text{sech}^2(\frac{k\pi/w}{2k_B\Theta})$  is shown on the right; its convolution with  $T = G(\Theta = 0)/G_0$  yields the corresponding  $G$ -profiles.

### 2.3.3 Transmission as conductance

In the limit of zero temperature, the shifted thermal broadening function  $F_\Theta(\mu - E)$  represents a Dirac  $\delta$ -function peaked at  $\mu$ ,

$$F_{\Theta \rightarrow 0}(\mu - E) = \delta(\mu - E), \quad (2.49)$$

which, when inserted into Eq. (2.46), yields that the linear conductance coincides with the transmission function evaluated at the Fermi energy,

$$G(\mu, \Theta \rightarrow 0) = G_0 T(\mu) = \frac{e^2}{\pi\hbar} T(\mu), \quad (2.50)$$

when measured in units of  $G_0$ . This is referred to as the zero-temperature *Landauer formula*.

Considering a perfect quantum wire as the device, with  $N(\mu)$  open channels at the Fermi level in which electrons transmit perfectly ( $R = 0$ ), current conservation gives  $T(\mu) = N(\mu)$ . Thus, assuming that the voltage drop along the device is measured between the source and contacts (thereby coinciding with  $V_{SD}$  in Eq. (2.45)), the conductance  $I/V_{VS}$  will increase in steps of  $G_0$  as  $\mu$  crosses (e.g., by tuning an applied top gate voltage) the subband thresholds of the wire. In other words,  $G_0$  constitutes the conductance of a single, perfect 1D channel, and therefore a ‘conductance quantum’. The experimental observation of conductance quantization [5, 6] was an important step to corroborate the present formalism of coherent transport.

Note that, in spite of its intuitive form (since  $T$  indeed simply expresses the ease with which electrons transmit through the device), Eq. (2.50) should not be considered obvious [154], since it gives the conductance between the decohering source and drain electrodes in terms of the scattering matrix elements connecting only the idealized leads in between. There has been no treatment here of the contacts where these leads connect to electron reservoirs, apart from the contacts being reflectionless. This assumption further raises the question why there should be a conductance quantum at all, as manifest in Eq. (2.50) for a QW: An ideal, perfectly transmitting wire above would be expected to provide zero resistance to the current flux.

In fact, it is essential to assume measurement of current and voltage drop at the same contacts (that is, connected through the same leads to the scatterer) to arrive at Eq. (2.38) and thus its limit in Eq. (2.50). If the voltage drop were measured only across the device

itself by separate voltage probes, attached though a different pair of ‘non-invasive’ contacts to the ideal leads (in the sense that they do not affect  $T(E)$ ), then the modified local quasi-Fermi levels  $\mu'_{S,D}$  of Eq. (2.41) should be assigned (considering a single open channel). The alternative current-voltage relation  $I = G'V'_{SD}$  in turn yields a *four-terminal* single-channel conductance

$$G' = G_0 \frac{T}{1-T} = \frac{G}{R'}, \quad (2.51)$$

which is the one originally derived by Landauer. Using this formula, the resistance  $(G')^{-1}$  of a single-channel perfect QW indeed vanishes. The total resistance of the device can now be written as a series addition

$$G^{-1} = (G')^{-1} + G_0^{-1} \quad (2.52)$$

of the resistance of the scatterer itself and of a contact resistance  $G_0^{-1}$  corresponding to the additional voltage drop in the leads. The origin, and quantization, of the contact resistance for a single channel can be traced to the *broadening* of a single isolated energy level when brought in contact with a reservoir of many closely spaced levels [127]. The concept of broadening will be introduced below in the effective Hamiltonian treatment of scattering, Sec. 3.3. For the multi-channel version of Eqs. (2.51) and (2.52), the individual channel velocities are taken into account [118]. However, by treating  $T$  as the average transmission per channel, the  $N$ -channel case can be approximated by the replacement  $G_0 \rightarrow G_0 N$  [127].

## 2.4 Multiterminal conductance

The discussion above concerning the different expressions of the conductance for two- and four-terminal measurements, summarized in Eq. (2.51), calls for a general approach to coherent transport in devices with more than two attached leads, as the one depicted in Fig. 2.1. In the four-terminal Landauer formula, current flows between the source and drain contacts, and the additional leads attached on either side of the scatterer are assumed to be ideal voltage probes that draw (or contribute) no net current, though remain in a local equilibrium with the quasi-Fermi levels  $\mu'_{S,D}$  whose difference is measured. Büttiker [150] introduced a unifying framework in which such current and voltage probes are treated equivalently as decohering contacts connected to the mesoscopic device, between which the coherent electronic propagation is described by the  $S$ -matrix of the scattering region.

### 2.4.1 Current from scattering states

Considering a structure with  $N_L$  leads connected to current or voltage probes, we can thus make use of the multiterminal  $S$ -matrix and the associated scattering states of Sec. 2.2 to arrive at the currents in the terminals  $p = 1, 2, \dots, N_L$ . Taking into account the cancellation of channel velocity and DOS, Eq. (2.37), the charge current carried by a scattering state  $|\Phi_{n,+}^{(q)}\rangle$  in lead  $p$  at energy  $E > E_n$  (so that channel  $n$  is open) is given by (see Eq. (2.11))

$$i_{n,+;p}^{(q)}(E) = \frac{e}{\pi\hbar} \left( \delta_{pq} - \sum_{m=1}^{N_p(E)} |\mathcal{S}_{pq}^{mn}(E)|^2 \right), \quad (2.53)$$

that is, an incident flux if  $p = q$  minus the fluxes transmitted from mode  $n$  in lead  $q$  into any mode (including the incident one for  $p = q$ ) in lead  $p$ . Each scattering state  $|\Phi_{n,+}^{(q)}\rangle$  is in equilibrium with the corresponding reservoir [127] at chemical potential  $\mu_q$ , which feeds the device with electrons according to its occupation function  $f_p(E; \Theta)$  (given in Eq. (1.39))

with  $q = 1, 2, \dots, N_L$ ). Thus, the total current in terminal  $p$  is obtained by summing over all scattering states (i.e., over  $n$  for each  $q$  and over all  $q$ ), each weighted by its corresponding occupation function  $f_q$ , and integrating over energy,

$$I_p = \int_E dE \sum_{q=1}^{N_L} \sum_{n=1}^{N_q} i_{n,+;p}^{(q)}(E) f_q(E; \Theta) \quad (2.54)$$

$$= \int_E dE \frac{e}{\pi \hbar} \left( N_p(E) f_p(E; \Theta) - \sum_{q=1}^{N_L} T_{pq}(E) f_q(E; \Theta) \right), \quad (2.55)$$

where Eq. (2.14) has been used. Taking flux conservation into account, expressed in the form of the sum rule in Eq. (2.18), the current can intuitively be written as the difference between the total flux transmitted from lead  $p$  to all other leads and the total weighted flux from all other leads into lead  $p$  (noticing that the reflected flux  $q = p$  back to lead  $p$  cancels out),

$$I_p = \frac{e}{\pi \hbar} \int_E dE \left( \sum_{q=1}^{N_L} T_{qp}(E) f_p(E; \Theta) - \sum_{q=1}^{N_L} T_{pq}(E) f_q(E; \Theta) \right), \quad (2.56)$$

but also as the total flux from all leads to lead  $p$ , weighted by the corresponding *differences* in occupation functions (note that  $f_p(E)$  is a common factor of all summands in the sum over  $q$ ),

$$I_p = \frac{e}{\pi \hbar} \int_E dE \sum_{q=1}^{N_L} T_{pq}(E) [f_p(E; \Theta) - f_q(E; \Theta)]. \quad (2.57)$$

This last form generalizes the two-terminal current, Eq. (2.38), to the multiterminal case. Equation (2.57) could, in fact, be arrived at equivalently by starting with an argument similar to that in Eqs. (2.34), (2.35) and (2.36), that is, treating in- and outflow separately. We have chosen here to treat the elementary current as that carried by a scattering state, Eq. (2.53), which includes in- and outflow simultaneously since the wave function of the scattering state generally extends into all leads, though occupied according to the lead of incidence. Forming a complete set, scattering states thus describe transport naturally without introducing ambiguities concerning the Pauli exclusion principle for the lead state occupation of electrons ‘arriving’ at a terminal [92, 127], since an electron (or two of opposite spin) occupying a scattering state automatically occupies lead states in *all* leads.

## 2.4.2 Conductance matrix

Assigning a voltage  $V_p$  to each quasi-Fermi level  $\mu_p$ , in the limit of small voltage differences between the leads all levels tend to a common one,  $\mu_p \rightarrow \mu \forall p$ , and the difference  $f_p - f_q$  in Eq. (2.57) can be approximated through the thermal broadening function (2.44), like in the two-terminal case. The current in terminal  $p$  thus becomes a linear combination of the voltage differences  $V_{pq}$  to all other terminals (the contribution of the same terminal obviously vanishes),

$$I_p = \sum_{q=1}^{N_L} G_{pq} V_{pq}, \quad V_{pq} \equiv V_p - V_q = \frac{\mu_p - \mu_q}{e} \rightarrow 0 \quad (2.58)$$

where the two-terminal conductance from lead  $q$  to lead  $p$  is given in direct analogy to Eq. (2.46),

$$G_{pq}(\mu, \Theta) = G_0 (T_{pq} \circ F_\Theta)(\mu) = \frac{e^2}{\pi \hbar} \int_0^\infty dE T_{pq}(E) F_\Theta(\mu - E, \Theta). \quad (2.59)$$

Collecting all currents and voltages into  $N_L \times 1$  vectors  $\mathbf{I} = (I_1, I_2, \dots, I_{N_L})^\top$  and  $\mathbf{V} = (V_1, V_2, \dots, V_{N_L})^\top$ , Eq. (2.58) can be written in the matrix form [118, 155]

$$\mathbf{I} = \Lambda \mathbf{V}, \quad \Lambda_{pq} \equiv \delta_{pq} \sum_{q'} G_{pq'} - G_{pq}. \quad (2.60)$$

Due to current conservation, the elements of any row or column of  $\Lambda$  add to zero (since the sum in Eq. (2.18) commutes with the integration in Eq. (2.59)). This becomes more evident in the limit of zero temperature, where the (dimensionless) conductance and transmission coefficients coincide, and  $\Lambda$  becomes

$$\Lambda_{pq}(\mu, \Theta \rightarrow 0) = \frac{e^2}{\pi \hbar} (\delta_{pq} N_p - T_{pq}). \quad (2.61)$$

Further, since the derivation of  $\Lambda$  was based on the multiterminal scattering matrix  $\mathcal{S}$ , the associated reciprocity relations in the presence of a magnetic field carry over to the general conductance coefficients,

$$G_{pq}(\mu, \Theta; \mathbf{B}) = G_{qp}(\mu, \Theta; -\mathbf{B}), \quad (2.62)$$

thus demonstrating the Onsager-Casimir microreversibility principle [151, 156] for coherent electron transport.

### 2.4.3 Current and (fictitious) voltage probes

Once the linear response conductance matrix  $\Lambda$  has been determined from the scattering matrix of the system, with contacts at a given temperature and close to the common chemical potential  $\mu$ , the distinction between current and voltage probes (which were treated equivalently) can be reintroduced: Considering a device with  $N_L$  probes in total, current probes are those upon which *externally* set voltages  $V_p^e$  ( $p = 1, 2, \dots, N_e$ ) are applied, and at which the flowing currents  $I_p^e$  measured, whereas voltage probes ideally let no current through,  $I_{p'}^i = 0$  ( $p' = 1, 2, \dots, N_i = N_L - N_e$ ), in order to reliably measure their voltages  $V_{p'}^i$  which are determined *internally* by the system. With this grouping of the elements of current and voltage vectors  $\mathbf{I}$  and  $\mathbf{V}$ , the matrix equation (2.60) can be written as

$$\begin{pmatrix} \mathbf{I}^e \\ \mathbf{I}^i \end{pmatrix} = \begin{pmatrix} \Lambda^{ee} & \Lambda^{ei} \\ \Lambda^{ie} & \Lambda^{ii} \end{pmatrix} \begin{pmatrix} \mathbf{V}^e \\ \mathbf{V}^i \end{pmatrix}, \quad (2.63)$$

where the diagonal blocks  $\Lambda^{ee(ii)}$  connect external (internal) currents and voltages, while the off-diagonal blocks provide the coupling between external and internal probes. Setting  $\mathbf{I}^i = \mathbf{0}$  for the internal (voltage probe) currents, and eliminating  $\mathbf{V}^i$  from the system of equations (2.63), we obtain the external currents in terms of the external voltages alone, but through an effective conductance matrix  $\tilde{\Lambda}$  (of dimension  $N_e$ ),

$$\mathbf{I}^e = \tilde{\Lambda} \mathbf{V}^e, \quad \tilde{\Lambda} = \Lambda^{ee} - \Lambda^{ei} (\Lambda^{ii})^{-1} \Lambda^{ie}. \quad (2.64)$$

This form of  $\tilde{\Lambda}$  is in analogy to the combined scattering matrix (2.28) of two connected scatterers (with unconnected/connected amplitudes playing the role of external/internal probes), and is quite general when treating the effect of a subsystem (or perturbation) on the (linear) response of a system. We will encounter it again when partitioning the Hamiltonian of the system in the Green function approach to scattering in Sec. 3.3.

Since the current through (ideal) voltage probes is zero, their only effect on the electronic transport between other terminals is that they constitute sources of decoherence: Electrons reinjected from the voltage probes (to maintain  $\mathbf{I}^i = \mathbf{0}$  above) have no phase relation to the

ones entering them, assuming that the contacts are reflectionless (see Sec. 2.1). The Büttiker formalism has therefore been used to phenomenologically model decoherence, that is, to introduce incoherent scattering without treating the microscopic phase-breaking processes [150, 157]. The internal probes are now *fictitious*: They need no longer be attached to the device through real contacts (although they might), but can be distributed over the system as localized scatterers which destroy the phase information of the electron waves (since multiterminal transmission coefficients are added incoherently). After determining the total conductance matrix  $\Lambda$ , internal voltages are eliminated by imposing zero internal currents, and the conductance matrix of between the ‘real’ terminals is given by  $\tilde{\Lambda}$ .

In the multiterminal systems studied here in Chaps. 4 and 7, we will not apply fictitious Büttiker probes to model decoherence; each (real) terminal will itself serve as a source of decoherence, but also of *dissipation* (since net flux will be transmitted through it), for the electron transport between other terminals.

# Stationary scattering in confining planar geometries

In the Landauer-Büttiker formalism developed previously, the multiterminal transmission function of a mesoscopic device constitutes the core of the description of coherent electron transport. In this chapter it will be seen how the asymptotic scattering matrix of the system as well as spatially resolved quantities of interest such as the full scattering wave function can be formally determined and practically calculated from the system Hamiltonian. This is achieved within the Green function formalism in terms of an effective, energy-dependent and non-Hermitian Hamiltonian describing the scattering region connected to the peripheral leads. The theoretical framework is reviewed from the particular viewpoint of (planar) confinement with generic, geometrically defined asymptotic scattering channels, highlighting the involved concepts and the main observable interference effects in transmission, Fano resonances and Aharonov-Bohm oscillations. We close with a brief analysis of scattering in locally symmetric systems through a formalism recently developed in Ref. [158].

## 3.1 In-plane Hamiltonian

As alluded to in Sec. 1.2.3, we will assume a total effective single-electron potential that is separable into its  $z$ -dependence along the vertical direction of growth of the heterostructure and the in-plane  $xy$ -dependence; see Eq. (1.19). Considering the quantum limit of a 2DES, motion is restricted to the lowest subband of the vertical confinement, as explained in Sec. 1.3, and we now work with the 2D projected Hamiltonian simply denoted as  $\mathcal{H}$ , which reads

$$\mathcal{H} = \frac{1}{2m} [\mathbf{p} - q_e \mathbf{A}(\mathbf{r})]^2 + V(\mathbf{r}) = \frac{1}{2m} \left[ \frac{\hbar}{i} \nabla_{\mathbf{r}} + e \mathbf{A}(\mathbf{r}) \right]^2 + V(\mathbf{r}), \quad (3.1)$$

where  $\mathbf{r} = (x, y) = x\hat{x} + y\hat{y}$ , with in-plane effective mass  $m$  and vector potential  $\mathbf{A}$ . The electrostatic potential  $V(\mathbf{r})$  is here the sum

$$V(\mathbf{r}) = V_{\text{dev}}(\mathbf{r}) + V_{\text{int}}(\mathbf{r}), \quad (3.2)$$

where  $V_{\text{dev}}(\mathbf{r})$  is the in-plane confinement potential resulting from the device design through depleting gates or direct etching, and  $V_{\text{int}}(\mathbf{r})$  is the effective single-particle potential approximating electron-electron interactions, see Sec. 1.2.3. Interactions are usually included as the mean field, or Hartree, electrostatic potential  $V_{\text{int}}(\mathbf{r}) \approx V_{\text{H}}(\mathbf{r})$  created by the average density  $n(\mathbf{r})$  of all electrons in the system through Poisson's equation,

$$\nabla_{\mathbf{r}} [\epsilon_0 \epsilon(\mathbf{r}) \nabla_{\mathbf{r}} V_{\text{H}}(\mathbf{r})] = -e^2 n(\mathbf{r}), \quad (3.3)$$

where  $\varepsilon(\mathbf{r})$  is the relative permittivity of the semiconducting medium which can vary spatially for the inhomogeneous device composition [124, 159]. The spatially varying electron density in the open system is generally given by

$$n(\mathbf{r}) = \sum_p \sum_{m=1}^{N_p} \int_{-\infty}^{+\infty} dE f_p(E; \Theta) |\psi_{m,+;E}^{(p)}(\mathbf{r})|^2 \quad (3.4)$$

in terms of the wave functions of the scattering states  $|\psi_{m,+;E}^{(p)}\rangle \equiv |\psi_{m,+}^{(p)}(E)\rangle$  with incident wave in mode  $m$  of lead  $p$ , weighted by the occupation functions  $f_p$  of the corresponding reservoir and added incoherently in the Landauer-Büttiker framework (see Sec. 2.4). The scattering states are in turn energy eigenstates of the stationary Schrödinger equation

$$[E - \mathcal{H}] \psi(\mathbf{r}) = 0 \quad (3.5)$$

with the corresponding (asymptotic) boundary conditions.<sup>1</sup> Equations (3.3) and (3.5) can then be solved *self-consistently* by iteratively updating  $V_H(\mathbf{r})$  in Eq. (3.5) from the solution of Eq. (3.3) with  $n(\mathbf{r})$  previously obtained from Eq. (3.5), until  $V_H(\mathbf{r})$  converges—a procedure known as a ‘Schrödinger-Poisson solver’.

Since the focus in later chapters will primarily on the combined effects of the device geometry and magnetic fields in a highly resolved parameter space, we will simply consider a fixed potential from the beginning (usually of the hard-wall billiard type). The extensive work on self-consistent device potentials [118, 160, 161] can then be consulted to add approximative potential gradients to simulate more realistic setups, as done in Chap. 6.

## 3.2 Greenian formulation of scattering

Let us now introduce some elemental concepts of Green functions in single-particle scattering theory, in part following Refs. [124, 127, 128, 146, 162]. Instead of exposing the subject in its formal rigor, we will adapt the description to a more intuitive understanding of the elastic scattering processes in terms of propagators in time and space.

### 3.2.1 Green functions

For a linear differential operator  $\mathcal{L}$  acting in (2D) space  $\mathbf{r}$  and time  $t$ , the inhomogeneous differential equation

$$\mathcal{L} \psi(\mathbf{r}, t) = \Phi(\mathbf{r}, t) \quad (3.6)$$

expresses the spatiotemporal evolution, or response, of the function  $\psi(\mathbf{r}, t)$  governed by  $\mathcal{L}$  in the presence of the ‘source’ term  $\Phi(\mathbf{r}, t)$ . The Green function  $\mathcal{G}(\mathbf{r}, \mathbf{r}'; t, t')$  associated with  $\mathcal{L}$  is defined as the response to a source localized at  $\mathbf{r}'$  at time  $t'$ ,

$$\mathcal{L} \mathcal{G}(\mathbf{r}, \mathbf{r}'; t, t') = \delta(\mathbf{r} - \mathbf{r}') \delta(t - t'). \quad (3.7)$$

It can be interpreted as the function that transfers, or propagates, the effect of the source  $\Phi$  on the response  $\psi$  from  $(\mathbf{r}', t')$  to  $(\mathbf{r}, t)$ , in the form

$$\psi(\mathbf{r}, t) = \int d\mathbf{r}' \int dt' \mathcal{G}(\mathbf{r}, \mathbf{r}'; t, t') \Phi(\mathbf{r}', t'), \quad (3.8)$$

---

<sup>1</sup> The subband energy of the vertical  $z$ -confinement is here included in the potential, and the energy  $E$  is thus the total energy of the in-plane motion, that is, offset to the ground level  $\epsilon_0$  of heterojunction well.

as can be verified from Eqs.(3.6) and (3.7). In other words,  $\mathcal{G}$  resolves the total effect of the source  $\Phi$  on  $\psi$  at a point  $(\mathbf{r}, t)$  under the action of  $\mathcal{L}$  into the partial effects of  $\Phi$  from individual points  $(\mathbf{r}', t')$ , which added produce the total response.

In many-body quantum theory, Green functions are defined as (various types of inter-dependent) correlation functions between field operators of interacting particles [124, 127, 163]. In the effective single-electron picture we have adapted to in Chap. 1, we start with the time-dependent Schrödinger equation,

$$\left[ i\hbar \frac{\partial}{\partial t} - \mathcal{H} \right] \psi(\mathbf{r}, t) = 0, \quad (3.9)$$

and the Green function for the differential operator  $\mathcal{L} = i\hbar \frac{\partial}{\partial t} - \mathcal{H}$  thus obeys the Green equation

$$\left[ i\hbar \frac{\partial}{\partial t} - \mathcal{H} \right] \mathcal{G}(\mathbf{r}, \mathbf{r}'; t, t') = \delta(\mathbf{r} - \mathbf{r}')\delta(t - t'). \quad (3.10)$$

In the presence of an excitation  $\Phi(\mathbf{r}, t) = \Phi(\mathbf{r})\delta(t - t_i)$  at some initial time  $t_i$ , the solution  $\psi(\mathbf{r}, t)$  of the associated inhomogeneous equation,

$$\left[ i\hbar \frac{\partial}{\partial t} - \mathcal{H} \right] \psi(\mathbf{r}, t) = \Phi(\mathbf{r})\delta(t - t_i), \quad (3.11)$$

will have a temporal discontinuity at  $t = t_i$  [124],

$$i\hbar [\psi(\mathbf{r}, t_i^+) - \psi(\mathbf{r}, t_i^-)] = \Phi(\mathbf{r}). \quad (3.12)$$

Treating  $t_i$  as the time signifying an initial (+) or final (−) condition, we can define corresponding wave functions  $\psi^\pm(\mathbf{r}, t) \equiv \psi(\mathbf{r}, t)\theta(\pm(t - t_i))$  to be the solutions to Eq.(3.11) at times  $t \gtrless t_i$ . The spatial part  $\Phi$  of the inhomogeneous term in (3.11) then simply imposes, through (3.12), the initial or final condition on  $\psi^+(\mathbf{r}, t)$  or  $\psi^-(\mathbf{r}, t)$ , respectively,

$$\pm i\hbar \psi^\pm(\mathbf{r}, t_i^\pm) = \Phi(\mathbf{r}). \quad (3.13)$$

From Eq.(3.8),  $\psi^+(\mathbf{r}, t)$  and  $\psi^-(\mathbf{r}, t)$  are then given by

$$\begin{aligned} \psi^\pm(\mathbf{r}, t) &= \pm i\hbar \int d\mathbf{r}' \int dt' \mathcal{G}^\pm(\mathbf{r}, \mathbf{r}'; t, t') \psi^\pm(\mathbf{r}', t_i) \delta(t' - t_i) \\ &= \pm i\hbar \int d\mathbf{r}' \mathcal{G}^\pm(\mathbf{r}, \mathbf{r}'; t, t_i) \psi^\pm(\mathbf{r}', t_i) \end{aligned} \quad (3.14)$$

in terms of the associated *retarded* and *advanced* Green functions  $\mathcal{G}^+(\mathbf{r}, \mathbf{r}'; t, t')$  and  $\mathcal{G}^-(\mathbf{r}, \mathbf{r}'; t, t')$ , respectively, which in turn are solutions to Eq.(3.10). This is written in representation-independent form as

$$|\psi^\pm(t)\rangle = \pm i\hbar \mathcal{G}^\pm(t, t_i) |\psi^\pm(t_i)\rangle, \quad (3.15)$$

such that  $\mathcal{G}^\pm(\mathbf{r}, \mathbf{r}'; t, t') = \langle \mathbf{r} | \mathcal{G}^\pm(t, t') | \mathbf{r}' \rangle$  is the spatial representation of the operator  $\mathcal{G}^\pm(t, t')$ , which we call the *resolvent*, or Greenian<sup>2</sup>, of the Hamiltonian operator (strictly speaking, of the operator  $\mathcal{L} = i\hbar \frac{\partial}{\partial t} - \mathcal{H}$ ). In view of the general unitary evolution of the state  $|\psi(t)\rangle$  from time  $t'$  to time  $t$ ,

$$|\psi(t)\rangle = \mathcal{U}(t, t') |\psi(t')\rangle, \quad (3.16)$$

---

<sup>2</sup>In order to avoid a multitude of naming for  $\mathcal{G}$ , since it is encountered as the Green *operator* acting on states, as the Green *function* in spatial representation, or even as the Green (function) *matrix* in the discretized (spatial) representation to follow, we will use the relatively unconventional though unifying term 'Greenian', just as is commonly done for the Hamiltonian.

we identify the time-dependent Greenian in Eq. (3.15) as the unitary evolution operator  $\mathcal{U}$  associated to  $\mathcal{H}$ , supplied with the information on the initial condition at  $t = t_i$  due to the source,

$$\mathcal{G}^\pm(t, t_i) = \pm \frac{1}{i\hbar} \mathcal{U}(t, t_i) \theta(\pm(t - t_i)). \quad (3.17)$$

Considering a time independent Hamiltonian, the evolution operator reads

$$\mathcal{U}(t, t') = \exp \left[ -\frac{i}{\hbar} (t - t') \mathcal{H} \right], \quad (3.18)$$

so that an eigenstate  $|\psi_E(t)\rangle$  of the Hamiltonian with eigenenergy  $E$  evolves simply as

$$|\psi_E(t)\rangle = e^{-\frac{i}{\hbar} \mathcal{H}(t-t')} |\psi_E(t')\rangle = e^{-\frac{i}{\hbar} \mathcal{E}(t-t')} |\psi_E(t')\rangle \equiv e^{-i\omega(t-t')} |\psi_E(t')\rangle, \quad (3.19)$$

that is, with a (relative) probability density  $\psi_E(t')$  constant in time, or *stationary*.

### Spectral expansion

We can now use the (limiting) integral representation of the Heaviside step function in Eq. (3.17) with  $\tau = t - t_i$ ,

$$\theta(\tau) = \pm \frac{i}{2\pi} \lim_{\eta \rightarrow 0} \int_{-\infty}^{+\infty} d\epsilon \frac{e^{-i\epsilon\tau/\hbar}}{\epsilon \pm i\eta}, \quad \eta > 0, \quad (3.20)$$

together with the completeness and orthonormality of the eigenstates  $|\phi_n\rangle$  of the Hermitian operator  $\mathcal{H}$ ,<sup>3</sup>

$$\sum_{n,k} |\phi_{n,k}\rangle \langle \phi_{n,k}| = 1; \quad \mathcal{H} |\phi_{n,k}\rangle = E_{n,k} |\phi_{n,k}\rangle, \quad (3.21)$$

to obtain the energy dependent Greenian from the Fourier transform of Eq. (3.17), as follows (setting  $t_i \equiv 0$  for simplicity):

$$\mathcal{G}^\pm(E) = \int_{-\infty}^{+\infty} dt e^{iEt/\hbar} \mathcal{G}^\pm(t, t_i = 0) \quad (3.22)$$

$$= \frac{1}{2\pi\hbar} \lim_{\eta \rightarrow 0} \int_{-\infty}^{+\infty} dt e^{iEt/\hbar} \mathcal{U}(t, t_i = 0) \int_{-\infty}^{+\infty} d\epsilon \frac{e^{-i\epsilon t/\hbar}}{\epsilon \pm i\eta} \quad (3.23)$$

$$= \frac{1}{2\pi\hbar} \lim_{\eta \rightarrow 0} \int_{-\infty}^{+\infty} d\epsilon \int_{-\infty}^{+\infty} dt \frac{e^{i(E-\mathcal{H}-\epsilon)t/\hbar}}{\epsilon \pm i\eta} \quad (3.24)$$

$$= \lim_{\eta \rightarrow 0} \int_{-\infty}^{+\infty} d\epsilon \frac{\delta(E - \mathcal{H} - \epsilon)}{\epsilon \pm i\eta} \quad (3.25)$$

$$= \lim_{\eta \rightarrow 0} [E - \mathcal{H} \pm i\eta]^{-1}. \quad (3.26)$$

The retarded and advanced Greenians are thus obtained by taking the real limit of the complex (energy) argument  $\zeta = E \pm i\eta$  of the resolvent operator  $\mathcal{G}$ ,

$$\mathcal{G}^\pm(E) = \lim_{\eta \rightarrow 0} \mathcal{G}(E \pm i\eta), \quad \mathcal{G}(\zeta) \equiv [\zeta - \mathcal{H}]^{-1}. \quad (3.27)$$

---

<sup>3</sup>The symbol  $\sum_{n,k}$  is here used explicitly to denote the summation over discrete eigenstates  $n$  together with the integration over continuous (momentum) eigenvalues  $k$ . For notational simplicity, we also use 1 throughout to denote the identity operator.

The completeness of the eigenstates of  $\mathcal{H}$ , already used implicitly in the steps (3.24)  $\rightarrow$  (3.25)  $\rightarrow$  (3.26) above, allows the Greenian to be written in its *spectral expansion*

$$\mathcal{G}(\zeta) = \sum_{n,k} \frac{|\phi_{n,k}\rangle \langle \phi_{n,k}|}{\zeta - E_{n,k}}, \quad (3.28)$$

a form that provides a powerful tool to calculate the Green function in spatial representation,

$$\mathcal{G}(\mathbf{r}, \mathbf{r}'; \zeta) = \langle \mathbf{r} | \mathcal{G}(\zeta) | \mathbf{r}' \rangle, \quad (3.29)$$

for the Hamiltonian under consideration (once its eigenstate wave functions  $\langle \mathbf{r} | \phi_{n,k} \rangle$  are known), usually by contour integration in the complex  $k$ -plane for a continuous energy spectrum  $E_n(\mathbf{k})$ .

### Greenian as a spatial propagator

Let us start now with an initial excitation  $|\Phi_0\rangle$  which is stationary at energy  $E$  (that is, time-periodic with constant density) but under some other Hamiltonian  $\mathcal{H}_0$ ,  $|\Phi_0(t')\rangle = e^{-iEt'/\hbar} |\Phi_0\rangle$ . This state is here simply imposed as a source. The state  $|\psi(t)\rangle$  at time  $t > t'$  of the system governed by  $\mathcal{H}$  will be given by the contribution of all times up to  $t$  through the propagator  $\mathcal{G}^+(t, t')$ , which is now the inverse Fourier transform of  $\mathcal{G}^+(E)$  [146], causally evolving the excitation:

$$|\psi(t)\rangle = \int_{-\infty}^t dt' \mathcal{G}^+(t, t') |\Phi_0(t')\rangle \quad (3.30)$$

$$= \lim_{\zeta \rightarrow 0^+} \frac{1}{2\pi\hbar} \int_{-\infty}^t dt' \int_{-\infty}^{+\infty} dE' \mathcal{G}^+(E') e^{-(iE'+\zeta)(t-t')/\hbar} e^{-iEt'/\hbar} |\Phi_0\rangle, \quad (3.31)$$

where a convergence parameter  $\zeta > 0$  has been included which is taken to zero in the end,

$$= \lim_{\zeta \rightarrow 0^+} \frac{1}{2\pi\hbar} \int_{-\infty}^{+\infty} dE' \mathcal{G}^+(E') e^{-i(E'-i\zeta)t/\hbar} \int_{-\infty}^t dt' e^{-i(E-E'+i\zeta)t'/\hbar} |\Phi_0\rangle \quad (3.32)$$

$$= \lim_{\zeta \rightarrow 0^+} \frac{1}{2\pi i} \int_{-\infty}^{+\infty} dE' \frac{\mathcal{G}^+(E')}{E' - E - i\zeta} e^{-iEt/\hbar} |\Phi_0\rangle \quad (3.33)$$

$$= \lim_{\zeta \rightarrow 0^+} \mathcal{G}(E + i\zeta) e^{-iEt/\hbar} |\Phi_0\rangle \quad \Rightarrow \quad |\psi(t)\rangle = \mathcal{G}^+(E) e^{-iEt/\hbar} |\Phi_0\rangle. \quad (3.34)$$

Projected in position space, Eq.(3.34) shows that the retarded (causal) Green function  $\mathcal{G}^+(\mathbf{r}, \mathbf{r}'; E)$  can also be regarded as a spatial propagator of an initial time-periodic excitation from  $\mathbf{r}'$  to  $\mathbf{r}$  at energy  $E$ , such that the temporal oscillation (that is, the energy) remains invariant. In the general case of an excitation  $|\Phi_0(E)\rangle = \int_{-\infty}^{+\infty} dt' \exp(iEt'/\hbar) |\Phi_0(t')\rangle$  which is not (necessarily) periodic, the response will be a superposition of harmonic phases [164],

$$|\psi(t)\rangle = \frac{1}{2\pi\hbar} \int_{-\infty}^{+\infty} dE e^{-iEt} |\Phi(E)\rangle, \quad (3.35)$$

where each weighing component is propagated by the Greenian,  $|\Phi(E)\rangle = \mathcal{G}^+(E) |\Phi_0(E)\rangle$ . In the cases of elastic scattering to be studied here, we will consider lead eigenstates at energy  $E$ , of the form (2.4), to be the excitation, that is, apart from a phase dependent on the longitudinal position in the lead, we have transversal modes in one (or more) of the leads as source, and Eq. (3.34) can be used.

From Eq. (3.27) it is seen immediately that the Greenian fulfills the property

$$\mathcal{G}^+(E) = [\mathcal{G}^-(E)]^* \quad (3.36)$$

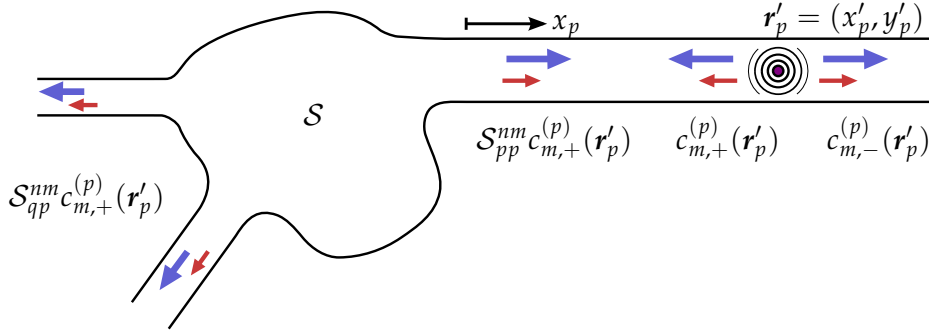


**Figure 3.1:** The response  $\mathcal{G}^+(r_q, r'_p; E)$  to an excitation at point  $r'_p = (x'_p, y'_p)$  in a lead  $p$  of a multiterminal scatterer will generate partial waves with expansion coefficients  $c_{m,s}^{(p)}(r'_p)$ , with  $s = \text{sgn}(x_{q=p} - x'_p)$ , which are scattered via the scattering matrix  $S$  into the modes of all leads.

which, in its spatial representation, yields the reciprocity relation [118, 164]

$$\mathcal{G}^+(r, r'; E, \mathbf{B}) = [\mathcal{G}^-(r', r; E, -\mathbf{B})]^*, \quad (3.37)$$

in similarity to the one for the  $S$ -matrix, Eq. (2.22). Thus, complex conjugation corresponds to the time reversal of propagation in the system. We have again included the magnetic field reversal accompanying time reversal, since the complex conjugated eigenstates, which are inserted in the spectral representation (3.28), are solutions of the same Schrödinger equation with reversed magnetic field [127].

### 3.2.2 Scattering matrix from Greenian

As we have seen, the retarded Greenian  $\mathcal{G}^+(E)$  acts in the form of a generalized ‘scattering matrix’, which connects wave function amplitudes not only asymptotically (in the leads in the case of an open quantum billiard) and between specific eigenmodes, but the amplitudes at any two points in the system. The Greenian thus carries the information of the scattering process continuously through the system and, evaluated at its asymptotic regions, will naturally be related to the  $S$ -matrix elements.

To arrive at this relation for an open quantum billiard, we consider the response from a localized ( $\delta$ -like) excitation in one of the leads connected to the scatterer, as shown schematically in Fig. 3.1, which is given by the spatial representation of  $\mathcal{G}^+(E)$ , as seen previously. An excitation at point  $r'_p = (x'_p, y'_p)$  in lead  $p$  will generate a wave in the form of a superposition of partial waves (in its channels  $m$ ) with expansion coefficients  $c_{m,s}^{(p)}(x'_p, y'_p)$ , as given in A.1 where the Green function of a perfect wire is derived. The sign  $s$  for each wave is the *opposite* of the direction of that wave; see (A.13) and (A.14). The partial waves going inwards are scattered in the cavity and transmitted to all channels  $n$  of the other leads  $q \neq p$  or reflected back to same lead  $q = p$ , according to the  $S$ -matrix of the system. Each lead  $p$  is equipped with a local Cartesian coordinate system  $(x_p, y_p)$  with unit vector  $\hat{x}_p$  pointing outwards from the scatterer.

Since we aim at the scattering matrix elements, we consider the ‘final’ points  $r_q = (x_q, y_q)$  to be in the asymptotic region of leads, so that the asymptotic expression of the scattering wave function Eq. (2.11) can be used for the transmitted and reflected amplitudes, taking into account only open channels. Some ambiguity seems to arise from the fact that the ‘initial’ point of excitation within lead  $p$  can be chosen to lie closer [124] or farther [145, 165] from the scatterer than the point of evaluation of  $\mathcal{G}^+(E)$  in the same lead, that is,  $x_{q=p} - x'_p > 0$  or  $< 0$ , respectively. We here treat both cases simultaneously and show that the result is

independent of this choice. In the absence of magnetic fields, the response at  $\mathbf{r}_q = (x_q, y_q)$  at energy  $E$  will be, according to the above (see Eqs. (2.11) and (A.13)),

$$\begin{aligned} \mathcal{G}^+(\mathbf{r}_q, \mathbf{r}'_p; E) &= \sum_m \left[ \tilde{\psi}_{m,+}^{(p)}(\mathbf{r}_q) - \delta_{qp} \theta(x_q - x'_p) \tilde{\Phi}_{m,-}^{(q)}(\mathbf{r}_q) \right] c_{m,+}^{(p)}(\mathbf{r}'_p) \\ &\quad + \sum_m \delta_{qp} \theta(x_q - x'_p) \tilde{\Phi}_{m,+}^{(q)}(\mathbf{r}_q) c_{m,-}^{(p)}(\mathbf{r}'_p) \end{aligned} \quad (3.38)$$

$$= \sum_m \delta_{qp} \tilde{\Phi}_{m,s}^{(q)} c_{m,-s}^{(p)} + \sum_m \sum_n \tilde{\mathcal{S}}_{qp}^{nm} \tilde{\Phi}_{n,+}^{(q)}(\mathbf{r}_q) c_{m,+}^{(p)}(\mathbf{r}'_p), \quad (3.39)$$

with the sign

$$s = \text{sgn}(x_{q=p} - x'_p) \quad (3.40)$$

determined by the relative position of excitation and evaluation point in lead  $p$ , where

$$c_{m,\pm}^{(p)}(\mathbf{r}'_p) = \frac{\tilde{\Phi}_{m,\pm}^{(p)}(\mathbf{r}'_p)}{i\hbar v_m^{(p)}}, \quad \tilde{\Phi}_{n,\pm}^{(q)}(\mathbf{r}_q) \equiv \sqrt{v_n^{(q)}} \Phi_{n,\pm}^{(q)}(\mathbf{r}_q) = \chi_n^{(q)}(y_q) \exp(\pm i k_n^{(q)} x_q). \quad (3.41)$$

Note that the ingoing wave  $\tilde{\Phi}_{m,-}^{(p)}$  of the scattering state  $\tilde{\psi}_{m,+}^{(p)}$  is replaced by an outgoing wave for  $x_{q=p} - x'_p > 0$  (there is here no wave coming in from  $x_p \rightarrow \infty$ ), but with opposite phase  $-i k_m^{(q)} x_q$  of the plane wave coefficient.

In order to use the form of the quantum wire response  $\mathcal{G}_{\text{qw}}^+$  (see A) in lead  $p$ , and to preserve the symmetry of channel indices in  $\mathcal{S}_{qp}^{nm}$  (see below), the asymptotic scattering states used in the expression for  $\mathcal{G}^+$  above,

$$\tilde{\psi}_{m,s}^{(p)}(\mathbf{r}_q) = \delta_{qp} \tilde{\Phi}_{m,-s}^{(q)}(\mathbf{r}_q) + \sum_n \tilde{\mathcal{S}}_{qp}^{nm} \tilde{\Phi}_{n,s}^{(q)}(\mathbf{r}_q), \quad s = +, - \quad (3.42)$$

(cf. Eq. (2.11)), are given in terms of ‘rescaled’ lead eigenstates (cf. Eq. (2.4))  $\tilde{\Phi}_{m,\pm}^{(p)}$  which are *not* flux normalized [124, 145, 166], and whose amplitudes in generic lead states are connected by a *non-unitary* scattering matrix

$$\tilde{\mathcal{S}}_{qp}^{nm} = \sqrt{\frac{v_m^{(p)}}{v_n^{(q)}}} \mathcal{S}_{qp}^{nm}. \quad (3.43)$$

As mentioned above, the Greenian resembles a generalized scattering matrix which connects spatially separated wave amplitudes at arbitrary positions and not only asymptotically. However, the flux normalization pertaining to the unitarity of the associated  $S$ -matrix (whose elements are *current* transmission amplitudes) relies on the well defined (asymptotic) velocities  $v_m$  in the channels, and can be incorporated in the connection between the corresponding *mode* amplitudes. This is not the case for the connection of wave amplitudes between arbitrary spatial *points*, to which no particular velocity is assigned; this becomes obvious for points inside the scatterer, where there are no channels to begin with. Therefore, it is more natural to express Green functions in terms of ‘bare’ eigenfunctions which are not flux normalized (though possibly space-normalized) and thus independent of the presence or not of a geometry with asymptotic leads.

Inserting the  $c_{m,\pm}^{(p)}(\mathbf{r}'_p)$  and  $\tilde{\Phi}_{n,\pm}^{(q)}(\mathbf{r}_q)$  into Eq. (3.38), we obtain

$$\begin{aligned} \mathcal{G}^+(x_q, y_q, x'_p, y'_p; E) &= \sum_m \frac{1}{i\hbar v_m^{(p)}} \delta_{qp} \chi_m^q(y_q) \chi_m^p(y'_p) e^{i s (k_m^q x_q - k_m^p x'_p)} \\ &\quad + \sum_m \sum_n \frac{1}{i\hbar v_m^{(p)}} \tilde{\mathcal{S}}_{qp}^{nm} \chi_n^q(y_q) \chi_m^p(y'_p) e^{i (k_n^q x_q + k_m^p x'_p)}, \end{aligned} \quad (3.44)$$

and it is now clearly seen that the excitation in lead  $p$  has caused scattered outgoing states at  $\mathbf{r}_q$  in all leads  $q$  plus the directly generated outgoing ( $s = +$ ) or ingoing ( $s = -$ ) wave in lead  $q = p$ . The initially generated amplitudes are given by the lead Green function in lead  $p$  and are proportional to the transversal wave function at the excitation point  $\mathbf{r}'_p$ , as expected [127]. Note also that  $\mathcal{G}^+$  is symmetric under the exchange  $\mathbf{r}_q \leftrightarrow \mathbf{r}'_p$  (recall that we have assumed zero magnetic field in the leads).

We can now use the orthogonality of the transversal eigenstates of the leads in order to isolate the desired  $S$ -matrix elements: multiplying by  $\chi_{n_0}^q(\mathbf{y}_q)\chi_{m_0}^p(\mathbf{y}'_p)$  and integrating over the cross section of lead  $q$  at  $x_q$  and lead  $p$  at  $x'_p$ , we have

$$\begin{aligned} & \int d\mathbf{y}_q \int d\mathbf{y}'_p \chi_{n_0}^q(\mathbf{y}_q) \mathcal{G}^+(x_q, \mathbf{y}_q, x'_p, \mathbf{y}'_p; E) \chi_{m_0}^p(\mathbf{y}'_p) \\ &= \delta_{qp} \sum_m \delta_{mn_0} \delta_{mm_0} \frac{e^{i s(k_m^q x_q - k_m^p x'_p)}}{i\hbar v_m^{(p)}} + \sum_m \sum_n \sqrt{\frac{v_m^{(p)}}{v_n^{(q)}}} \mathcal{S}_{qp}^{nm} \delta_{nn_0} \delta_{mm_0} \frac{e^{i(k_n^q x_q + k_m^p x'_p)}}{i\hbar v_m^{(p)}} \end{aligned} \quad (3.45)$$

$$= \delta_{qp} \delta_{n_0 m_0} \frac{e^{i|k_{n_0}^q x_q - k_{m_0}^p x'_p|}}{i\hbar \sqrt{v_{n_0}^{(q)} v_{m_0}^{(p)}}} + \mathcal{S}_{qp}^{n_0 m_0} \frac{e^{i(k_{n_0}^q x_q + k_{m_0}^p x'_p)}}{i\hbar \sqrt{v_{n_0}^{(q)} v_{m_0}^{(p)}}}, \quad (3.46)$$

where the first term has been symmetrized in the indices since it vanishes for  $q \neq p$  or  $n_0 \neq m_0$ . We thus arrive at the desired relation between the  $S$ -matrix elements and the Green function (dropping now the prime on  $\mathbf{r}'_p$  above),

$$\begin{aligned} \mathcal{S}_{qp}^{nm}(E) = & \left[ i\hbar \sqrt{v_n^{(q)} v_m^{(p)}} \int d\mathbf{y}_q \int d\mathbf{y}_p \chi_n^q(\mathbf{y}_q) \mathcal{G}^+(x_q, \mathbf{y}_q, x_p, \mathbf{y}_p; E) \chi_m^p(\mathbf{y}_p) \right. \\ & \left. - \delta_{qp} \delta_{nm} e^{i|k_n^q x_q - k_m^p x_p|} \right] e^{-i(k_n^q x_q + k_m^p x_p)}, \end{aligned} \quad (3.47)$$

confirming that  $\mathcal{S}$  is symmetric (see Eq. (2.20)),  $\mathcal{S}_{qp}^{nm} = \mathcal{S}_{pq}^{mn}$ , in the considered time-reversal invariant setting. It is here implicit that

$$E_{m, k_m^{(p)}} = E_{n, k_n^{(q)}} = E, \quad E_{m, k_m^{(p)}} = E_m^{(p)} + \frac{\hbar^2}{2m_e} k_m^{(p)}, \quad (3.48)$$

so that energy is conserved during the elastic scattering. Equation (3.47) is usually attributed to Fisher and Lee [166] who derived it for an effectively 1D setting. The case of an arbitrary confinement geometry with attached leads connected to reservoirs (the ‘quantum billiards’ described in Sec. 1.2) introduces conceptual implications, to be discussed at the end of Sec. 3.2.3. A generalized multiterminal version of the Fisher-Lee relation for such systems was developed subsequently by Stone and Szafer [165] and analyzed in a time-dependent picture by Sols [145].

As we see from Eq. (3.47), the  $S$ -matrix elements depend on the coordinates  $\mathbf{r}_p, \mathbf{r}_q$  where  $\mathcal{G}^+$  is evaluated. In 1D scattering, this dependence is conventional since it only introduces constant phases fixed by the choice of the (common) spatial origin. In the present 2D scattering, this is not the case: Considering the spectral expansion of  $\mathcal{G}^+(E)$  into (scattering) eigenstates of the system Hamiltonian, Eq. (3.28), we anticipate that its projection onto the lead eigenmodes in Eq. (3.47) can generally contain contributions from *evanescent* modes in the leads and not only from propagating ones. Although we started out to obtain the (asymptotic)  $S$ -matrix, there is no formal reason to truncate the sums over  $m$  and  $n$  above to open channels, and thus the matrix elements  $\mathcal{S}_{qp}^{nm}$  in Eq. (3.47) are generalized to evanescent modes  $m$  for which  $E_m^{(p)} > E$  (and which thus have an imaginary longitudinal wave vector

$k_m^{(p)}$ ) causing exponential decay into lead  $p$ . An extended  $S$ -matrix is thus defined which includes evanescent modes by analytic continuation of the channel momenta in the complex  $k$ -plane [128]. This extended  $S$ -matrix is, however, non-unitary, since the evanescent modes do not allow for the propagation of flux away from the system in order to conserve the total current.

To extract the  $S$ -matrix elements between open channels only, the points of evaluation of  $\mathcal{G}^+(E)$  should be taken to the asymptotics  $x_p, x_q \rightarrow \infty$ , where the evanescent contributions have vanished. Alternatively, though, one can simply discard matrix elements corresponding to closed channels by multiplying (3.47) with step functions  $\theta(E - E_m^{(p)})$  and  $\theta(E - E_n^{(q)})$ . Doing so, the positions  $x_p, x_q$  indeed become a matter of convention, introducing only phase factors. They could be set at the origins of the attached leads,  $x_p, x_q \equiv 0_p$ , which in turn are put right after the opening of the quantum billiard into each lead (or shifted outwards to points where any applied magnetic field has vanished; see below). The final formula to be used for obtaining the  $S$ -matrix elements from the Greenian can then be compactly written as

$$S_{qp}^{nm}(E) = i\hbar \sqrt{v_n^{(q)} v_m^{(p)}} \langle \chi_n^q | \mathcal{G}^+(E) | \chi_m^p \rangle - \delta_{qp} \delta_{nm}, \quad (3.49)$$

where the shorthand notation

$$\langle \chi_n^q | \mathcal{G}^+(E) | \chi_m^p \rangle = \int dy_q \int dy_p \chi_n^q(y_q) \mathcal{G}^+(x_q \equiv 0, y_q, x_p \equiv 0, y_p; E) \chi_m^p(y_p) \quad (3.50)$$

for the chosen projection of the Greenian onto the lead modes has been used, and it is implicitly understood that only open channels  $m$  and  $n$  are taken into account.

### Scattering matrix in magnetic fields

Throughout the above discussion the absence of magnetic field has been assumed. In particular, the steps pertaining to the simple relation of the  $S$ -matrix elements to the spatial projection of the Greenian on the lead modes relies on a zero magnetic field in the leads, which renders the transversal mode eigenfunction orthogonal. In the presence of a magnetic field in the leads, the orthogonality is broken [127] due to the coupling of spatial and motional degrees of freedom (see Sec. 1.3), and thus transversal modes cannot be simply projected out as in Eq. (3.46). More precisely, a modified orthogonality relation and associated projection can be used to extract  $S$ -matrix elements in terms of  $\mathcal{G}^+$ , as shown by Baranger and Stone [167], implemented also more recently [50] to study transport through quantum billiards at high magnetic fields.

A simpler approach, which we will make use of here, is to let the applied magnetic field in the model system spatially attenuate within the leads along their directions  $\hat{x}_p$ , until it vanishes at distant points  $x_p = L_B^{(p)}$ . If this adaptation region is long enough, so that the field drops off very gradually outside the billiard confinement geometry, the setup qualifies in simulating a transport device where a homogeneous field is applied; the stronger the simulated field, the longer the required adaptation regions.<sup>4</sup> In practice, this ‘adaptation’ region for the magnetic field in the leads is included as part of the scattering structure itself, and the origins  $x_p = 0_p$  of the actual attached leads are shifted by the length  $L_B^{(p)}$ . The

---

<sup>4</sup> Although the adaptation region for the magnetic field attenuation is usually implemented in practice to describe a homogeneous applied field, it is by far no extraordinary challenge for current technology to produce local magnetic field gradients, even at the nanoscale [168]. This can be achieved, e.g., by fabrication of hybrid structures with superconducting nanopatterned components [169] which expel the magnetic field locally, or by using ferromagnetic microstructures which produce field variation patterns [170, 171] with large field gradients.

Fisher-Lee formula for zero field, Eq. (3.49), is then used with  $\mathcal{G}^+$  projected on the lead modes at the shifted positions where  $\mathbf{B}(x_p = 0_p, y_p) = \mathbf{0}$ . Employing a linear decrease of the magnetic field in simulations, the following form of the peripheral vector potential in the lead coordinates  $\mathbf{r}_p$  can be used:

$$\mathbf{A}(\mathbf{r}_p) = -By_p \left( 1 - \frac{x_p + L_B^{(p)}}{L_B^{(p)}} \right) \hat{\mathbf{x}}_p, \quad (3.51)$$

where  $B$  is the field strength in the billiard region, which will be homogeneous in the studies undertaken here. It is appropriate to choose set vector potential in the local Landau gauge  $\mathbf{A}(\mathbf{r}_p) \parallel \hat{\mathbf{x}}_p$  so that no spurious contributions from  $\partial A_y / \partial x_p$  enter the field  $\mathbf{B}(\mathbf{r}_p) = \nabla \times \mathbf{A}(\mathbf{r}_p)$  [127, 172].

This approach had early proved sufficient for the study of magnetotransport in multi-terminal devices [91, 94] and is particularly suitable for the investigation of the combined effects of the applied field and the geometry of the billiard itself, as pursued in Chaps. 5, 6 and 7. These effects are determined by the dynamics *within* the billiard region together with positioning of the lead openings. The magnetic field adaptation region merely provides a very smooth ‘magnetic ramp’ for the incoming electrons, since they need to overcome the Landau energy in the magnetoelectric subbands, which becomes relevant at higher fields (see Sec. 1.3). In other words, once the electron wave has made it into the billiard, the transport properties (including orbital and interference effects) are determined by the homogeneous field there. If the field had extended homogeneously into the leads then this energy threshold would just be a sharp one instead; the dynamics of electrons just above the magnetoelectric threshold is not expected to alter much for a small field gradient in the model. The actual length of the adaptation region in simulations may be determined by the convergence of the transmission function with varying field gradient.

Apart from using the simple zero-field Fisher-Lee formula, the method described has the further advantage that analytical expressions can be derived for the (semi-infinite) lead Green function in the considered case of flat, hard-wall model leads, as is done in A. Note, however, that for leads  $p$  and  $q$  in different directions,  $\hat{\mathbf{x}}_p \nparallel \hat{\mathbf{x}}_q$ , an implication is added by the adaptation regions by the different local gauges for the vector potential. In order to avoid artificial field components from discontinuities of  $\mathbf{A}(\mathbf{r})$  at the lead openings, the gauge in each lead must match the one of the billiard just before the opening, which can be achieved in two different ways: Either

- (i) a smooth function  $\mathbf{A}(\mathbf{r})$  is determined that matches the gauges at each lead opening for a given billiard geometry and lead positioning, or
- (ii) the total device structure is ‘dissected’ into the main scatterer, the lead parts with the field adaptation regions, and the semi-infinite leads with zero field, and then the propagators for the different parts are successively ‘combined’ into a total  $\mathcal{G}^+$  after being transformed to a common gauge,

where one of the two approaches can be followed according to the needs of each individual case. Method (i) is obviously more restricted, since it is specific for given lead positions. Method (ii) can be uniformly used for treating arbitrary billiard geometries and lead positions, which renders it particularly powerful for the cases of interest here, but requires a procedure for ‘combining’ spatially separated Greenians—this will partially be the objective of the computational approach in Chap. 4.

### 3.2.3 Elements of formal scattering theory

In most scattering systems, the total Hamiltonian of the system is written as the sum of an ‘unperturbed’ part  $\mathcal{H}_0$  and a ‘perturbing’ part  $\mathcal{V}$  which causes the actual scattering processes considered. In potential scattering,  $\mathcal{H}_0$  usually describes the kinetic energy of a free particle, and  $V(\mathbf{r}) = \delta(\mathbf{r} - \mathbf{r}') \langle \mathbf{r} | \mathcal{V} | \mathbf{r}' \rangle = \langle \mathbf{r} | \mathcal{V} | \mathbf{r} \rangle$  is the local (diagonal) potential off which it is scattered. Alternatively,  $\mathcal{H}_0$  might already include a potential for which the solution is already known, like the (ideal) confining potential of a quantum wire. In any case, with this separation the Schrödinger equation can be written

$$\left[ i\hbar \frac{\partial}{\partial t} - \mathcal{H}_0 \right] |\psi\rangle = \mathcal{V} |\psi\rangle, \quad \mathcal{H}_0 + \mathcal{V} \equiv \mathcal{H}, \quad (3.52)$$

so that, in analogy with Eq. (3.11), the term  $\mathcal{V} |\psi\rangle$  takes the form of a source for the system governed by  $\mathcal{H}_0$ . The general stationary state of the system is then formally written in terms of the Greenian  $\mathcal{G}_0 = (\zeta - \mathcal{H}_0)^{-1}$ , with  $\zeta = E \pm i\eta$ , associated to the *unperturbed* Hamiltonian  $\mathcal{H}_0$  in the form of a ‘response’ [173]

$$|\psi\rangle = |\psi_0\rangle + \mathcal{G}_0 \mathcal{V} |\psi\rangle \quad (3.53)$$

to the ‘source term’  $\mathcal{V} |\psi\rangle$  with retarded and advanced versions

$$|\psi^\pm(E)\rangle = |\psi_0(E)\rangle + \mathcal{G}_0^\pm(E) \mathcal{V} |\psi^\pm(E)\rangle \quad (3.54)$$

$$= |\psi_0(E)\rangle + \frac{1}{E - \mathcal{H}_0 \pm i\eta} \mathcal{V} |\psi^\pm(E)\rangle, \quad (3.55)$$

where a solution  $|\psi_0\rangle$  to the homogeneous problem  $(E - \mathcal{H}_0) |\psi_0\rangle = 0$  has been added and, as usual, it is understood that the limit  $\eta \rightarrow 0$  is taken, as in Eq. (3.27). Of course, the ‘source’ term  $\mathcal{V} |\psi\rangle$  is here unknown, and Eq. (3.53) constitutes an integral equation for  $|\psi\rangle$ , known as the Lippmann-Schwinger equation [148, 174]; in spatial representation, it reads

$$\psi^\pm(\mathbf{r}; E) = \psi_0(\mathbf{r}, E) + \int d\mathbf{r}' \mathcal{G}^\pm(\mathbf{r}, \mathbf{r}'; E) V(\mathbf{r}') \psi(\mathbf{r}'; E). \quad (3.56)$$

Recursion of Eq. (3.56), that is, repeated re-insertion of  $\psi^\pm(\mathbf{r}; E)$ , yields the so-called Brillouin-Wigner series for  $\psi^\pm$  [173].

An analogous integral equation can be formed for the Greenian itself: With  $\mathcal{A}_0 \equiv \zeta - \mathcal{H}_0$ , and assuming the existence of the power series expansion of  $[\mathcal{A}_0 - \mathcal{V}]^{-1}$ , we can make use of the identity [148]

$$\mathcal{A}_0 - \mathcal{V}^{-1} = \mathcal{A}_0^{-1} + \mathcal{A}_0^{-1} \mathcal{V} [\mathcal{A}_0 - \mathcal{V}]^{-1} = \mathcal{A}_0^{-1} + [\mathcal{A}_0 - \mathcal{V}]^{-1} \mathcal{V} \mathcal{A}_0^{-1} \quad (3.57)$$

to write an integral (Lippmann-Schwinger-like) equation for  $\mathcal{G}$  in terms of the unperturbed Greenian  $\mathcal{G}_0$ ,

$$\mathcal{G} = \mathcal{G}_0 + \mathcal{G}_0 \mathcal{V} \mathcal{G} = \mathcal{G}_0 + \mathcal{G} \mathcal{V} \mathcal{G}_0, \quad (3.58)$$

which in spatial representation becomes

$$\mathcal{G}(\mathbf{r}, \mathbf{r}') = \mathcal{G}_0(\mathbf{r}, \mathbf{r}') + \int ds \mathcal{G}_0(\mathbf{r}, s) V(s) \mathcal{G}(s, \mathbf{r}'). \quad (3.59)$$

Equation (3.58) is often referred to as the Dyson equation for the single-particle picture of the scattering system considered [173] due to its similarity to the form obtained in diagrammatic perturbation theory for many-body systems: The associated so-called ‘self-energy’ operator  $\Sigma$ , which modifies the vacuum propagator in the presence of interactions, reduces here

simply to the influence of the external perturbing potential  $\mathcal{V}$ . We will encounter a more suggestive form of the analogue of a self-energy in Sec. 3.3.2 after spatially partitioning the scattering system.

We can write Eq. (3.58) alternatively as

$$\mathcal{G} = \mathcal{G}_0 + \mathcal{G}_0 \mathcal{T} \mathcal{G}_0 \quad (3.60)$$

in terms of the *transition* operator [175]

$$\mathcal{T} = \mathcal{V} + \mathcal{V} \mathcal{G}_0 \mathcal{V} + \mathcal{V} \mathcal{G}_0 + \mathcal{V} \mathcal{G}_0 \mathcal{V} + \dots = \mathcal{V} [1 - \mathcal{G}_0 \mathcal{V}]^{-1} = [1 - \mathcal{V} \mathcal{G}_0]^{-1} \mathcal{V} \quad (3.61)$$

satisfying the equations

$$\mathcal{T} = \mathcal{V} + \mathcal{V} \mathcal{G}_0 \mathcal{T} = \mathcal{V} + \mathcal{T} \mathcal{G}_0 \mathcal{V}. \quad (3.62)$$

The transition operator plays a central role in scattering off finite-range potentials since its matrix elements between an initial and a final unperturbed (asymptotic) state yields the corresponding scattering amplitude. Here, in Eq. (3.60), we see that  $\mathcal{T}$  represents the multiple (virtual) scattering processes (expressed by  $\mathcal{V}$  in the scattering region connected by the unperturbed propagator  $\mathcal{G}_0$ ).

To obtain a ‘closed form’ for  $|\psi^\pm\rangle$ , though necessarily containing the full propagator  $\mathcal{G}$  of the system, we can restate Eq. (3.52) for the *unperturbed* system (assuming stationary scattering) as [148]

$$\mathcal{A} |\psi_0\rangle \equiv [\zeta - \mathcal{H}] |\psi_0\rangle = -\mathcal{V} |\psi_0\rangle, \quad (3.63)$$

and express its formal solution in terms of  $\mathcal{G} = \mathcal{A}^{-1}$  by adding a solution  $|\psi\rangle$  to the homogeneous problem  $\mathcal{A} |\psi_0\rangle = 0$ , just as was done equivalently in Eq. (3.53). This yields

$$|\psi\rangle = |\psi_0\rangle + \mathcal{G} \mathcal{V} |\psi_0\rangle \quad (3.64)$$

$$= [1 + \mathcal{G}_0 + \mathcal{G}_0 \mathcal{V} \mathcal{G}_0 + \dots] \mathcal{V} |\psi_0\rangle, \quad (3.65)$$

where in the second equality the full propagator  $\mathcal{G}$  has been expanded into a (Born) series in the potential by its recursive insertion into Eq. (3.58). Keeping only the first order in  $\mathcal{V}$  in Eq. (3.65) gives the (first) Born approximation to the scattering state.<sup>5</sup> The counterpart of Eq. (3.54) now becomes

$$|\psi^\pm(E)\rangle = \mathcal{W}_\pm(E) |\psi_0(E)\rangle, \quad (3.66)$$

where (from the series expansion in Eq. (3.65))

$$\mathcal{W}_\pm(E) = 1 + \mathcal{G}^\pm(E) \mathcal{V} = \frac{1}{1 - \mathcal{G}_0^\pm(E) \mathcal{V}} \quad (3.67)$$

is the *wave* (or Møller) operator, parametrized here in energy for the stationary (time-independent) picture considered.  $\mathcal{W}_\pm$  is in turn closely connected to the transition operator through the relations [175]

$$\mathcal{T}_\pm = \mathcal{V} \mathcal{W}_\pm = \mathcal{W}_\pm \mathcal{V}, \quad (3.68)$$

where the  $\pm$  sign corresponds to taking  $\mathcal{G}_0^\pm$  in Eq. (3.61), meaning that their matrix elements provide equivalent information for a given potential.

In correspondence to a time-dependent picture [177],  $|\psi_0\rangle$  in Eq. (3.66) represents either an initial state  $|\Phi_i\rangle$  or a final state  $|\Phi_f\rangle$  of the system described by the Hamiltonian  $\mathcal{H}_0$ , transformed by  $\mathcal{W}_\pm$  to the scattering state  $|\psi^+\rangle$  or  $|\psi^-\rangle$ , respectively, of the actual system

---

<sup>5</sup> This approximation was employed by Born in the same paper [176] where, in a footnote, the interpretation of the squared absolute wave function amplitude as a probability (density) was originally proposed.

described by  $\mathcal{H}$  at the same energy  $E$ . In this sense, the wave operators define the system's *scattering* operator  $\mathcal{S}$  as

$$\mathcal{S} = \mathcal{W}_-^\dagger \mathcal{W}_+, \quad (3.69)$$

whose matrix elements (constituting the  $S$ -matrix introduced previously) in the basis of unperturbed states are given by the projection of the outgoing on the ingoing scattering state,

$$\mathcal{S}_{\beta\alpha} = \langle \Phi_{f;\beta} | \mathcal{S} | \Phi_{i;\alpha} \rangle = \langle \Phi_{f;\beta} | \mathcal{W}_-^\dagger \mathcal{W}_+ | \Phi_{i;\alpha} \rangle = \langle \psi_\beta^- | \psi_\alpha^+ \rangle, \quad (3.70)$$

where the indices  $\alpha, \beta$  denote (asymptotic) quantum numbers such as channels and momenta. This is in direct analogy to Eq. (2.10), with  $\alpha, \beta$  representing (collectively) the lead and mode indices associated with an open quantum billiard system.

### The need for a spatial decomposition of confined systems connected to leads

We have seen how, in the framework of stationary scattering theory, the asymptotic response of an open system to an incoming excitation, given by its  $S$ -matrix, is directly related to the resolvent (the Greenian) of the governing Hamiltonian. It also provides the general approach for treating modifications or additional contributions to a given Hamiltonian in the form of recursive (Dyson-like) expressions for the Greenian, as in Eq. (3.58), which will be utilized in the following chapters to efficiently assemble desired system setups. More importantly, however, the above outline of the formalities of scattering theory reveal an essential peculiarity of the generic case of the open system we consider, that is, a 2D confining potential with openings into semi-infinite leads: Contrary to the case of scattering off a potential which vanishes asymptotically, allowing for the inclusion of solutions  $|\psi_0\rangle$  of the homogeneous Schrödinger equation  $(E - \mathcal{H}_0)|\psi_0\rangle$  to the scattering states  $|\psi\rangle$ , here the potential  $V(\mathbf{r})$  by definition extends to infinity in the form of the (multiple) perfect lead confinement. Since perturbed and unperturbed states must obey common (asymptotic) boundary conditions, the latter are necessarily identified as eigenstates of an 'unperturbed' Hamiltonian  $\mathcal{H}_0$  which *includes*, however, the asymptotic confinement; any additional modification  $\mathcal{V}$  is then added to the active scattering region upon which the leads are attached. In fact, the original generalization of the Fisher-Lee formula in Ref. [165] to multiterminal geometries, Eq. (3.47), made use of a disorder potential present in the scattering region, with the derivation based essentially on Eq. (3.70); once the general relation between the  $S$ -matrix amplitudes and  $\mathcal{G}^+$  is established, it naturally holds also for vanishing disorder, that is, for the geometrically defined scatterer alone.<sup>6</sup>

The particular implications of asymptotic confinement in modeling quantum transport is underlined when commonly expressing the on-shell scattering operator in terms of the (causal) transition operator  $\mathcal{T}_+ \equiv \mathcal{T}$  for scattering off a finite-range potential (a localized scatterer in otherwise free space) as [175, 177]

$$\mathcal{S}(E) = 1 - 2\pi\delta(E - \mathcal{H}_0)\mathcal{T}, \quad (3.71)$$

---

<sup>6</sup> In a derivation of the Fisher-Lee formula based on the scattering formalism of the present chapter, which will not be repeated here, flux normalized asymptotic lead states can be used throughout: Since the scattering state is initially expressed in terms of the spatially represented Greenian [165, 166] and then projected on the lead eigenstates to obtain the  $S$ -matrix (and not vice versa), the lead indices present in the corresponding fluxes enter symmetrically among the leads. In the (perhaps more intuitive) derivation presented in Sec. 3.2.2, the selective evaluation of the Green function from a selected lead  $n$  carries this index via the flux normalization in this lead, which would replace  $\sqrt{v_n^{(q)} v_m^{(p)}}$  with  $v_n^{(q)}$  in Eq. (3.47). To avoid this technical issue, the rescaled (in general non-unitary)  $S$ -matrix Eq. (3.43) has to be used in Eq. (3.42).

with matrix elements thus given by

$$\mathcal{S}_{\beta\alpha} = \delta_{\beta\alpha} - 2\pi\delta(E_\beta - E_\alpha) \langle \Phi_{f;\beta} | \mathcal{T} | \Phi_{i;\alpha} \rangle. \quad (3.72)$$

The role of  $\mathcal{T}$  is here clearly revealed: It is responsible for the actual scattering part of the  $S$ -matrix arising due to the presence of the potential. This also holds for a potential with translationally invariant asymptotic confinement, such as a perfect quantum wire with a finite scatterer *within* it. For  $\mathcal{V} = 0$  (and thus  $\mathcal{T} = 0$  in Eq. (3.71)), any incoming state is preserved and no scattering occurs.

For a generic multiterminal system, the term  $\delta_{\beta\alpha}$  in Eq. (3.72) at most expresses the orthogonality of ‘unperturbed’ scattering eigenstates  $|\psi_{0;\alpha}\rangle$  of  $\mathcal{H}_0$  (containing the asymptotic confinement), which would be transformed into ‘perturbed’ states  $|\psi_\alpha^\pm\rangle$  in the presence of an *additional* potential  $\mathcal{V}$ . Since we want, however,  $\mathcal{S}_{\beta\alpha}$  to express scattering between different *lead* states, as in Eq. (2.10) (that is, with  $\alpha \equiv (m, p)$ ), the form in Eq. (3.72) cannot be used here appropriately because the term  $\delta_{\beta\alpha}$  would imply total reflection into the incoming lead at any energy.<sup>7</sup>

In other words, there are no ‘free’ states corresponding to unperturbed wave propagation in the total system of the 2D cavity connected to leads, since the corresponding Hamiltonian causes scattering already due to the geometric confinement alone. The closest notion of free wave propagation is that of the *isolated* lead states, that is, eigenstates of separate leads disregarding the cavity, which were indeed used to obtain the  $S$ -matrix in Sec. 3.2.2. It thus becomes clear that, in order to treat the multiterminal system within integral scattering theory (using the resolvents of the Hamiltonian), a spatial *decomposition* of the total system into the scattering region and the connected leads on the level of the Hamiltonian itself is needed. As will be seen in the following, this scheme will allow for the formulation of the scattering problem in terms of an effective Hamiltonian for the isolated scatterer which incorporates the presence of the semi-infinite leads. Conceptually, we turn from a description through eigenstates of different Hamiltonians (perturbed and unperturbed in the presence and absence of a scattering potential, respectively) with the same boundary conditions to a description through eigenstates of the same total Hamiltonian but with different boundary conditions (corresponding to the separate parts of configuration space).

### 3.3 Non-Hermitian approach to scattering

Following the discussion above, we now outline the formulation of the scattering problem in terms of a propagator for the scattering region alone which incorporates the coupling to the attached leads, based on the motivated spatial decomposition.

#### 3.3.1 Decomposition of configuration space

As before, we start with the total Hamiltonian  $\mathcal{H}$  describing single-electron motion within a potential  $V(\mathbf{r}) = \langle \mathbf{r} | \mathcal{V} | \mathbf{r} \rangle$  consisting of a 2D cavity attached to  $N_L$  semi-infinite leads which in turn represent the connection to (separate) electron reservoirs. We now consider a connected spatial domain  $\mathbb{D}_S \subset \mathbb{R}^2$  containing the scattering (or ‘reaction’) region (the region where coherent transport is assumed for a mesoscopic device), enclosed by a fictitious boundary  $\partial\mathbb{D}_S$  which cuts the attached leads transversally at some depth into each lead, as shown in Fig. 3.2. The leads (starting from  $\partial\mathbb{D}_S$ ) thus belong to the complement  $\bar{\mathbb{D}}_S = \mathbb{R}^2 - \mathbb{D}_S$  of  $\mathbb{D}_S$ ,

---

<sup>7</sup> On the other hand, if the total confining potential is included in  $\mathcal{V}$ , as was done in Chap. 2,  $\delta_{\beta\alpha}$  would have no meaning since no leads would exist for  $\mathcal{V} = 0$ .

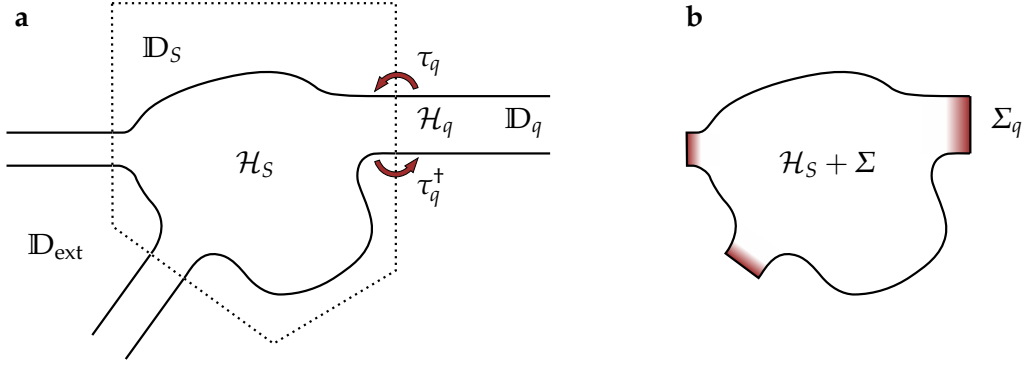


**Figure 3.2:** (a) Decomposition of a multiterminal system into a scatterer domain  $\mathbb{D}_S$  attached to  $N_L = 3$  non-overlapping lead domains  $\mathbb{D}_q$ ,  $q = 1, 2, 3$ , with  $\mathbb{D}_L = \bigcup_{q=1}^{N_L} \mathbb{D}_q$ . The scatterer projected Hamiltonian  $\mathcal{H}_S$  is coupled to the lead-projected Hamiltonian  $\mathcal{H}_L = \sum_{q=1}^{N_L} \mathcal{H}_q$  through a coupling operator  $\tau = \sum_{q=1}^{N_L} \tau_q$ . (b) The scattering system can be mapped to an isolated scatterer with non-Hermitian Hamiltonian  $\tilde{\mathcal{H}}_S = \mathcal{H}_S + \Sigma$ , where the self-energy operator  $\Sigma = \sum_{q=1}^{N_L} \Sigma_q$  represents the coupling to the leads.

which can be further refined into the actual (rectangular) regions  $\mathbb{D}_q$  of the different leads  $q$  and the ‘exterior’ space  $\mathbb{D}_{\text{ext}}$  between them. In summary:

$$\mathbb{D}_S \cup \bar{\mathbb{D}}_S = \mathbb{R}^2, \quad \bar{\mathbb{D}}_S = \mathbb{D}_{\text{ext}} \cup \mathbb{D}_L, \quad \mathbb{D}_L = \bigcup_{q=1}^{N_L} \mathbb{D}_q. \quad (3.73)$$

In order to maintain a representation-independent formulation here, we define spatial projection operators [178]  $\mathcal{Q}$  and  $\mathcal{P}$  as

$$\mathcal{Q} = \mathcal{Q}^2 = \int_{\mathbb{D}_S} d\mathbf{r} |\mathbf{r}\rangle \langle \mathbf{r}|, \quad (3.74)$$

$$\mathcal{P} = \mathcal{P}^2 = \int_{\bar{\mathbb{D}}_S} d\mathbf{r} |\mathbf{r}\rangle \langle \mathbf{r}| = \int_{\mathbb{D}_{\text{ext}}} d\mathbf{r} |\mathbf{r}\rangle \langle \mathbf{r}| + \mathcal{P}_L, \quad (3.75)$$

which project any state onto the scattering and lead regions, respectively, with

$$\mathcal{P}_L = \sum_q \mathcal{P}_q, \quad \mathcal{P}_q = \int_{\mathbb{D}_q} d\mathbf{r}_q |\mathbf{r}_q\rangle \langle \mathbf{r}_q|, \quad (3.76)$$

projecting onto the leads. Since  $\mathcal{Q}$  and  $\mathcal{P}$  cover the whole configuration space, and since any lead state vanishes in the exterior region  $\bar{\mathbb{D}}_{\text{ext}}$ , the completeness relations

$$\mathcal{Q} + \mathcal{P} = 1 = \mathcal{Q} + \mathcal{P}_L, \quad (3.77)$$

are fulfilled (recall that the symbol 1 is used to denote the identity operator), as is the ‘complementarity’

$$\mathcal{Q}\mathcal{P} = 0 = \mathcal{P}\mathcal{Q} \quad (3.78)$$

of the projections.

Writing a total stationary scattering state of the system (at energy  $E$ ) as

$$|\psi_E\rangle = (\mathcal{Q} + \mathcal{P}) |\psi_E\rangle \equiv |\psi\rangle + |\Phi\rangle, \quad (3.79)$$

where  $\mathcal{Q}|\psi_E\rangle = |\psi\rangle$  and  $\mathcal{P}|\psi_E\rangle = |\Phi\rangle = \sum_q |\Phi_q\rangle$  are cavity and (collectively expressed) lead states at energy  $E$ , respectively, the associated stationary Schrödinger equation

$$(E - \mathcal{H})|\psi_E\rangle = (E - \mathcal{H})(\mathcal{Q}|\psi\rangle + \mathcal{P}|\Phi\rangle) = 0 \quad (3.80)$$

is decomposed, by acting from the left with  $\mathcal{Q}$  or  $\mathcal{P}$ , respectively, as

$$\mathcal{H}_{\mathcal{Q}\mathcal{Q}}|\psi\rangle + \mathcal{H}_{\mathcal{Q}\mathcal{P}}|\Phi\rangle = E|\psi\rangle, \quad (3.81)$$

$$\mathcal{H}_{\mathcal{P}\mathcal{P}}|\Phi\rangle + \mathcal{H}_{\mathcal{P}\mathcal{Q}}|\psi\rangle = E|\Phi\rangle. \quad (3.82)$$

The projected parts

$$\mathcal{H}_{\mathcal{Q}\mathcal{Q}} = \mathcal{Q}\mathcal{H}\mathcal{Q} \equiv \mathcal{H}_S, \quad \mathcal{H}_{\mathcal{P}\mathcal{P}} = \mathcal{P}\mathcal{H}\mathcal{P} \equiv \mathcal{H}_L \quad (3.83)$$

of the Hamiltonian govern the system in the *isolated* scatterer and lead regions, respectively, while

$$\mathcal{H}_{\mathcal{Q}\mathcal{P}} = \mathcal{Q}\mathcal{H}\mathcal{P} = [\mathcal{P}\mathcal{H}\mathcal{Q}]^\dagger = \mathcal{H}_{\mathcal{P}\mathcal{Q}}^\dagger \equiv \tau \quad (3.84)$$

stands for the *coupling* between the two subdomains, which ensures hermiticity of  $\mathcal{H}$  in any representation.

### 3.3.2 Effective scattering Hamiltonian for finite system

The above decomposition scheme for configuration space is the basis of the reaction matrix ( $R$ -matrix) theory of scattering [179], originally developed by Wigner and Eisenbud [180], which has been applied extensively to quantum transport in open billiards [178, 181–183]. In this context, the scatterer- and lead-projected states are expanded in the corresponding eigenbases, and an explicit (singular [178]) form of the coupling operators Eq. (3.84) is assumed. Our target here is the Greenian of the scatterer, in the presence of the leads, for a generic transport device setup, to be represented on a discretized spatial basis (tight-binding lattice) in Chap. 4. With this in mind, we keep the present approach at the general level of decomposition.

It is instructive, nevertheless, to make a conceptual distinction between the scatterer and the leads, in that the latter are connected to (large) electron reservoirs in the transport model, following [159]. Without the distinction, the system of equations (3.81) and (3.82) is completely symmetric in the two subdomains, and can be solved equivalently for either  $|\psi\rangle$  or  $|\Phi\rangle$  in terms of the coupling to the complementary subdomain. Let us now write the lead state as

$$|\Phi\rangle = |\Phi_L\rangle + |\Phi_S\rangle, \quad (3.85)$$

where  $|\Phi_L\rangle$  represents the state of the isolated lead (occupied by electrons originating from the reservoir) and  $|\Phi_S\rangle$  the contribution from the scatterer into the lead upon their connection (through the coupling  $\tau$ ), and consider for a moment the eigenvalue problem  $(E - \mathcal{H}_L)|\Phi_L\rangle = 0$  of the isolated lead.<sup>8</sup> Adding and subtracting an imaginary part  $i\eta$  to the lead Hamiltonian  $\mathcal{H}_L$ , this becomes a ‘scattering’ problem for  $|\Phi_L\rangle$  at a given energy  $E$ ,

$$(E - \mathcal{H}_L + i\eta)|\Phi_L\rangle = |\Phi_R\rangle, \quad (3.86)$$

where  $+i\eta$  represents an outflow (loss) of electrons from the lead, compensated by an inflow (gain) of electrons from the reservoir represented by the source term  $|\Phi_R\rangle = i\eta|\Phi_L\rangle$ . The rate  $\eta$ , which adds a width to each energy level of the isolated lead, is to be taken to zero in

---

<sup>8</sup> Treating all leads on an equal footing, we have dropped here the index  $q$  of an individual lead, and describe all leads collectively by  $\mathcal{H}_L$ .

a final calculation, as usual, but it is conceptually important here that even its infinitesimal presence does not alter the description: In contrast to the isolated scatterer, whose density of states would be affected by the level broadening due to its finite energy level spacing (depending on the confining potential), the leads connected to the large reservoirs have practically (and semi-infinite leads truly) continuous density of states, with level spacing smaller than any fictitious  $\eta$ . With this distinction, it becomes natural to add the infinitesimal  $-i\eta$  to the lead Hamiltonian, to determine the state in the scatterer after the connection.

The system of equations (3.81) and (3.82) can now be written in operator-matrix notation (recall that no representation has yet been chosen) as

$$\begin{pmatrix} E - \mathcal{H}_S & -\tau \\ -\tau^\dagger & E - \mathcal{H}_L + i\eta \end{pmatrix} \begin{pmatrix} |\psi\rangle \\ |\Phi\rangle \end{pmatrix} = \begin{pmatrix} 0 \\ |\Phi_R\rangle \end{pmatrix}, \quad (3.87)$$

where the equilibrating in- and outflow  $\pm i\eta |\Phi_L\rangle$  between leads and reservoirs just discussed is assumed unaffected by the presence of the scattered state  $|\Phi_S\rangle$  in the leads. Eliminating  $|\Phi_R\rangle$  from (3.86) and (3.87) we obtain

$$\begin{pmatrix} E - \mathcal{H}_S & -\tau \\ -\tau^\dagger & E - \mathcal{H}_L + i\eta \end{pmatrix} \begin{pmatrix} |\psi\rangle \\ |\Phi_S\rangle \end{pmatrix} = \begin{pmatrix} \tau |\Phi_L\rangle \\ 0 \end{pmatrix} \equiv \begin{pmatrix} |\psi_L\rangle \\ 0 \end{pmatrix}, \quad (3.88)$$

whose lower equation yields

$$|\Phi_S\rangle = \mathcal{G}_L^+ \tau^\dagger |\psi\rangle, \quad (3.89)$$

where

$$\mathcal{G}_L^+(E) = [E - \mathcal{H}_L + i\eta]^{-1} \quad (3.90)$$

is the retarded Greenian of the lead region. We thus see that the billiard state  $|\psi\rangle$  is coupled onto the leads by  $\tau^\dagger$  and acts a source which excites the scattered state  $|\Phi_S\rangle$  in the lead by action of its propagator  $\mathcal{G}_L$ .

We can now reinsert Eq.(3.89) into Eq.(3.88) to arrive at the following equation for  $|\psi\rangle$ :

$$[E - \mathcal{H}_S - \Sigma^+(E)] |\psi\rangle = |\psi_L\rangle, \quad (3.91)$$

where

$$\Sigma^\pm(E) = \tau \mathcal{G}_L^\pm(E) \tau^\dagger \quad (3.92)$$

is the so-called self-energy operator (including here both its retarded (+) and advanced (-) version), with the formal solution

$$|\psi\rangle = \tilde{\mathcal{G}}_S |\psi_L\rangle = \tilde{\mathcal{G}}_S \tau |\Phi_L\rangle, \quad (3.93)$$

where

$$\tilde{\mathcal{G}}_S(E) = [E - \mathcal{H}_S - \Sigma^+(E)]^{-1}. \quad (3.94)$$

is the Greenian of a modified Hamiltonian describing the scatterer coupled to the leads. In similarity to Eq.(3.89),  $|\psi_L\rangle$  now represents an inhomogeneous source term from (incident) states in the leads which give rise to the scattering state  $|\psi\rangle$  in the billiard region. The decomposition scheme has thus allowed for a description of scattering in the total (infinitely extended) system in terms of the projection to the system of interest—the scatterer constituting the active transport device. In the (discretized) spatial representation to be employed in Chap. 4, this truncates the dimension of the Hamiltonian matrix from infinity to that of the scatterer alone. The price to pay is that the scatterer is now governed by a Hamiltonian

$$\tilde{\mathcal{H}}_S^+(E) = \mathcal{H}_S + \Sigma^+(E) \quad (3.95)$$

which is *non-hermitian* and *energy dependent* due to the presence of the lead propagator  $\mathcal{G}_L^+$  in  $\Sigma^+$ .

### Self-energy, broadening and spectral operators

The Greenians associated with the modified scatterer Hamiltonian are written (see Eq. (3.57))

$$\tilde{\mathcal{G}}_S = [E - \tilde{\mathcal{H}}_S]^{-1} = \mathcal{G}_S + \mathcal{G}_S \Sigma \tilde{\mathcal{G}}_S = \mathcal{G}_S + \tilde{\mathcal{G}}_S \Sigma \mathcal{G}_S \quad (3.96)$$

(with the retarded/advanced  $\pm$  sign suppressed), where no infinitesimal  $i\eta$  is now needed since  $\tilde{\mathcal{H}}_S$  is already complex and thus moves the poles away from the real  $E$ -axis. The above form gives the self-energy  $\Sigma$  its name more suggestively due to the formal similarity of Eq. (3.96) to Dyson's equation, as mentioned below Eq. (3.58): The self-energy here represents the influence of the 'environment' of the attached leads on the unperturbed propagator  $\mathcal{G}_S = [\zeta - \mathcal{H}_S]^{-1}$  of the isolated scatterer by coupling (through  $\tau$ ) the single particle to 'itself' in a separate spatial region (the lead propagator  $\mathcal{G}_L$ ). Distinguishing again between different leads in a multiterminal setup, the total self-energy is given by the sum

$$\Sigma(E) = \sum_p^{N_L} \Sigma_p(E), \quad \Sigma_p = \tau_p \mathcal{G}_p \tau_p^\dagger \quad (3.97)$$

of the (in general different) self-energies due to individual leads, meaning that their influences on the scatterer state are independent. It should be noted here that Eq. (3.96) is so far an exact result within the employed single-electron picture. In contrast to self-energies in many-body theory, which provide an approximative account of electron-electron or electron-phonon interactions [173], here the effect of the (externally defined) leads is taken into account exactly through the self-energy terms.<sup>9</sup>

To deduce the connection between the self-energy and the spectral properties of the scattering system, we write the effective (non-hermitian, energy dependent) Hamiltonian  $\tilde{\mathcal{H}}_S^+(E)$  and its adjoint  $\tilde{\mathcal{H}}_S^-(E)$  as [159]

$$\tilde{\mathcal{H}}_S^\pm(E) = \mathcal{H}_S + \Sigma^\pm(E) = \mathcal{H}_S + \Delta\mathcal{H}_S(E) \mp \frac{i}{2}\Gamma(E), \quad (3.98)$$

where

$$\Delta\mathcal{H}_S = \Sigma_H = \frac{1}{2}[\Sigma^+ + \Sigma^-] \quad (3.99)$$

is the hermitian component of the self-energy, while its anti-hermitian component is used to define the *broadening* operator

$$\Gamma = 2i\Sigma_A = i[\Sigma^+ - \Sigma^-] = -i[(\tilde{\mathcal{G}}_S^+)^{-1} - (\tilde{\mathcal{G}}_S^-)^{-1}] \quad (3.100)$$

which determines the broadening (resonant widths) of the scatterer states due to their coupling to the lead continua. To illustrate this, we consider the generalized eigenvalue problem for the effective Hamiltonian [184]

$$\tilde{\mathcal{H}}_S^\pm(E) |\psi_n^{(\pm)}\rangle = [\mathcal{H}_S + \Sigma^\pm(E)] |\psi_n^{(\pm)}\rangle = \tilde{E}_n^\pm |\psi_n^{(\pm)}\rangle, \quad (3.101)$$

where the right (+) and left (-) eigenstates  $|\psi_n^{(\pm)}\rangle$  (not to be confused with the out- and in-going scattering states of the hermitian Hamiltonian of previous sections) have the property

$$|\psi_n^{(-)}(\zeta)\rangle = |\psi_n^{(+)}(\zeta^*)\rangle \quad (3.102)$$

---

<sup>9</sup> Moreover, one of the reasons for maintaining a representation-independent description here is to separate the notion of the effective scatterer propagator from its discrete spatial (matrix) representation to be used in the next chapter. Using the more common [118,127] matrix formulation from the beginning might suggest that its validity is subject to the approximative tight-binding approach, which is not the case.

in the complex energy  $\zeta$ -plane and the (quasi-particle) eigenenergies are proper solutions [184–186] of

$$\tilde{E}_n^+(\zeta) = \zeta \quad (3.103)$$

with

$$\tilde{E}_n^+(\zeta^*) = [\tilde{E}_n^+(\zeta)]^*, \quad \tilde{E}_n^- = [\tilde{E}_n^+]^* \quad (3.104)$$

The energy dependent ‘eigenvalues’ are complex due to the non-hermiticity of  $\tilde{\mathcal{H}}_S^\pm(E)$  and can be written as

$$\tilde{E}_n^\pm(E) = \langle \psi_n^{(\pm)} | \tilde{\mathcal{H}}_S^\pm(E) | \psi_n^{(\pm)} \rangle = E_n + \Delta E_n(E) \mp \frac{i}{2} \gamma_n(E). \quad (3.105)$$

The presence of the leads thus shifts the eigenlevels  $E_n$  of the isolated scatterer by  $\Delta E_n$  and broadens them to finite widths  $\gamma_n$  (proportional to the escape rate from the scatterer in a time dependent picture), according to the real and imaginary parts of the self-energy, respectively. Being eigenstates of adjoint non-hermitian Hamiltonian operators, the states  $|\psi_n^{(\pm)}\rangle$  fulfill the bi-orthonormality relation [164]

$$\langle \psi_n^{(+)} | \psi_m^{(-)} \rangle = \delta_{nm}, \quad (3.106)$$

and therefore the spectral expansion of the Greenian (see Eq. (3.28)) is now written [184,187]

$$\tilde{\mathcal{G}}_S^\pm(E) = \sum_n \frac{|\psi_n^{(\pm)}\rangle \langle \psi_n^{(\mp)}|}{E - E_n - \Delta E_n(E) \pm \frac{i}{2} \gamma_n(E)}. \quad (3.107)$$

The spectral effects of the leads become more explicit if we consider the *spectral* operator of the scatterer, defined here as

$$\mathcal{F} \equiv i[\tilde{\mathcal{G}}_S^+ - \tilde{\mathcal{G}}_S^-] = \tilde{\mathcal{G}}_S^+ \Gamma \tilde{\mathcal{G}}_S^- = \tilde{\mathcal{G}}_S^- \Gamma \tilde{\mathcal{G}}_S^+, \quad (3.108)$$

where Eq. (3.100) has been used in the latter equalities. With the right/left eigenstate expansion of  $\tilde{\mathcal{G}}_S^\pm(E)$ , Eq. (3.107), it can be written as [127,184]

$$\mathcal{F}(E) = \sum_n \frac{|\psi_n^{(+)}\rangle \gamma_n \langle \psi_n^{(-)}|}{(E - E_n - \Delta E_n)^2 + (\gamma_n/2)^2}. \quad (3.109)$$

The spectral operator describes the response of the system upon an external excitation, taking the role of a generalized density of states in a given representation which incorporates the presence of the leads (the openness of the system). We see from Eq. (3.109) that, if the self-energy operator were constant or slowly varying in  $E$ , then  $\mathcal{F}$  would have a Lorentzian form peaked at  $E_n + \Delta E_n$ . The energy dependence of the shifts  $\Delta E_n$  and broadenings  $\gamma_n$ , however, which is enhanced for stronger coupling to the leads (represented by the operator  $\Gamma$ ), typically leads to a drastically varying (and largely unpredictable) energy-dependent response. This will be seen in practice when studying the transmission through the open billiard setups in the following chapters, where the challenge will be to control the energy dependent transport properties.

### Local density of states

The role of the spectral operator as a generalized density operator is illuminated if we write it in the form [159]

$$\mathcal{F}(E) = 2\pi\delta(E - \tilde{\mathcal{H}}_S) \quad (3.110)$$

where the eigenbasis of the scatterer Hamiltonian has implicitly been used. The (representation-independent) trace of  $\mathcal{F}$  indeed gives the DOS in energy for the open system, which becomes the usual DOS (see Eq. (1.36)) in the limit of vanishing coupling to the leads,

$$\mathcal{N}(E) = \frac{1}{2\pi} \text{Tr}[\mathcal{F}(E)] = \sum_n \frac{\gamma_n}{(E - E_n - \Delta E_n)^2 + (\gamma_n/2)^2} \quad (3.111)$$

$$\rightarrow \sum_n \delta(E - E_n - \Delta E_n) \quad (\gamma_n \rightarrow 0). \quad (3.112)$$

In real-space representation, the *local* density of states (LDOS) is given by the diagonal elements of the spectral function,

$$\rho(\mathbf{r}; E) = \frac{1}{2\pi} \langle \mathbf{r} | \mathcal{F}(E) | \mathbf{r} \rangle = \frac{1}{2\pi} \mathcal{F}(\mathbf{r}, \mathbf{r}; E) = -\frac{1}{\pi} \text{Im} \tilde{\mathcal{G}}_S^+(\mathbf{r}, \mathbf{r}; E). \quad (3.113)$$

Again using the spectral expansion of  $\mathcal{F}$ , the LDOS reads

$$\rho(\mathbf{r}; E) = \sum_n \psi_n^{(+)}(\mathbf{r}) \psi_n^{(-)*}(\mathbf{r}) \frac{\gamma_n}{(E - E_n - \Delta E_n)^2 + (\gamma_n/2)^2} \quad (3.114)$$

$$\rightarrow \sum_n |\psi_n(\mathbf{r})|^2 \delta(E - E_n - \Delta E_n) \quad (\gamma_n \rightarrow 0), \quad (3.115)$$

and hence is also determined by the coupling to the leads, while converging to the DOS with each state weighted by its (isolated) probability density when the lead couplings vanish.

Since, now, the self-energies due to different leads are additive, see Eq. (3.97), the same holds for the broadening operators, and the spectral operator can therefore also be viewed as a sum of contributions  $\mathcal{F}_p$  from all leads  $p = 1, 2, \dots, N_L$ :

$$\mathcal{F} = \sum_{p=1}^{N_L} \mathcal{F}_p, \quad \mathcal{F}_p = \tilde{\mathcal{G}}_S^+ \Gamma_p \tilde{\mathcal{G}}_S^-, \quad (3.116)$$

where

$$\Gamma_p = i[\Sigma_p^+ - \Sigma_p^-], \quad \sum_{p=1}^{N_L} \Gamma_p = \Gamma. \quad (3.117)$$

A *partial* LDOS can then be defined as

$$\rho_p(\mathbf{r}; E) = \frac{1}{2\pi} \langle \mathbf{r} | \mathcal{F}_p(E) | \mathbf{r} \rangle = \frac{1}{2\pi} \langle \mathbf{r} | \tilde{\mathcal{G}}_S^+ \Gamma_p \tilde{\mathcal{G}}_S^- | \mathbf{r} \rangle, \quad (3.118)$$

representing the spatially resolved response of the system upon an excitation (that is, an incoming matter wave) selectively in lead  $p$ .

As we will see, the LDOS provides a unique tool to gain insight into the transport properties and spectral features of the open quantum billiards to be studied. It also constitutes a quantity which is accessible experimentally for typical quantum transport setups by probing the charge density with the device under bias. Indeed, the spectral function entering (3.113) and Eq. (3.118) can be measured via the differential conductance of a device [188], and even direct imaging of spatially resolved densities in electron billiards via scanning gate microscopy [54] has recently been reported.

### 3.3.3 Connection to electronic transport

With the spatial decomposition of the total system into scatterer and attached leads, the formalism presented can be embedded into the Landauer-Büttiker picture of electronic transport, that is, by considering *coherent* transport—within the scatterer region—of matter waves emitted and absorbed *incoherently* from the leads, each of which is in local equilibrium with an electron reservoir.

### Local charge density

The actual local *charge* density in the scattering region is obtained by weighing the partial LDOS from each lead by the Fermi distribution function of the reservoir with which the lead is in equilibrium,

$$n(\mathbf{r}) = \sum_p \int_{-\infty}^{+\infty} dE \rho_p(\mathbf{r}) f_p(E; \Theta) \quad (3.119)$$

where a factor 2 (not present) may be included to account for spin degeneracy.<sup>10</sup> This is in accordance with the Landauer picture of transport developed in Chap. 2, where electrons are emitted *incoherently* from the reservoirs, and thus the corresponding probability densities instead of the scattering wave functions themselves are added in the charge density; see Eq. (3.4) where the lead channels are explicitly summed over.

This result is rigorously obtained as the space-represented diagonal of the (single-particle) density operator in *non-equilibrium* Green function theory [163, 172, 188], originally developed by Keldysh [189] and Kadanoff and Baym [190] and appropriately formulated and extensively employed later for stationary electronic transport in mesoscopic devices [3, 4, 191–193] and molecular junctions [194, 195] as well as for time dependent transport [196–201]. It relies on the so-called *fluctuation-dissipation* theorem [163, 188] for the equilibrium single-particle propagators in many-fermion systems,

$$\mathcal{G}_0^e(E) \equiv -i\mathcal{G}^<(E) = \mathcal{F}(E)f_0(E) \quad (\text{electrons}), \quad (3.120)$$

$$\mathcal{G}_0^h(E) \equiv i\mathcal{G}^>(E) = \mathcal{F}(E)[1 - f_0(E)] \quad (\text{holes}), \quad (3.121)$$

which connects the (Fourier transformed) two-time electron and hole correlation functions  $\mathcal{G}_{ij}^<(t, t') \equiv -i \langle c_j^\dagger(t') c_i(t) \rangle$  and  $\mathcal{G}_{ij}^>(t, t') \equiv i \langle c_i(t) c_j^\dagger(t') \rangle$  ( $c_j^\dagger$  and  $c_i$  being electronic creation and annihilation operators), respectively, describing fluctuations of the particle numbers, to their dissipation to the environment described by  $\mathcal{F}$  (through the broadening operator  $\Gamma$ , as seen above).<sup>11</sup> The equilibrium condition is described by the Fermi distribution function  $f_0(E)$ , suppressing here the temperature dependence  $\Theta$ .

For a system in equilibrium with a single reservoir at chemical potential  $\mu_0$  (which we imagine to be connected to the system through a perfect lead), we thus have the electronic density operator [159]

$$\varrho_0 = \sum_n |\psi_n\rangle f_0(E_n) \langle \psi_n| = f_0(\tilde{\mathcal{H}}_S) = \int \frac{dE}{2\pi} \mathcal{F}(E) f_0(E) = \int \frac{dE}{2\pi} \mathcal{G}_0^e(E) \quad (3.123)$$

where Eq. (3.110) has been used.

The non-equilibrium character of the system now enters when the device is connected to multiple reservoirs, each at equilibrium with a different chemical potential  $\mu_p$ . In the multiterminal setup, the spectral function is split into the contributions from each lead,

<sup>10</sup> In the considered 2D system the charge density naturally has units  $[\text{area}]^{-1}$  (integrated over some area it gives the average number of enclosed electrons), though it is occasionally explicitly multiplied also with electronic charge  $e$  (in order to give the enclosed charge when integrated).

<sup>11</sup>  $\mathcal{G}_{ij}^<(t, t')$  and  $\mathcal{G}_{ij}^>(t, t')$  are the so-called *lesser* and *greater* Green functions, respectively, defined as the corresponding expectation values of products of creation and annihilation operators (that is, as correlation functions) in the second quantization picture for many-body systems. They are related, owing to the fluctuation-dissipation theorem, to the retarded and advanced Green functions through the relation

$$\mathcal{G}^> - \mathcal{G}^< = \mathcal{G}^+ - \mathcal{G}^-, \quad (3.122)$$

which connects the occupancy of states (represented by  $\mathcal{G}^{\lessgtr}$ ) to their spectral features (represented by  $\mathcal{G}^{\pm}$ ).

Eq. (3.116), and the reduced density operator for the scatterer is a weighted sum [202] of the operators  $|\psi_m^p\rangle\langle\psi_m^p|$  due to each lead  $p$ ,

$$\varrho = \sum_p \sum_m |\psi_m^p\rangle f_p(E_m) \langle\psi_m^p| \quad (3.124)$$

$$= \sum_p \int dE f_p(E) \sum_m \delta(E - E_m) |\psi_m^p\rangle \langle\psi_m^p| \quad (3.125)$$

$$= \sum_p \int dE f_p(E) \tilde{\mathcal{G}}_S^+ \tau \left[ \sum_m \delta(E - E_m) |\Phi_m^p\rangle \langle\Phi_m^p| \right] \tau^\dagger \tilde{\mathcal{G}}_S^- \quad (3.126)$$

$$= \sum_p \int \frac{dE}{2\pi} f_p(E) \tilde{\mathcal{G}}_S^+ \tau \mathcal{F}_p^{(L)}(E) \tau^\dagger \tilde{\mathcal{G}}_S^-, \quad (3.127)$$

where  $\mathcal{F}_p^{(L)}(E) = 2\pi\delta(E - \mathcal{H}_p) = i[\mathcal{G}_p^+ - \mathcal{G}_p^-]$  is the spectral function of the isolated lead  $p$ , in analogy to Eqs. (3.110) and (3.108), and where scatterer state  $|\psi_m^p\rangle$  is excited by a source term  $\tau |\Phi_m^p\rangle$  from lead  $p$ , see Eq. (3.93) [159]. With  $\tau \mathcal{F}_p^{(L)}(E) \tau^\dagger = i[\Sigma_p^+ - \Sigma_p^-] = \Gamma_p$ , and writing the non-equilibrium electronic correlator as (see Eq. (3.116))

$$\mathcal{G}^e(E) = \sum_p \mathcal{G}_p^e(E) = \sum_p \mathcal{F}_p(E) f_p(E), \quad (3.128)$$

we have, finally, the multiterminal charge density operator

$$\varrho = \sum_p \int \frac{dE}{2\pi} \mathcal{F}_p(E) f_p(E) = \int \frac{dE}{2\pi} \mathcal{G}^e(E), \quad (3.129)$$

whose space-represented diagonal yields the electron density in Eq. (3.119),  $n(\mathbf{r}) = \langle \mathbf{r} | \varrho | \mathbf{r} \rangle$ .

Since we will be focusing on the effects of geometry on magnetotransport in the linear response regime, as described in Sec. 2.3.2, the chemical potential will be the same in all attached reservoirs, so that the spatial distribution of electrons within the device is effectively described by the LDOS (3.113) alone. The non-equilibrium case outlined above also provides, however, the generic connection of the effective scatterer Hamiltonian (and an associated transmission function) to the electronic current in the Landauer-Büttiker picture, as is shown next.

### Transmission trace formula

To express the charge current  $I_q$  at a terminal  $p$  of a multiterminal device in terms of the elements in the present spatial decomposition scheme, it is natural to start from the continuity equation for the total net current

$$I_{\partial\mathbb{D}_S} = \sum_p^{N_L} I_p = 0 \quad (3.130)$$

flowing between the defined scatterer domain  $\mathbb{D}_S$  and the surrounding leads (see Fig. 3.2), which vanishes for the steady state transport we consider according to Kirchoff's law (conservation of charge).  $I_{\partial\mathbb{D}_S}$  equals the rate of change of the total charge  $Q$  within the scatterer, that is, the probability density integrated over  $\mathbb{D}_S$ , in which the projected state is  $|\psi\rangle$ , see

Eqs. (3.79) and (3.93); applying also the divergence theorem we have<sup>12</sup>

$$\frac{I_{\partial\mathbb{D}_S}}{-e} \equiv \frac{d}{dt} \frac{Q}{e} = -\frac{d}{dt} \langle \psi | \psi \rangle = -\frac{d}{dt} \int_{\mathbb{D}_S} d\mathbf{r} |\psi(\mathbf{r})|^2 \quad (3.131)$$

$$= \int_{\mathbb{D}_S} d\mathbf{r} \nabla \cdot \mathbf{j}(\mathbf{r}) = \int_{\partial\mathbb{D}_S} ds \mathbf{j}(s) \cdot \hat{\mathbf{n}}_{\partial\mathbb{D}_S} = \sum_p^{N_L} \int dy_p \mathbf{j}(x_p \in \partial\mathbb{D}_S, y_p) \cdot \hat{\mathbf{x}}_p, \quad (3.132)$$

with the probability current density (generally in the presence of a vector potential  $\mathbf{A}(\mathbf{r})$ )

$$\mathbf{j}(\mathbf{r}) = \frac{1}{2mi} [\psi^*(\mathbf{r})(\nabla + ie\mathbf{A})\psi(\mathbf{r}) - \psi(\mathbf{r})(\nabla - ie\mathbf{A})\psi^*(\mathbf{r})] \quad (3.133)$$

$$= \frac{1}{m} \text{Re}[\psi^*(\mathbf{r})\nabla\psi(\mathbf{r})] + \frac{e}{m} \mathbf{A}(\mathbf{r}) |\psi(\mathbf{r})|^2, \quad (3.134)$$

simply showing that the total net current is indeed the sum of net currents flowing at the terminals. Using the relation

$$i\hbar \nabla \cdot \mathbf{j}(\mathbf{r}) = \psi(\mathbf{r}) [\mathcal{H}_S \psi(\mathbf{r})]^* - \psi^*(\mathbf{r}) [\mathcal{H}_S \psi(\mathbf{r})], \quad (3.135)$$

and substituting  $\langle \mathbf{r} | \mathcal{H}_S | \psi \rangle$  from Eq. (3.82) the total charge current can be written as

$$I_{\partial\mathbb{D}_S} = -\frac{e}{\hbar} (2\text{Im} \langle \psi | \psi_L \rangle - \langle \psi | \Gamma | \psi \rangle), \quad (3.136)$$

which illustrates the role of the broadening  $\Gamma$  as an escape rate which balances the outgoing flux to that corresponding to the incident source state(s)  $|\psi_L\rangle$ .

To establish the direct connection of the terminal currents to the scatterer Greenian, we define a total charge current operator [159, 202]

$$\mathcal{J} = \frac{d}{dt} \varrho = \sum_p \mathcal{J}_p, \quad (3.137)$$

whose trace gives the charge current  $I = -e \text{Tr}(\mathcal{J})$ . Employing the time-dependent Schrödinger equation corresponding to Eq. (3.87),

$$i\hbar \frac{d}{dt} |\psi\rangle = (\mathcal{H}_S + \Sigma^+) |\psi\rangle + \tau |\Phi_L\rangle \quad (3.138)$$

to substitute the eigenstates  $|\psi_m^p\rangle$  in Eq. (3.124), the partial current operator of lead  $p$  becomes (with energy arguments dropped for clarity)<sup>13</sup>

$$\mathcal{J}_p = \frac{1}{i\hbar} \int \frac{dE}{2\pi} \left\{ [\mathcal{H}_S, \mathcal{G}^e] + \Sigma_p^+ \mathcal{G}^e - \mathcal{G}^e \Sigma_p^- + f_p (\Gamma_p \tilde{\mathcal{G}}_S^- - \tilde{\mathcal{G}}_S^+ \Gamma_p) \right\} \quad (3.139)$$

where Eqs. (3.127), (3.129) and  $\tau \mathcal{F}_p^{(L)} \tau^\dagger = \Gamma_p$  have been used. The net current at terminal  $p$ , including the factor 2 for spin degeneracy, is then given by

$$I_p = 2e \text{Tr} = \frac{e}{\pi\hbar} \int dE \text{Tr} [f_p \Gamma_p \mathcal{F} - \Gamma_p \mathcal{G}^e], \quad (3.140)$$

<sup>12</sup> Note that the symbol  $d\mathbf{r}$  is used simply as a shorthand for the 2D volume element of integration  $d\mathbf{r} \equiv dx dy$  (and not to denote an infinitesimal vector);  $ds$  is the 1D surface element on  $\partial\mathbb{D}_S$  with outward normal unit vector  $\hat{\mathbf{n}}_{\partial\mathbb{D}_S}$  coinciding with the direction  $\hat{\mathbf{x}}_p$  in each (straight) lead  $p$ .

<sup>13</sup> We here use  $\frac{d}{dt} |\psi\rangle \langle \psi| = (\frac{d}{dt} |\psi\rangle) \langle \psi| + |\psi\rangle (\frac{d}{dt} \langle \psi|)$  and the fact that the Hamiltonian of the isolated scatterer is hermitian.

which, using Eqs. (3.128) and (3.116), can be written as a sum of weighted differences ( $f_p - f_q$ ) over all leads  $q \neq p$  (excluding the terminal of incidence),

$$I_p = \frac{e}{\pi\hbar} \int dE \sum_q^{N_L} (f_p - f_q) \text{Tr}[\Gamma_p \mathcal{F}_q], \quad (3.141)$$

while the contribution from the same terminal  $q = p$  obviously vanishes. We have thus arrived at the multiterminal Landauer-Büttiker formula, Eq. (2.57), where the transmission function has acquired the compact form

$$T_{pq} = \text{Tr}[\Gamma_p \mathcal{F}_q] = \text{Tr}[\Gamma_p \tilde{\mathcal{G}}_S^+ \Gamma_q \tilde{\mathcal{G}}_S^-], \quad p \neq q \quad (3.142)$$

known as the Meir-Wingreen [203] (or Caroli [204]) formula. It is important to notice that the trace formula for  $T_{pq}$  is a general result relying here only on the assumption of coherent transport within the scattering region and the incoherent contribution of electrons from the terminals. Indeed, the presence of the open boundaries (leads) has been incorporated exactly in the stationary scattering through the self energies.<sup>14</sup> Note further that, although the trace is representation-independent, the information of the spatial decomposition of the total Hamiltonian is necessarily carried over via the lead indices  $p, q$ . In particular, the reciprocity relation of  $T_{pq}$  in a magnetic field, following from Eq. (3.37), can be rigorously shown [92] in a real-space representation.

### 3.4 Multi-state interference effects

Having developed the framework of scattering through a multiterminal confined system, we now briefly outline the general effects arising from the interference between multiple available states and the particular aspects of these effects for the electron billiard systems to be studied. Multi-state interference in electron billiard manifests itself when varying either the wave vector of the incoming wave or the strength of the magnetic field penetrating the billiard, giving rise to Fano resonances [35] and Aharonov-Bohm oscillations [56], respectively. When the geometry of the billiard or generally the parameters of the confining potential are varied, these two effects are effectively combined, since the underlying interfering states are collectively modified. In essence, characteristic fluctuations of the linear response conductance of mesoscopic systems arising from coherent transport, such as the so-called *universal* conductance fluctuations [155], can be deduced from combined multi-state interference.

#### 3.4.1 Fano interference

In a generic setting of stationary potential (single-particle) scattering, a *resonance* occurs when the incoming scattering state becomes energetically degenerate with a quasi-bound state supported by the potential. Quasi-bound states are here to be thought of as states which would be truly bound in the absence of the coupling of the reaction region to its environment. In the present context, we saw that this coupling is expressed by the self-energy operator  $\Sigma$ , with matrix elements whose real and imaginary part cause a shift and a broadening of a the energy level of given state  $\nu$ , respectively. On the one hand, the level broadening expresses the rate at which a particle in this state can escape from the reaction

---

<sup>14</sup> Equation (3.142) is often derived directly from the Fisher-Lee formula (3.49) by considering explicit self-energy matrices in a specific representation, usually within a certain approximation scheme such as the tight-binding approach which we will employ in practice in the following chapters.

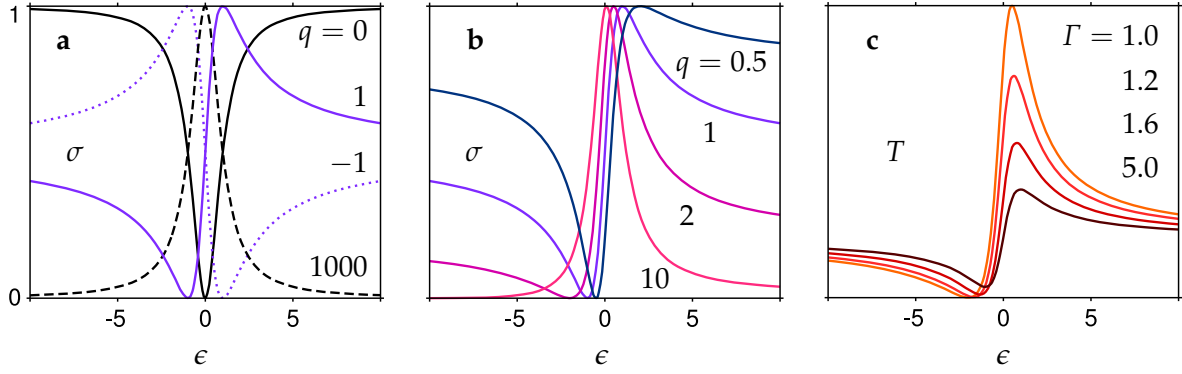


**Figure 3.3:** Fano resonance lineshape. (a,b) Plot of the normalized Fano lineshape formula  $\sigma = (\epsilon + q)(\epsilon^2 + 1)^{-1}(1 + q^2)^{-1}$  for different values of the asymmetry parameter  $q$ . The curve has a zero at  $\epsilon = -q$ , is antisymmetric in  $\pm q$  and becomes a symmetric Lorentzian dip or peak for  $q = 0$  or  $|q| \rightarrow \infty$ , respectively. (c) Plot of the transmission function (3.147) across an isolated Fano resonance, choosing a constant background transmission  $\bar{T} = |\mathcal{S}_{12}|^2 = 0.2$  and lead couplings  $\gamma_1 = \sqrt{\mathcal{S}_{12}}/2$  and  $\gamma_2 = (1 + 2i)\sqrt{\mathcal{S}_{12}}/2$ , for different resonance width parameters  $\Gamma$ . For  $\Gamma > 1$ , the asymmetry parameter  $q_{12}$  becomes complex, such that the maximum is lowered from one and the Fano minimum is raised from zero.

region, and on the other hand it signifies the accessibility of the same state by a particle impinging from the outside.

In collision theory, it is usually the case that the target (or projectile, or both) possesses *internal structure*, with internal states corresponding to individual scattering potentials—in most cases differing through a shift in energy—which then constitute different *channels* of scattering. Now, bound states of higher lying channels may energetically lie in the continuum of lower lying channels, and their coupling to this continuum renders them quasi-bound.<sup>15</sup>

If an energy eigenstate in the continuum of one channel becomes energetically degenerate (that is, within the spectral width) with a quasi-bound state of another (higher lying) channel, then scattering can occur either through the *direct* path of the continuum or the *indirect* path of the resonant quasi-bound state, with the total scattering cross section (the 3D counterpart of transmission) resulting from the superposition of the two paths. As shown by Fano [35], the interference between the a resonant path and a background continuum necessarily results in a *zero* of scattering cross section within the spectral width of the resonance, since the two states interfere with *opposite phase* on one side of the resonance position.<sup>16</sup> This is schematically illustrated in Fig. 3.3.

As a result of the coexistence with a zero in the scattering intensity, the usual symmetric lineshape of a Lorentzian peak around  $E_\nu^r = E_\nu + \Delta E_\nu$  is generically modified into an

<sup>15</sup> The type of coupling between states in different channels is specific to the system considered; Fano used the general notion of (many-body) configuration interaction between the quasi-bound state and the continuum in the context of atomic auto-ionization [35]. In the simplest case, the coupling amounts to the (real-space) projection between the state wave functions via the (single-particle effective) Hamiltonian in the reaction region of the scattering potential [14, 40, 44].

<sup>16</sup> Fano originally [205, 206] considered a single channel and neglected the energy shift of the quasi-bound state, and treated the subject later more rigorously [35]. A generalization to multiple channels and overlapping resonances was provided by Feshbach [207] in the context of nuclear reaction theory, using a projection scheme as here in Sec. 3.3.1 but in state space (into closed and open channels) instead of configuration space. The subject of discrete states coupled to the continuum by configuration interaction was firstly treated, however, by Majorana in 1931 [208–210]

asymmetric lineshape, with the degree of asymmetry determined by the ratio

$$q_\nu = \frac{1}{\pi V_{E,\nu}^*} \frac{\langle \psi_\nu^r | \mathcal{T} | \phi_i \rangle}{\langle \psi_E | \mathcal{T} | \phi_i \rangle}, \quad (3.143)$$

between the transition matrix elements of an initial state  $|\phi_i\rangle$  to the resonant state  $|\psi_\nu^r\rangle$  and to the non-resonant continuum state  $|\psi_E\rangle$ , where  $V_{E,\nu}$  is the (energy dependent and in general complex) coupling between the latter two ( $\Gamma_\nu = 2\pi|V_{E,\nu}|^2$  being the spectral width of the resonant state). The lineshape of the scattering cross section  $\sigma_\nu$  in the vicinity of the resonance then acquires the form

$$\sigma_\nu = \frac{(\epsilon + q_\nu)^2}{\epsilon^2 + 1}, \quad \epsilon = \frac{E - E_\nu^r}{\Gamma_\nu/2} \quad (3.144)$$

in terms of the dimensionless energy variable  $\epsilon$ . This is Fano's famous lineshape formula, with its ubiquitous presence across various fields of physics owing to its general applicability to wave propagation in systems with many degrees of freedom (supporting simultaneous resonant and non-resonant paths). In particular, with the advent of mesoscopic physics, it has found numerous applications in the investigation of nanoscale structures [36]. The peak and zero are given by

$$\sigma_{\nu,\max}(\epsilon = 1/q_\nu) = 1 + q_\nu^2 \quad (3.145)$$

$$\sigma_{\nu,\min}(\epsilon = -q_\nu) = 0, \quad (3.146)$$

so that  $q_\nu$  determines the asymmetry of the lineshape, which becomes a (symmetric) Lorentzian dip or peak for  $q_\nu = 0$  or  $|q_\nu| \rightarrow \infty$ , respectively; see Fig. 3.3.

The Fano asymmetry parameter  $q_\nu$ , introduced phenomenologically in the general lineshape formula, depends on the specific characteristics of the system under consideration. Recently, however, a general classification of Fano resonances with respect to the types of complex poles of a system's Green functions has been proposed, with microscopically determined asymmetry parameters using model Hamiltonians [211].

Adapted to the quantum billiard system with asymptotic Q1D lead confinement considered here, the Fano formula for the partial transmission coefficients  $T_{qp}^{nm} = |\mathcal{S}_{qp}^{nm}|^2$  from (lead,mode) =  $(p, m)$  to  $(q, n)$  in the vicinity of the resonant energy  $E_\nu^r$  can be written as [40, 65]

$$T_{qp}^{nm} = \bar{T}_{qp}^{nm} \frac{|\epsilon + q_{qp;\nu}^{nm}|^2}{\epsilon^2 + 1}, \quad q_{qp;\nu}^{nm} = i - \frac{2i}{\bar{\mathcal{S}}_{qp}^{nm}} \frac{\gamma_{q;\nu}^n \tilde{\gamma}_{p;\nu}^m}{\Gamma_\nu}, \quad (3.147)$$

where  $\gamma_{q;\nu}^n = \langle \Phi_n^{(q)} | \psi_\nu^+ \rangle$ ,  $\tilde{\gamma}_{p;\nu}^m = \langle \Phi_m^{(p)} | \psi_\nu^- \rangle$  are the projections of the resonant left and right eigenstates of the effective Hamiltonian  $\tilde{\mathcal{H}}_S$  on the lead eigenstates. This expression arises from a superposition

$$\mathcal{S}_{qp}^{nm} = \bar{\mathcal{S}}_{qp}^{nm} + i \frac{\gamma_{q;\nu}^n \tilde{\gamma}_{p;\nu}^m}{E - E_\nu^r + i\Gamma_\nu/2} \quad (3.148)$$

of a non-resonant background  $S$ -matrix element  $\bar{\mathcal{S}}_{qp}^{nm}$  (with  $\bar{T}_{qp}^{nm} = |\bar{\mathcal{S}}_{qp}^{nm}|^2$ ), not including the resonant state  $\nu$ , and the resonant one expressed via the (bi-orthonormal) spectral expansion of the open system's Green function; see Eq. (3.107).

In the case of an isolated Fano resonance in single-channel scattering, as in the case of a long-lived resonant state  $\nu$  in a two-terminal quantum dot in the first channel of the leads, the asymmetry parameter  $q_\nu$  is real [40] and the Fano zero occurs. In the case of multiple channels or leads  $q_\nu$  is in general complex and the lineshape minimum is lifted from zero. The same occurs for overlapping resonances, that is, with resonant widths larger than their

spacing in energy [44]. Further, considering that additional leads/channels act effectively as sources of decoherence for a selected channel in the Landauer-Büttiker transport picture, complex asymmetry parameters in single-channel transport can be used as probes of decoherence in the system [212]; Fano resonances have even been used to identify the *type* of decoherence (dissipation versus unitary dephasing) according to the loci of  $q$ -parameters in the complex plane [213].

To make the connection between Fano interference and the spectral and self-energy operators of the previous sections, we note that the diagonal matrix element of the retarded Greenian  $\tilde{\mathcal{G}}_S^+$  with respect to a resonant state  $|\psi_v^+\rangle$  can be written, in the vicinity of the (complex) resonant energy  $\tilde{E}_v^+$ , as [185, 186]

$$\tilde{\mathcal{G}}_{vv} \approx \frac{Z_{vv}}{\zeta - \tilde{E}_v^+(\zeta)} \Big|_{\zeta = \tilde{E}_v^+}, \quad Z_{vv} \equiv \left[ 1 - \frac{\partial \Sigma_{vv}^+(\zeta)}{\partial \zeta} \right]^{-1}, \quad (3.149)$$

so that the corresponding matrix element of the spectral operator becomes

$$\mathcal{F}_{vv}(E) = \frac{1}{\pi} \frac{|\text{Im}\tilde{E}_v^+ \text{Re}Z_{vv} - (E - \text{Re}\tilde{E}_v^+) \text{Im}Z_{vv}|}{(E - \text{Re}\tilde{E}_v^+)^2 + (\text{Im}\tilde{E}_v^+)^2}. \quad (3.150)$$

We thus identify the appearance of a Fano energy dependence with resonant width  $\Gamma_v = 2|\text{Im}\tilde{E}_v^+|$  and strength  $|\text{Re}Z_{vv}|$ , and with  $|\text{Im}Z_{vv}|$  determining the asymmetry of the lineshape [186]. The asymmetric lineshape is then carried over to the transmission function through the trace formula (3.142) once taking into account the coupling to the relevant leads  $p$  and  $q$ .

A conceptual difference should here be noted between channel-coupled scattering in free space due to the internal structure of the reactants and scattering through a geometrically confined structure via attached leads: In the former case, scattering occurs with *different* potentials (energetically shifted) in channels defined *globally*, with channel thresholds determined by the portion of energy attributed to the internal structure (e. g., the Zeeman energy of spins in a magnetic field). In contrast, electron transport through a quantum billiard device occurs in channels defined only in the attached leads and through a *common* scattering potential defined by the confinement in the billiard region. Here, the *total* energy, which was partitioned into transversal modes in the leads, becomes available for propagation within the cavity. Moreover, as discussed above, there is no freely propagating component in the scattered wave: the background, non-resonant part in the Fano interference consists here simply of another, broader resonant state coupled very strongly to the leads.

In fact, the whole transmission spectrum of a single quantum billiard will in principle consist of multiple overlapping Fano resonances [14, 44] with complex asymmetry parameters, which collectively give rise to a highly fluctuating transport response in a typical mesoscopic structure. The central challenge addressed in later chapters will be to gain control over the transport behavior in this overlapping Fano regime through the geometry of the confining potential.

### 3.4.2 Aharonov-Bohm oscillations

The fundamental importance of potentials in quantum theory, as opposed to the fields they produce, was underlined by Aharonov and Bohm [56, 214] by considering electrons interfering at the intersection of distinct paths. The so-called Aharonov-Bohm effect consists in the influence of a magnetic vector potential (or time dependent scalar potential) on the observable quantum behavior of a charged particle, even when it moves in regions where the magnetic (or electric) field vanishes. The effect can be suitably demonstrated for an electron

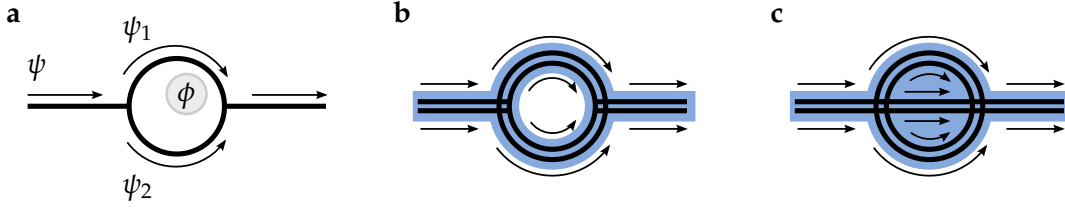


**Figure 3.4:** Aharonov-Bohm interference. (a) In an ideal 1D loop (here a circular ring), an incoming wave  $\psi$  from the left follows the two possible paths along the arms of the ring, with wavefunction  $\psi_1$  and  $\psi_2$  on the upper and lower arm, respectively. The interference of the two waves at the exit on the right, and in turn the transmission amplitude, depends periodically on the flux  $\phi$  piercing the loop, even if does not overlap with the arms. (b) In a loop structure with arms of finite width, several paths are available within the arms leading to multimode AB interference, and in applications the (uniform) magnetic field is usually present also within the leads and arms. (c) For a singly connected device structure, paths along the boundary additionally interfere with bulk paths, but also bulk paths with other bulk paths, leading to collective overlapping AB oscillations in the transmission.

moving on a line containing an ideal 1D ring (or a loop of arbitrary shape) penetrated by a magnetic flux  $\phi$  whose density  $B$  vanishes on the ring, as shown in Fig. 3.4. The spatially confined magnetic field  $\mathbf{B} = \nabla \times \mathbf{A}$  is produced by a vector potential  $\mathbf{A}(\mathbf{r})$  which modifies the (minimal coupling) kinetic momentum into  $\boldsymbol{\pi} = \mathbf{p} - q\mathbf{A} = \mathbf{p} + e\mathbf{A}$ .

Assuming zero reflection at the connecting nodes, an incident stationary electronic wave of unit amplitude from the left will propagate through the upper (1) and lower (2) arm of the ring with wave functions<sup>17</sup>

$$\psi_i = \frac{1}{2} \exp \left[ \frac{i}{\hbar} (\mathbf{p}_i \cdot \mathbf{r}_i + e\mathbf{A} \cdot \mathbf{r}_i) \right], \quad i = 1, 2. \quad (3.151)$$

While being in-phase at the entrance point  $\mathbf{r}_{\text{in}}$  of the loop, along the two (oriented) paths  $\mathcal{C}_1$  and  $\mathcal{C}_2$  the two waves  $\psi_1$  and  $\psi_2$  acquire different phase shifts, which at the exit point  $\mathbf{r}_{\text{out}}$  become

$$\vartheta_i = \frac{1}{\hbar} \int_{\mathcal{C}_i} \mathbf{p}_i \cdot d\mathbf{r} + \frac{e}{\hbar} \int_{\mathcal{C}_i} \mathbf{A} \cdot d\mathbf{r} \equiv \zeta_i + \varphi_i, \quad i = 1, 2, \quad (3.152)$$

in dependence of the gauge of  $\mathbf{A}$ , where  $\zeta_i = \vartheta_i(\mathbf{A} = 0)$  are the phase shifts due to the momentum alone.

The total wave function at the exit will be the superposition of  $\psi_1$  and  $\psi_2$  with square modulus (equal here to the transmission coefficient)

$$T = |\psi(\mathbf{r}_{\text{out}})|^2 = |\psi_1(\mathbf{r}_{\text{out}}) + \psi_2(\mathbf{r}_{\text{out}})|^2 = \frac{1}{2} (1 + \cos(\Delta\zeta + \Delta\varphi)). \quad (3.153)$$

The phase difference between the two paths due to the vector potential,  $\Delta\varphi$ , is proportional to the *gauge-independent* total flux  $\phi$  of the field through the surface  $S$  enclosed by the loop:

$$\begin{aligned} \Delta\varphi = \varphi_1 - \varphi_2 &= \frac{e}{\hbar} \left( \int_{\mathcal{C}_1} \mathbf{A} \cdot d\mathbf{r} - \int_{\mathcal{C}_2} \mathbf{A} \cdot d\mathbf{r} \right) = \frac{e}{\hbar} \left( \int_{\mathcal{C}_1} \mathbf{A} \cdot d\mathbf{r} + \int_{-\mathcal{C}_2} \mathbf{A} \cdot d\mathbf{r} \right) \\ &= \frac{e}{\hbar} \oint_{\text{loop}} \mathbf{A} \cdot d\mathbf{r} = \frac{e}{\hbar} \int_S \mathbf{B} \cdot d\mathbf{s} = \frac{e}{\hbar} \phi = 2\pi \frac{\phi}{\phi_0}, \end{aligned} \quad (3.154)$$

where we define  $\phi_0 \equiv h/e$  as the magnetic flux quantum. The transmission thus oscillates in varying magnetic flux with period  $\phi_0$ .<sup>18</sup>

<sup>17</sup>The normalization is chosen such that  $|\psi_1(\mathbf{r}_{\text{in}}) + \psi_2(\mathbf{r}_{\text{in}})|^2 = 1$  at the entrance point  $\mathbf{r}_{\text{in}}$  of the loop.

<sup>18</sup>Note that this is the ‘first order’ AB effect for the loop system considered: There will in principle be contributions from any number of windings of paths around the loop, including half windings if reflection at the nodes is included [124]. As a result, higher frequencies appear in the AB oscillations; these are, however, suppressed in experimental spectra due to the finite electronic coherence length.

Since the experimental verification of such AB oscillations [215], they have been extensively studied in various mesoscopic ring-like systems [131] in the context of magnetotransport. The experimental setups, of course, far from fulfill the simplistic assumptions of the toy model above, which has posed challenges for the unambiguous confirmation of the effect [216]. The following variations on the above description, among other more system specific ones, modify the observed oscillations:

- (i) Even for ideally controllable systems used in simulations, the elements composing the structure (the ring and the attached leads) are not strictly 1D but have finite width [155], as shown schematically in Fig. 3.4 (b). In the picture of interfering paths, there will thus be an infinite set of trajectories contributing to the interference at the exit. Alternatively, propagation in the leads and ring arms occurs in different transversal modes [68], and there will be a finite coupling between modes in the leads to modes in the ring caused by the connecting nodes, but also coupling between the modes in each arm due to its curvature [217]. Finally, each transmission coefficient  $T_{nm}$  between modes  $m$  and  $n$  of the leads will be a coherent (squared) sum of transmission amplitudes between the leads and the ring arms [127], introducing additional frequencies in the observed oscillations.
- (ii) Although the original aim was the manifestation of the influence of  $A$  in regions of vanishing  $B$ , most experiments as well as simulations are carried out with an external magnetic field covering the whole structure (since it is not trivial to confine the flux to an area in the interior of the loop), though still referring to AB oscillations in the transport. The presence of the field in the ring arms further alters the oscillations by modifying the couplings between transversal modes and by deforming the wave function at higher field strengths.
- (iii) The nodes connecting the loop to the leads are in general not reflectionless (also in a 1D model [218]), meaning that the AB oscillation pattern changes in energy due to (broad or narrow) single-channel resonant states in the ring arms. Even for a fixed energy, however, the AB oscillations may be modified due to the  $B$ -field dependence of resonant states. In particular, Fano resonances will inevitably form due to quasi-bound states in the connecting node regions or in the arms, whose energy position and width in general varies with the magnetic field. Specifically, a Fano resonance may generally be shifted [37] onto the fixed energy considered by varying  $B$ , thus drastically affecting the AB oscillations in transmission. In fact, the interplay between the AB effect and Fano interference from scatterers connected to the arm(s) of a quantum ring has been a topic of intensive interest [62–65], not least as a mechanism for tunable magnetotransport.

The above aspects of AB oscillations in quantum rings are generalized for the quantum billiard systems studied here, as will be seen in Chaps. 5, 6 and 7. There are now additional (semiclassical) paths in the bulk of the billiard interfering with each other and with those along the boundary, as illustrated in Fig. Fig. 3.4 (c), leading to a superposition of AB oscillations with frequencies corresponding to the virtual loops formed by the paths. In the full quantum picture at low energies, the wave functions are in general spatially extended across the whole 2D area of the billiard and cannot be identified with well defined paths as for the ring systems. AB-like oscillations in transmission can here be recognized as the interference of quasi-degenerate (close in energy) states at the terminals, with the phase of each modulated by the applied magnetic field. In fact, specific confining geometries may lead to spatial distributions of states at zero field which are localized along (wide but distinct) paths along

the periphery of the billiard or in its interior, allowing for an association of the resulting transmission oscillations in  $B$ -field to the flux penetrating the system. An extreme case is that of interfering edge states at high field strengths: Interestingly, the transport in the extended system is then mediated by effectively 1D states like in the toy model we started with above, and clear oscillations with definite periodicity are induced in the magnetotransport [60]. Finally, AB-like interference can occur along effective loop structures forming around potential hills of the potential landscape in the 2DEG of electronic nanostructures, caused by (remote) impurities or other sources of disorder. Such loops, whose coherent coupling is modulated by a magnetic field, appear and disappear in a random manner with varying Fermi energy (as it enters valleys or covers hills in the potential, respectively) and can form the basis for an intuitive understanding of the widely investigated phenomena of *weak localization* [98,219] and *universal conductance fluctuations* [96] in disordered mesoscopic systems [118].

### 3.5 Scattering in locally symmetric structures

Let us end this chapter with a note on scattering in systems which are *locally symmetric*, meaning that they obey a certain spatial symmetry within one or more finite spatial domains. Although important phenomenological properties of physical systems are often explained through a model with global symmetry, in the most general case a symmetry of a system under spatial transformations is globally broken but retained on a local scale. Local symmetries are indeed generic for many forms of matter, such as groups of atoms within large molecules or impurities and defects in within crystals. But also artificially designed systems can usually be decomposed into locally symmetric pieces, a representative example being the nanoelectronic devices described previously in Chap. 1. Further, structurally complex systems such as quasicrystals, systems with long-range aperiodic order or even partially disordered systems have inherent local symmetries. The pursuit to develop a theoretical framework for generic (and thereby also matter) wave propagation in locally symmetric systems has recently been undertaken in collaboration with F. K. Diakonov and P. A. Kalozoumis and led to a series of joint works, Refs. [158,220–222]. The focus has so far been on 1D systems, and therefore the topic will only be briefly presented here since the quantum billiard systems to be studied in the following chapters are 2D structures by definition. Nevertheless, the developed formalism and the introduced key concepts render a generalization to Q1D and 2D systems such as nanoelectronic transport devices plausible, making it instructive to demonstrate some main considerations and findings.

#### 3.5.1 Local symmetry induced invariants

Considering scattering in one dimension, there are two discrete symmetry transformations which can be rendered local, inversion through a given point and translation by a given length. In a unified wave-mechanical framework, 1D stationary scattering of a complex wave field  $\psi(x)$  in absence of sinks and sources is described by the Helmholtz equation

$$\psi''(x) + V(x)\psi(x) = 0, \quad (3.155)$$

where the prime denotes differentiation with respect to the spatial variable  $x$ , and where the real potential  $V(x)$  is assumed to be overall finite and asymptotically positive. We now consider the spatial symmetry of  $V(x)$  under inversion through a point  $a$  and translation by a length  $L$ , which can be treated uniformly by defining the linear transformation

$$F : x \rightarrow \bar{x} = F(x) = \sigma x + \rho, \quad (3.156)$$

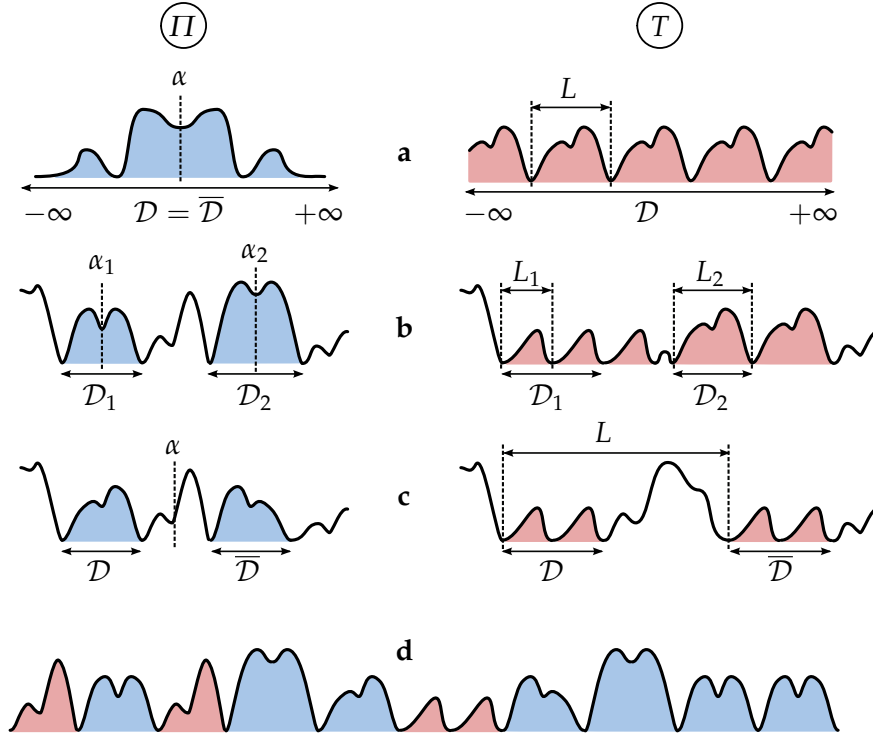


**Figure 3.5:** Different types of symmetry under inversion ( $\Pi$ ) through  $\alpha$  or translation ( $T$ ) by  $L$ , mapping a domain  $\mathcal{D}$  to  $\overline{\mathcal{D}}$ : (a) global symmetry, (b) simple local symmetry, (c) gapped local symmetry, (d) complete local symmetry.

whose type is determined by the parameters  $\sigma$  and  $\rho$  as follows:

$$\sigma = -1, \quad \rho = 2\alpha \Rightarrow F = \Pi \quad : \text{inversion through } \alpha \quad (3.157)$$

$$\sigma = +1, \quad \rho = L \Rightarrow F = T \quad : \text{translation by } L \quad (3.158)$$

Assume now that the potential  $V(x)$  obeys the symmetry

$$V(x) = V(F(x)) \quad \forall x \in \mathcal{D}, \quad (3.159)$$

for an arbitrary domain  $\mathcal{D} \subseteq \mathbb{R}$ . If  $\mathcal{D} = \mathbb{R}$ , then the above symmetry is global, otherwise the symmetry is called local. The latter can be of different types (see Fig. 3.5), as discussed below. The transformations  $F$  generally map a domain  $\mathcal{D}$  to a different one,  $F(\mathcal{D}) = \overline{\mathcal{D}} \neq \mathcal{D}$ , the exception being inversion of a connected domain through its center  $\alpha$  (as seen in Fig. 3.5 (a) and (b) for  $F = \Pi$ ).

The general local symmetry property of the potential can be exploited to construct locally spatial invariant quantities from the field  $\psi(x)$ , as follows. Evaluating Eq. (3.155) at a point  $x$  and at its image  $\bar{x} = F(x)$ , we construct the difference  $\psi(\bar{x})\psi''(x) - \psi(x)\psi''(\bar{x})$ , which in general is non-zero and varies in  $x$ . For a potential  $V(x)$ , however, which fulfills the considered symmetry property in Eq. (3.159), this expression vanishes for all  $x \in \mathcal{D}$ ,

$$\psi(\bar{x})\psi''(x) - \psi(x)\psi''(\bar{x}) = 2iQ'(x) = 0, \quad (3.160)$$

which implies that the complex quantity

$$Q = \frac{1}{2i} [\sigma\psi(x)\psi'(\bar{x}) - \psi(\bar{x})\psi'(x)] \quad (3.161)$$

is spatially invariant (constant in  $x$ ) within the domain  $\mathcal{D}$ . Here  $\psi'(\bar{x}) = \left. \frac{d\psi(x)}{dx} \right|_{x=\bar{x}}$  denotes the derivative function evaluated at  $\bar{x} = F(x)$ , so that  $\sigma$  distinguishes between the  $Q$ 's for inversion ( $F = \Pi$ ) and translation ( $F = T$ ).

The procedure can be repeated using the complex conjugate of Eq. (3.155) evaluated at  $x$  to obtain another invariant in the same domain,

$$\tilde{Q} = \frac{1}{2i} [\sigma\psi^*(x)\psi'(\bar{x}) - \psi(\bar{x})\psi'^*(x)]. \quad (3.162)$$

The invariants defined by Eqs. (3.161) and (3.162) have the form of a 'non-local current' involving points connected by the corresponding symmetry transformation. Note that, because of their constancy in  $\mathcal{D}$ ,  $Q$  and  $\tilde{Q}$  can be evaluated from any chosen symmetry-related points  $x$  and  $\bar{x}$  in this domain. The non-local currents within a symmetry domain  $\mathcal{D}$  are related, for each of the two cases  $F = \Pi, T$  ( $\sigma = -1, +1$ ), by

$$|\tilde{Q}|^2 - |Q|^2 = \sigma J^2, \quad (3.163)$$

where  $J$  is the usual 1D probability (or energy) current carried by the matter (or electromagnetic) wave,

$$J = \frac{1}{2i} [\psi^*(x)\psi'(x) - \psi(x)\psi'^*(x)], \quad (3.164)$$

which is locally defined and globally invariant in one dimension for the real potential  $V(x)$ . The assumptions on the potential provided above guarantee that we have a propagating scattering state with  $J \neq 0$ .

### 3.5.2 Generalized parity and Bloch theorems

We can now use the invariants  $Q, \tilde{Q}$  to obtain a definite relation between the wave field  $\psi(x)$  and its image  $\psi(\bar{x})$  under a symmetry transformation. Let us define an operator  $\hat{O}_F$  which acts on  $\psi(x)$  by transforming its argument through  $F = \Pi$  or  $T$  as given in Eqs. (3.156)-(3.158),  $\hat{O}_F\psi(x) = \psi(\bar{x} = F(x))$ . The image  $\psi(\bar{x})$  can then be solved for from the system of Eqs. (3.161), (3.162), which finally yields

$$\hat{O}_F\psi(x) = \psi(\bar{x}) = \frac{1}{J} [\tilde{Q}\psi(x) - Q\psi^*(x)] \quad (3.165)$$

for all  $x \in \mathcal{D}$ . Equation (3.165), which remains valid in any type of domain  $\mathcal{D}$  for states with  $J \neq 0$ , is a central result of the introduced local symmetry formalism. It explicitly gives the image  $\psi(\bar{x})$  in the target domain  $\bar{\mathcal{D}}$  as a linear combination of  $\psi(x)$  and its complex conjugate in  $\mathcal{D}$ , with the constant weights determined exclusively by  $Q$  and  $\tilde{Q}$  (recall that  $J$  is given from Eq. (3.163)). In other words, the invariant non-local currents  $Q$  and  $\tilde{Q}$ , induced by the local symmetry of  $V(x)$  in Eq. (3.159), provide the mapping between the field amplitudes at points related by this symmetry, regardless if the symmetry is global or not. This transformation of the field can therefore be identified as a remnant of symmetry in the case when it is globally broken.

To anticipate the meaning of Eq. (3.165), consider the scenario where  $\hat{O}_F$  commutes with the Helmholtz operator  $\hat{\mathcal{H}} = \frac{d^2}{dx^2} + V(x)$ , and thus  $V(x)$  obeys global symmetry under  $F$  with  $\mathcal{D} = \mathbb{R}$  in Eq. (3.159), but the (asymptotic) boundary conditions on the field  $\psi(x)$  prevent it from being an eigenfunction of  $\hat{O}_F$ . This is typically the case in a scattering situation, where incident waves are considered only on one side of the potential, thus breaking the  $\Pi$ -symmetry of the problem even if the potential is globally inversion symmetric. Remarkably, within the present framework the benefit of an underlying symmetry is retained in the

treatment of the problem: In spite of the asymptotic conditions breaking global symmetry, the quantities  $Q$  and  $\tilde{Q}$  are constant in the entire space, relying on the global symmetry of  $V(x)$ , and Eq. (3.165) still provides the mapping of the most general wave function under the action of  $\hat{O}_F$ .

From Eq. (3.165) it is now clearly seen that a nonvanishing  $Q$  is a manifestation of broken global symmetry under the discrete transformation  $F$ . As shown in Ref. [158], this leads us to the recovery of the usual parity and Bloch theorems for globally  $\Pi$ - and  $T$ -symmetric systems. Indeed, when  $Q = 0$ , the field  $\psi(x)$  becomes an eigenfunction of the symmetry operation,  $\hat{O}_F\psi(x) = \lambda_F\psi(x)$ , with definite parity eigenvalues  $\lambda_\Pi = \pm 1$  for inversion symmetry and the Bloch phase  $\lambda_\Pi = e^{ikL}$  (up to multiples of  $\pi$ ) for translation symmetry [158].

### 3.5.3 Types of locally symmetric potentials

We end this section by illustrating the possible local symmetry structure of a system and the induced invariants  $Q$  and  $\tilde{Q}$  which explicitly relate the symmetry information to the scattering wave amplitudes via Eq. (3.165). In the extreme case of total  $F$ -symmetry breaking, there is no remnant of symmetry present in  $V(x)$ , and therefore also no domain  $\mathcal{D}$  with constant  $Q$ . Although one can still define spatial functions  $Q(x)$ ,  $\tilde{Q}(x)$  as in Eqs. (3.161), (3.162), leading to Eq. (3.165), their non-constancy brings no advantage to the representation of the scattering problem. If local symmetry is present in  $V(x)$ , we can distinguish the following characteristic cases, which are sketched in Fig. 3.5.

(i) Simple local symmetries: In this case, a symmetry domain  $\mathcal{D}$  either coincides, overlaps, or connects with its image  $\bar{\mathcal{D}} = F(\mathcal{D})$  (that is,  $\bar{\mathcal{D}} \cup \mathcal{D}$  is connected). There can exist one or many such domains of symmetry along the total potential landscape  $V(x)$ , in general with non-symmetric parts in between; see Fig. 3.5 (b). To each local symmetry domain  $\mathcal{D}_i$  ( $i = 1, 2, \dots, N$ ) a pair of spatially invariant (within  $\mathcal{D}_i$ ) non-local currents  $Q_i$  and  $\tilde{Q}_i$  is associated, whose different values change with energy. Within each domain, Eq. (3.165) spatially maps  $\psi(x)$  to its image under the corresponding symmetry transformation: For local  $\Pi$ -symmetry, the field in one half of  $\mathcal{D}_i$  is determined from the field in the other half through the  $Q_i$  and  $\tilde{Q}_i$ , which can be evaluated at the center of inversion  $\alpha_i$ . For local  $T$ -symmetry, the field within the first interval of length  $L$  in  $\mathcal{D}_i$  successively determines its images along a locally periodic part of  $V(x)$ , and the pair of invariants can be evaluated at the corresponding boundaries.

(ii) Gapped local symmetries: In this case, a domain  $\mathcal{D}$  has no overlap with its symmetry-related image ( $\bar{\mathcal{D}} \cap \mathcal{D} = \emptyset$ ). In other words, there is a gap between them in configuration space, within which  $V(x)$  can obey another or no symmetry; see Fig. 3.5 (c). This can of course occur if the source domain  $\mathcal{D}$  is not connected, that is, already has gaps in it. For connected  $\mathcal{D}$ , gapped  $\Pi$ -symmetry occurs if the inversion point lies outside the associated domain ( $\alpha \notin \mathcal{D}$ ), and gapped  $T$ -symmetry if the translation length  $L$  exceeds the size of  $\mathcal{D}$ . Interestingly, once  $Q$  and  $\tilde{Q}$  have been evaluated from a pair of symmetry-connected points, Eq. (3.165) maps the wave function from one part of the potential to a remote part, although there is an arbitrary field variation in the intervening gap.

(iii) Complete local symmetry (CLS): An appealing situation occurs when the potential  $V(x)$  can be completely decomposed into locally symmetric domains, each one characterized by a remnant of the broken symmetry; see Fig. 3.5 (d). This can be realized by attached domains of simple local  $\Pi$ - or  $T$ -symmetry, of a single kind or mixed. Also gapped local symmetries can be part of such a structure, with the gaps between their source ( $\mathcal{D}_i$ ) and image ( $\bar{\mathcal{D}}_i$ ) domains all filled either by simple local symmetry domains or by the source or image domain of other gapped symmetries. The latter case can then result in multiply

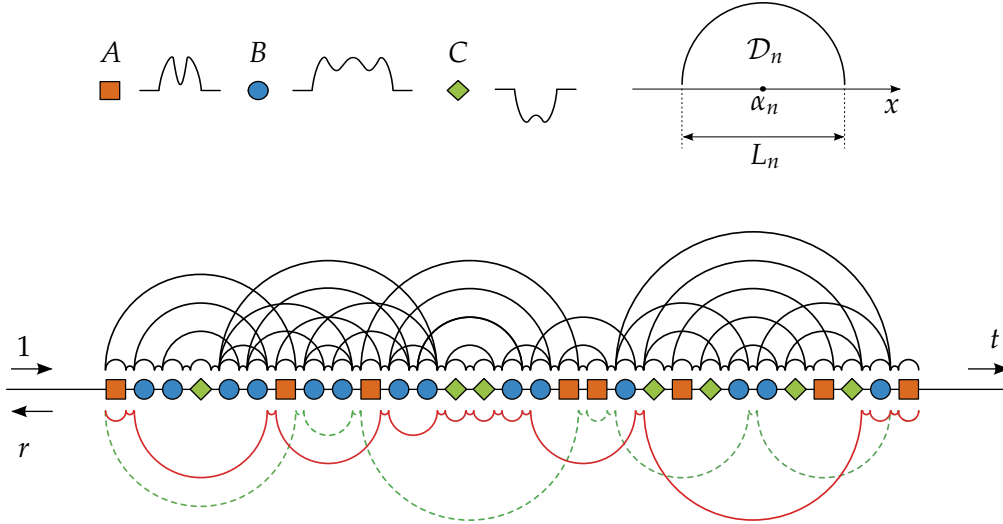


**Figure 3.6:** Local inversion symmetries in 1D. Schematic of a completely locally symmetric potential composed of three different arbitrary mirror-symmetric scatterers, labeled  $A, B, C$ , and intervening potential-free regions (gaps). The circular arcs above the scatterer array provide all possible spatial decompositions into local symmetry domains  $\mathcal{D}_n$ , of lengths  $L_n$  and center positions  $\alpha_n$ , which completely cover the potential region (up to variations including part of the intervening gaps). Two selected decompositions are shown below the array (solid red and dashed green lines), demonstrating the presence of nested local symmetries within the same system. In a scattering setup, unit amplitude plane waves incident on the left are transmitted and reflected with amplitudes  $t$  and  $r$ , respectively.

intertwined symmetry domains, in a way that makes even the presence of a local symmetry structure far from evident. The non-local currents  $Q, \tilde{Q}$  can then be utilized as a detection tool for local symmetry: Calculating them for every pair  $(x, \bar{x})$ , using different  $\alpha$  or  $L$ , their constancy would reveal underlying symmetry domains, if present.

A schematic of a completely locally  $II$ -symmetric 1D potential is shown in Fig. 3.6, where the multitude of local symmetries at different scales as well as their possible nested configurations are depicted. In the context of mesoscopic electronic systems, the setup could correspond to an inhomogeneous array of different types of quantum dots or (equivalently) to a quantum wire with locally symmetric transverse confinement modulation. For the case of 1D complete local  $II$ -symmetry, in Ref. [221] it was demonstrated how the local invariants  $Q_n$  within different domains  $\mathcal{D}_n$  can be used to classify perfectly transmitting (resonant) states in 1D setups in terms of the spatial profile of the scattered wave. An immediate extension of the local symmetry framework to Q1D would yield a similar relation of resonant transmission to symmetries in single-channel scattering, and opens up the perspective of application to multichannel transport. Finally, it is noted that a promising platform for the systematic construction of non-trivial CLS structures is provided by aperiodic symbolic sequences: As shown in Ref. [222], local (inversion) symmetries are not only dense in 1D scatterer lattices with typical long-range aperiodic order, but their distribution also follows exactly the renormalized discrete dynamics of the underlying aperiodic sequence.

---

# Computational quantum transport in multiterminal and multiply connected structures

---

In this chapter we will address the actual determination of the propagator of a system, in terms of which all quantities of interest for coherent transport are derived. To maintain a high flexibility in setup variations, the numerical computation is performed on a tight-binding grid upon which arbitrary device confining potentials can be defined. After a brief review of relevant computational schemes, we introduce the matrix form of the discretized theory, and then develop a block-partitioning technique for computing transport as well as local density properties of multiterminal systems with arbitrary geometry and topology. The approach constitutes an extended version of the recursive Green function method based on the assembly of multiply connected structures from given inter- and intra-connected subsystems with multiple leads. It is combined with a block-reordered recursive computation of subsystem propagators, thus enabling the efficient investigation of a large diversity of system setups in a highly resolved parameter space.

## 4.1 Computational schemes for quantum transport

The computation of the stationary propagator of the active scattering region of a mesoscopic device in the presence of attached leads lies at the core of the Landauer picture of transport based on the Greenian formulation of confined scattering. Formally, the propagator is obtained by a straightforward inversion of the discretized Hamiltonian matrix once the effect of the leads have been incorporated via self-energies. However, for the grid resolution required to describe arbitrary potential variations and also to remain close to the continuum of the effective mass description, the cost of a direct inversion becomes prohibitive, both in terms of computational time and storage. In fact, though, only parts of the full Greenian are relevant for the description of the response of the system upon an external excitation. Moreover, within the tight-binding approximation, used in the vast majority of approaches, the grid Hamiltonian matrix is sparse which makes its full storage and processing redundant.

An approach which takes into the sparse structure of the Hamiltonian is the so-called recursive Green function (RGF) method which has become a standard in nanoelectronic device modeling [118]. The original formulation of the method [97, 119, 120] addressed the computation of transport properties in terms of the inter-terminal part of the propagator, while later implementations [223, 224] have included the computation of local device quantities such as the LDOS and current densities derived from the terminal-to-interior propagator.

In its standard form, the RGF technique is based on a decomposition of the grid-discretized scatterer into (vertical) slices of sites [121,225,226], which are recursively appended by solving a matrix Dyson equation involving the isolated slice Greenians. This scheme can be extended to the case where the connected parts are extended (rectangular) stacks of slices (of constant potential) whose Greenians can be obtained analytically [121].

The computational efficiency in the standard RGF implementation is essentially determined by the (vertical) extent along the slices whose isolated Hamiltonians are inverted. The modeled systems thus preferably have an elongated geometry composed of long (horizontal) arrays of short connected slices. For systems with considerable extent in both directions, such as quantum antidot superlattices [227], hybrid versions of the RGF have been developed [80,81,228,229] where the slices are computed in their eigenstate representation, adapted to straight boundaries or smooth boundary variations.

A specialization of the connection of extended units is the ‘modular’ RGF method developed by Rotter *et al.* [122], where the eigenstate expansion of individual parts is used and allows for ballistic transport computations at high energies [117] and strong magnetic fields [50]. Although a multitude of geometries and interesting effects can be studied, the advantage in performance is here practically obtained for structures that can be dissected into basic module shapes (rectangles, circles etc.) and potentials (e.g. parabolic confinement [12]) with analytically known eigenfunctions, or separable potentials with rapidly calculated eigenfunctions.

For large system sizes of arbitrary potential, efficient computations with high performance can be achieved through parallelized computation of the device propagator among multiple communicating processors. A parallel implementation of the RGF algorithm was developed by Drouvelis *et al.* [230] based on a Schur complement partitioning scheme for the Hamiltonian and generalized to multiple terminals by D. Buchholz. Other renormalization schemes for parallel solvers of sparse systems have also been proposed [231,232]. In parallel processing the communication between processors must be taken into account, which may limit the performance advantage for smaller systems. Especially when a well resolved *parameter* space is desired (such as energy, magnetic field, and geometry/potential parameters), it can be preferable to let independent processors perform serial computations for different parameters (thus avoiding communication overhead) instead of parallelized computations for fewer parameters.

An important development of Greenian based methods is the generalization to multiple attached electrodes on the boundary of the device scattering region instead of only source and drain contacts on opposite ends. Multiterminal computations were initially adapted to specific geometries such as Hall bars [91,94,233] and have been further generalized since. In a method by Mamaluy *et al.* [234,235] the eigenstate expansion of the Greenian is computed numerically for arbitrary dot potentials and coupled to multiple attached leads. Within the tight-binding approach, Wimmer *et al.* [236] have developed an optimal matrix reordering algorithm for efficient transport computations based on graph partitioning. Another recent method for multiterminal transport utilizes a circular slicing procedure [237]. Finally, the ‘knitting’ algorithm by Kazymyrenko *et al.* [123] provides a computational scheme for generic device geometries with arbitrary lead attachment, where the scatterer sites are appended (knitted) one by one onto the part already included.

In the present work, we develop a hybrid computational scheme which combines the latter knitting concept with a modular decomposition of the transport device region. The method enables the assembly of multiply connected composite structures from a finite number of different module types, with arbitrarily positioned multiple lead terminals. The propagator of a single multiterminal module is computed via a block-reordered RGF iteration

which separates the surface (lead-connected) part from the interior allowing for a selective computation of local quantities (state and current densities). The assembly of modules is based on a block-Gaussian elimination scheme to solve the matrix Dyson equation for inter-connection between two modules or intra-connection of a module with itself. This provides a flexible and efficient way to perform transport computations on generic looped devices with internal structure assembled from different or repeated units.

## 4.2 From operators to matrices

To start with the description of a numerical approach to the transport problem, we now introduce the tight-binding grid on which abstract operators of the previously developed theory are represented. This gives the opportunity to define the notation and theoretical formalities of the resulting matrix formulation, but also to address particular considerations arising from the system discretization.

### 4.2.1 Grid discretization and tight-binding Hamiltonian

In order to treat the scattering system numerically, we need to ‘discretize’ it, meaning that we select a discrete set of points in 2D space, the *grid*, on which any spatially represented quantity is evaluated. The points of the grid on which the wave function of interest will actually reside we call *sites*, and, since we will ultimately express the scattering problem within a *finite* 2D domain  $\mathbb{D}$  (see Sec. 3.3.1), those sites can be counted by a *single* running index  $\alpha$ . Considering a uniform square grid oriented as the Cartesian coordinate system  $(x, y)$ , we can represent each site position as

$$\mathbf{r}_\alpha = (x_\alpha, y_\alpha) = (sa_0, ra_0) \Rightarrow \alpha \leftrightarrow (s, r), \quad (4.1)$$

each site index  $\alpha$  thus corresponding to a pair  $(s, r)$ , where the index  $s$  counts  $y$ -oriented ‘slices’ of the grid along the  $x$ -direction and  $r$  counts  $x$ -oriented ‘rows’ along the  $y$ -direction, with common distance  $a_0$  (the *lattice constant*) between consecutive gridpoints in each direction. For the infinitely extended scattering system the total number of slices  $n_s$  and rows  $n_r$  is of course infinite,  $n_s = \sum_s = n_r = \sum_r = \infty$ .<sup>1</sup> Further, we consider states  $|\mathbf{r}_\alpha\rangle$ , localized on each site  $\alpha$ , which form a complete orthonormal set,

$$\langle \mathbf{r}_\alpha | \mathbf{r}_\beta \rangle = \delta_{\alpha\beta}, \quad \sum_\alpha |\mathbf{r}_\alpha\rangle \langle \mathbf{r}_\alpha| = 1, \quad (4.2)$$

so that any state  $|\psi\rangle$  is represented as a column vector  $\Psi$  with components

$$\Psi_\alpha = \langle \mathbf{r}_\alpha | \psi \rangle. \quad (4.3)$$

The Hamiltonian of the system

$$\mathcal{H} = \sum_{\alpha, \beta} |\mathbf{r}_\alpha\rangle H_{\alpha\beta} \langle \mathbf{r}_\beta| \quad (4.4)$$

---

<sup>1</sup> Note that, for a system infinitely extended in both  $x$ - and  $y$ -directions, like the generic multiterminal scatterer attached to semi-infinite leads, the coordinates  $(s, r)$  can in general *not* be counted in a slice- or row-major scheme (e.g., bottom to top and then left to right) by a single site index  $\alpha$ , since some slice or row may contain infinite sites. The only alternative would be a rather inconvenient outward spiral-like counting scheme for  $\alpha$ . With the decomposition scheme used here, together with the tight-binding approximation to follow, only sites of the finite scatterer domain will be used in the description, such that a single-index counting is well defined.

is now represented by the square matrix

$$\mathbf{H} = \mathbf{K} + \mathbf{V}, \quad (4.5)$$

where  $V_{\alpha\beta} = \delta_{\alpha\beta}V(\mathbf{r}_\alpha)$  is the (local) potential at site  $\alpha$  and  $\mathbf{K}$  is the grid-represented kinetic energy operator.<sup>2</sup> The stationary Schrödinger equation in the single-band effective mass picture of the 2DEG is now written in the matrix form

$$(\mathbf{E} - \mathbf{H})\boldsymbol{\Psi} = \mathbf{0} \quad \Rightarrow \quad \sum_{\beta} (E\delta_{\alpha\beta} - H_{\alpha\beta})\Psi_{\beta} = 0 \quad \forall \alpha \in \mathbb{D}, \quad (4.6)$$

where  $\mathbf{E} = E\mathbf{I}$  and  $\mathbf{I}$  is the identity matrix of dimension equal to the number of sites within the total domain

$$\mathbb{D} = \mathbb{D}_S \cup \mathbb{D}_L = \mathbb{D}_S \cup \bigcup_{q=1}^{N_L} \mathbb{D}_q \quad (4.7)$$

of the scatterer ( $\mathbb{D}_S$ ) attached to  $N_L$  leads, which in turn will be determined by the imposed boundary conditions.

### Tight-binding approximation

Employing a finite difference approximation to the first one-dimensional partial derivative of an arbitrary function  $f(x, y)$ ,

$$\left. \frac{\partial f}{\partial x} \right|_{\mathbf{r}=(x_\alpha+a_0/2, y)} = \frac{1}{a_0} [f(x_\alpha + a_0, y) - f(x_\alpha, y)], \quad (4.8)$$

we get the second derivative on slice  $s$  as

$$\left. \frac{\partial^2 f}{\partial x^2} \right|_{\mathbf{r}=(x_\alpha, y)} = \frac{1}{a_0^2} [f(x_\alpha + a_0, y) - 2f(x_\alpha, y) + f(x_\alpha - a_0, y)], \quad (4.9)$$

and similarly for row  $r$ , so that the five-point stencil Laplacian evaluated at site  $\alpha$  becomes

$$\nabla^2 f \Big|_{\mathbf{r}=\mathbf{r}_\alpha=(sa_0, ra_0)} = \frac{1}{a_0^2} [f_{(s+1, r)} + f_{(s-1, r)} + f_{(s, r+1)} + f_{(s, r-1)} - 4f_{(s, r)}], \quad (4.10)$$

where we have defined  $f_{(s, r)} \equiv f(sa_0, ra_0)$ . In the absence of a magnetic vector potential the Hamiltonian matrix elements on the grid are thus given by

$$H_{\alpha\alpha'} = H_{(s, r)(s', r')} = K_{(s, r)(s', r')} + V_{(s, r)(s', r')} \quad (4.11)$$

$$= -\frac{\hbar^2}{2ma_0^2} [\delta_{s\pm 1, s'}\delta_{r, r'} + \delta_{s, s'}\delta_{r\pm 1, r'} - 4\delta_{s, s'}\delta_{r, r'}] + V_{(s, r)}\delta_{s, s'}\delta_{r, r'} \quad (4.12)$$

$$= [4t + V_{(s, r)}]\delta_{s, s'}\delta_{r, r'} - t[\delta_{s\pm 1, s'}\delta_{r, r'} + \delta_{s, s'}\delta_{r\pm 1, r'}] \quad (4.13)$$

where  $t \equiv \frac{\hbar^2}{2ma_0^2}$  is the *hopping energy*. Writing the Hamiltonian as

$$\mathcal{H} = \sum_{\alpha} |\mathbf{r}_\alpha\rangle U_{\alpha} \langle \mathbf{r}_\alpha| + \sum_{\alpha \neq \beta} |\mathbf{r}_\alpha\rangle J_{\alpha\beta} \langle \mathbf{r}_\beta| \quad (4.14)$$

---

<sup>2</sup> Bold upright letters ( $\mathbf{H}, \boldsymbol{\Psi}$ ), possibly with sub- or superscripts, will be used to denote matrices represented on the spatial grid, with their thin variant ( $H_{\alpha\beta}, \Psi_{\alpha}$ ) denoting individual matrix elements.

we see that the approximation procedure used for the kinetic term  $\mathbf{K}$  effectively contributes an energy  $t$  (which increases when the grid nodes come closer) to the ‘on-site’ energy of site  $\alpha$  from each one of its four nearest neighbors,

$$U_\alpha = V(\mathbf{r}_\alpha) + 4t, \quad (4.15)$$

while ‘hopping’ to one of those sites costs energy  $t$ ,

$$J_{\alpha\beta} = -t, \quad |\mathbf{r}_\alpha - \mathbf{r}_\beta| = a_0. \quad (4.16)$$

In other words, we have obtained the simplest form of a *tight-binding* Hamiltonian, used widely as an approximation to describe a lattice of atoms where only interactions with the closest neighboring atoms are taken into account [238, 239]—though here the ‘atoms’ have no internal structure. Despite this similarity, the mathematical grid used here does *not* simulate the atomic lattice of the material (heterojunction between two semiconductors) where electrons propagate; it merely approximates numerically the continuous medium within the effective mass picture we started out with, and approaches this continuum as  $a_0 \rightarrow 0$ .

### Peierls phase factor

In the presence of a magnetic vector potential

$$\mathbf{A}(\mathbf{r}_\alpha) = \mathbf{A}_\alpha = A_x(\mathbf{r}_\alpha)\hat{\mathbf{x}} + A_y(\mathbf{r}_\alpha)\hat{\mathbf{y}} = A_\alpha^x\hat{\mathbf{x}} + A_\alpha^y\hat{\mathbf{y}}, \quad (4.17)$$

the diagonal (on-site) matrix elements of the lattice Hamiltonian remain unchanged, and the off-diagonal (hopping) elements acquire a local Aharonov-Bohm-like phase factor, known as the Peierls phase factor [240], corresponding to the straight path from a site  $\alpha$  to a nearest neighbor  $\alpha'$ ,

$$J_{\alpha\alpha'}^{A \neq 0} = J_{\alpha\alpha'}^{A=0} \exp\left(i\frac{e}{\hbar} \int_{\mathbf{r}_{\alpha'}}^{\mathbf{r}_\alpha} d\mathbf{r} \cdot \mathbf{A}(\mathbf{r})\right). \quad (4.18)$$

Relying on the gauge invariance of the Schrödinger equation (and thus of observable quantities), Peierls’ phase factor is here exact and unambiguous [241] for the (trivially) orthonormal basis set of the grid, within the tight-binding framework. An approximation does enter for generic spatially varying magnetic fields if we evaluate the path integral by means of the trapezoidal rule,

$$\int_{\mathbf{r}_{\alpha'}}^{\mathbf{r}_\alpha} d\mathbf{r} \cdot \mathbf{A}(\mathbf{r}) \approx \frac{1}{2}(\mathbf{r}_\alpha - \mathbf{r}_{\alpha'}) \cdot (\mathbf{A}_\alpha + \mathbf{A}_{\alpha'}), \quad (4.19)$$

for adjacent grid points  $\alpha$  and  $\alpha'$ . However, for the cases of homogeneous (in the billiard) or linearly varying (in the leads)  $\mathbf{B}(\mathbf{r})$ , which we will consider here, also this interpolation becomes exact. It yields the following explicit form of hopping elements:

$$\begin{aligned} J_{(s,r)(s',r')} = -t \left( \right. & \delta_{s+1,s'}\delta_{r,r'} e^{-i\pi a_0[A_{(s,r)}^x + A_{(s+1,r)}^x]}/\phi_0 \\ & + \delta_{s-1,s'}\delta_{r,r'} e^{+i\pi a_0[A_{(s,r)}^x + A_{(s-1,r)}^x]}/\phi_0 \\ & + \delta_{s,s'}\delta_{r+1,r'} e^{-i\pi a_0[A_{(s,r)}^y + A_{(s,r+1)}^y]}/\phi_0 \\ & \left. + \delta_{s,s'}\delta_{r-1,r'} e^{+i\pi a_0[A_{(s,r)}^y + A_{(s,r-1)}^y]}/\phi_0 \right), \end{aligned} \quad (4.20)$$

where  $\phi_0$  is the flux quantum.

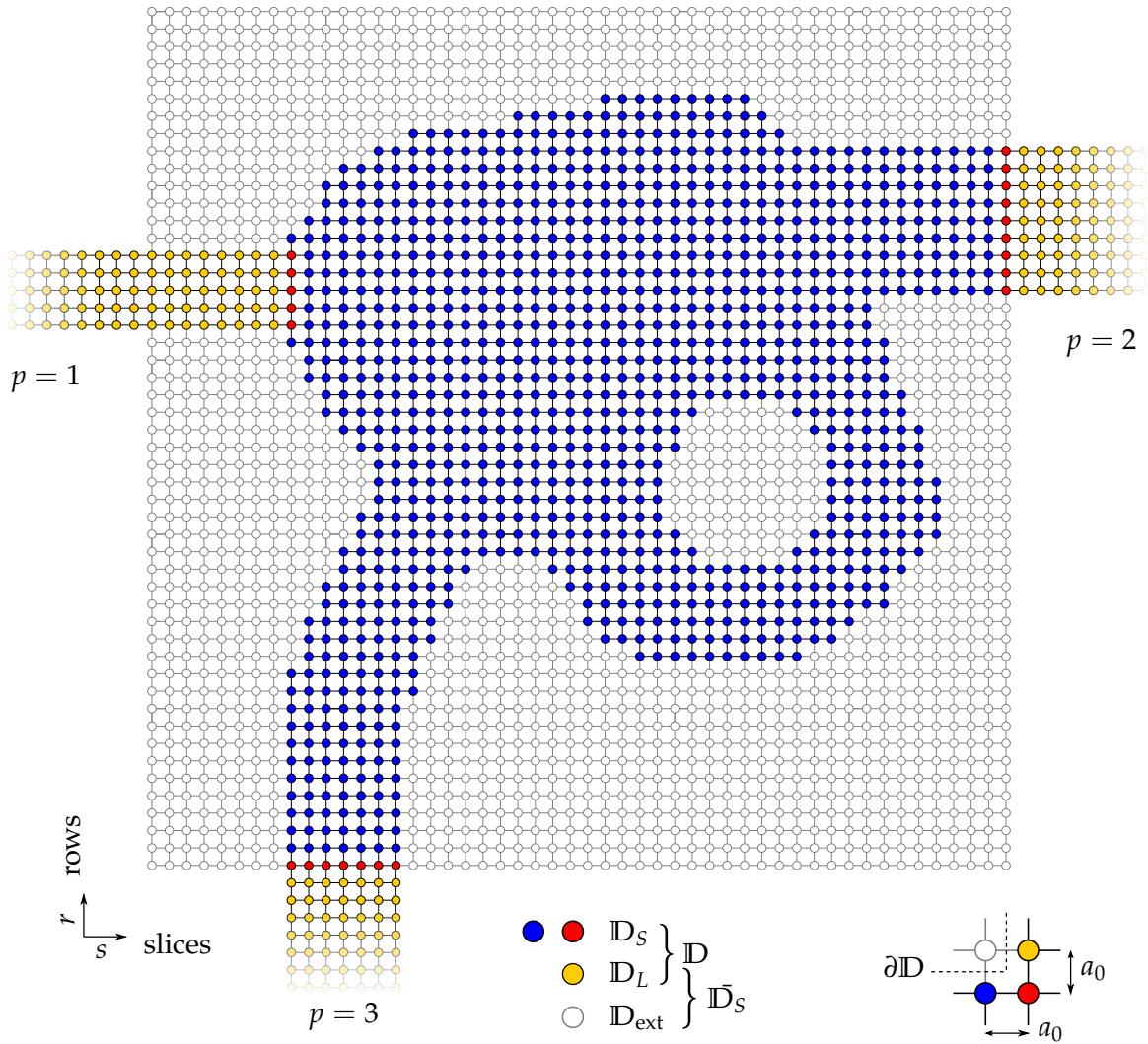


**Figure 4.1:** Schematic of a two-dimensional device discretized on a uniform square grid of lattice constant  $a_0$ . The scatterer is contained in the spatial domain  $\mathbb{D}_S$  with 1059 internal sites (blue) and 21 surface sites (red) connected to three leads (yellow, domain  $\mathbb{D}_L$ ) which together with the scatterer make up the total domain  $\mathbb{D}$  of the model device defined by hard-wall boundary conditions. An arbitrary scatterer potential (e.g. with smooth boundaries) is generally contained within a finite rectangular computational box (gray sites), and after its design slices and rows are counted within  $\mathbb{D}$ . The schematic illustrates that (i) the device can have multiple, arbitrarily positioned semi-infinite leads attached along the  $x$ - or  $y$ -direction, (ii) a tilted lead ( $p = 3$ ) can be implemented by smooth (adiabatic) continuation in a larger computational box into a straight horizontal or vertical outer lead, (iii) leads can be attached directly on appropriate boundary segments of the device ( $p = 1$ ) or after lead stubs ( $p = 2, 3$ ) extending to the box boundary, (iv) the scatterer can contain hard-wall holes (antidots) whose sites are discarded from the Hamiltonian.

### Hard-wall boundaries

As its name implies, a ‘hard wall’ along the boundary of a given 2D domain  $\mathbb{D}$  means that any wave inside the domain is perfectly reflected at the boundary, that is, the wave function  $\psi(\mathbf{r}; E)$  describing it vanishes just outside the boundary for arbitrarily high energies  $E$ . This is achieved by letting  $V(\mathbf{r}) \rightarrow \infty$  for  $\mathbf{r} \notin \mathbb{D}$  in the theoretical model, leading to (homogeneous) Dirichlet boundary conditions along the boundary,

$$\psi(\mathbf{r}) = 0, \quad \mathbf{r} \in \partial\mathbb{D}, \quad (4.21)$$

due to the required continuity of the wave function.

In the spatially discretized system, the boundary  $\partial\mathbb{D}$  is drawn between gridpoints lying inside ( $\in \mathbb{D}$ ) an outside ( $\in \bar{\mathbb{D}}$ ) the scatterer, and the Dirichlet condition amounts to setting the wave function of those outside to zero. In the tight-binding scheme, this is equivalent to setting the hopping elements between nearest neighbor gridpoints on either side of the boundary to zero,

$$\Psi_\alpha = 0, \quad \mathbf{r}_\alpha \in \bar{\mathbb{D}} \quad \Leftrightarrow \quad J_{\alpha\beta} = 0, \quad \mathbf{r}_\beta \in \mathbb{D}. \quad (4.22)$$

The discrete Schrödinger equation (4.6) is then solved only for the scattering domain of interest (including the leads)  $\mathbb{D} = \mathbb{D}_S \cup \mathbb{D}_L$  which is separated from the surrounding gridpoints. In other words, gridpoints outside the hard-wall boundary are simply discarded from the Hamiltonian matrix. A schematic of an arbitrary multiterminal device—with very crude grid resolution—is shown in Fig. 4.1, with a scattering region (blue nodes) attached to three leads (yellow nodes) and the rest of the grid (white nodes) discarded.

Note that the Dirichlet boundary need not necessarily define the active confinement geometry: It can just as well be used as a finite grid section on which a smooth potential is defined, which becomes large enough along a designed boundary to practically confine the wave function (i.e., cause it to drop off exponentially to zero before reaching the hard-wall boundary of the finite grid) at energies of interest. Any chosen scatterer potential should also match the potential in the leads at the terminal openings.

## 4.2.2 Dispersion relation

The degree of approximation in the tight-binding approach can be estimated more quantitatively by comparing the dispersion relations for a ‘free’ 2D matter wave (in the sense of an electron in a 2DEG) in the continuous and discrete space. In the continuous case, the free particle stationary wave function  $\psi_k(\mathbf{r}) \propto e^{i\mathbf{k}\cdot\mathbf{r}}$  yields the parabolic dispersion  $E(k) = \hbar^2 k^2 / 2m$ . In the discrete case, the corresponding plane wave  $\Psi_\alpha = \Psi_{(s,r)} \propto e^{ik_x s a_0} e^{ik_y r a_0}$  is a solution of the free Schrödinger equation (4.6) (that is, in the absence of confinement or magnetic field), with tight-binding Hamiltonian matrix elements (4.13), if the energy is related to the (discrete) wave vectors as [118, 127]

$$E(k_x, k_y) = 2t[1 - \cos(k_x a_0)] + 2t[1 - \cos(k_y a_0)] \quad (4.23)$$

$$\xrightarrow{a_0 \rightarrow 0} t(k_x^2 + k_y^2) a_0^2 = \frac{\hbar^2 k^2}{2m}. \quad (4.24)$$

The discrete dispersion thus becomes parabolic in the continuum limit  $a_0 \rightarrow 0$ , as expected, and the deviation for finite  $a_0$  provides an estimate for the accuracy of the simulation in terms of spatial resolution: The larger the energy of the incoming matter wave, the finer the grid should be in order to simulate the energy continuum in the effective mass picture of the 2DEG.

When the confinement potential is introduced to create the quantum billiard, wave propagation is free only along the attached Q1D leads. Just like in the continuum case, we then obtain a free particle dispersion relation for the longitudinal direction for each energy subband of the transversal lead confinement. For flat leads (zero potential) with hard-wall boundaries, we have the sinusoidal transverse eigenfunctions (1.27), now with discrete wave numbers

$$k_{y,m}^p = \frac{m\pi}{(N_w^p + 1)a_0}, \quad (4.25)$$

where  $N_w^p$  is the number of transversal sites in the wire.<sup>3</sup> The total, mode-resolved dispersion relation thus becomes

$$E_m^p(k_x) = 4t - 2t \cos(k_x a_0) - 2t \cos\left(\frac{m\pi}{N_w^p + 1}\right), \quad (4.26)$$

which yields the corresponding velocity

$$v_m^p = \frac{1}{\hbar} \left. \frac{\partial E_m^p}{\partial k_x} \right|_{k_x=k_{x,m}^p} = \frac{2ta_0}{\hbar} \sin(k_{x,m}^p a_0) = \frac{\hbar}{m_{\text{eff}} a_0} \sin(k_{x,m}^p a_0) \quad (4.27)$$

in mode  $m$  of lead  $p$ , to be used in the following, where  $k_{x,m}^p$  for a given energy  $E$  is obtained as

$$k_{x,m}^p = \frac{1}{a_0} \arccos \left[ 2 - \frac{E}{2t} - \cos\left(\frac{m\pi}{N_w^p + 1}\right) \right] \quad (4.28)$$

by inverting Eq. (1.29).

Note here that, although the full dispersion relation determines  $k_{x,m}^p$ , the channel *thresholds* alone are given by the energies  $E_m = 2t[1 - \cos(k_{y,m} a_0)]$ . The relative deviation between the continuum and discrete channel thresholds  $\Delta E_m / E_m^{\text{cont}} = 1 - 2[1 - \cos(k_{y,m} a_0)] / (k_{y,m} a_0)^2$  with  $k_{y,m} = m\pi / (N_w + 1)$  illustrates the approximation introduced in dependence of the number of transversal sites used in a lead: For  $N_w = 32$ , as will be the case in following implementations, we have relative deviation  $\Delta E_m / E_m^{\text{cont}} = 0.000755, 0.003017, 0.006779$  for thresholds  $m = 1, 2, 3$ , respectively.

### 4.3 Scattering via spatial decomposition

We will now use the decomposition scheme developed in Sec. 3.3 to express the scattering problem in terms of an effective Hamiltonian projected on the scattering region  $\mathbb{D}_S$  alone. Within the tight-binding approximation, this will provide an *exact* mapping of the infinite-dimensional, grid-represented scattering problem to a finite-dimensional one, though described by an energy-dependent and non-Hermitian Hamiltonian. The corresponding Greenian will then provide any quantity of interest such as transmission functions and state densities.

#### 4.3.1 Truncation of the Hamiltonian

Although imposing Dirichlet boundary conditions—either as a hard-wall scatterer boundary or around a computational box within which a smooth confining potential is defined—discards most part of the 2D grid, the Hamiltonian matrix (4.5) is still of infinite dimension due to the formal semi-infinite extent of the leads:  $y$ -oriented leads yield a finite number  $n_s < \infty$  of infinite slices ( $n_r = \infty$ ) of sites within the total scattering domain  $\mathbb{D}$ , and  $x$ -oriented (or any non- $y$ -oriented) leads yield an infinite number  $n_s = \infty$  of finite slices ( $n_r < \infty$ ).

We now consider the decomposition of the total scattering domain into that containing the actual scatterer,  $\mathbb{D}_S$ , and the one containing all leads,  $\mathbb{D}_L$ . As shown in Sec. 3.3 the open scatterer system can be described by a modified Hamiltonian  $\tilde{\mathcal{H}}_S^+(E) = \mathcal{H}_S + \Sigma^+(E)$ , where the (generally energy-dependent and non-Hermitian) retarded self-energy operator  $\Sigma$  takes

---

<sup>3</sup> On the grid, one can think of the boundary  $\partial\mathbb{D}$  as drawn in the middle between gridpoints (see inset of Fig. 4.1), so that hard-wall (Dirichlet) boundaries for lead  $p$  are implemented by setting  $\psi(x_p, y_p = -a_0/2) = \psi(x_p, y_p = N_w a_0 + a_0/2) = 0$  at the gridpoints just outside the lead; the effective width of the lead is thus  $w = (N_w^p + 1)a_0$ .



wall boundary, as shown in Fig. 4.1.<sup>5</sup> Thus, although the diagonals of the blocks  $\mathbf{H}_{s,s}$  are always full, with the sites enclosed in the hole being discarded, the side-diagonals (upper and lower) may contain zeros corresponding to unconnected sites on either side of the hole.

Also, since the slices of included sites are generally of different lengths  $N_r^{(s)}$ , the blocks  $\mathbf{H}_{s,s\pm 1}$  on the side-block-diagonals of  $\mathbf{H}$  are sparse (with at most one non-zero element per row or column) but in general rectangular  $N_r^{(s)} \times N_r^{(s\pm 1)}$  matrices, and not square diagonal as would be the case for a rectangular domain  $\mathbb{D}_S$ .

With the addition of the self energies representing the connection to the semi-infinite leads, the total Hamiltonian matrix  $\tilde{\mathbf{H}}$  acquires blocks which do not follow the above structure, to be discussed next. It should be noted, however, that the matrix elements of  $\Sigma$  are assigned solely to sites *within* the scatterer domain  $\mathbb{D}_S$ , independently of whether a tight-binding approximation is employed or not. In other words, the truncation of the Hamiltonian matrix itself relies only on the projection scheme applied to the domain decomposition into scatterer and leads, and the approximation involved is independently determined by the type of coupling and grid resolution.<sup>6</sup>

### Self-energies

The coupling matrix  $\tau$  is the sum of matrices  $\tau_p$  coupling the leads  $p$  to the scatterer, which, in the tight-binding approach, consist simply of the hopping elements  $J_{\alpha\beta}$  across the lead interfaces,

$$\tau = \sum_{p=1}^{N_L} \tau_p, \quad \tau_{p;\alpha\beta} = J_{\alpha\beta}, \quad \alpha \in \mathbb{D}_S, \beta \in \mathbb{D}_p, \quad (4.33)$$

and  $\tau_{p;\alpha\beta} = 0$  otherwise. Thus, the self-energy matrix

$$\Sigma = \sum_{p=1}^{N_L} \Sigma_p, \quad \Sigma_p = \tau_p \mathbf{g}(E) \tau_p^\dagger, \quad (4.34)$$

also has nonzero elements only for sites adjacent (nearest neighbors) to the first sites in the leads at local coordinates  $\mathbf{r}_{\alpha;p} \equiv (x_p = a_0, y_p)$ . It couples, however, *all* such ‘surface’ or ‘lead-coupled’ sites of the scatterer connected to a terminal  $p$  to *each other* via the matrix elements  $\mathbf{g}_{\alpha_p\beta_p}$  of the lead Greenian along the interface,

$$\Sigma_{p;\alpha\beta} = \tau_{p;\alpha\alpha_p} \mathbf{g}_{\alpha_p\beta_p} \tau_{p;\beta_p\beta}^\dagger = t^2 \mathbf{g}_{\alpha_p\beta_p}. \quad (4.35)$$

With the self-energy due to the leads, the scatterer thus effectively interacts with ‘itself’, *beyond* nearest neighbors at the surface sites.

A schematic of a four-terminal toy scatterer with 42 sites is shown in Fig. 4.2 (a), with the corresponding effective Hamiltonian  $\tilde{\mathbf{H}}$  (or the structurally equivalent matrix  $\mathbf{\Delta} \equiv E - \tilde{\mathbf{H}}$ , ultimately to be inverted) shown in Fig. 4.2 (b). For horizontal leads attached to a single slice on the left or on the right of the scatterer, the self-energy contributes full blocks on the

<sup>5</sup> Such structures are called ‘antidots’ in the context of nanoelectronic systems, since they expel the electrons instead of trapping them like quantum dots do. If their (negative) potential is low, then their appearance may depend on the quasi-Fermi level in the 2DEG, leading to fluctuating Aharonov-Bohm-like loops, as discussed in Sec. 3.4.2. For strong and steep enough potential, the antidot can be modeled by a correspondingly shaped closed hard wall, with the enclosed sites discarded from the Hamiltonian matrix, as done in Fig. 4.1 and Fig. 4.2

<sup>6</sup> For example, if next-to-nearest-neighbor coupling were included (that is, via a higher order, nine-point stencil approximation to the 2D Laplacian), the coupling matrix  $\tau$  would ‘reach’ further (by one more site in each direction) across the interfaces to the leads, but since  $\tau^\dagger$  projects back onto the scatterer domain (see Eq. (3.84)), the matrix  $\Sigma$  remains of the size of  $\mathbf{H}$ .

diagonal of  $\tilde{\mathbf{H}}$ , and the block-tri-diagonal structure is preserved. For vertical leads (more than two sites wide), however, the self-energy couples slices with sites which are not nearest neighbors, and  $\tilde{\mathbf{H}}$  is no longer block-tridiagonal: In principle, any block of  $\tilde{\mathbf{H}}$  can be populated sparsely by the elements of  $\Sigma$ .

For the flat hard-wall semi-infinite leads considered here, the Green function for zero magnetic field is derived in App. A.2; in the grid representation, the lead Greenian connecting sites  $\alpha_p, \beta_p$  along the interface of lead  $p$  to the scatterer is then [127]

$$\mathbf{g}_{\partial\text{D}}^p = -\frac{1}{t} \sum_m \chi_m^p e^{ik_{x,m}^p a_0} \chi_m^{p\dagger} \Rightarrow \mathbf{g}_{\alpha_p \beta_p}^p = -\frac{1}{t} \sum_m \chi_{m;\alpha_p}^p e^{ik_{x,m}^p a_0} \chi_{m;\beta_p}^{p*} \quad (4.36)$$

where  $\chi_m^p$  is the  $N_w^p \times 1$  transversal wave function column vector of lead  $p$  (which is chosen real for zero magnetic field). The self-energy matrix for the scatterer sites connected to lead  $p$  thus becomes

$$\Sigma_p = -t \sum_m \chi_m^p e^{ik_{x,m}^p a_0} \chi_m^{p\dagger} \Rightarrow \Sigma_{p;\alpha\beta} = -t \sum_m \chi_{m;\alpha_p}^p e^{ik_{x,m}^p a_0} \chi_{m;\beta_p}^{p*}, \quad (4.37)$$

which is seen to be manifestly non-Hermitian and energy-dependent. The sum is here over all modes in lead  $p$ , which, in the discretized system, are restricted to the number of considered transversal sites  $N_w^p$ . Note that evanescent modes with  $E_m^p > E$ , corresponding to exponential decay through an imaginary  $k_{x,m}^p$ , are here inherently taken into account in the summation.

### 4.3.2 Open system propagator

With the self-energies  $\Sigma_p$  added to the truncated scatterer Hamiltonian  $\mathbf{H}$ , the Greenian of the open system is given by the grid-represented form of Eq. (3.94),

$$\tilde{\mathbf{G}} = (\mathbf{E} - \tilde{\mathbf{H}})^{-1} = (\mathbf{E} - \mathbf{H} - \Sigma)^{-1}. \quad (4.38)$$

which is obtained here equivalently by matrix algebra after decomposing the system into scatterer and attached leads, as shown below in Sec. 4.4.1 Formally, the propagator is thus obtained by a single matrix inversion. In view of the spatial grid resolution needed to simulate a quantum device accurately, however, the resulting  $N \times N$  matrix is usually too large to be directly inverted in an efficient way. Recall that matrix inversion and its underlying matrix multiplication are ‘level 3’ operations [242] with computational cost  $C$ , or ‘numerical complexity’, scaling asymptotically as

$$C \propto f N^3, \quad N \gg 1 \quad (4.39)$$

for large  $N$ , meaning that the number of floating point operations (addition or multiplication of two scalars) performed is approximately proportional to  $fN^3$ , where the factor  $f$  depends on the particular algorithm used [243]. For example, even for a moderately resolved circular billiard with a radius of 100 gridpoints we have  $N \approx 31415$  and a direct inversion is already computationally expensive. Apart from the computational cost, only storing the inverse (which, in contrast to the sparse Hamiltonian  $\tilde{\mathbf{H}}$ , is generally a full matrix) requires too much memory to be practicable.

In fact, though, only a small fraction of the matrix elements of the full Greenian  $\tilde{\mathbf{G}}$  are relevant for describing transport through the system: Since transport in principle regards the response of the system upon an incident excitation in one of the attached leads, the essential part of  $\tilde{\mathbf{G}}$  is the one which propagates from surface (lead-connected) sites to the interior of the scatterer and to other surface sites. We will now briefly list the lattice forms of quantities employed directly or indirectly in the description of transport, and in the following sections the computational procedure to efficiently obtain the needed blocks of  $\tilde{\mathbf{G}}$  will be presented.

### Scattering wave function

To find the wave function within the scatterer domain as a response to an incoming wave in one or more leads at energy  $E$ , just like in Sec. 3.3.2, we write the matrix Schrödinger equation for the total system (scatterer + leads) as

$$\begin{pmatrix} E - \mathbf{H}_S & -\boldsymbol{\tau} \\ -\boldsymbol{\tau}^\dagger & E - \mathbf{H}_L \end{pmatrix} \begin{pmatrix} \boldsymbol{\Psi} \\ \boldsymbol{\Phi}_S + \boldsymbol{\Phi}_L \end{pmatrix} = \begin{pmatrix} \mathbf{0} \\ \mathbf{0} \end{pmatrix}, \quad (4.40)$$

where  $\boldsymbol{\Phi}_L = \sum_p \boldsymbol{\Phi}_p$  is an eigenstate of the isolated lead(s),  $\mathbf{H}_L \boldsymbol{\Phi}_L = E \boldsymbol{\Phi}_L$ . Upon connection of the lead(s) via  $\boldsymbol{\tau}$  to the scatterer,  $\boldsymbol{\Phi}_L$  acts as an excitation giving rise to a wave  $\boldsymbol{\Psi}$  in the scatterer and a wave  $\boldsymbol{\Phi}_S$  in the leads. From the lower equation we have

$$\boldsymbol{\Phi}_S = (E - \mathbf{H}_L)^{-1} \boldsymbol{\tau}^\dagger \boldsymbol{\Psi} = \mathbf{g} \boldsymbol{\tau}^\dagger \boldsymbol{\Psi}, \quad (4.41)$$

where  $\mathbf{g} = (E - \mathbf{H}_L)^{-1}$  is the Greenian of the isolated leads.<sup>7</sup> Inserting  $\boldsymbol{\Phi}_S$  into the upper equation in (4.40) yields the scattering wave function in the scatterer region,

$$\boldsymbol{\Psi} = (E - \mathbf{H} - \boldsymbol{\Sigma})^{-1} \boldsymbol{\tau} \boldsymbol{\Phi}_L = \tilde{\mathbf{G}} \boldsymbol{\tau} \boldsymbol{\Phi}_L, \quad (4.42)$$

as the response to a source  $\boldsymbol{\Psi}_L = \boldsymbol{\tau} \boldsymbol{\Phi}_L$  at the interface to the leads, propagated by the Greenian  $\tilde{\mathbf{G}}$  of the connected scatterer. Since, in the Landauer-Büttiker picture of transport, electrons are injected incoherently in different lead channels from different reservoirs, in practice  $\boldsymbol{\Phi}_L$  is the wave function of a single mode  $m$  in a single lead  $p$ , and the response becomes

$$\boldsymbol{\Psi} = \tilde{\mathbf{G}} \boldsymbol{\tau} \boldsymbol{\Phi}_m^p, \quad \boldsymbol{\Phi}_m^p = \chi_m^p e^{i\theta}, \quad (4.43)$$

where the phase  $\theta = -k_m^p x_p \equiv 0$  of the incoming wave is conventionally set to zero considering the origin of the lead at the interface to the scatterer. Further, since only surface sites are coupled to the leads via  $\boldsymbol{\tau}$  in the tight-binding approach, it is clear that only the part of the propagator  $\tilde{\mathbf{G}}$  connecting the surface sites at terminal  $p$  to the scatterer interior is needed above for computing  $\boldsymbol{\Psi}$ .

### Probability current density

Because of its non-local character in the discretized spatial representation (due the finite-difference approximation to the gradient  $\nabla\psi$ ), the lattice current density is not defined at a single site but on the *link* between two neighboring sites  $\alpha$  and  $\beta$ . Using the spatial representation of the velocity operator  $\boldsymbol{v} = [\boldsymbol{r}, \mathcal{H}]$ , the link current from  $\boldsymbol{r}_\beta$  to  $\boldsymbol{r}_\alpha$  can be written as [94, 244]

$$\boldsymbol{j}_{\alpha\beta} = \frac{1}{2i\hbar} (\boldsymbol{r}_\alpha - \boldsymbol{r}_\beta) [\boldsymbol{\Psi}^*(\boldsymbol{r}_\alpha) \langle \boldsymbol{r}_\alpha | \tilde{\mathcal{H}} | \boldsymbol{r}_\beta \rangle \boldsymbol{\Psi}(\boldsymbol{r}_\beta) - \boldsymbol{\Psi}^*(\boldsymbol{r}_\beta) \langle \boldsymbol{r}_\beta | \tilde{\mathcal{H}} | \boldsymbol{r}_\alpha \rangle \boldsymbol{\Psi}(\boldsymbol{r}_\alpha)], \quad (4.44)$$

where  $|\boldsymbol{r}_\alpha - \boldsymbol{r}_\beta| = a_0$ . In the finite-difference scheme considered, the  $x$ - and  $y$ -components of the current vector between *internal* lattice sites (not connected to leads) become

$$\boldsymbol{j}_{\alpha\beta}^x = \boldsymbol{j}_{(s,r)(s\pm 1,r)} = \pm \frac{a_0}{2i\hbar} [\boldsymbol{\Psi}_{(s,r)}^* \boldsymbol{J}_{(s,r)(s\pm 1,r)} \boldsymbol{\Psi}_{(s\pm 1,r)} - \boldsymbol{\Psi}_{(s\pm 1,r)}^* \boldsymbol{J}_{(s\pm 1,r)(s,r)} \boldsymbol{\Psi}_{(s,r)}], \quad (4.45)$$

$$\boldsymbol{j}_{\alpha\beta}^y = \boldsymbol{j}_{(s,r)(s,r\pm 1)} = \pm \frac{a_0}{2i\hbar} [\boldsymbol{\Psi}_{(s,r)}^* \boldsymbol{J}_{(s,r)(s,r\pm 1)} \boldsymbol{\Psi}_{(s,r\pm 1)} - \boldsymbol{\Psi}_{(s,r\pm 1)}^* \boldsymbol{J}_{(s,r\pm 1)(s,r)} \boldsymbol{\Psi}_{(s,r)}], \quad (4.46)$$

---

<sup>7</sup> The coupling of the leads themselves to reservoirs is here implicit, with a corresponding imaginary term  $i\eta$  absorbed in  $\mathbf{H}_L$  which makes  $\mathbf{g}$  convergent, as shown in App. A.2.

where the hopping matrix elements  $J_{(s,r)(s',r')}$  are given in Eq. (4.20). For surface sites connected to the leads also the self-energy coupling elements  $\Sigma_{(s,r)(s\pm 1,r\pm 1)}$  should be included.

Although the discrete current defined along links between sites, it is convenient (e. g., in order to visualize current flow) to assign to each site itself a current vector equal to the sum of the currents on the links connected to the site; this yields a total 'on-site' current vector [80]

$$\mathbf{j}_\alpha = \mathbf{j}_{(s,r)} = [j_{(s,r)(s-1,r)} + j_{(s,r)(s+1,r)}] \hat{\mathbf{x}} + [j_{(s,r)(s,r-1)} + j_{(s,r)(s,r+1)}] \hat{\mathbf{y}} \quad (4.47)$$

$$= \frac{\hbar}{2ma_0} \text{Im} \left\{ \Psi_{(s,r)}^* [e^{i\gamma_-^s} \Psi_{(s-1,r)} - e^{-i\gamma_+^s} \Psi_{(s+1,r)}] \hat{\mathbf{x}} + \Psi_{(s,r)}^* [e^{i\gamma_-^r} \Psi_{(s,r-1)} - e^{-i\gamma_+^r} \Psi_{(s,r+1)}] \hat{\mathbf{y}} \right\} \quad (4.48)$$

at site  $\alpha \leftrightarrow (s, r)$ , where the Peierls phases  $\gamma_\pm^s = \pi a_0 [A_{(s,r)}^x + A_{(s\pm 1,r)}^x] / \phi_0$ ,  $\gamma_\pm^r = \pi a_0 [A_{(s,r)}^y + A_{(s,r\pm 1)}^y] / \phi_0$  depend on the chosen gauge for the vector potential  $\mathbf{A}$ . Thus, once the scattering wave function  $\Psi$  has been determined as a response to an incoming wave from Eq. (4.43), the current within the scatterer region is computed from Eq. (4.48) (in the same gauge, of course).<sup>8</sup>

### Broadening matrices and spectral function

The quantities relevant for the actual observables in an electron transport setting are obtained in their discrete form simply by representing the corresponding operators, derived in the general framework of Sec. 3.3, on the tight-binding lattice.

Resonant widths (equivalent to decay rates) of quasibound states in the scattering region are described by the anti-Hermitian part of the self-energy matrix,

$$\mathbf{\Gamma} = \sum_{p=1}^{N_L} \mathbf{\Gamma}_p, \quad \mathbf{\Gamma}_p = i[\mathbf{\Sigma}_p - \mathbf{\Sigma}_p^\dagger], \quad (4.49)$$

with each partial broadening matrix  $\mathbf{\Gamma}$  having non-zero on-site and hopping elements only for sites coupled to the corresponding leads. For flat hard-wall leads, with the self-energy given by Eq. (4.37), their explicit form becomes

$$\mathbf{\Gamma}_p = 2t \sum_m \chi_m^p \sin[k_{x,m}^p a_0] \chi_m^{p\dagger} = \frac{\hbar}{a_0} \sum_m \chi_m^p v_m^p \chi_m^{p\dagger}, \quad (4.50)$$

where the discrete dispersion relation (4.26) was used.

Together with the propagator  $\tilde{\mathbf{G}}$ , the broadening matrices determine the lattice spectral function of the system, which also can be written as the sum of partial spectral matrices (see Eq. (3.116)),

$$\mathbf{F} = \sum_{p=1}^{N_L} \mathbf{F}_p, \quad \mathbf{F}_p = \tilde{\mathbf{G}} \mathbf{\Gamma}_p \tilde{\mathbf{G}}^\dagger, \quad (4.51)$$

with each part  $\mathbf{F}_p$  determining the observable response upon an excitation (incoming electron) in the corresponding lead  $p$ . Note here that, since  $\mathbf{\Gamma}_p$  has nonzero elements only for sites connected to lead  $p$ , to obtain  $\mathbf{F}_p$  only the corresponding part of the propagator  $\tilde{\mathbf{G}}$  needs

---

<sup>8</sup> Note that the  $\Psi$  is determined from the effective Hamiltonian  $\tilde{\mathbf{H}}$ , and only the evaluation of the current at surface points is skipped here for simplicity, since they do not affect the current streamline pattern in the interior which is of interest. If leadpoints were added as Büttiker decoherence probes in the bulk of the scatterer, then the current should be evaluated at those sites as well, including the corresponding self-energy couplings on the links.

to be computed (like for  $\Psi$  in Eq. (4.43)); that is, the part propagating from the interior of the scatterer to lead  $p$  (or its Hermitian conjugate propagating from the lead to the interior), and not the (comparatively huge) part propagating between sites in the interior. Nevertheless, the  $\mathbf{F}_p$  are generally full matrices of the dimension  $N$  of the scattering region, providing the spatial correlations between all site upon excitations at the terminals. In practice, however, not all of their elements are required for the analysis of transport properties.

### Local density of states

The diagonal elements of the spectral matrix  $\mathbf{F}$  provide the total LDOS of the scatterer (cf. Eq. (3.113)),<sup>9</sup>

$$\rho = \frac{1}{2\pi} \text{diag}(\mathbf{F}) \quad \Rightarrow \quad \rho_\alpha = \frac{1}{2\pi} F_{\alpha\alpha} = -\frac{1}{\pi} \text{Im } G_{\alpha\alpha}, \quad (4.52)$$

which can be viewed as a generalized probability density with incoherent contributions from excitations in the lead channels. As seen in Sec. 3.3.3, these contributions are weighted by the Fermi occupation functions of the reservoirs connected through the corresponding terminals in order to obtain the charge distribution in the device. For equilibrium transport, where all reservoirs are assumed at the same chemical potential, the (scaled) charge density is effectively described by  $\rho$  above. We will here, however, still use the partial LDOS

$$\rho_p = \frac{1}{2\pi} \text{diag}(\mathbf{F}_p) \quad \Rightarrow \quad \rho_{p;\alpha} = \frac{1}{2\pi} F_{p;\alpha\alpha} = \frac{1}{2\pi} \sum_{\beta, \beta'} G_{\alpha\beta} \Gamma_{p;\beta\beta'} G_{\alpha\beta'}^*, \quad (4.53)$$

as a tool to analyze the spatial distribution of the response from an incident wave in a lead  $p$ .

### Scattering matrix and transmission function

The mode-resolved  $S$ -matrix of a multiterminal scatterer in the tight-binding grid representation is given by the discrete version of the Fisher-Lee formula (3.49) (choosing the convention of setting the origin in each lead at the terminal interface),

$$\mathcal{S}_{qp}^{nm} = i\hbar \sqrt{v_n^{(q)} v_m^p} \mathbf{X}_n^{q\dagger} \tilde{\mathbf{G}}_{qp} \mathbf{X}_m^p - \delta_{qp} \delta_{nm} \quad (4.54)$$

where  $\tilde{\mathbf{G}}_{qp}$  is the part of the scatterer Greenian propagating from lead  $p$  to lead  $q$ , with the mode velocities  $v_m^p$  given in Eq. (4.27) (recall here that the factor  $a_0$  from the matrix product in the first term is absorbed in  $\tilde{\mathbf{G}}_{qp}$ , so that the result is indeed dimensionless). The transmission function  $T_{qp}(E) = \sum_{n,m} T_{qp}^{nm}(E) = \sum_{n,m} |\mathcal{S}_{qp}^{nm}(E)|^2$  (see Eq. (2.14)) determines, upon thermal averaging, the linear-response conductance between terminals  $p$  and  $q$ , as was seen in Sec. 2.3.2, which is of primary interest in equilibrium transport.

If resolution into channel transmission coefficients  $T_{qp}^{nm}$  is not needed, some computational cost (and storage) is saved by employing directly the trace formula (3.142) for the transmission, which in the discretized tight-binding case reads

$$T_{pq} = \text{Tr}[\mathbf{\Gamma}_p \mathbf{F}_q] = \text{Tr}[\mathbf{\Gamma}_p \tilde{\mathbf{G}}_{pq} \tilde{\mathbf{G}}_q^\dagger], \quad p \neq q, \quad (4.55)$$

with the trace taken explicitly over the diagonal elements of grid-represented matrices; that is, a single number is computed and stored for each lead pair instead of an  $S$ -matrix of dimension equal to the number of transversal sites in the leads. In fact, Eq. (4.55) is readily

---

<sup>9</sup> The symbol  $\text{diag}()$  denotes (with a single matrix argument) the column vector of the diagonal elements or (with multiple arguments) the (block-) diagonal matrix with elements (matrices) on the diagonal.

obtained from Eq. (4.54) by taking the absolute square and using Eq. (4.50). As noted previously, however, it should be kept in mind that the trace formula is of general validity for coherent transport and does not rely on the tight-binding approximation.

Whether we want to determine resolved matrix elements  $\mathcal{S}_{qp}^{nm}$  or the transmission  $T_{pq}$ , it is clear that only the part  $\tilde{\mathbf{G}}_{qp}$  of propagator connecting leads  $p$  and  $q$  needs to be computed, which is typically a very small portion of the full  $\tilde{\mathbf{G}}$ -matrix. This fact will be exploited in the computational method developed in the following sections.

### Natural units

For convenience as well as numerical stability in computations, but also as a means of presenting results in an easily scalable fashion, in the following we adapt to a ‘natural’ system of units where the length scale is defined by the lattice constant  $a_0$ , that is, we set  $a_0 \equiv 1$ . In addition, we set

$$\hbar = m_{\text{eff}} = e = a_0 \equiv 1 \quad (4.56)$$

in terms of which all other units of interest are defined.<sup>10</sup> In particular, the natural units of energy and magnetic flux density become

$$[E] = \frac{\hbar^2}{m_{\text{eff}} a_0^2}, \quad [B] = \frac{\hbar}{e a_0^2}, \quad (4.57)$$

respectively, that is, both scale as  $a_0^{-2}$ . In this manner,  $E$ - or  $B$ -resolved results can be scaled according to the size of the system in correspondence to realistic length scales, taking into account the conditions under which coherent transport would be achieved experimentally. Appendix E provides tables including derived natural units for relevant quantities (Table E.1), the conversion factors for certain quantities for an experimentally relevant choice  $a_0 = 2$  nm (Table E.2), as well as the numerical values of relevant constants (Table E.3) for easy reference. In natural units, the hopping energy has the value  $t = \frac{\hbar^2}{2m_{\text{eff}} a_0^2} = \frac{1}{2}$ .

## 4.4 Computation of the propagator

Having established the grid-discretized versions of quantities of interest and their relation to the open system Greenian, we will now address its actual computation for a generic multiterminal quantum billiard system. First, we describe a generic partitioning scheme for the matrix Hamiltonian pertaining to a solution based on block-Gaussian elimination (BGE), and then present two alternative computational procedures for the relevant multiterminal  $\tilde{\mathbf{G}}$ -matrix parts.

### 4.4.1 Block-partitioning of the Hamiltonian

An often recurring concept in the following will be the partitioning of a grid-discretized Hamiltonian matrix  $\tilde{\mathbf{H}}$ , which could be the total (effective) Hamiltonian matrix of the system or some part of it, into blocks  $\mathbf{H}_1$  and  $\mathbf{H}_2$  on the block-diagonal coupled by a block-antidiagonal matrix  $\mathbf{W}$ ,

$$\tilde{\mathbf{H}} = \begin{pmatrix} \tilde{\mathbf{H}}_{11} & \tilde{\mathbf{H}}_{12} \\ \tilde{\mathbf{H}}_{21} & \tilde{\mathbf{H}}_{22} \end{pmatrix} \equiv \mathbf{H} + \mathbf{W} = \begin{pmatrix} \mathbf{H}_1 & \mathbf{W}_{12} \\ \mathbf{W}_{21} & \mathbf{H}_2 \end{pmatrix}, \quad (4.58)$$

<sup>10</sup> Note that, in contrast to the units used in the theory of previous chapters, here we do *not* set  $c = 1$  for the speed of light. In fact, since  $[\text{length}] = a_0$  and  $\text{time} = \hbar/[E] = m_{\text{eff}} a_0^2 / \hbar$ , velocity scales as  $a_0^{-1}$ .

for which the corresponding Greenian  $\tilde{\mathbf{G}}$  is to be computed in terms of the Greenians  $\mathbf{G}_1$  of  $\mathbf{H}_1$  and  $\mathbf{G}_2$  of  $\mathbf{H}_2$  as well the couplings  $\mathbf{W}_{12}$  and  $\mathbf{W}_{21}$ . As shown in App. B, the total Greenian of the connected subdomains  $\mathbb{D}_1$  and  $\mathbb{D}_2$ , described by  $\mathbf{H}_1$  and  $\mathbf{H}_2$  when isolated, is found by BGE to be

$$\tilde{\mathbf{G}} = \begin{pmatrix} \tilde{\mathbf{G}}_{11} & \tilde{\mathbf{G}}_{12} \\ \tilde{\mathbf{G}}_{21} & \tilde{\mathbf{G}}_{22} \end{pmatrix} = \begin{pmatrix} \tilde{\mathbf{G}}_{11} & \tilde{\mathbf{G}}_{11} \mathbf{W}_{12} \mathbf{G}_2 \\ \mathbf{G}_2 \mathbf{W}_{21} \tilde{\mathbf{G}}_{11} & \mathbf{G}_2 + \mathbf{G}_2 \mathbf{W}_{21} \tilde{\mathbf{G}}_{11} \mathbf{W}_{12} \mathbf{G}_2 \end{pmatrix} \quad (4.59)$$

$$= \begin{pmatrix} \mathbf{G}_1 + \mathbf{G}_1 \mathbf{W}_{12} \tilde{\mathbf{G}}_{22} \mathbf{W}_{21} \mathbf{G}_1 & \mathbf{G}_1 \mathbf{W}_{12} \tilde{\mathbf{G}}_{22} \\ \tilde{\mathbf{G}}_{22} \mathbf{W}_{21} \mathbf{G}_1 & \tilde{\mathbf{G}}_{22} \end{pmatrix}, \quad (4.60)$$

with

$$\tilde{\mathbf{G}}_{11} = [\mathbf{E}_1 - (\mathbf{H}_1 + \boldsymbol{\Sigma}_1)]^{-1}, \quad \boldsymbol{\Sigma}_1 \equiv \mathbf{W}_{12} \mathbf{G}_2 \mathbf{W}_{21}, \quad (4.61)$$

$$\tilde{\mathbf{G}}_{22} = [\mathbf{E}_2 - (\mathbf{H}_2 + \boldsymbol{\Sigma}_2)]^{-1}, \quad \boldsymbol{\Sigma}_2 \equiv \mathbf{W}_{21} \mathbf{G}_1 \mathbf{W}_{12}, \quad (4.62)$$

where  $\boldsymbol{\Sigma}_1$  and  $\boldsymbol{\Sigma}_2$  are the self-energies of subsystems 1 and 2 due to the coupling to 2 and 1, respectively. This is equivalent to solving the matrix Dyson equation

$$\tilde{\mathbf{G}} = \mathbf{G} + \mathbf{G} \mathbf{W} \tilde{\mathbf{G}} = \mathbf{G} + \tilde{\mathbf{G}} \mathbf{W} \mathbf{G} \quad (4.63)$$

for the disconnected subsystems [121] with block-diagonal propagator

$$\tilde{\mathbf{G}} = \begin{pmatrix} \mathbf{G}_1 & \mathbf{0} \\ \mathbf{0} & \mathbf{G}_2 \end{pmatrix}, \quad (4.64)$$

perturbed by the interaction  $\mathbf{W}$  between them. Solving in terms of  $\boldsymbol{\Sigma}_1$ , the explicit propagators between sites in the domains  $\mathbb{D}_1$  and  $\mathbb{D}_2$  then read

$$\tilde{\mathbf{G}}_{21} = \mathbf{G}_2 \mathbf{W}_{21} (\mathbf{I}_1 - \mathbf{G}_1 \boldsymbol{\Sigma}_1)^{-1} \mathbf{G}_1, \quad (4.65)$$

$$\tilde{\mathbf{G}}_{11} = \mathbf{G}_1 + \mathbf{G}_1 \boldsymbol{\Sigma}_1 (\mathbf{I}_1 - \mathbf{G}_1 \boldsymbol{\Sigma}_1)^{-1} \mathbf{G}_1, \quad (4.66)$$

$$\tilde{\mathbf{G}}_{12} = \mathbf{G}_1 (\mathbf{I}_1 - \boldsymbol{\Sigma}_1 \mathbf{G}_1)^{-1} \mathbf{W}_{12} \mathbf{G}_2, \quad (4.67)$$

$$\tilde{\mathbf{G}}_{22} = \mathbf{G}_2 + \mathbf{G}_2 \mathbf{W}_{21} \mathbf{G}_1 (\mathbf{I}_1 - \boldsymbol{\Sigma}_1 \mathbf{G}_1)^{-1} \mathbf{W}_{12} \mathbf{G}_2, \quad (4.68)$$

as shown in App. B.2, where  $\mathbf{I}_1$  is the identity matrix of the dimension of  $\mathbf{H}_1$ .

A particular case of the above partition scheme arises when decomposing the infinitely extended scattering system into scatterer and attached semi-infinite leads. We then obtain the Greenian of the open scatterer  $\tilde{\mathbf{G}}_S \equiv \tilde{\mathbf{G}}_{11}$  in terms of the self-energy  $\boldsymbol{\Sigma} \equiv \boldsymbol{\Sigma}_1$  due to coupling to the leads in the familiar form of Eq. (4.38), with coupling matrix  $\boldsymbol{\tau} \equiv \mathbf{W}_{12}$  and lead Greenian  $\mathbf{G}_{22} = \mathbf{G}_L = \mathbf{g}$ . The partitioning here simply consists in implicitly counting first all the sites within  $\mathbb{D}_S$  and then those in  $\mathbb{D}_L$ .

For actually computing the parts of the inverse  $\tilde{\mathbf{G}}_S = (\mathbf{E} - \tilde{\mathbf{H}}_S)$  needed for the observables relevant to transport (such as transmission and LDOS), the scatterer Hamiltonian is further partitioned into blocks  $\tilde{\mathbf{H}}_{s,s'}$  corresponding to slices  $s, s'$  of  $\mathbb{D}_S$ . In the present context, the subsystems 1 and 2 will correspond to subdomains  $\mathbb{D}_1$  and  $\mathbb{D}_2$  of the discretized scatterer domain  $\mathbb{D}$  consisting of one or more slices of (internal or lead-connected) sites. The BGE procedure will then be applied on the level of single slices and parts of connected slices.

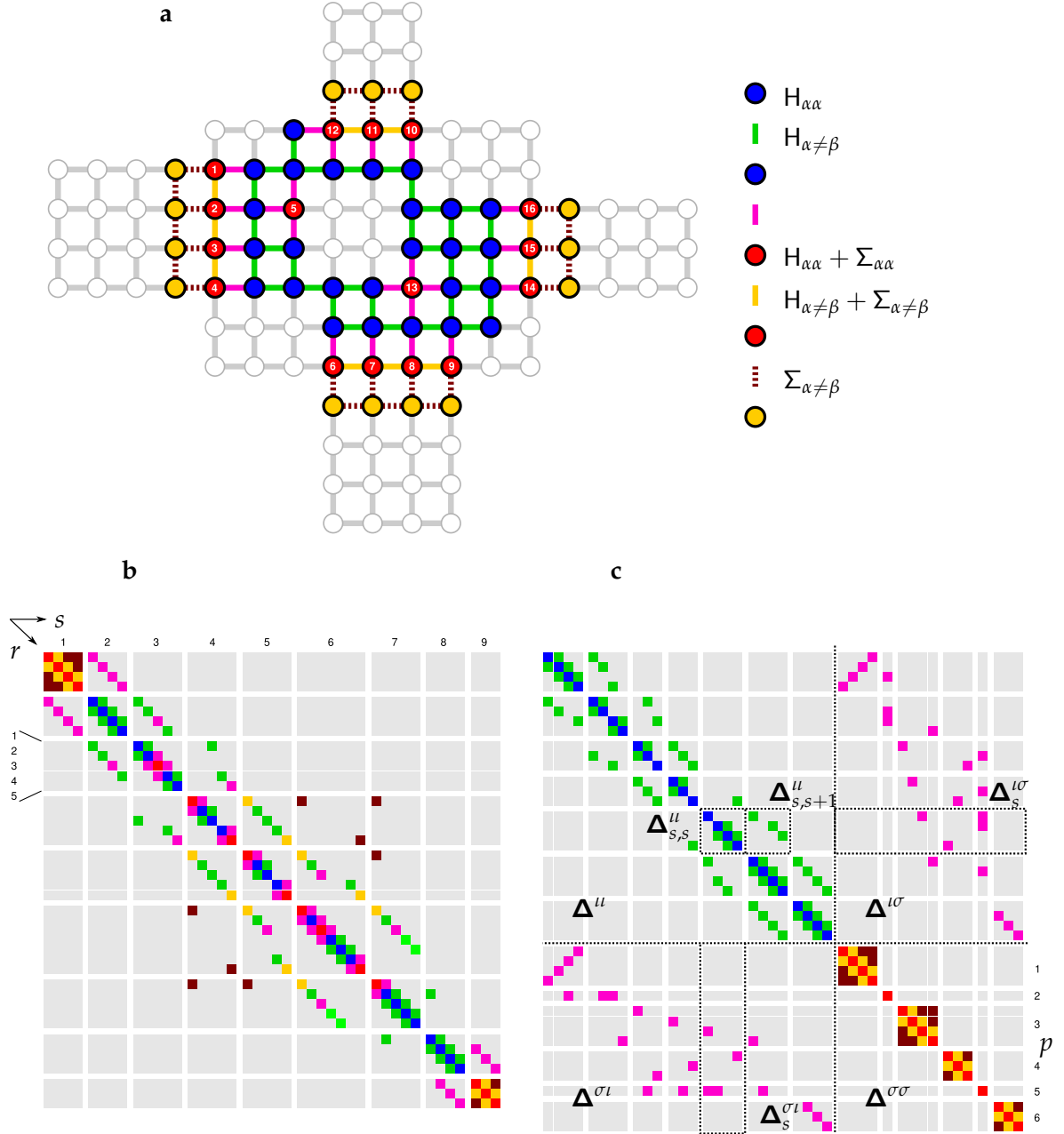


**Figure 4.2:** (a) Toy device with 26 internal sites (blue) and 16 surface sites (red) of which 14 are connected to four terminals (yellow) and two represent decoherence probes. The scatterer also has a hole of 4 discarded sites. The legend on the right indicates the effective Hamiltonian on-site and hopping matrix elements describing the truncated scatterer, where lead sites (yellow) participate via their Green function in the self-energy  $\Sigma$ . (b) Effective Hamiltonian matrix  $\hat{\mathbf{H}}$  (or equivalently  $\hat{\Delta} = \mathbf{E} - \hat{\mathbf{H}}$ ) of the lead-connected scatterer with all sites (including red surface sites) indexed from left to right by slice numbers  $s = 1 : 9$  and from bottom to top by row number  $r = 1 : N_r^{(s)}$  in each slice. Self-energies (on-site = red, nearest-neighbor coupling = orange, remote coupling = brown) contribute full diagonal blocks for horizontal leads (attached on the left or right) and scattered off-diagonal blocks for vertical leads (attached on the bottom or top). (c) Block-reordered  $\hat{\Delta}$ -matrix by indexing first internal sites and then surface sites as numbered in (a), with leads numbered as encountered from left to right and bottom to top. The reordered matrix has block-tridiagonal internal superblock  $\hat{\Delta}^u$ , block-diagonal surface superblock  $\hat{\Delta}^{\sigma\sigma}$  and surface-internal coupling  $\hat{\Delta}^{i\sigma} = [\hat{\Delta}^{\sigma i}]^\dagger$ . Indicated subblocks  $\hat{\Delta}_{s,s}^u$ ,  $\hat{\Delta}_{s,s+1}^u$  and  $\hat{\Delta}_s^{i\sigma} = [\hat{\Delta}_s^{\sigma i}]^\dagger$  are used in  $s$ -th iteration of the BGE process.

#### 4.4.2 Standard recursive Green function method

Considering the toy scatterer in Fig. 4.2 (a), if we count *all* sites of the scatterer (internal/blue and lead-connected/red) from left to right (starting from the leftmost slice  $s \equiv 1$ ) and bottom to top (starting from the lowest site  $(s, r = 1)$  in each slice), we obtain the effective Hamiltonian matrix illustrated in Fig. 4.2 (b). It consists of a block-tridiagonal matrix corresponding to the internal sites, with self-energy elements  $\Sigma_{\alpha\beta}$  added including hoppings between all surface sites connected to a each lead; the  $\Sigma_{\alpha\beta}$  can thus, in general, occupy any block of  $\tilde{\mathbf{H}}$ , since remote (not nearest-neighbor) slices can be coupled by vertical leads.

We can now assemble the scatterer slice by slice, starting from the left and, for each slice  $s + 1$  added to the part of already assembled slices  $1 : s$ , solve the Dyson equation (4.63) by identifying

$$\mathbf{G} = \begin{pmatrix} \mathbf{G}_{1:s} & \mathbf{0} \\ \mathbf{0} & \mathbf{G}_{s+1} \end{pmatrix}, \quad \mathbf{W} = \begin{pmatrix} \mathbf{0} & \mathbf{H}_{(1:s,s+1)} + \boldsymbol{\Sigma}_{(1:s,s+1)} \\ \mathbf{H}_{(s+1,1:s)} + \boldsymbol{\Sigma}_{(s+1,1:s)} & \mathbf{0} \end{pmatrix} \quad (4.69)$$

as the propagator of the isolated domains  $\mathbb{D}_{1:s} \cup \mathbb{D}_s$  and the coupling between them, respectively. The solution for  $\tilde{\mathbf{G}} \equiv \tilde{\mathbf{G}}_{1:s+1}$  is given by performing BGE on the corresponding block-partitioned Hamiltonian  $\tilde{\mathbf{H}} \equiv \tilde{\mathbf{H}}_{1:s+1}$  in Eq. (4.58) and, since the slice  $s + 1$  being attached is the smaller of the two subsystems, the solution form in Eq. (4.59) with Eq. (4.61) is chosen where  $\mathbf{G}_2 \equiv \mathbf{G}_{s+1}$  must be computed while  $\mathbf{G}_1 \equiv \mathbf{G}_{1:s}$  is already known from the previous iteration. The explicit forms of the propagators between sites in the connected domains are then given by Eqs. (4.65)–(4.68) For each added slice  $s + 1$ , the *same* computational steps are performed using, as input, the *output*  $\tilde{\mathbf{G}}_{1:s}$  from the previous iteration, and so the procedure is referred to as the *recursive* Green function (RGF) method.

Let us now assume that we are only interested in the transmission function  $T_{qp}$  (or the mode-resolved scattering matrix  $S_{qp}^{nm}$ ) between the terminals of a transport device. We then only need the propagator between surface (lead-connected) gridpoints of the scatterer. Considering the toy scatterer in Fig. 4.2 (a), with the first (horizontal) lead connected to the first slice, according to the above procedure we start by computing the Greenian  $\tilde{\mathbf{G}}_{s=1} = (\mathbf{E}_{s=1} - \mathbf{H}_{s=1} - \boldsymbol{\Sigma}_{s=1})^{-1}$  and  $\tilde{\mathbf{G}}_{s=2} = (\mathbf{E}_{s=2} - \mathbf{H}_{s=2} - \boldsymbol{\Sigma}_{s=2})^{-1}$  of the first and second slices (here  $\boldsymbol{\Sigma}_{s=2}$  happens to be zero) which become the inputs  $\mathbf{G}_1$  and  $\mathbf{G}_2$  to compute  $\tilde{\mathbf{G}} \equiv \tilde{\mathbf{G}}_{1:2}$  from Eq. (4.59). In the same manner  $\tilde{\mathbf{G}}_{1:3}$  is computed in the next step, with slice  $s = 3$  being connected to the second lead (which happens here to be a decoherence probe).

In performing the computation, we may discard the computation of the propagator between *internal* sites of slices 2 and 3 which is not required. However, in order to obtain the lead-to-lead parts of the propagator  $\tilde{\mathbf{G}}_{1:3}$  needed, we have now also computed the propagator between *internal* sites of slice 3 to *surface* sites of slice 1. In other words, with the standard RGF method the *complete* BGE *including* back-substitution is performed for each added slice in the recursion in order to obtain the corresponding Greenian, even though the added slice contains internal points.

We next introduce a scheme which avoids this issue by a further block-partitioning of the Hamiltonian into internal and surface blocks, enabling selective computation of needed propagators.

#### 4.4.3 Reordered block-Gaussian elimination scheme

In order to separate the computation of the surface-surface part from the internal-surface part of the scatterer propagator, we reorder the matrix

$$\tilde{\mathbf{\Delta}} = \mathbf{E} - \tilde{\mathbf{H}} = \mathbf{\Delta} - \boldsymbol{\Sigma} = \mathbf{E} - \mathbf{H} - \boldsymbol{\Sigma} \quad (4.70)$$

as shown in Fig. 4.2 (c) for the toy scatterer in Fig. 4.2 (a). The reordering essentially consists in scanning through the scatterer domain from the left slice-by-slice (and from bottom to top in each slice), though first only indexing all internal sites of the scatterer; the surface sites are then indexed lead-by-lead in the order they are encountered from left to right and then from bottom to top, with the index following the local  $y$ -coordinate in each lead (that is, anti-clockwise), as shown by the numbers on the red sites in Fig. 4.2 (a).

The  $\tilde{\mathbf{D}}$ -matrix (or, equivalently, Hamiltonian) then acquires the large-scale block-partitioned form

$$\tilde{\mathbf{D}} = \begin{pmatrix} \tilde{\mathbf{D}}^{\iota\iota} & \tilde{\mathbf{D}}^{\iota\sigma} \\ \tilde{\mathbf{D}}^{\sigma\iota} & \tilde{\mathbf{D}}^{\sigma\sigma} \end{pmatrix}, \quad (4.71)$$

where the off-diagonal blocks  $\tilde{\mathbf{D}}^{\iota\sigma} = [\tilde{\mathbf{D}}^{\sigma\iota}]^\dagger$  couple the surface part (labeled  $\sigma$ ) to the internal part (labeled  $\iota$ ).

Since the self-energy matrix elements are now exclusively contained in the  $\tilde{\mathbf{D}}^{\sigma\sigma}$  block, the Hermitian internal part  $\tilde{\mathbf{D}}^{\iota\iota}$  now retains the block-tridiagonal structure of the isolated scatterer Hamiltonian (4.30). Considering no coupling between sites of different leads, the non-Hermitian surface block  $\tilde{\mathbf{D}}^{\sigma\sigma}$  is block-diagonal,<sup>11</sup>

$$\tilde{\mathbf{D}}^{\sigma\sigma} = \text{diag}_{\mathcal{G}_{p=1}^{N_L}}(\tilde{\mathbf{D}}_p^{\sigma\sigma}) = \text{diag}_{\mathcal{G}_{p=1}^{N_L}}(\mathbf{E}_p - \mathbf{H}_p - \boldsymbol{\Sigma}_p), \quad (4.72)$$

where  $\boldsymbol{\Sigma}_p$  is the full  $N_w^p \times N_w^p$  self-energy matrix for lead  $p$  and  $\mathbf{H}_p$  the corresponding tridiagonal isolated Hamiltonian matrix for the straight site array connected to lead  $p$ .<sup>12</sup> The coupling block  $\tilde{\mathbf{D}}^{\iota\sigma} = [\tilde{\mathbf{D}}^{\sigma\iota}]^\dagger$  is a block-column of block-rows  $\tilde{\mathbf{D}}_s^{\iota\sigma}$  ( $s = 1 : N_s$ ) of sizes  $N_r^{(s)} \times \sum_p N_w^p$ ,

$$\tilde{\mathbf{D}}^{\iota\sigma} = \begin{pmatrix} \tilde{\mathbf{D}}_1^{\iota\sigma} \\ \vdots \\ \tilde{\mathbf{D}}_s^{\iota\sigma} \\ \vdots \\ \tilde{\mathbf{D}}_{N_s}^{\iota\sigma} \end{pmatrix}, \quad \tilde{\mathbf{D}}_s^{\iota\sigma} = \begin{pmatrix} \tilde{\mathbf{D}}_{s;1}^{\iota\sigma} & \cdots & \tilde{\mathbf{D}}_{s;p}^{\iota\sigma} & \cdots & \tilde{\mathbf{D}}_{s;N_L}^{\iota\sigma} \end{pmatrix}, \quad (4.73)$$

where  $s$  now counts only the slices of internal sites in the reordered indexing.

In the internal-surface block-partitioning scheme, the Green equation to be solved becomes

$$\begin{pmatrix} \tilde{\mathbf{D}}^{\iota\sigma} & \tilde{\mathbf{D}}^{\iota\sigma} \\ \tilde{\mathbf{D}}^{\sigma\iota} & \tilde{\mathbf{D}}^{\sigma\sigma} \end{pmatrix} \begin{pmatrix} \tilde{\mathbf{G}}^{\iota\iota} & \tilde{\mathbf{G}}^{\iota\sigma} \\ \tilde{\mathbf{G}}^{\sigma\iota} & \tilde{\mathbf{G}}^{\sigma\sigma} \end{pmatrix} = \begin{pmatrix} \mathbf{I}^{\iota\iota} & \mathbf{0}^{\iota\sigma} \\ \mathbf{0}^{\sigma\iota} & \mathbf{I}^{\sigma\sigma} \end{pmatrix}, \quad (4.74)$$

<sup>11</sup> Note that this is in accordance with the Landauer-Büttiker framework for transport, on which the formulation of the scattering problem is based: Recall that semi-infinite leads merely represent an (ideal form of) electron reservoirs, which in turn correspond to electrodes attached to the transport device. Coupling (that is, hopping elements) between surface (lead-connected) sites of two different leads would, in the continuum limit  $a_0$ , correspond to a connection between the respective electrodes, in which case they would equilibrate (short-circuit) to the same chemical potential and effectively constitute a single attached electrode, to be modeled by a single semi-infinite lead.

<sup>12</sup> For simplicity, we consider only horizontal or vertical semi-infinite leads attached to the computational box containing the scatterer, for which the lead Greenians are easily evaluated. That surface sites connected to one lead are then  $y$ - or  $x$ -collinear, respectively, leading the tridiagonal  $\mathbf{H}_p$ . Leads at arbitrary angles can be implemented by ‘adiabatic bending’ into a horizontal or vertical lead by enlarging the computational box accordingly, as shown schematically (for very low grid resolution) in Fig. 4.1. With sufficiently smooth bending, the Fano resonance width of quasi-bound states in the bent wire becomes negligible (that is, affects the transmission profile of the system only at distinct points in energy). If the lattice Greenian for a tilted lead is known, then attaching the lead can be trivially implemented in the present scheme and would simply introduce zeros on the side-diagonals of  $\mathbf{H}_p$ .

with obvious superscript notation. We can now perform BGE on this high-level-partitioned total  $\tilde{\mathbf{A}}$ -matrix, as shown generically in Sec. 4.4.1. The part  $\tilde{\mathbf{G}}^{\sigma\sigma}$  of the full Greenian propagating between surface sites (from lead to lead) is then simply given by the inverse Schur complement of the internal  $\tilde{\mathbf{A}}^u$ -block,

$$\tilde{\mathbf{G}}^{\sigma\sigma} = \left[ \tilde{\mathbf{A}}^{\sigma\sigma} - \tilde{\mathbf{A}}^{\sigma l} [\tilde{\mathbf{A}}^u]^{-1} \tilde{\mathbf{A}}^{l\sigma} \right]^{-1}, \quad (4.75)$$

while the part  $\tilde{\mathbf{G}}^{l\sigma}$  propagating from the surface to the interior is given by

$$\tilde{\mathbf{G}}^{l\sigma} = -[\tilde{\mathbf{A}}^u]^{-1} \tilde{\mathbf{A}}^{l\sigma} \tilde{\mathbf{G}}^{\sigma\sigma} \quad (4.76)$$

as shown in App. B (see Eq. (B.6)). Thus, if only the scattering matrix (4.54) or the transmission function (4.55) of the system are desired, then only forward elimination needs to be carried out to obtain  $\tilde{\mathbf{G}}^{\sigma\sigma}$ ; to compute, additionally, the scattering wave function (4.43) (and in turn the current density (4.48)) or the LDOS (4.53), backward substitution is performed which yields  $\tilde{\mathbf{G}}^{\sigma\sigma}$ .

### Forward elimination

The final (outer) inversion to be computed in Eq. (4.75) is of the relatively small dimension  $N_\sigma = \sum_{p=1}^{N_L} N_w^p$ , equal to the number of sites of the total interface to the attached leads, and can be carried out directly using an efficient inversion scheme such as via LU (lower-upper-triangular) factorization; we use the standard routines `zgetrf` (LU factorization) and `zgetri` (inversion of LU-factorized matrix) from the Linear Algebra PACKage [245]. On the contrary, the intermediate (inner) inversion  $[\tilde{\mathbf{A}}^u]^{-1}$  is, despite being sparse, computationally expensive, with dimension  $N_l$  equal to the internal sites of the whole scatterer. This is not evident in the toy example in Fig. 4.2, of course, where  $N_l = 26$ ,  $N_\sigma = 16$ . Already in the schematic of Fig. 4.1, though, which has  $N_l = 1059$ ,  $N_\sigma = 21$ , the difference in order of magnitude is anticipated. In actual simulations we will usually have  $N_l \sim \mathcal{O}(10^4)$  while  $N_\sigma = \mathcal{O}(10^1)$  (in applications presented here we use  $N_\sigma = 2^5 = 32$ ), for which (i) the confinement is enough resolved for computed results to be converged and (ii) the deviation of the discrete dispersion from the continuum limit is negligibly small at the considered energies.

More importantly, however, we do not need the *full* inverse  $[\tilde{\mathbf{A}}^u]^{-1}$  to obtain  $\tilde{\mathbf{G}}^{\sigma\sigma}$  and  $\tilde{\mathbf{G}}^{l\sigma}$ , as Eqs. (4.75) and (4.76) above might suggest. Indeed, the strategy to compute  $[\tilde{\mathbf{A}}^u]^{-1}$  is, in similarity to the standard RGF, to perform BGE on the total matrix  $\tilde{\mathbf{A}}$  on the level of blocks corresponding to slices of the internal part of the scatterer, though only carrying out the *forward* elimination steps to obtain the surface propagator.

With Fig. 4.2 as a guide: The block updates are done until  $\tilde{\mathbf{A}}^u$  becomes upper triangular and the large-scale lower off-diagonal block  $\tilde{\mathbf{A}}^{\sigma l}$  is eliminated, which leaves the Schur complement  $[\tilde{\mathbf{G}}^{\sigma\sigma}]^{-1}$  on the lower right (in the place of  $\tilde{\mathbf{A}}^{\sigma\sigma}$ ). The pseudocode for the explicit steps of the forward elimination algorithm and the final inversion of Schur's complement is as follows ( $\leftarrow$  denoting assignment of the expression on the right to the variable on the

left):

$$\text{for } s = 1 : N_s - 1$$

$$\mathbf{Z} \longleftarrow [\tilde{\mathbf{A}}_{s,s}^{II}]^{-1} \quad (4.77)$$

$$\tilde{\mathbf{A}}_{s,s+1}^{II} \longleftarrow \mathbf{Z} \tilde{\mathbf{A}}_{s,s+1}^{II} \quad \star \quad (4.78)$$

$$\tilde{\mathbf{A}}_{s+1,s+1}^{II} \longleftarrow \tilde{\mathbf{A}}_{s+1,s+1}^{II} - \tilde{\mathbf{A}}_{s+1,s}^{II} \tilde{\mathbf{A}}_{s,s+1}^{II} \quad (4.79)$$

$$\tilde{\mathbf{A}}_s^{I\sigma} \longleftarrow \mathbf{Z} \tilde{\mathbf{A}}_s^{I\sigma} \quad \star \quad (4.80)$$

$$\tilde{\mathbf{A}}_{s+1}^{I\sigma} \longleftarrow \tilde{\mathbf{A}}_{s+1}^{I\sigma} - \tilde{\mathbf{A}}_{s+1,s}^{II} \tilde{\mathbf{A}}_s^{I\sigma} \quad (4.81)$$

$$\tilde{\mathbf{A}}^{\sigma\sigma} \longleftarrow \tilde{\mathbf{A}}^{\sigma\sigma} - \tilde{\mathbf{A}}_s^{\sigma I} \tilde{\mathbf{A}}_s^{I\sigma} \quad (4.82)$$

end

$$\tilde{\mathbf{G}}^{\sigma\sigma} \longleftarrow [\tilde{\mathbf{A}}^{\sigma\sigma}]^{-1} \quad (4.83)$$

where  $s$  counts the blocks corresponding to slices of internal sites. The colored blocks  $\tilde{\mathbf{A}}_{s,s+1}^{II}$  and  $\tilde{\mathbf{A}}_s^{I\sigma}$  of the  $\tilde{\mathbf{A}}$ -matrix are updated and used in the same iteration. Note that the blocks are generally overwritten (or finally deleted) in memory when no longer needed. However, the recurring and final inversions are assigned to separate variables  $\mathbf{Z}$  and  $\tilde{\mathbf{G}}^{\sigma\sigma}$ , respectively, in order to check the inversion for numerical accuracy (by comparing  $\mathbf{Z}\tilde{\mathbf{A}}_{s,s}^{II}$  and  $\tilde{\mathbf{G}}^{\sigma\sigma}\tilde{\mathbf{A}}^{\sigma\sigma}$  with the identity matrix). In particular, the starred ( $\star$ ) expressions saved to the offdiagonal blocks  $\tilde{\mathbf{A}}_s^{I\sigma}$  and  $\tilde{\mathbf{A}}_{s,s+1}^{II}$  are *selectively* stored if the corresponding part  $\tilde{\mathbf{G}}^{I\sigma}$  of the propagator is to be computed by backward substitution.

The inversions of the slice blocks are performed directly using the standard routines `zgetrf` and `zgetri` of LAPACK. The numerical complexity of the forward block-elimination follows the scaling (4.39) of level-3 operations on the  $N_r^{(s)}$ -dimensional matrices of the slices for large  $N_s$ ,

$$C_{FE} \propto 6 f \sum_{s=1}^{N_s} [N_r^{(s)}]^3, \quad N_s \gg 1, \quad (4.84)$$

for the 1 matrix inversion + 5 matrix products in each  $s$ -iteration.<sup>13</sup> This means that the scatterer is preferably oriented such that it is narrower (has less internal sites) in the vertical  $x$ -direction. This scaling is the same as for the standard RGF method. The advantage is here that no backward substitution steps are (unnecessarily) performed for computing terminal properties (transport coefficients), in contrast to a standard implementation of the RGF method where back-substitution is performed internally for each slice iteration. Thus, although the asymptotic scaling of the complexity is the same, the proportionality factor in Eq. (4.84) is smaller since the back-substitution multiplications are discarded.

### Backward substitution

The backward substitution following forward BGE consists simply of matrix products of the stored offdiagonal blocks  $\tilde{\mathbf{A}}_s^{I\sigma}$  with the (common) computed surface propagator  $\tilde{\mathbf{G}}^{\sigma\sigma}$ , performed *backwards* from the last internal slice to the first ( $N_s : 1 = N_s, N_s - 1, \dots, 1$ ):

$$\text{for } s = N_s : 1$$

$$\tilde{\mathbf{G}}_s^{I\sigma} \longleftarrow -\tilde{\mathbf{A}}_s^{I\sigma} \tilde{\mathbf{G}}^{\sigma\sigma} \quad (4.85)$$

$$\tilde{\mathbf{G}}_s^{\sigma\sigma} \longleftarrow -\tilde{\mathbf{A}}_{s,s+1}^{II} \tilde{\mathbf{G}}^{\sigma\sigma} \quad (4.86)$$

end

<sup>13</sup> Note here that the proportionality factor is affected by the matrix additions, scaling as  $[N_r^{(s)}]^2$ , but mostly by the fact that the offdiagonal blocks are usually not square.

In the same manner, parts  $\tilde{\mathbf{G}}_{s,s'}^{\mu}$  of the full propagator between internal sites could be computed, but they are not used in the present context of transport to obtain relevant observables. The two iterated matrix multiplications above yield an asymptotic numerical cost

$$C_{\text{BS}} \propto 2f \sum_{s=1}^{N_s} [N_r^{(s)}]^3, \quad N_s \gg 1, \quad (4.87)$$

which is avoided in the present reordered BGE scheme by performing only the forward elimination if only surface properties are desired. The exact amount of computational gain depends, of course, on the particular system setup in terms of its geometry and topology and, more importantly, on the relative width of the attached leads determining the size of the (total) terminal interface.

Another advantage of the reordered block partitioning, which is of practical nature rather than computationally essential, is that the two propagator parts  $\tilde{\mathbf{G}}^{l\sigma}$  and  $\tilde{\mathbf{G}}^{\sigma\sigma}$  are automatically separated a priori by the indexing order of the sites in the scatterer. In other words, having counted the sites in the order described above (see Fig. 4.2), there is no need to keep track of internal versus surface propagator elements during computation. Further, the indexing convention for the surface sites (continuous index for each lead) readily yields the multiterminal blocks of  $\tilde{\mathbf{G}}^{\sigma\sigma}$ .

Once the recursion is done, the respective parts of  $\tilde{\mathbf{G}}^{l\sigma}$  are used in the post-processing shown in Sec. 4.3.2 to obtain the scattering wave function (4.43) (and in turn the current density (4.48)) and the (partial) LDOS (4.53), while  $\tilde{\mathbf{G}}^{\sigma\sigma}$  yields the scattering matrix (4.54) and the transmission function (4.55).

## 4.5 Extended recursive Green function method for multiterminal, multiply connected structures

The slice-by-slice recursion in the RGF method, in its standard form or in the internal-surface block-reordered scheme above, constitutes an efficient way to compute the system propagator which takes into account the sparsity of the tight-binding Hamiltonian. There are cases, however, where it is advantageous to partition the Hamiltonian on a higher level, decomposing the system into subsystems containing several slices each. In this section, we present a computational method based on the general BGE scheme of Sec. 4.4.1 to treat generic structures with singly or multiply connected subsystems and with multiple terminals.

### 4.5.1 Modular partitioning

Relying on the lateral structure of the confining potential, a nanoelectronic device can be virtually cut into smaller pieces whose individual propagators are computed with less computational effort in total than for the composite system. The propagator of the composite system can then be expressed in terms of the propagators of the individual parts; as discussed in Sec. 4.4.1, this is achieved in the tight-binding approach by introducing appropriate coupling elements between the parts and then solving the corresponding matrix Dyson equation. With the individual, spatially extended parts connected one by one to obtain the total propagator, this procedure is known as an *extended* RGF method [118, 121].

A special case arises when the propagator of one or more parts can be determined analytically, in which case the computation is effectively reduced to the connection of the parts. Such a method has been developed by Rotter *et al.* [122], where the system constituents

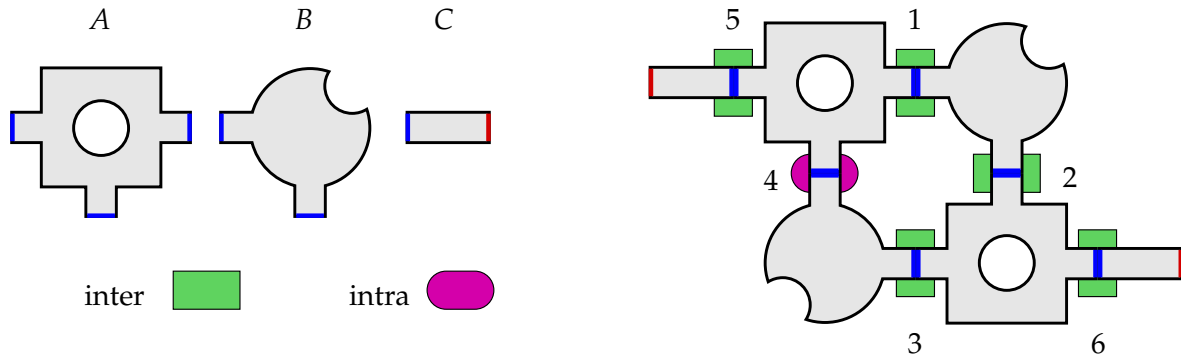


**Figure 4.3:** Assembly of three different module types  $A$ ,  $B$  and  $C$  into a multiterminal looped scatterer (doubly connected on the level of modules) via five inter-connections and one intra-connection. A possible order of connections is indicated by the numbers 1 to 6. Blue boundary segments on the modules indicate internal (inter- or intra-) connection interfaces and red segments denote surface (lead-connected) interfaces. The straight stub module  $C$  is used as a magnetic field adaptation region where the field strength drops to zero outwards. In each inter-connection, the module to be connected (or equivalently the already assembled part) is shifted and rotated into place (so that the blue connection segments match), and its Greenian is accordingly gauge transformed prior to connection. Note that here module  $A$  is already doubly connected and could itself have been assembled by appropriate sub-modules.

are coined *modules*. Since the grid discretization is virtually effectively circumvented, this method allows for wave transport calculations at high energies and magnetic fields [50], but is restricted to structures which are decomposable into analytically solvable subsystems (such as rectangles and (semi-) circles). We will here use the term ‘module’, meaning though a generic part of the system which has not necessarily regular geometry, since our aim will be the study of magnetotransport in devices with the full flexibility of varying geometry parameters at low energies.

Another particular case arises when the total system consists of units which occur repeatedly at different locations. Then, the computation is effectively restricted to the number of different units, since their computed propagators can be reused in the extended recursion. Consider for example the schematic scatterer shown in Fig. 4.3, which consists of three different types of connected modules. One of the modules is a ‘peripheral’ one which forms a lead stub connected to the semi-infinite leads; in the applications to follow, it will serve (being of appropriate length) as the magnetic field adaptation region described in Sec. 3.2.2. The other two modules are of arbitrary geometry/potential and can be connected to any number of arbitrarily placed (vertical or horizontal) leads. With the three module types composing the total structure, we only need to compute the corresponding three individual propagators  $\mathbf{G}_A$ ,  $\mathbf{G}_B$  and  $\mathbf{G}_C$ ; the remaining computational effort comes from the connection between the modules along their interfaces.

### Connectivity: inter- and intra-connection of modules

Note now that the schematic scatterer in Fig. 4.3 is *doubly* connected, that is, the connected modules form a loop in the total system. This gives rise to an implication in applying the standard form of an extended [118, 121] or modular [50, 122] version of the RGF method: Using the matrix Dyson equation (4.63) and its solution, Eqs. (4.65)–(4.68), for two connected modules, the present setup cannot be assembled in the considered modular partitioning connecting the modules one by one over a *single* connection interface in each step. Letting the lead stub modules aside for a moment: We would either have to connect  $A$  and  $B$  into

$AB$  and then connect the two  $AB$ -modules over a double interface, or assemble, say,  $ABA$  and connect it to  $B$ , again over a double interface.

Apart from complicating the implementation of the connection, a larger interface leads to larger computational cost through the matrix inversions involved (which are of the dimension of the interface; see Eq. (4.61)). In order to have only single connections in each step, after *inter*-connecting  $ABA$  to  $B$  over a single interface, we need to *intra*-connect the resulting module  $ABAB$  with *itself* over the interface between the outer (left)  $A$  and  $B$ , as shown in Fig. 4.3. However, in view of the standard Dyson equation for connecting two separate subsystems [121], it is not obvious which paths along the connected structure should now be selected in order to solve for the total propagator elements.

We now present a unified approach for the inter-connection of two modules and intra-connection of a module with itself, based on BGE of correspondingly partitioned  $\tilde{\mathbf{A}}$ -matrix of the total system.

## 4.5.2 Inter-connection

For the case of inter-connection, the grid-represented Hamiltonian  $\mathbf{H}_i$  of each of two modules  $i = 1, 2$  is partitioned into a part describing the section to be connected (denoted  $c$ ) and a part describing the section which remains unconnected (denoted  $u$ ) with respect to the present connection procedure,

$$\mathbf{H}_i = \begin{pmatrix} \mathbf{H}_i^{uu} & \mathbf{H}_i^{uc} \\ \mathbf{H}_i^{cu} & \mathbf{H}_i^{cc} \end{pmatrix}, \quad i = 1, 2, \quad (4.88)$$

where  $\mathbf{H}^{uc} = [\mathbf{H}^{cu}]^\dagger$  is the coupling between them; see Fig. 4.4 (a). Here,  $\mathbf{H}_i^{cc}$  contains matrix elements for the internal scatterer sites along the boundary of the module specified for connection, and  $\mathbf{H}_i^{uu}$  the elements for all other internal sites as well as the surface sites attached to leads or interface sites to be connected to other modules (or to the module itself via intra-connection).

The inter-connection between the two modules is defined through a Hermitian coupling matrix  $\mathbf{W}$  which, in the above partitioning, couples the connection sections ( $c$ ) of  $\mathbf{H}_1$  and  $\mathbf{H}_2$ . The total Hamiltonian matrix describing the connected subsystems then becomes

$$\tilde{\mathbf{H}} = \mathbf{H} + \mathbf{W} = \left( \begin{array}{cc|cc} \mathbf{H}_1^{uu} & \mathbf{H}_1^{uc} & \mathbf{0} & \mathbf{0} \\ \mathbf{H}_1^{cu} & \mathbf{H}_1^{cc} & \mathbf{0} & \mathbf{W}_{12}^{cc} \\ \hline \mathbf{0} & \mathbf{0} & \mathbf{H}_2^{uu} & \mathbf{H}_2^{uc} \\ \mathbf{0} & \mathbf{W}_{21}^{cc} & \mathbf{H}_2^{cu} & \mathbf{H}_2^{cc} \end{array} \right), \quad (4.89)$$

where the blocks  $\mathbf{W}_{12}^{cc}$  and  $\mathbf{W}_{21}^{cc}$  contain the ordinary tight-binding hopping matrix elements  $J_{\alpha\beta}$  (see Eq. (4.20)) corresponding to the sites to be connected (evaluated in a common gauge of the vector potential, as discussed below).

Following the BGE procedure given in App. C.1, the propagator of the connected system

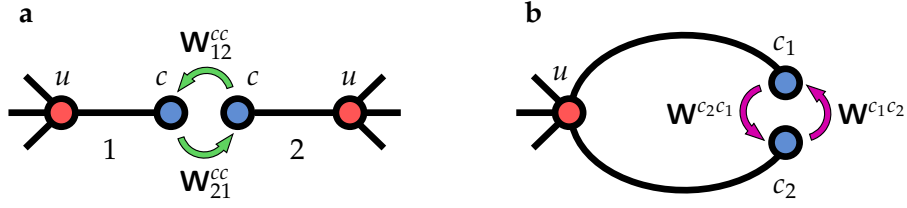


**Figure 4.4:** Inter- and intra-connection of modules represented by lines (propagators of disconnected system) containing the parts  $c$  to be connected and  $u$  to remain unconnected in the present connection. (a) Inter-connection of two modules 1 and 2: The parts  $c$  of the disconnected modules are connected to each other via the coupling  $\mathbf{W}_{12}^{cc} = [\mathbf{W}_{21}^{cc}]^\dagger$ . (b) Intra-connection of a module: The parts  $c_1$  and  $c_2$ , while already indirectly coupled via  $u$ , are directly connected to each other via the coupling  $\mathbf{W}^{c_1c_2} = [\mathbf{W}^{c_2c_1}]^\dagger$ . In both cases, the part  $u$  may contain sections (to be) connected to leads (represented by outgoing lines), to other modules, or to each other.

in terms of the propagators  $\mathbf{G}_1$  and  $\mathbf{G}_2$  of the isolated modules reads

$$\tilde{\mathbf{G}} = \begin{pmatrix} \mathbf{G}_1^{uu} + \mathbf{G}_1^{uc} \tilde{\sigma}_1 \mathbf{G}_1^{cu} & \mathbf{G}_1^{uc} + \mathbf{G}_1^{uc} \tilde{\sigma}_1 \mathbf{G}_1^{cc} & \mathbf{G}_1^{uc} \mathbf{W}_{12}^{cc} \tilde{\mathbf{G}}_{22}^{cu} & \mathbf{G}_1^{uc} \mathbf{W}_{12}^{cc} \tilde{\mathbf{G}}_{22}^{cc} \\ \mathbf{G}_1^{cu} + \mathbf{G}_1^{cc} \tilde{\sigma}_1 \mathbf{G}_1^{cu} & \mathbf{G}_1^{cc} + \mathbf{G}_1^{cc} \tilde{\sigma}_1 \mathbf{G}_1^{cc} & \mathbf{G}_1^{cc} \mathbf{W}_{12}^{cc} \tilde{\mathbf{G}}_{22}^{cu} & \mathbf{G}_1^{cc} \mathbf{W}_{12}^{cc} \tilde{\mathbf{G}}_{22}^{cc} \\ \tilde{\mathbf{G}}_{22}^{uc} \mathbf{W}_{21}^{cc} \mathbf{G}_1^{cu} & \tilde{\mathbf{G}}_{22}^{uc} \mathbf{W}_{21}^{cc} \mathbf{G}_1^{cc} & \mathbf{G}_2^{uu} + \mathbf{G}_2^{uc} \sigma_2 \tilde{\mathbf{G}}_{22}^{cu} & \mathbf{G}_2^{uc} + \mathbf{G}_2^{uc} \sigma_2 \tilde{\mathbf{G}}_{22}^{cc} \\ \tilde{\mathbf{G}}_{22}^{cc} \mathbf{W}_{21}^{cc} \mathbf{G}_1^{cu} & \tilde{\mathbf{G}}_{22}^{cc} \mathbf{W}_{21}^{cc} \mathbf{G}_1^{cc} & \gamma \mathbf{G}_2^{cu} & \gamma \mathbf{G}_2^{cc} \end{pmatrix}, \quad (4.90)$$

where

$$\tilde{\sigma}_1 = \mathbf{W}_{12}^{cc} \tilde{\mathbf{G}}_{22}^{cc} \mathbf{W}_{21}^{cc} = \mathbf{W}_{12}^{cc} \gamma \mathbf{G}_2^{cc} \mathbf{W}_{21}^{cc}, \quad (4.91)$$

with

$$\gamma = (\mathbf{I}^{cc} - \mathbf{G}_2^{cc} \sigma_2)^{-1}, \quad \sigma_2 = \mathbf{W}_{21}^{cc} \mathbf{G}_1^{cc} \mathbf{W}_{12}^{cc}. \quad (4.92)$$

The matrix  $\sigma_2$  is here the self-energy of module 2 due to the coupling to module 1, in analogy to the case where subsystem 1 is a semi-infinite lead. Note that the subsystems 1 and 2 are equivalent with respect to the connection, and the form of  $\tilde{\mathbf{G}}$  simply results from a ‘lower-major’ elimination order of  $\tilde{\mathbf{A}}$  (see App. B). In other words,  $\tilde{\mathbf{G}}$  is invariant under simultaneous exchange of indices ( $1 \leftrightarrow 2$ ) and (left  $\leftrightarrow$  right) block-columns and (upper  $\leftrightarrow$  lower) block-rows.

Note also that  $\tilde{\mathbf{G}}$  in the present form is nested, in the sense that  $\tilde{\mathbf{G}}_{22}^{cc} = \gamma \mathbf{G}_2^{cc}$  is (indirectly) present in the other blocks  $\tilde{\mathbf{G}}_{ij}^{xy}$  ( $i, j = 1, 2, x, y = u, c$ ). This dictates the following order in the computation of the surface part of the connected propagator, starting with  $\sigma_2$ :

$$\begin{aligned} \sigma_2 &\longrightarrow \gamma &\longrightarrow \tilde{\mathbf{G}}_{22}^{cc}, \tilde{\mathbf{G}}_{22}^{cu} &\longrightarrow \tilde{\sigma}_1, \tilde{\mathbf{G}}_{22}^{uc}, \tilde{\mathbf{G}}_{22}^{uu} \\ & & &\longrightarrow \tilde{\mathbf{G}}_{ij}^{uu}, \end{aligned} \quad i, j = 1, 2. \quad (4.93)$$

Thus, six matrix multiplications and a single matrix inversion of the dimension of the connection interface need to be performed to arrive at  $\tilde{\sigma}_1$ , and then further matrix multiplications are needed depending on the part of the propagator required.

The connected system propagator  $\tilde{\mathbf{G}}_{qp}$  from lead  $p$  to lead  $q$  (which might be attached to the same module or the connected one) is contained in  $\tilde{\mathbf{G}}_{ij}^{uu}$ . If only the transmission is needed, then only the surface section  $u_\sigma$  of the unconnected parts  $u$  need to be considered (discarding the interior sections  $u_i$ ). If also the LDOS (or wave function) is needed, then the parts  $\tilde{\mathbf{G}}_{ij}^{u_i u_\sigma}$  and  $\tilde{\mathbf{G}}_{ij}^{u_\sigma u_i}$  are required.

### Gauge transformation of the Green function

Note that connecting two modules, whose separate propagators were computed in their individual coordinate systems, implies that one of the modules is *shifted* and *rotated* so that the  $c$ -sites along its boundary, to be connected, become adjacent to the corresponding ones of the other module. In fact, the modules are no longer ‘real grid’ modules, in the sense that there is no specific coordinate system associated with the modules in the process of connecting them (the matrix  $\tilde{\mathbf{H}}$  is never set up explicitly); they are abstractly represented by their propagators  $\mathbf{G}_1$  and  $\mathbf{G}_2$ . However, the shift and rotation of, say, module 2 to match module 1 at the connection interface requires a *gauge transformation* to be applied to  $\mathbf{G}_2$ , so that the new gauge matches the gauge in which  $\mathbf{G}_1$  was computed (and no artificial magnetic field components are introduced at the interface). The explicit form of this gauge transformation is derived in App. D. The coupling elements in  $\mathbf{W}$  are then determined according to the common gauge (coinciding with that of  $\mathbf{G}_1$  in this example).

#### 4.5.3 Intra-connection

For the case of intra-connection, the Hamiltonian  $\mathbf{H}$  of a single module is partitioned into a part  $u$  describing the section which remains unconnected and two parts  $c_1$  and  $c_2$  describing the sections to be connected in the present connection procedure; see Fig. 4.4 (b). The interface sections  $c_1$  and  $c_2$  must be of equal size and the sites of  $c_1$  must be pairwise nearest neighbors with the sites of  $c_2$  on the tight-binding lattice. Upon connection, they are coupled through a Hermitian matrix  $\mathbf{W}$  contributing blocks  $\mathbf{W}^{c_1c_2} = [\mathbf{W}^{c_2c_1}]^\dagger$  to the total Hamiltonian of the connected module which reads

$$\tilde{\mathbf{H}} = \mathbf{H} + \mathbf{W} = \left( \begin{array}{c|cc} \mathbf{H}^{uu} & \mathbf{H}^{uc_1} & \mathbf{H}^{uc_2} \\ \hline \mathbf{H}^{c_1u} & \mathbf{H}^{c_1c_1} & \mathbf{W}^{c_1c_2} \\ \mathbf{H}^{c_2u} & \mathbf{W}^{c_2c_1} & \mathbf{H}^{c_2c_2} \end{array} \right). \quad (4.94)$$

Here,  $\mathbf{H}^{c_i c_i}$  contains the matrix elements for sites along side  $i$  of the connection interface and  $\mathbf{H}^{uu}$  the elements for all other internal sites, surface (lead-connected) sites, or connection interface sites to be connected in another connection procedure.  $\mathbf{H}^{uc_i} = [\mathbf{H}^{c_i u}]^\dagger$  ( $i = 1, 2$ ) couples the interior of the module as well as any surface sites to the present connection interface.  $\mathbf{W}$  again contains simply the tight-binding hopping matrix elements  $J_{\alpha\beta}$  for the nearest neighbor connection sites on each side of the interface. Note that, since the connection interface sections are here (neighboring) sections of one and the same module, there is obviously no need to shift or rotate any module part, and thus no need for a gauge transformation of any of the propagators  $\mathbf{G}^{uu}$ ,  $\mathbf{G}^{uc_i}$  etc. of the disconnected module, since they are already in the same gauge.

The disconnected module Hamiltonian  $\mathbf{H}$  is here not block-diagonal, and so the corresponding Greenian  $\mathbf{G}$  is generally already a full matrix describing the propagation between all sections  $u$ ,  $c_1$  and  $c_2$ . It is thus expected that some more matrix algebra, in the form of matrix inversion, will be needed to solve the Dyson equation associated with the connected module. The derivation given in App. C.2 now yields the following propagator of the connected module in terms of the disconnected module propagator (having set  $c_i \rightarrow i$

for brevity):

$$\tilde{\mathbf{G}} = \left( \begin{array}{c|cc} \mathbf{G}^{uu} + \tilde{\mathbf{G}}_W^{uu} & \mathbf{G}^{u1} + \tilde{\mathbf{G}}_W^{u1} & \mathbf{G}^{u2} + \tilde{\mathbf{G}}_W^{u2} \\ \hline \theta(\mathbf{G}^{1u} + \mathbf{G}^{11}\mathbf{W}^{12}\tilde{\mathbf{G}}^{2u}) & \theta(\mathbf{G}^{11} + \mathbf{G}^{11}\mathbf{W}^{12}\tilde{\mathbf{G}}^{21}) & \theta(\mathbf{G}^{12} + \mathbf{G}^{11}\mathbf{W}^{12}\tilde{\mathbf{G}}^{22}) \\ \lambda(\mathbf{G}^{2u} + \mathbf{G}^{22}\mathbf{W}^{21}\theta\mathbf{G}^{1u}) & \lambda(\mathbf{G}^{21} + \mathbf{G}^{22}\mathbf{W}^{21}\theta\mathbf{G}^{11}) & \lambda(\mathbf{G}^{22} + \mathbf{G}^{22}\mathbf{W}^{21}\theta\mathbf{G}^{12}) \end{array} \right), \quad (4.95)$$

using the shorthand notation

$$\tilde{\mathbf{G}}_W^{uz} = \mathbf{G}^{u1}\mathbf{W}^{12}\tilde{\mathbf{G}}^{2z} + \mathbf{G}^{u2}\mathbf{W}^{21}\tilde{\mathbf{G}}^{1z}, \quad (z = 1, 2, u) \quad (4.96)$$

where

$$\theta = [\mathbf{I} - \mathbf{G}^{12}\mathbf{W}^{21}]^{-1}, \quad (4.97)$$

$$\lambda = [\mathbf{I} - \mathbf{G}^{21}\mathbf{W}^{12} - \mathbf{G}^{22}\mathbf{W}^{21}\theta\mathbf{G}^{11}\mathbf{W}^{12}]^{-1}. \quad (4.98)$$

Again, the block-matrix  $\tilde{\mathbf{G}}$  follows the symmetry of  $\tilde{\mathbf{H}}$  under simultaneous index exchange ( $1 \leftrightarrow 2$ ) and block-column/row permutations.

We now indeed have two matrix inversions of the dimension of the connection interface in total instead of one, together with six matrix multiplication of the same dimension to arrive at  $\lambda$ . Like in the inter-connection case, there is an ordered procedure to obtain the surface propagator, now starting with  $\theta$ :

$$\begin{array}{ccccccc} \theta & \longrightarrow & \lambda & \longrightarrow & \tilde{\mathbf{G}}^{2u}, (\tilde{\mathbf{G}}^{21}), (\tilde{\mathbf{G}}^{22}) & \longrightarrow & \tilde{\mathbf{G}}^{1u}, (\tilde{\mathbf{G}}^{11}), (\tilde{\mathbf{G}}^{12}) \\ & & & & & & \longrightarrow & \tilde{\mathbf{G}}^{uu}, (\tilde{\mathbf{G}}^{u1}), (\tilde{\mathbf{G}}^{u2}) \end{array} \quad (4.99)$$

where the blocks in brackets are additionally to be computed to obtain internal properties (LDOS).

The connected system propagator  $\tilde{\mathbf{G}}_{qp}$  from lead  $p$  to lead  $q$  (which might be attached to the same module or the connected one) is contained in  $\tilde{\mathbf{G}}_{ij}^{uu}$ . If only the transmission is needed, then only the surface section  $u_\sigma$  of the unconnected parts  $u$  need to be considered (discarding the interior sections  $u_i$ ). If also the LDOS (or wave function) is needed, then the parts  $\tilde{\mathbf{G}}_{ij}^{u_i u_\sigma}$  and  $\tilde{\mathbf{G}}_{ij}^{u_i u_\sigma}$  are required.

#### 4.5.4 Computational efficiency and considerations

From the above it becomes clear that, for a typical composite setup consisting of connected modules, the total computational cost is essentially determined by the number of *different* modules used in the assembly. Once the computation of all necessary elimination steps in the bulk of a module have been carried out pertaining to its propagator, then the latter can be reused with the relatively very small cost of operations of the dimension of its connecting interface to another module. Thus, if the absolute number of modules participating in the total structure is small enough (i. e., if the number of connection interface operations is negligible compared to the total number of internal slice operations), then the cost for computing the surface propagator will scale as

$$C_{\text{mod}} \propto 6 f \sum_{m=1}^M \sum_{s=1}^{N_s^m} [N_r^{(s)}]^3, \quad N_s^m \gg 1, \quad (4.100)$$

where  $M$  is the number of different modules used and  $N_s^m$  is the (average) number of slices in the  $m$ -th of these modules. The preliminary task for a given transport device geometry is therefore to identify in which way the total structure can be decomposed into as few different modules as possible, though each with the smallest possible size.

As mentioned above in reference to the schematic in Fig. 4.3, a composite structure could in general be assembled by means of inter-connections only, though over multiple connection interfaces (for example, by connecting modules  $A$  and  $B$  in Fig. 4.3 first and then perform connections 2 and 4 in a single inter-connection step over the double interface). However, for larger number of connected modules, such multiple interfaces will increase in total size rendering their one-step connection inefficient. More importantly, this alternative reduces the flexibility in assembling diverse setups from a set of modules: only fixed groups of combined modules would be available as building blocks (like the fixed group  $AB$  in the above example). Such a specialized connection protocol could be useful when assembling a uniform lattice of identical modules, by connecting modules into a row (over single interfaces) and then rows to each other (over multiple interfaces). With the use of intra-connections, modules are added one at a time and can be chosen freely from the set of different modules as long as their interfaces match (in Fig. 4.3, for example, we could have put module  $B$  on the lower right in the place of  $A$ ). A useful application thereof could be the insertion of modules with prescribed defects at desired positions in a composite structure such as a quantum dot lattice. In total, the developed scheme of combined inter- and intra-connections thus provides a high flexibility in assembling multiterminal and multiply connected transport structures of high diversity.

## 4.6 Transport through multiterminal and multiply connected billiard systems

We close this chapter with an exemplifying demonstration of the use of the developed computational techniques on a multiterminal quantum billiard which is then multiply connected into a multiterminal composite structure, for varying input energy  $E$  and applied magnetic field  $B$ . For the single billiard we briefly analyze the origin of the transmission features and the impact of a magnetic field on the mode-resolved transmission coefficients. The multiterminal transmission of the looped transport device is not directly relevant for the controllable (and thereby desirably smooth in parameter variations) conductance profiles aimed at in the following chapters. It rather serves to illustrate the very complex transmission features that may typically arise from the combination of Fano and AB interference processes, but also gives the opportunity to explore spatial electron density patterns at individual  $(E, B)$ -points.

### 4.6.1 Single three-terminal elliptic billiard

As a building block of the composite system we choose a tilted elliptically shaped hard-wall billiard with two horizontal and one vertical attached leads of equal width  $w$ , as shown in the upper inset of Fig. 4.5. The orientation and positioning of the lead openings are chosen such that one and the same scatterer can be easily used repeatedly as a module for inter- and intra-connections later.

For this single multiterminal billiard we compute the mode-resolved transmission coefficients  $T_{qp}^{nm}$  from (lead, mode) =  $(p, m)$  to  $(q, n)$  for energies in the first three open channels of the leads, at zero and finite field strength, as shown compactly in Fig. 4.5. The energy variable is here scaled into a dimensionless total incoming momentum  $\kappa = kw/\pi = \sqrt{2E}w/\pi$  (recall that  $\hbar = m^* = 1$  in our natural units; see Table E.1).

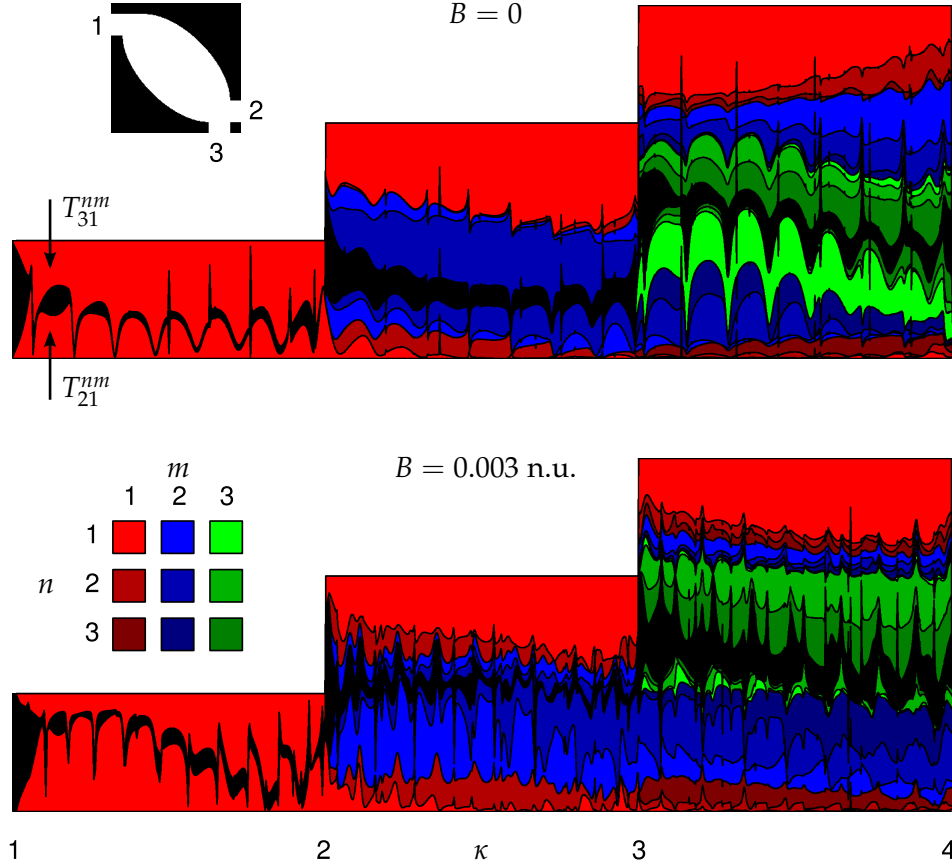


**Figure 4.5:** Mode resolved transmission as a function of  $\kappa = k w / \pi$  through a three-terminal tilted elliptic billiard (upper inset) with semi-axes  $(a, b) = (100, 52)$  and common lead width  $w = 32$  grid points, at  $B = 0$  (upper panel) and  $B = 0.003$  n.u. (lower panel). The lower inset shows the color code for transmission from mode  $m$  to mode  $n$  which are open for propagation for  $\kappa > m, n$ . In each panel,  $T_{21}^{nm}$  is plotted from below and  $T_{31}^{nm}$  is plotted from above, with the black area in the middle representing the total (summed over all modes) reflection  $R_1 = \sum_{m,n} T_{11}^{nm} = T_{11}$  back to the incoming lead 1. The sum  $R_1 + T_{21} + T_{31}$  increases by unity for each new open mode  $n$  at  $\kappa = n$ .

The modular version of the RGF technique with inter-connections comes in handy already for the single scatterer in the transmission computation at finite magnetic field: The scatterer module is inter-connected at each interface to a finite and straight lead module (not shown) along which the magnetic field drops off to zero over an appropriate length (large enough for the transmission results to have converged) and which is in turn connected to the outer semi-infinite leads through the contribution of corresponding (zero-field) self-energies. Upon each inter-connection to the lead module, the Green function of the already assembled part is gauge-transformed into the axial gauge of the lead module as described previously.

### Regular response from geometric focusing

Let us first concentrate on the first open channel with the single-mode transmission coefficients  $T_{21}^{11}$  (plotted from below in each plot) and  $T_{31}^{11}$  (plotted from above, such that the black region in between represents the reflection coefficient  $R_1 = T_{11}^{11}$ ). We see that the transmission lineshape of  $T_{21}^{11}$  for  $B = 0$  varies rather smoothly in energy with a regular oscillation within a low envelope, apart from occasional superimposed very sharp dips and peaks. This is not a universal transmission feature, but relies on the chosen elongated shape

of the hard-wall billiard together with the positioning of leads 1 and 2: As will be demonstrated in Chap. 5 for oval billiards, the elongated shape causes a geometric separation of energetically available states within the billiard into states that are strongly coupled to the leads (with amplitude that ‘leaks’ into them) and those that are very weakly coupled to the leads (because of their confinement away from the lead openings). The former type of states interfere with each other leading to the smooth oscillation of the background, and the latter constitute long-lived quasi-bound states whose (weak) coupling to the continuum results in sharp Fano resonances in the transmission lineshape. Note that, since the setup with attached leads has no mirror symmetry, and thereby no parity eigenstates in the direction transverse to any pair of attached leads, in principle all energetically available eigenstates of the isolated billiard contribute here to transmission.

### Boundary guiding

The transmission  $T_{31}^{11}$  to lead 3 is complementary to  $T_{21}^{11}$  in the chosen setup: The reflection back into lead 1 is overall small (apart from energies at the lower threshold), so that any probability flux not going into lead 2 leaves through lead 3<sup>14</sup>. This is again due to the design of the setup: Leads 1 and 3 constitute a continuation of the upper convex boundary of the ellipse, and therefore a wave incident in lead 1 is ‘guided’ along the smooth boundary into lead 3. This mechanism will be exploited in Chap. 7 to achieve directional magneto-transport in a four-terminal device. In the present setup, boundary guiding is disturbed by the presence of lead 2, whose sharp openings (and especially the lower right corner) cause strong diffraction of the guided wave back into the cavity.

The Fano resonance dips and peaks in  $T_{31}^{11}$  are also complementary to those in  $T_{21}^{11}$ ; it is clear that, since leads 2 and 3 are closely placed at the far end of the billiard, confined quasi-bound states will have similar coupling strengths to those leads and thereby similar resonant shifts and widths. Note, however, that the Fano minima are lifted from zero, since the two output leads effectively provide two different scattering channels (already in the first energy subband of the leads) for the quasi-bound states to couple to and lead to a complex asymmetry parameter; see Sec. 3.4.1 and Refs. [40, 65].<sup>15</sup> For the same reason, the Fano maxima do not reach unity. Essentially, each lead constitutes a source of decoherence due to dissipation for the transmission between the other two [213].

### Magnetically dependent multimode coupling

In the second and third transport channels of the leads,  $2 < \kappa < 4$ , the zero-field transmission  $T_{21}^{n1}$  in the first mode of leads 1 and 2 is almost completely suppressed, and transmission is mediated by higher common modes ( $T_{21}^{22}$  and  $T_{21}^{33}$ ) but also by cross-mode coupling; especially  $T_{21}^{13}$  is enhanced in the third channel  $3 < \kappa < 4$  (light green in upper panel of Fig. 4.5). On the contrary, the first mode transmission  $T_{31}^{11}$  to lead 3 remains high throughout all channels: it has the largest longitudinal momentum in the ingoing lead 1 and is thus less affected by diffraction when guided along the upper billiard boundary. Additionally, there is large contribution from higher modes to  $T_{31}$  in the higher channels.

The effect of an applied magnetic field on the transmission spectra is twofold: It modulates the AB-like phase interference between transmitting states of the billiard, and simultaneously gives rise to Lorentz deflection of the spatial density distribution if the field is strong enough. We have here chosen a moderate field  $B = 0.003$  n.u. corresponding to a

---

<sup>14</sup> Note that conservation of flux implies  $T_{21}^{11} + T_{31}^{11} + R_1 = 1$  in the first channel.

<sup>15</sup> The resolution in this transmission spectrum is not fine enough to resolve all Fano resonances, and the ones that are visible are also not resolved in full detail.

cyclotron radius  $r_c \approx b$  at the center  $\kappa = 1.5$  of the first channel, where  $b$  is the minor ellipse semi-axis.

In the first channel, the combination of the two effects causes an increased transmission  $T_{21}^{11}$  in the lower half of the channel, while  $T_{31}^{11}$  there becomes suppressed and vice versa. This can be understood qualitatively as the dominance of a skipping orbit which first matches the distance to lead 2 and then skips over to lead 3 when energy increases, although it should be noted that such classical descriptions have only a very rough correspondence to the quantum result at the low energies considered. In the second channel, the partial transmission  $T_{q1}^{m2}$  from mode 2 (blue area) is almost completely transferred from lead 3 to lead 2 when the field is switched on, while the total lowest mode components (red area) remain largely intact. In the third channel, although the *total* transmission coefficients  $T_{21}$  and  $T_{31}$  are not much affected on average by the field, there is a drastic redistribution of the partial coefficients that contribute: Switching on the field suppresses completely the transmission from mode 3 into lead 2 ( $T_{21}^{m3}$ , green areas) and from mode 2 into lead 3 ( $T_{31}^{m2}$ , blue areas).

The multiterminal linear-response conductance of the device is proportional to the total transmission functions summed over all contributing modes. The above mode-resolved analysis, however, provides insight into what components of the scattering matrix actually contribute and how these are affected by the applied field. This in turn adds to an understanding of what processes in the billiard area are responsible for transport, which can be also be useful in applications. In the present setup, for example, an additional transversal constriction could be applied to the incoming lead 1 such that only the third mode is let through. Then, only the  $T_{qp}^{m3}$  (green areas) partial coefficients would be non-zero and, according to the above, the chosen field would switch the conductance from finite to zero in the third channel.

#### 4.6.2 Transmission and localization patterns in a looped multiterminal structure

We now use the previous three-terminal elliptic billiard as a building block to assemble a composite structure of eight identical ellipses doubly connected into the structure shown in the inset of Fig. 4.6 (a). The connected structure consists of two large loops, each containing the two ellipses on the upper and lower arm, which are further connected via a smaller loop in the middle. The assembly is done in analogy to the procedure in Fig. 4.3, using here three intra-connections (since we have three loops in total), with connecting ‘bridges’ between the ellipses of common length  $d = w$ .<sup>16</sup> Note that, apart from the peripheral lead modules which are used as magnetic field adaptation regions (not shown), we here actually have two different modules to compute, the three-terminal ellipse and its mirror image with respect to the  $x$ -axis (vertical). This is because, in the presence of magnetic field, the propagators of mirror images are not equivalent and cannot be obtained by gauge transformation through shift and/or rotation. With the above setup specifications, the multiply connected modular RGF method was applied to compute the multiterminal surface propagator and extracted the transmission coefficients for an  $(E, B)$  grid of (1400, 2001) points. The average CPU time with the modular connection algorithm was  $\approx 1.72$  s per point on a modern quad-

<sup>16</sup> We have here in fact also separated the lead stubs from the previous three-terminal module, which now serve as separate bridge modules, in order to be able to vary the bridge length without re-computing the ellipse module. This increases the number of inter-connections in the assembly, but does not practically affect the computation time.

core processor.<sup>17</sup> In comparison, the corresponding average CPU time for the composite structure computed directly as a *single* large module (including the long magnetic field adaptation stubs at the outer leads) is  $\approx 22.70$  s, more than 10 times longer, demonstrating the performance advantage of the modular inter- and intra-connection algorithm.

The transmission function of the structure from lead 1 (upper left) to lead 2 (upper right) and to lead 4 (lower right) within the first channel  $1 < \kappa < 2$  is plotted in the central panels of Fig. 4.6 (a) and (b), respectively, for the magnetic field in both  $\pm z$ -directions with field strength varying in the interval  $0 < |B| < 0.01$  n.u.. We refer to these plots of  $T_{qp}(B, \kappa)$  as transmission maps.

### Regimes of magnetotransport

Although the transmission maps contain irregular detail features, to be addressed next, there is an overall large-scale structure which is typical and qualitatively similar for most coherent transport devices.

For low magnetic field strengths, the maps are dominated by multi-state interference in varying field and energy which leads to complicated and non-universal features depending on the geometry of the device (on the present case, of the individual connected billiards).

For intermediate fields the Lorentz deflection of the electron paths becomes dominant, which leads to a large-scale stripe-like pattern (within the V-like area between the points  $(B, \kappa) = (0, 0)$  and  $(\max, \pm\max)$ ). For a hard-wall structure, the stripes have approximately constant slope and are characteristic of the commensurability between the bouncing of (qualitatively associated) skipping orbits and the distance between lead openings: For higher energy, a stronger magnetic field is needed to maintain a skipping orbit escaping through a given output lead. This regime is thus largely determined by the lead positioning along the billiard boundaries.

For even stronger field we enter the edge-state regime, where transmission is determined by the topology of the structure: Independently of the detailed geometry of a hard-wall flat billiard (with zero potential inside), an edge state will be mostly transmitted into the next encountered lead on the boundary. As explained in Sec. 1.3, edge states have their origin in Landau levels which become dispersive in the vicinity of a boundary. In the  $T_{qp}(B, \kappa)$ -maps they are recognized as transmission stripes with slope opposite to  $B$  (visible here in the lower part  $1 < \kappa < 1.25$  of the channel): Their energy is lowered with increasing field strength until they ‘condense’ into bulk Landau levels [49] whose energy then increases with the field strength. For the present setup, we see that  $T_{21}$  is overall maximal ( $\rightarrow 1$ ) in the edge-state area between the first and second Landau level on the right side of the map in Fig. 4.6 (a). At low energies there is, however, a small portion of the edge states transmitted into lead 4, as seen in the bottom part of the map in Fig. 4.6 (b).<sup>18</sup>

### Fano and Aharonov-Bohm interference

The resolution of the computed transmission maps is high enough to discern the fine structure of the transmission features in varying energy and magnetic field which arise from the

---

<sup>17</sup> This is about twice the time  $\approx 0.75$  s needed for each ellipse module (the original one and its mirror image) plus some additional time  $\approx 0.31$  s for a 1024 gridpoints long magnetic field adaptation module intervening between the billiard and each attached lead.

<sup>18</sup> Note here that, due to the geometrical  $x$  and  $y$  mirror symmetry (or symmetry under an in-plane rotation through  $\pi$ ) of the setup, transmission between leads 1 and 4 is symmetric in  $B$ ,  $T_{41}(B) = T_{41}(-B)$ . This is a consequence of the reciprocity relation  $T_{41}(-B) = T_{14}(B)$  and the fact that the symmetry operation exchanging leads 1 and 4 brings  $B \parallel \hat{z}$  to itself.

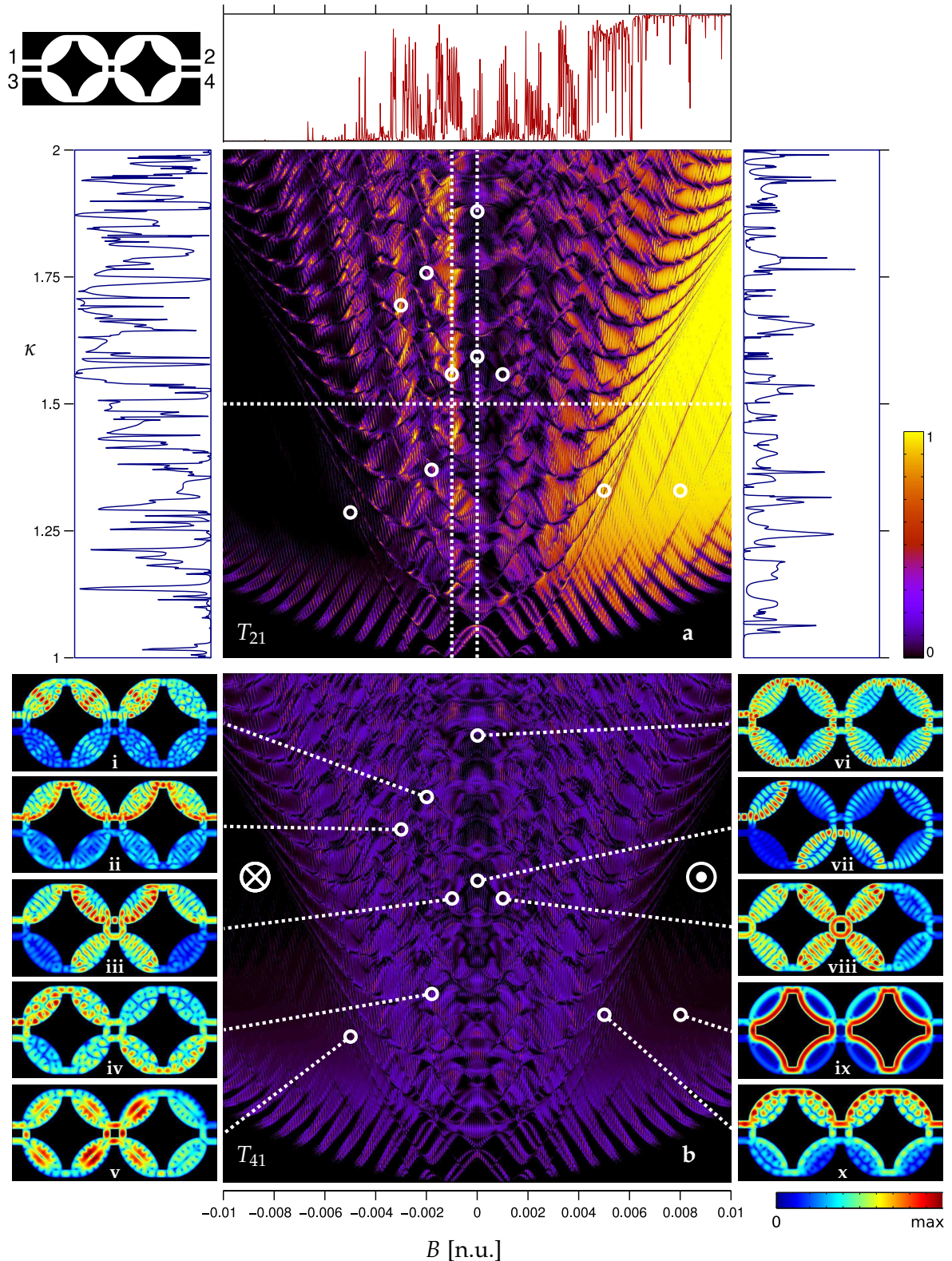


**Figure 4.6:** Transmission maps (a)  $T_{21}(B, \kappa)$  and (b)  $T_{21}(B, \kappa)$  in the first channel  $1 < \kappa < 2$  (1400 points) and at magnetic field strengths  $-0.01 \leq B \leq 0.01$  n.u. (2001 points), for the four-terminal structure shown in the upper inset composed of the three-terminal billiard of Fig. 4.5 connected via bridges of common length  $l = w$ . The upper, right and left panels in (a) show  $T_{21}(B, \kappa)$  along the cuts  $(B, \kappa = 1.5)$ ,  $(B = -0.001, \kappa)$  and  $(B = 0, \kappa)$  through the maps, respectively, indicated by dotted lines. The panels (i)–(x) on the left and right of (b) show the LDOS for an incoming wave in the upper left lead 1 of the setup at the  $(B, \kappa)$ -points indicated in the transmission maps, with the colormap normalized to the maximum in each subplot and scaled as  $\sqrt{\rho(x, y)}$  to increase contrast.

geometry and topology of the composite structure. These are determined by the Fano interference between quasi-bound states of each of the connected billiards in varying energy, and by the AB interference along the various closed paths present in the looped topology.

The energy dependence of the  $T_{21}$  is more clearly seen in the vertical cuts through the map at zero field and at a finite negative (pointing inwards) field, shown on the right and left panels of Fig. 4.6, respectively. In the connected system, the resonant states of the individual elliptic dots are coupled through the connecting bridges and therefore the corresponding sharp Fano resonances in energy are multiply split, with the splitting proportional to the strength of this inter-dot coupling. The background transmission is also affected by developing additional shape resonances due to multiple reflection within the bridges. This effect will be studied in more detail in Chap. 5 for a singly connected dot array, where these shape (or Breit-Wigner) resonances form transmission bands with increasing number of connected dots. In the present setup the multiple connectivity leads to a highly irregular transmission function compared to the one of the single billiard of the previous subsection. This is because both transmission profiles  $T_{21}^s$  and  $T_{31}^s$  of the single billiard are effectively present in any path taken between leads of the composite system, and thus the corresponding features are mixed in the final output  $T_{21}$ .

The field strength dependence of the transmission coefficients is characterized by a superposition of AB oscillations with dominant frequencies corresponding to the approximate area of the loop structures in the setup (note that any pair of neighboring loops also forms a further larger loop). In particular, the larger loops containing the elliptic dots give rise to the very fine vertical stripes which are present essentially over the whole map. The details of this superimposed AB interference pattern varies along the  $\kappa$ -axis due to the energy dependence of the dot states leaking into the connecting bridges, as discussed previously in Sec. 3.4.2. The upper panel in Fig. 4.6 (a) shows  $T_{21}(B)$  at the middle  $\kappa = 1.5$  of the channel, where the fine oscillations are seen on top of the larger transmission feature in the intermediate field regime. AB oscillations also arise in the strong-field regime from the interference between (effectively 1D) edge states [49] which is caused by their diffraction [50] at abrupt changes (corners in the present setup) of the confining boundary. An applicational perspective of the multiply connected RGF method developed is the study of such AB oscillations in extended lattices (or networks) of loops with internal structure.

### Density localization patterns

The rather complex features of the transmission maps of the particular looped setup simulated here do not contribute to the controllable conductance aimed at in the following chapters. However, it provides a means to study the controllability of the electronic *spatial distribution* among the constituent dots of the structure. In the panels (i)-(x) of Fig. 4.6 the partial LDOS for an incoming wave in lead 1 (upper left) of the device is shown for different points in  $(B, \kappa)$ -space, computed via the reordered BGE scheme of Sec. 4.4.3. We see that, depending on the regime of energy and magnetic field, different kinds of localization patterns can be induced.<sup>19</sup> States (i), (iii), (iv), (v), (viii), for example, are dominantly localized in the interior of the constituent ellipses, though each in a different constellation along the loops—state (viii) additionally shows a strong localization on the central small connecting loop. States (ii), (vi), (vii), (ix) and (x) are primarily localized along the boundaries of the ellipses. The latter two are examples of edge state propagation; in (x), different edge states interfere into a skipping-like pattern leading to AB oscillations in the transmission (see correspond-

---

<sup>19</sup> To have a qualitative picture of the effect of moderate to strong fields, recall that classical trajectories are deflected anticlockwise for  $B > 0$  and clockwise for  $B < 0$ .

ing point in the upper map  $T_{21}(B, \kappa)$ ; in (ix), a single edge state transmits completely from 1 to 2, though after ‘hopping’ (at the narrow input constriction) onto the inner boundary of the loops where it builds up a high density. State (vi) displays the wave guiding caused by the convex elliptic boundary alone (at zero magnetic field), which extends onto both outer loops. Finally, an interesting non-local pattern is induced in state (vii), also at zero field: The incoming wave populates the boundary of the first encountered dot and the remote lower central dots, though with almost completely depleted density in between. With the above patterns for this small looped structure at hand, further explorations could reveal possible manipulation of localized electron waves in larger looped networks with embedded dot structures.



# Magnetoconductance switching by phase modulation in arrays of oval quantum billiards

In this chapter we employ oval shaped quantum billiards connected by quantum wires as the building blocks of a linear quantum dot array which allows for the control of magnetoconductance in the linear response regime. In particular, we aim at a maximal finite- over zero-field ratio of the magnetoconductance, achieved by optimizing the geometry of the billiards. The switching effect arises from a relative phase change of scattering states in the single oval quantum dot through the applied magnetic field, which lifts a suppression of the transmission characteristic for a certain range of geometry parameters. A sustainable switching ratio is reached for a very low field strength, which is drastically enhanced already in the double-dot array. The impact of disorder is addressed in the form of remote impurity scattering, which poses a temperature dependent lower bound for the switching ratio. The results are partially published in Ref. [246]

## 5.1 System setup, approximations and computational approach

We consider a linear array of identical oval billiards connected via bridges of common length, as shown in Fig. 5.1. The confining potential of the structure is taken to be of hard-wall character, leading to Dirichlet boundary conditions for the wave function, with zero potential inside. The shape of an individual oval billiard is parametrized as [247]

$$\begin{aligned} x(\phi) &= R \left[ \left( \frac{\delta}{2} + 1 \right) \sin(\phi) + \frac{\delta}{6} \sin(3\phi) \right], \\ y(\phi) &= R \left[ \left( \frac{\delta}{2} - 1 \right) \cos(\phi) - \frac{\delta}{6} \cos(3\phi) \right], \end{aligned} \quad (5.1)$$

with  $0 \leq \phi < 2\pi$ ; note that the parametric curve starts at  $(x, y) = (0, -R(1 - \delta/3))$ . The parameter  $\delta$  tunes the deformation of the dot, which becomes a circular billiard of radius  $R$  if  $\delta = 0$ . In this case the classical dynamics of the closed system is integrable, whereas for  $\delta > 0$  it becomes non-integrable with mixed phase space [247, 248]. For reference with respect to device specific parameters, a mesoscopic size of  $R = 220$  nm is used. For the single dot setup, at the right and left ends of the elongated structure semi-infinite leads of width  $w = 0.3 R$  are connected along the  $x$ -axis, representing the coupling to electron reservoirs. The use of semi-infinite leads models the ideal case of vanishing reflection of the electrons upon reaching the reservoirs.

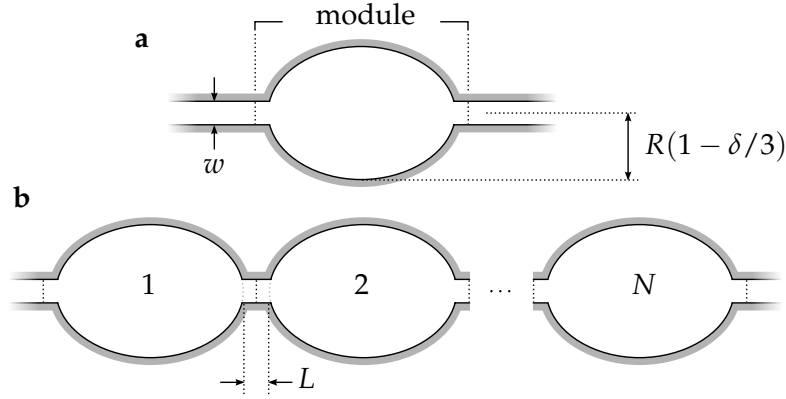


**Figure 5.1:** Geometry of the model hard-wall potential for (a) a single billiard attached to semi-infinite leads and (b) an array of  $N$  connected billiards, with  $L = w = 0.3 R$  and oval deformation parameter  $\delta = 0.5$ .

In the multidot case, the single cavity is replaced by a chain of  $N$  identical oval dots connected to each other through lead bridges of common length  $L$  between adjacent oval edges, as shown in Fig. 5.1. The bridges have width  $w$  and are aligned with the outer semi-infinite leads.

Restricting ourselves to low temperatures and a small system size we neglect inelastic processes, and do not account for electron-electron or electron-phonon interactions. The single particle Hamiltonian is, within an effective mass approach, of the form

$$\mathcal{H} = \frac{1}{2m^*} \left[ \frac{\hbar}{i} \nabla + e\mathbf{A}(\mathbf{r}) \right]^2 + V(\mathbf{r}), \quad (5.2)$$

where an effective electron mass  $m^* = 0.069 m_e$  is chosen corresponding to a GaAs/AlGaAs heterojunction.  $V(\mathbf{r})$  is the total electrostatic potential comprised of the hard-wall boundary of the structure as well as the potential induced by impurities to be included later. The vector potential  $\mathbf{A}$  produces a magnetic field perpendicular to the plane of the structure (pointing in the positive  $z$ -direction). The field extends homogeneously with strength  $B$  in the device region and drops off linearly to zero in the outer leads; the length of the magnetic field adaptation region is chosen long enough to effectively simulate an overall homogeneous field. We will concentrate on the magnetoconductance switching effect at a very low magnetic field strength ( $\sim 0.02$  T), where the Zeeman splitting for GaAs ( $\sim 3.6 \mu\text{eV}$ ) is negligible ( $\sim 0.1\%$ ) with respect to the Fermi energies we consider; thereby the coupling of the electronic spin to the magnetic field is not taken into account. The weak spin-orbit coupling of the simulated heterostructure is also neglected.

The transmission through the device and the LDOS within it are determined from the single particle Greenian

$$\mathcal{G}(E) = [E - (\mathcal{H} + \Sigma_r + \Sigma_l)]^{-1} \quad (5.3)$$

of the system at energy  $E$  after discretizing the Hamiltonian on a square tight-binding lattice, with the magnetic vector potential incorporated through Peierls phase factors [240, 241] (see Sec. 4.2.1). The self-energies  $\Sigma_{l/r}$  account for the coupling of the truncated system to the external semi-infinite leads placed on the left ( $l$ ) and right ( $r$ ); they are analytically obtained for  $B = 0$  and contribute non-Hermitian blocks to the Hamiltonian matrix, as discussed in Sec. 4.3.1.

The part  $\mathcal{G}_{rl} = \langle r_r | \mathcal{G} | r_l \rangle$  describing the propagation from the left to the right lead (where  $r_{r/l}$  are points at the corresponding interfaces) for the single dot is computed using the re-ordered block-Gaussian elimination scheme of the recursive Green function method (RGM)

presented in Sec. 4.4.3. In the multidot case, the chain is built up by a repeated module consisting of the oval cavity with lead stubs of length  $d = L/2$  on the right and left (see Fig. 5.1). Having found  $\mathcal{G}_{rl}$  for one module (with no attached outer leads yet), the Green function connecting the two outer leads in the assembled system is computed using the modular variant of the RGM described in Sec. 4.5, where the propagator for each inter-connected module is the solution of a matrix Dyson equation.

The transmission of the device is finally evaluated via the two-terminal trace formula [166, 203, 204]

$$T(E) = \text{Tr}[\Gamma_r \mathcal{G} \Gamma_l \mathcal{G}^\dagger] \quad (5.4)$$

with left/right broadening operators  $\Gamma_{l/r} = i[\Sigma_{l/r} - \Sigma_{l/r}^\dagger]$ . It is worthwhile noting that in the two-terminal device studied, even in the presence of a magnetic field, the transmission function is symmetric under exchange of the outer leads, i. e. the transmission from left to right equals that from right to left [150]. The computed propagator from the leads to the interior of the device is used to obtain the LDOS at site  $r$  through the relation

$$\rho(r, E) = \frac{1}{2\pi} \langle r | \mathcal{F}(E) | r \rangle, \quad \mathcal{F} = \mathcal{G} \Gamma \mathcal{G}^\dagger, \quad (5.5)$$

where  $\mathcal{F}$  is the spectral operator and  $\Gamma$  generally a weighted sum of  $\Gamma_l$  and  $\Gamma_r$  according to the Fermi distributions of incoming states in the two leads. In the cases presented here, we have chosen  $\Gamma = \Gamma_l$ , i. e.  $\rho(r, E)$  corresponds to the probability density resulting from an incoming monochromatic wave of energy  $E$  from the left lead.

The calculated transmission determines the macroscopically measurable conductance of the device. In the linear response regime at low temperature  $\Theta$ , the conductance for given Fermi energy  $E_F$  is obtained by the Landauer formula [1, 249] in the form

$$G(E_F, \Theta) = G_0 \int_0^\infty dE T(E) F_\Theta(E; E_F, \Theta), \quad (5.6)$$

where  $G_0 = \frac{e^2}{\pi h}$  is the (spin-degenerate) conductance quantum and

$$F_\Theta(E; E_F, \Theta) = \frac{1}{4k_B\Theta} \text{sech}^2 \left( \frac{E - E_F}{2k_B\Theta} \right) \quad (5.7)$$

is the thermal broadening function [127, 153]. The conductance in this regime is thus essentially given by the thermally averaged transmission around the electron Fermi energy, with a thermal width determined by the temperature  $\Theta$  (see Sec. 2.3.2).

Within the above theoretical and computational framework, in the following we will investigate the magnetotransport properties of the single- and multi-dot system in terms of geometry variations. In Sec. 5.2 we explore the transmission of the single oval dot and identify the mechanisms underlying the spectral features, in particular the suppression of zero-field transmission. In Sec. 5.3 the transmission properties induced by the inter-dot coupling in the array setup are discussed together with corresponding LDOS characteristics. In Sec. 5.4 we analyze the magnetoconductance switching effect in dependence of the oval deformation, the magnetic field strength and the length of the multidot chain at different temperatures, in order to determine a device setup optimal for switching within an achievable parameter range. The modification of the switching ratio in the presence of disorder is studied in Sec. 5.5, and Sec. 5.6 provides a summary of results, concluding on the functionality of the switching mechanism.

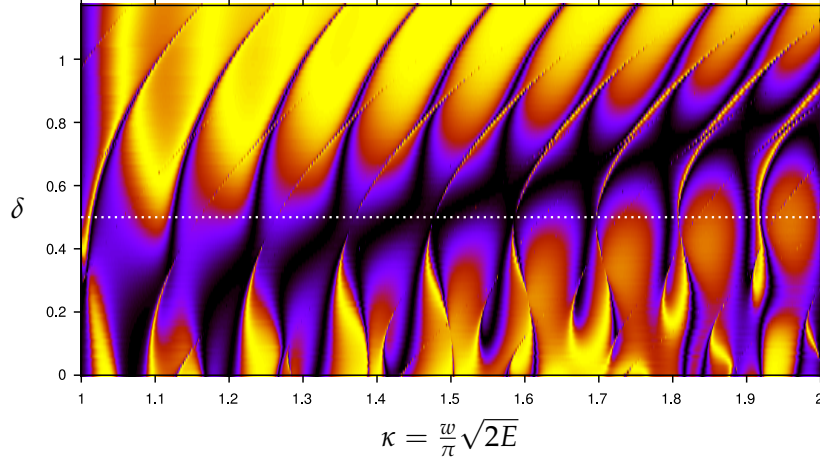


**Figure 5.2:** Transmission function  $T(\kappa)$  of the single oval billiard of Fig. 5.1 (a) in the first channel  $1 < \kappa < 2$  of the attached leads, for varying deformation parameter  $\delta$  (with relatively large step  $\Delta\delta = 0.01$  causing discontinuities along  $\delta$ ). The colormap ranges from black ( $T = 0$ ) to yellow ( $T = 1$ ).

## 5.2 Single oval billiard: transmission suppression from selective eigenstate interference

We start by exploring the transmission characteristics of the single oval open dot without magnetic field in terms of the eigenstates of its closed dot counterpart, in order to obtain an understanding of the mechanism underlying the conductance switching effect aimed at later. This eigenstate analysis of the single-dot transmission was thoroughly carried out by Buchholz *et al.* in Ref. [52], and is here summarized and supplemented with an investigation of further parametric dependences.

In Fig. 5.2 the transmission function  $T(\kappa)$  is shown for scaled dimensionless momenta  $\kappa = \sqrt{2m^*E}w/\hbar/\pi$  in the first channel of the attached leads,  $1 < \kappa = 2$ , as a function of the deformation parameter  $\delta$  of the oval at zero magnetic field. For the size of the device specified, the first channel corresponds to a Fermi energy in the range  $1.2 \text{ meV} < E_F < 5 \text{ meV}$ . As the channel number  $\kappa$  measures the wave number in units of  $\pi/w$ ,  $T(\kappa)$  depends only on the ratio  $w/R$ . Our calculations show that changing  $w/R$  within  $0.2 \lesssim w/R \lesssim 0.4$  introduces mainly a shift in  $T(\kappa)$  according to the implicit energy scaling, i. e. the transmission is largely determined by the geometry of the billiard and not by the leadwidth. For values of  $w/R > 2$ , the transmission obviously has to acquire the value of the unperturbed quantum wire. In the following we restrict ourselves to the case of  $w/R = 0.3$ .

The aim of this plot is to provide the overall change of  $T$  in this 2D  $(\kappa, \delta)$  parametric space which is rather coarse: very fine resonant features along  $\kappa$  are not resolved, and the evolution with  $\delta$  shows discontinuities due to a large variation step.

For large  $\delta$  the oval is very elongated, so that it essentially constitutes a (non-adiabatic) perturbation of a homogeneous quantum wire (e. g., for  $\delta = 1.2$  the vertical extent of the oval is  $2w$ ).  $T$  is then practically maximal (unity) along the whole channel, apart from distinct narrow resonant dips corresponding to quasi-bound states which are very weakly coupled to the leads. The dips correspond to the zeros of Fano resonances, described in Sec. 3.4.1, arising here from the coupling of the quasi-bound states to the highly transmitting background continuum. As  $\delta$  is decreased, these resonances respectively are shifted to lower energies, since the transversal wavelength of the quasi-bound states overall increases, and become broader due to a stronger coupling to the leads. Additionally, further narrower res-

onances appear which are also shifted (with a faster pace) with varying  $\delta$ . Apart from the resonant features, also the background transmission is drastically modified: As  $\delta$  decreases, a  $\kappa$ -range of highly suppressed transmission appears in the upper part of the channel and is shifted downwards. For  $\delta \approx 0.5$  (dotted line in Fig. 5.2), this ‘suppression valley’ is approximately centered around the middle  $\kappa \approx 1.5$  of the channel. As  $\delta$  is further decreased, broad overlapping resonances appear which ultimately lead to a highly irregular transmission spectrum for the circular billiard ( $\delta = 0$ ). Note that the transmission features in varying dot elongation is not specific to the exact oval shape, but qualitatively similar for, e.g., an elliptical billiard.<sup>1</sup>

The geometry-induced features of the transmission function can be qualitatively explained [52] in terms of the eigenstates of the closed oval billiard (that is, where the semi-infinite leads have been blocked by hard walls at some distance  $d$  from the oval boundary), by analyzing how these contribute to the transmission in the open system. The closed dot eigenstates for the oval with  $\delta = 1/2$  and with a short lead stubs ( $d = w/2$ ) are shown in Fig. 5.3. Eigenenergies and eigenvectors of the closed system Hamiltonian are obtained with standard sparse eigenproblem solvers from the ARnoldi PACKage [251]. Due to the  $x$ - and  $y$ -mirror-symmetry and the elongated shape of the oval, approximate longitudinal and vertical quantum numbers  $m$  and  $n$ , respectively, can be assigned to the eigenstates at low energies according to the spatial pattern of their probability density: State  $(m, n)$  has approximately  $m - 1$  and  $n - 1$  nodes in the  $x$ - and  $y$ -directions, respectively, within the billiard region.<sup>2</sup>

Although there are many eigenstates within the energy range of the first propagating channel, only few contribute substantially to the zero-field transmission. First of all, any eigenstate with even  $n$  has vanishing overlap with the ground transversal lead states due to its negative  $y$ -parity, which yields effectively zero coupling to the leads and thereby no contribution to the transmission for  $1 < \kappa < 2$ . This symmetry is broken in the presence of the magnetic field, as will be seen in the next section.

Of the remaining states with odd  $n$ , the majority (for the chosen  $\delta = 1/2$ ) has a spatial distribution which practically vanishes in the region of the lead openings and is concentrated (symmetrically) about the  $y$ -axis of the oval; we refer to such states as ‘confined’ states. They lead to the sharp Fano resonances in the transmission profile mentioned above, with widths typically much smaller than the level spacing. For fixed  $n$ , the  $x$ -extent of the confined states and thereby their coupling to the leads increases with  $m$ , leading to increasing resonant width at higher energies, as seen in Fig. 5.2.

The eigenstates (with positive  $y$ -parity) which determine the overall (background) transmission—and hence the linear response conductance through thermal averaging—are those with a large density at the lead openings leading to a strong coupling to the leads in the open system; we refer to these states as ‘leaking’ states. The width of the resonances corresponding to such short-lived states exceeds the level spacing, and the resulting transmission from the multiply overlapping resonances is no longer described by a simple Fano lineshape as the isolated ones. The transmission function is rather determined by the interference of leaking states at the lead openings.

<sup>1</sup> In Ref. [250] the transmission through a two-terminal elliptical cavity is investigated in terms of the effect of finite leads, and for particular values of the semiaxes a clear suppression of transmission is indeed seen which becomes more irregular close to the circular limit.

<sup>2</sup> Note that, although the symmetry of the dot (and thereby parity of the eigenstates) and the lead positioning are essential in the description of the transmission features, the nomenclature of nodal pairs serves simply as a handy way of labeling the states for convenient reference. It becomes unambiguous at higher energies where the number of nodes varies along cross-sections in each direction; see, e.g., state  $\nu = 102$  in the upper row of Fig. 5.3.

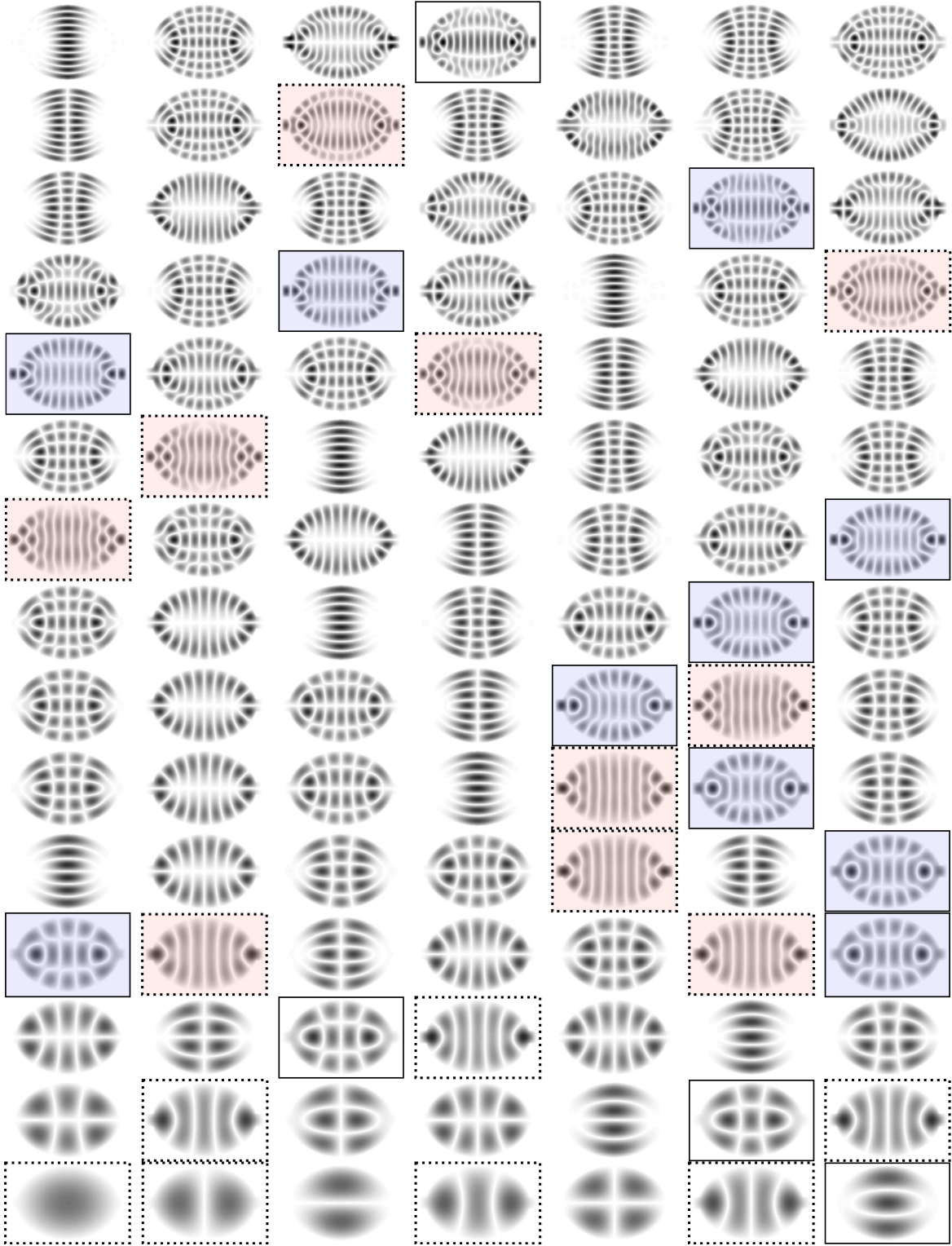


**Figure 5.3:** Probability densities of eigenstates  $\nu = 1 : 105$  (from left to right and bottom to top) of the closed oval billiard with deformation parameter  $\delta = 0.5$  and added stubs of width  $w = 0.3R$  and length  $d = w/2$  on the left and right. Levels  $\nu = 22$  to 98 (rows 4 to 14 from the bottom) for this stub length lie within the first channel of transport,  $1 \leq \kappa_\nu \leq 2$ . Solid and dotted boxes indicate leaking states of a common type characterized by approximate (longitudinal, vertical) pairs of quantum numbers  $(m, n = 1)$  and  $(m, n = 3)$  at low energies, respectively (see text). The transmission background of the open billiard in the first channel is determined by the terminal interference of pairs of quasi-degenerate (closest in energy)  $(m, 1)$ -states (light red) and  $(m, 3)$ -states (light blue). The grayscale is normalized to the total maximum in the plot and scales as  $\sqrt{\rho_\nu(\mathbf{r})}$ .

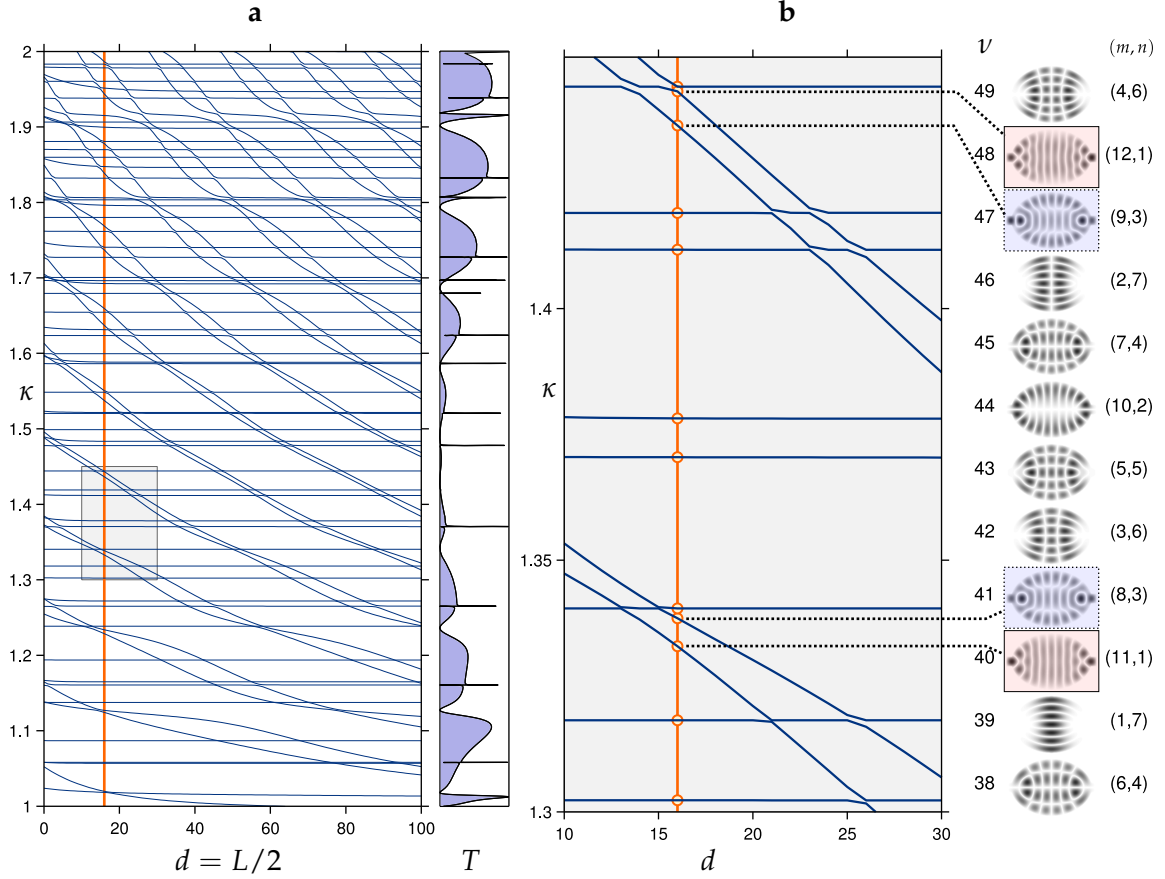


**Figure 5.4:** (a) Scaled energy levels  $\kappa_\nu = \sqrt{2m^*E_\nu w}/\hbar/\pi$  of the closed billiard of Fig. 5.3 for varying length  $d$  of the added lead stubs. The right panel shows the transmission for the open billiard at the dotted cut at  $\delta = 1/2$  in Fig. 5.2. (b) Closeup of the eigenspectrum  $\kappa_\nu(d)$  indicated in (a) around the stub length  $d = 16 a_0$  (indicated by the vertical line) to be used for the array setup. The probability densities of all eigenstates within the inset range are shown in the right panel together with their eigenenergy number  $\nu$  and their approximate  $(m, n)$  quantum numbers labeling the  $(x, y)$  nodal patterns. Two pairs of destructively  $x$ -interfering leaking states (colored) are indicated by dotted lines.

For  $\delta > 1$ , there are only leaking eigenstates of the type  $(m, n = 1)$  which are energetically well separated and lead to the high transmission background. As  $\delta$  decreases, however, also  $(m, n = 3)$  states become leaking, and their interference with the  $(m, n = 1)$  ones drastically modifies the non-resonant transmission. These two types of leaking states constitute two scattering channels which interfere constructively or destructively at the outgoing lead. In particular, when  $\delta \approx 0.5$ , the series of  $(m, 1)$  and  $(m, 3)$  states (indicated by red dotted and blue solid boxes in Fig. 5.3, respectively) are pairwise degenerate, with paired states of opposite parity [52]: Their destructive interference causes the wide suppression valley in the transmission function around the middle of the channel.

The ‘leakiness’ of the leaking states can be anticipated by varying the length  $d$  of the lead stubs of the closed billiard, as is done in Fig. 5.4. As a consequence of the perturbing lead stubs (but also of the non-integrable shape of the oval itself), the spectrum  $\kappa_\nu$  as a function of  $d$  consists of lines undergoing avoided crossings, upon which the character  $(m, n)$  nodal pattern of the corresponding states is exchanged. The more an eigenstate leaks into the lead stub, the more it is affected by the imposed Dirichlet boundary condition at the stub end, and the larger is the shift of the eigenenergy. The slopes of the  $\kappa_\nu(d)$  lines thus provide a relative estimate for the coupling of the zero-field eigenstates to the leads

within the first channel. Confined states and even- $n$  (odd- $y$ -parity) states correspond to flat lines, as expected from their negligible coupling to the leads.<sup>3</sup> The leaking states yield lines with varying slope depending on the details of their nodal pattern and corresponding energy distribution in the vertical and longitudinal direction. As we see, they indeed come in quasi-degenerate pairs (10 pairs for the indicated stub length  $d = 16a_0$ ); the closeup in Fig. 5.4(b) shows the two  $(m, n)$ -pairs  $(11, 1), (8, 3)$  and  $(9, 3), (12, 1)$ , surrounded by confined and even- $n$  states. Note that there is no correspondence here of the limit  $d \rightarrow \infty$  with the semi-infinite leads: The open boundary conditions in the scattering system are qualitatively different. As  $d$  is increased, more leaking eigenstates simply enter the range of the first channel and become denser in energy. However, we notice that on average (that is, considering a finite  $d$ -range in Fig. 5.4(a)) the destructively interfering leaking states within each pair lie energetically closer in the middle of the channel for the chosen  $\delta = 0.5$ , which qualitatively explains the according enhanced suppression in the transmission function (plotted for comparison in the right panel of Fig. 5.4(a)).

It should here be pointed out that this mechanism for conductance suppression does not rely on the exact shape of the oval used, but is robust against moderate changes of the geometry [52] (such as an elliptic billiard of the same aspect ratio and size relative to the leads): The decisive ingredient is the geometric separation of pairwise destructively interfering leaking states from weakly lead-coupled ones. When  $\delta$  is further decreased towards the circular limit, this scheme is perturbed by further eigenstates which become leaking, and then the multiple mixed (not pairwise destructive) interference of quasi-degenerate states yield an irregular fluctuating transmission, as seen in Fig. 5.2.

### 5.3 Quantum dot array: composite resonant states and magnetically controlled transmission bands

Having analyzed the origin of the suppression valley in the single-dot transmission function, we now focus on the modification of the transmission when dots are connected to form an array as well as the impact of an applied magnetic field. The zero- and finite-field transmission  $T(\kappa)$  through the coupled-dot device is shown in Fig. 5.5 for different numbers of dots  $N$  in the chain, with deformation parameter  $\delta = 0.5$  and interdot distance  $L = w$ . As discussed previously, the zero-field transmission in the single dot case consists of a rather smoothly varying background, on which sharp Fano resonances are superimposed. In the multi-oval case the sharp Fano resonances corresponding to confined billiard eigenstates are  $N$ -fold split (this very small splitting is generally not resolved on the scale of Fig. 5.5); additionally, Breit-Wigner (BW) type resonances of varying width emerge. The latter subsequently undergo a splitting into  $N - 1$  sub-peaks for an array of  $N$  dots. The resonances of BW type, although generally asymmetric on a varying background, are distinguished from the Fano resonances by the absence of the accompanying zero in the transmission. Their origin is the resonant scattering of the incoming wave through the system on the level of the connected dots, as will be demonstrated in the following for our setup. For sufficiently many dots (represented in Fig. 5.5 by the case of  $N = 20$ ), the multiply split resonances saturate into bands of densely positioned peaks, which is reminiscent of the band structure of energy levels in a periodic quantum system. In the presence of the weak field the smooth background transmission is overall increased, the sharp resonances are slightly shifted in

---

<sup>3</sup> In this case, the practically vanishing influence of varying  $d$  on the even- $n$  states is not due to a zero overlap with an even  $y$ -parity lead state, but due to the fact that odd  $y$ -parity billiard states decay exponentially in the lead stubs (and thus reach the ends with practically zero amplitude).

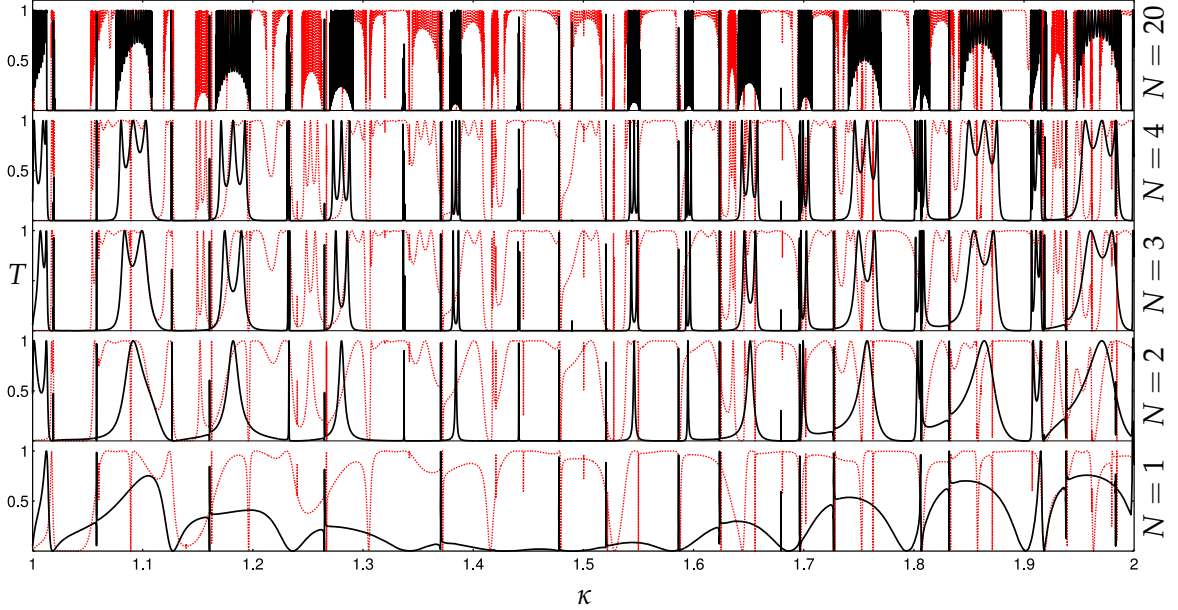


**Figure 5.5:** Transmission spectra in the first transversal channel for varying number of dots  $N$  with deformation parameter  $\delta = 0.5$  and connecting lead length  $L = w = 0.3 R$ , at  $B = 0$  (solid black line) and  $B = B_c \approx 20 \text{ mT}$  (dotted red line).

energy and the transmittive bands for large  $N$  are broader.

As seen in the previous section, the interference of leaking states belonging to different transversal billiard excitations generates a smooth oscillation in the single dot transmission  $T(\kappa)$ , with constructive interference hills of substantial  $T$  separated by destructive interference dips of vanishing  $T$ . The slowly varying envelope behavior of the transmission spectrum exhibits a wide energy range where the overall transmission is strongly suppressed. For the specific shape of the cavity corresponding to the chosen value of  $\delta = 0.5$ , this suppression valley is centered around the middle of the first channel.

In order to analyze the transmission of the multidot chain, in Fig. 5.6 (A) we focus on the transmission around the BW resonance appearing for  $N = 2$  at  $\kappa = \kappa_p \approx 1.384$ , and show its  $(N - 1)$ -fold splitting for increasing  $N$ . Also the sharp Fano resonance just below is included, whose splitting (of the order of  $\Delta\kappa \sim 2 \times 10^{-5}$  or  $\Delta E \sim 0.1 \text{ } \mu\text{eV}$ ) remains unresolved even at this scale. The  $N$ -fold splitting of the Fano resonances is a consequence of the degeneracy of the confined single dot eigenstates in the case of  $N$  dots, which are coupled very weakly through the connecting lead due to their strong localization within the ovals. It is thus similar to the splitting of the energy levels of atoms brought together to form a weakly bound molecule, with an energy split proportional to the interatomic coupling. The BW type resonances of the multidot case, which are narrower (wider) at energies where the single dot transmission  $T^{(N=1)}(\kappa)$  is lower (higher), are of different origin: They arise from the resonant scattering of the incoming wave through the system of the ovals and the connecting bridges via leaking states (which are strongly coupled to the bridges). Indeed, the emergence of these resonances and their  $(N - 1)$ -fold splitting can effectively be deduced from the 1D scattering through  $N$  potential barriers (or equivalently,  $N - 1$  resonators), where the transmission amplitude of scattering through each barrier possesses an energy dependent norm and phase. Two barriers  $\alpha, \beta$  with transmissions  $T_\alpha, T_\beta$  give the total transmission [127]

$$T_{\alpha\beta} = \frac{T_\alpha T_\beta}{1 + R_\alpha R_\beta - 2\sqrt{R_\alpha R_\beta} \cos \theta} , \quad (5.8)$$

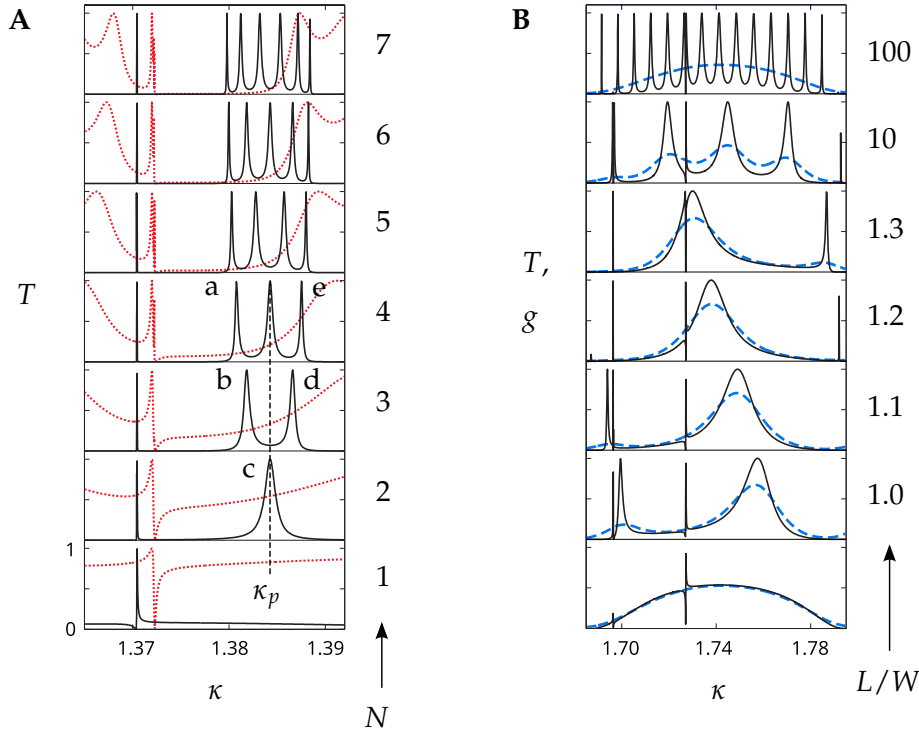


**Figure 5.6:** (A)  $T(\kappa)$  for  $B = 0$  (solid black line) and  $B = B_c$  (dotted red line) for  $L = w$  and varying  $N$ , in the vicinity of  $\kappa_p \approx 1.384$ , with labels a, b, c, d, e for the transmission resonances referred to in the text. (B)  $T(\kappa)$  (solid black line) and  $g(\Theta = 0.2 \text{ K}; \kappa_F)$  (dashed blue line) for a single dot (bottom) and for two dots with varying bridge length  $L$ , within a small window of the channel number  $\kappa$  covering the energy range of a smooth hill in the single dot transmission.

where  $R_{\alpha/\beta} = 1 - T_{\alpha/\beta}$  and  $\theta$  is the phase shift acquired by reflection from  $\beta$  to  $\alpha$  and back to  $\beta$ . For  $T_\alpha = T_\beta = T^{(N=1)}$  and  $\theta \propto \kappa$  this gives rise to resonance peaks in  $T^{(N=2)}$  which are equidistant in  $\kappa$  and have a width that increases with  $T^{(1)}$ . In our case though, due to the structure of the ovals that constitute the barriers, the phase shift  $\theta$  is not linear in  $\kappa$ . This perturbs the periodicity of the resonances, as we observe for  $T^{(2)}(\kappa)$  in Fig. 5.5, or equivalently, yields an energy dependent effective resonator length  $\tilde{L}(\kappa) \propto \theta(\kappa)/\kappa$ . Formula (5.8) can be iterated to obtain the transmission for  $N \geq 2$  ovals, i. e.

$$T^{(N)} = T_{\alpha\beta}; \quad T_\alpha = T^{(1)}, \quad T_\beta = T^{(N-1)}, \quad \theta_{\alpha,\beta} = \theta_{1,N-1}, \quad (5.9)$$

where  $\theta$  now results from reflections between 1 and  $N - 1$  barriers. The  $(N - 1)$ -fold splitting of the  $T^{(2)}$  resonance, shown in Fig. 5.6 (A), and the saturation into a band in the transmission spectrum for large  $N$ , are then reproduced for a system that is symmetric under the exchange  $\alpha \leftrightarrow \beta$  (which, in our case, renders the dots identical), provided that the phase difference between transmission and reflection amplitude of the single barrier is equal to  $\pm\pi/2$ , as is the case for the single oval with symmetrically attached leads.

Varying the resonator length modifies the conditions for resonant transmission by shifting the resonances in energy and changing their periodicity. In Fig. 5.6 (B) the transmission through  $N = 2$  connected dots, as well as the normalized conductance at  $\Theta = 0.2 \text{ K}$ , are plotted over the energy range of a single-dot transmission hill, for varying connecting bridge length  $L$ . With a slight increase in  $L$  ( $L/w = 1.0, 1.1, 1.2, 1.3$ ) the BW resonances are shifted to lower energy, and for longer bridges ( $L/w = 10, 100$ ) the number of resonances in the same interval increases. We notice that the center positions of the (split) Fano resonances are unaffected by the variation of the bridge length. Detailed features of the transmission lineshape,

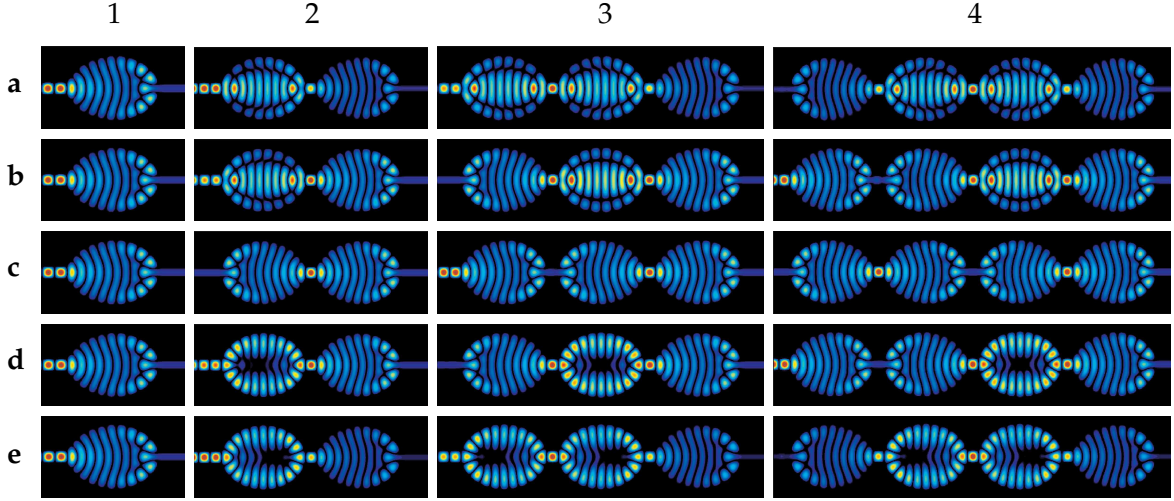


**Figure 5.7:** Zero-field LDOS for  $N = 1, 2, 3, 4$  dots with  $\delta = 0.5$  and  $L = w$  for energies in the vicinity of the  $(N - 1)$ -fold split resonance peak at  $\kappa = \kappa_p \approx 1.384$ , with incoming electron on the left. Rows (a), (b), (c), (d), (e) correspond to the energies of the resonances labeled with the same letters in Fig. 5.6 (A). The colormap for each sub-plot is normalized to its maximal value and scales as  $\sqrt{\rho}$  to enhance contrast.

such as the Fano resonances and the BW resonance peaks for large  $L$ , are washed out at finite temperature  $\Theta$  by thermal averaging through formula (5.6), making their contribution to the conductance  $G(E_F)$  negligible compared to the smooth background.

As we see in Fig. 5.6 (A), the addition of a dot to the existing chain of  $N$  dots at resonance energy lowers the transmission from unity to the single oval value  $T^{(1)}(\kappa)$  at that energy (note that the transmission at the dips between the resonances in  $T^{(N \geq 4)}(\kappa)$  can acquire values even lower than  $T^{(1)}(\kappa)$ ). In particular, the transmission at the energy position of the central resonance at  $\kappa = \kappa_p$  oscillates between unity and  $T^{(1)}(\kappa_p)$  with even and odd  $N$ , respectively:

$$T^{(N \text{ even})}(\kappa_p) = 1, \quad T^{(N \text{ odd})}(\kappa_p) = T^{(1)}(\kappa_p). \quad (5.10)$$

Furthermore, the resonances for each  $N$  are positioned symmetrically around  $\kappa_p$ , so that the forming bands in the transmission for large  $N$  are centered around the  $T^{(2)}(\kappa)$  resonance peaks.

In Fig. 5.7 this behavior of the transmission function for varying number of dots is illustrated in terms of the states forming in the system for  $N = 1, 2, 3, 4$  dots, by plotting the zero-field LDOS at the energies (rows a,b,c,d,e) of the resonance peaks labeled (with the same letters) in Fig. 5.6 (A), for an electron incident on the left. The spatial oscillations of the LDOS in the incoming lead come from the interference of the incoming wave with the wave that is backscattered from the dot array. Their absence is a signature of a resonance peak in the transmission spectrum, as there is no overall backscattering and transmission is unity. Starting with the single oval in the first column [Fig. 5.7 (a1)–(e1)], we see that the incoming wave is reflected at all energies (a) to (e) around  $\kappa_p$ , leading to a transmission significantly less than unity ( $T^{(1)}(\kappa_p) \approx 0.07$ ). When a second oval is added, there is an energy between (a) and (e), namely  $\kappa = \kappa_p$  represented by row (c), for which the backscattering of the single oval is canceled by the presence of the added oval and the connecting bridge: The wave is multiply reflected between the two ovals through the bridge, resulting in a quasi-standing wave along the chain [see (c2)] that constitutes a resonant state for the open system, leading to a transmission of unity. A third oval added in front of the two

introduces the backscattering again at  $\kappa_p$  [see (c3)], while the transmitted part from this first oval is perfectly propagated through the remaining two as in (c2). Thus the transmission in (c3) equals the single dot transmission,  $T^{(3)}(\kappa_p) = T^{(1)}(\kappa_p)$ . The backscattering of the third oval at  $\kappa_p$  is canceled by addition of a fourth oval [see (c4)], just as we went from (c1) to (c2), so that the  $T^{(2)}(\kappa_p)$  resonance peak is recovered in  $T^{(4)}(\kappa_p)$ , although with a smaller width.

Thus, the sequential cancellation of the backscattered wave leads to the even-odd oscillations of  $T^{(N)}(\kappa_p)$  seen in Fig. 5.6 (A). Resonant states are also accessed for 3 and 4 dots in (b3) and (a4) below  $\kappa_p$  and in (d3) and (e4) symmetrically above  $\kappa_p$ . Similarly, for each number of dots  $N$  there are  $N - 1$  accessible resonant states, including the one at  $\kappa_p$  for even  $N$ , at energies symmetrically positioned with respect to  $\kappa_p$ . Just as the  $T^{(2)}$  resonance is recovered in  $T^{(4)}$ , each  $T^{(N)}$  resonance is recovered at multiples of  $N$ , where the resonant state in the chain can be decomposed into multiple connected resonant states. We notice that the two branches of resonances, one below and one above  $\kappa_p$ , are associated with two different leaking eigenstates of the isolated single oval with lead stubs, with the closest nodal labeling  $(m, n)$  being  $(8, 3)$  and  $(11, 1)$ — they inhabit, for example, the central oval in (b3) and (d3), respectively.<sup>4</sup> Their interference in the open single oval system forms the scattering wave in column (1). These three wave patterns are combined among the  $N$  ovals in the open chain, to form the  $N - 1$  resonant states leading to the peaks around  $\kappa_p$ . The formation of resonant states occurs similarly around all  $T^{(2)}$  resonances of BW type (seen in Fig. 5.5). Characteristically, moving from a  $T^{(2)}$  resonance to the next one at higher energy adds a node in the quasi-standing wave within the two ovals and the connecting bridge. Increasing the length of the bridge shifts the resonances to lower energies and reduces the  $\kappa$ -distance between them, as the wavelength in the quasi-standing wave overall increases, in accordance to the effective resonator picture described above.

Conclusively, there are two types of resonances to be distinguished in the transmission spectra for the array of  $N$  dots:

- (i) the series of equidistant Fano resonances, arising from the confined single dot excitation modes in the continuum of the channel, which are  $N$ -fold split due to coupling between the ovals, and
- (ii) the series of nonequidistant BW resonances, resulting from resonant bridge-coupled states that form in the chain, which are  $(N - 1)$ -fold split.

### Modulation in a magnetic field

Following the discussion above, we now consider the influence of a weak perpendicular homogeneous magnetic field on the transport through the device. When the field is switched on, although the density distributions of the oval eigenstates remain largely unaffected at this low field strength, their phases are modulated and consequently the interference of the states contributing to transmission changes. Thus, depending on the field strength, the transmission spectra for the single and multiple dots are accordingly modified. In particular, while the pairs of the  $(m, 1)$  and  $(m, 3)$  leaking states responsible for the suppression valley in  $T(\kappa)$  still remain close in energy, the field changes their Aharonov-Bohm-like phases and prevents the destructive interference [52]. Also, the even- $m$  states, which did not mediate transport due to symmetry at zero field, now couple to the leads and in general contribute to the transmission.

---

<sup>4</sup> Note that the resonant energies in the open system do not happen to coincide with the energies of the corresponding closed dot eigenstates for the stub length chosen in Fig. 5.6 (b), but for smaller stub lengths. This shows that the transmission spectrum cannot generally be deduced from a given closed dot eigenspectrum.

As seen in Fig. 5.5 (dotted line) for the chosen field strength the slowly varying background of the single oval case is indeed generally raised throughout the channel, removing the characteristic suppression around its middle in the absence of the field. The overall very high transmission is interrupted by series of dips in its lineshape. The existing sharp Fano resonances undergo only a very slight energy shift (visible for the Fano resonance in Fig. 5.6 (A)), because the spatial distribution of the wave function remains practically unaffected at this weak field. Again the multidot chain provides a more complex transmission spectrum, resulting from the subsequent matching conditions for the wave function at the connections between the dots. The BW and Fano resonances are multiply split like in the field free case, and dips and plateaus become sharper and more pronounced as dots are added to the chain, saturating into a banded transmission. In contrast to the field free case, the transmission pattern is now dominated by narrower gaps and wider transmittive bands. Thus, also for the long chain of dots the overall transmission is drastically raised by the applied field. A more detailed analysis of the modification of the conductance with varying field will be presented in the next subsection.

## 5.4 Conductance switching

The conductance  $G(\Theta; E_F)$  at temperature  $\Theta$  and Fermi energy  $E_F$  is calculated by thermally averaging the transmission  $T(E)$  around  $E_F$  according to Eq. (5.6). For direct comparison to  $T(\kappa)$ , the dashed curve in Fig. 5.6 (B) shows the normalized conductance  $g(\Theta; \kappa_F) = G(\Theta; \kappa_F)/G_0 = \frac{\pi\hbar}{e^2} G(\Theta; \kappa_F)$  as a function of the Fermi channel number  $\kappa = \kappa_F = \sqrt{2m^*E_F/\hbar^2} w/\pi$  for  $\Theta = 0.2$  K. At zero temperature the conductance coincides with the transmission, but as  $\Theta$  is increased peaks and dips in the conductance become less pronounced due to the increasing width of the thermal broadening function (5.7). Already at the low temperature chosen in Fig. 5.6 (B) ( $\Theta = 0.2$  K), the detailed structure of the transmission is essentially lost: the sharp resonant peaks are washed out, reflecting their negligible contribution to the conductance. Also the formation of sharp transmittive bands for the multidot chain is relaxed with thermal averaging. For long interdot leads ( $L/w = 10, 100$  in Fig. 5.6 (B)) the conductance features follow the trend of the single dot case, that is, it exhibits similar hills in energy, yet with smaller amplitude. Similar modifications of the transmission spectra through thermal averaging hold for the conductance profile in the presence of the magnetic field (not shown).

A key feature of the oval shaped cavity is the formation of the wide suppression valley in the transmission spectrum of the first transversal channel, which is essentially retained also for the conductance at low temperature. In order to demonstrate the suitability of the chain of dots as a magnetically induced conductance switch, we exploit the lifting of this suppression when the field is turned on, aiming at a high ratio of finite- over zero-field conductance. In the following we optimize the switching ratio taking into account all relevant parameters ( $\delta, B, L, N$ ) as well as finite temperature and impurity scattering effects (see Sec. 5.5). First we consider the quantity  $G_{\text{off}}^{\text{min}}$  which is the zero-field finite temperature conductance minimized with respect to the position of the Fermi energy in the first channel.

In Fig. 5.8,  $g_{\text{off}}^{\text{min}} = G_{\text{off}}^{\text{min}}/G_0$  is plotted as a function of  $\delta$  at different temperatures for a single oval dot. We see that an optimal value for  $g_{\text{off}}^{\text{min}}$  is obtained around  $\delta = 0.5$ , with a small dip at  $\delta = 0.55$ , while it increases for larger or smaller deformation of the oval. It should be noted here that the modification in the spatial extension of the oval for a change  $\Delta\delta \approx 0.05$  is of the order of 1%, a challenging accuracy for an experimental realization of the device. We therefore keep the roughly optimized value of  $\delta = 0.5$  as a reference for

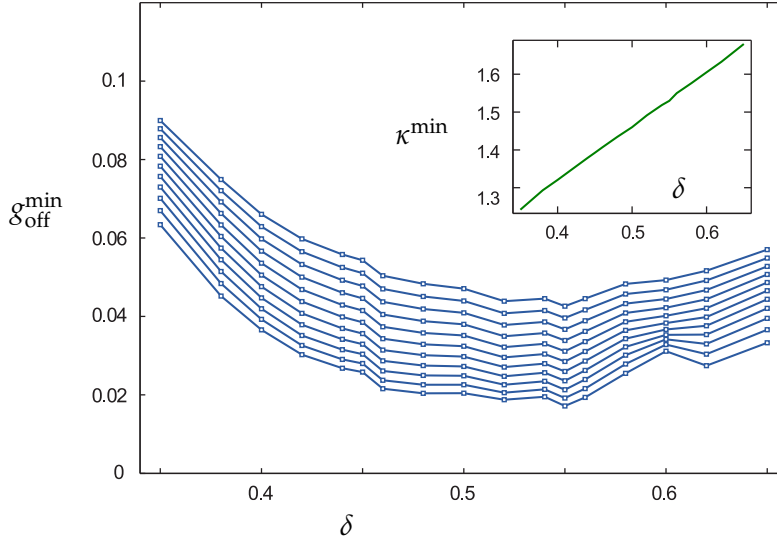


**Figure 5.8:** Minimal zero-field conductance  $g_{\text{off}}^{\text{min}}$  (see text) as a function of the deformation parameter  $\delta$  for a single dot, at temperatures (bottom to top)  $\Theta = 1.0, 1.1, \dots, 2.0$  K; the inset shows the change of the optimized channel number  $\kappa^{\text{min}}$  with  $\delta$  at  $\Theta = 2$  K (the dependence is the same for the other temperature values).

the following analysis. As shown in the inset of Fig. 5.8, the channel number  $\kappa^{\text{min}}$  of this minimum depends approximately linearly on  $\delta$  where the corresponding Fermi energies are located close to the center of the first channel. For  $\delta = 0.5$  we have  $\kappa_c = \kappa^{\text{min}}(\delta = 0.5) \approx 1.46$  in the single dot case ( $N = 1$ ). This shift of the optimal Fermi energy, that holds for all temperatures considered, is due to the modification of transversal modes inside the dot, which are shifted to higher energies as the oval becomes narrower with increasing  $\delta$ .

The single dot switching ratio  $S^{(N=1)}(B) = G_{\text{on}}^{(N=1)}(B)/G_{\text{off}}^{(N=1)}$  at  $\kappa = \kappa_c$  is shown in Fig. 5.9 for varying magnetic field strength at different temperatures. As  $S^{(1)}(B)$  equals the finite field conductance normalized to  $G_{\text{off}}^{(1)}$ , it describes the changes of the conductance induced by the field. For low field strengths (inset of Fig. 5.9) the modulation of the phase of the leaking states in the dot leads to Aharonov-Bohm (AB) like oscillations in the conductance. At the energies we consider here, only three of these leaking states are present [52]. However, the presence of more than two scattering channels inside the dot gives rise to the superposition of magnetoconductance oscillations, so that  $S^{(1)}(B)$  loses the periodicity expected for AB oscillations of a 1D quantum ring. As the field strength is increased, apart from their phase, also the spatial distribution of the states in the dot is affected. Confined states are eventually deformed into leaking ones, opening further channels for the transmission. The first magnetoconductance peak at  $B_c \approx 0.02$  T is seen to be the highest in the low field regime, giving a switching ratio of  $S^{(1)}(B = B_c) \approx 65$  at  $\Theta = 0.7$  K. For higher field strengths the transmittive states are gradually localized into edge states (with classical cyclotron radius  $\lesssim R/4$  for  $B \gtrsim 0.8$  T) along the border of the cavity, all within the first Landau level [50]. Following the edges of the billiard, the electrons are now more easily transmitted, resulting in an increased overall conductance. At a field strength of  $B \approx 1.2$  T these modes become perfectly transmittive along the edges of the structure, and the switching ratio reaches a plateau of maximal value ( $S^{(1)}(1.2 \text{ T} \lesssim B \lesssim 2.2 \text{ T}) \approx 70$  at  $\Theta = 0.7$  K). For even higher magnetic field strength the transmission decreases drastically as the incoming electrons gradually fail to overcome the magnetic barrier provided by the first Landau level, and the conductance drops to zero. At higher temperatures the features of the mag-

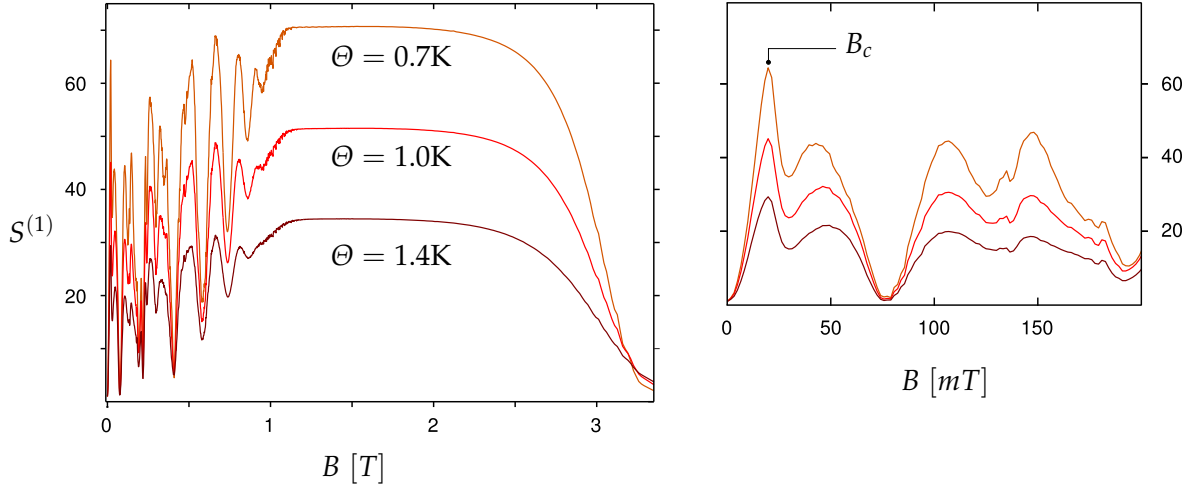


**Figure 5.9:** Single dot switching ratio  $S^{(1)}$  at  $\kappa = \kappa_c \approx 1.46$  as a function of the magnetic field, for temperatures (top to bottom)  $\Theta = 0.7, 1.0, 1.4$  K. The inset shows the irregular oscillations for low field strengths.

netoconductance remain; however, as a broader energy window with higher transmission parts is contributing to the thermal averaging in (5.6) through the broadening function (5.7), the switching ratio is generally lowered, because  $G_{\text{off}}^{(1)}$  increases. Also the amplitude of the oscillations decreases with temperature, as the magnetically induced changes in the detailed structure of the transmission have a smaller impact on average. For  $N > 1$  the magnetoconductance behaves similarly, but the switching ratio overall acquires higher values, because of the even lower zero-field conductance  $G_{\text{off}}^{(N)}$  resulting from the formation of gaps in the transmission spectra.

The magnetoconductance is calculated for spinless particles and hence does not describe electronic transport for high magnetic field strengths. But, as we are aiming at a high switching ratio, we concentrate in the following on the first maximum  $S_c^{(N)} = S^{(N)}(B = B_c)$ , which occurs approximately at the same field strength  $B_c \approx 20$  mT for all considered numbers of dots  $N$ . For this weak magnetic field we can neglect the Zeeman splitting. In Fig. 5.10,  $S_c^{(N)}$  is presented for a varying number of dots in the chain, again at different temperatures. We allow for the parameter  $\kappa_c^{(N)}$ , which represents the scaled Fermi energy of the incoming electrons, to be optimized individually in order to minimize  $G_{\text{off}}^{(N)}$  for each dot number  $N$ . At sufficiently low temperature, by connecting a second oval to the single one we gain a substantial factor with respect to the increase from  $S_c^{(1)}$  to  $S_c^{(2)}$  ( $\approx 320$  for  $\Theta = 0.7$  K), which, as pointed out, results from the lower zero-field conductance. For  $N > 2$  the switching ratio fluctuates around a temperature dependent mean value, due to its high sensitivity with respect to the optimized  $G_{\text{off}}^{(N)}$  at low temperatures, which changes for each  $N$ . At higher temperatures the fluctuations are weakened, but  $S_c^{(N)}$  is then also lowered drastically.

It is obvious that the optimization of the switching ratio strongly depends on the temperature: High switching ratios require low temperatures,  $\Theta \lesssim 2$  K for our setup. Nevertheless, we see that the current switching functionality of the device is significantly enhanced throughout the temperature range considered already with only two connected dots instead of a single one. This is of advantage in an experimental realization of the system, since optimal switching can be achieved with a relatively small double-dot system (instead of a long multidot chain) where phase coherence is more easily maintained.

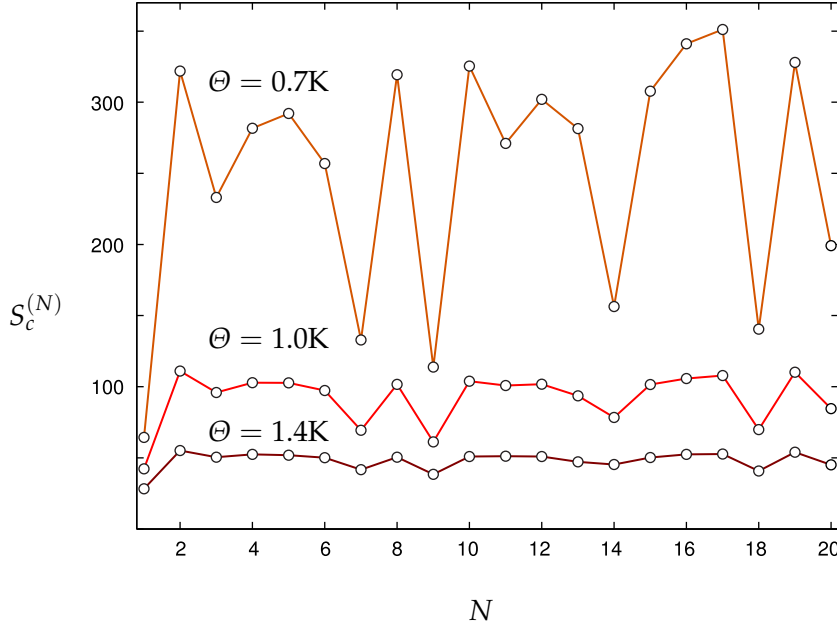


**Figure 5.10:** Switching ratio  $S_c^{(N)} = S^{(N)}(B = B_c \approx 20 \text{ mT})$  for varying number of dots  $N$  with connecting bridge length  $L = w$ , for different temperatures  $\Theta$ .

## 5.5 The impact of impurities

Let us now explore the impact of potential disorder on the magnetoconductance. This is implemented in the form of remote impurity scattering in the presence of a modulation-doped layer above the 2D structure. We consider pointlike negatively charged impurities of 2D density  $n_{\text{imp}}$  distributed on a plane at distance  $d$  above the 2D electron gas (2DEG), excluding them from the region of the semi-infinite leads. The plane is partitioned into small pieces of area  $1/n_{\text{imp}}$ , within each of which one impurity is placed at random position, thus constituting a quasi-random distribution of impurities, with an upper bound on their local concentration. The electrostatic potential of each impurity is screened by the 2DEG at the plane of the device structure; for the effective potential that an electron feels at lateral distance  $r_{\text{imp}}$  from the impurity we use the model screening potential of Sec. 1.1.3,

$$V_{\text{scr}}(r_{\text{imp}}) = \frac{e^2}{4\pi\epsilon_0\epsilon_b} \frac{q_{\text{TF}}(1 + q_{\text{TF}}d)}{q_{\text{TF}}^3} \frac{1}{(r_{\text{imp}}^2 + d^2)^{\frac{3}{2}}}, \quad (5.11)$$

where  $q_{\text{TF}} = 2/a_B$  is the low- $\Theta$  Thomas-Fermi screening wave number, with relative permittivity  $\epsilon_b = 13.8$  and effective Bohr radius  $a_B = 9.8 \text{ nm}$  for a GaAs [75].

As the distance  $d$  of the impurity layer is made very short ( $d \lesssim 30 \text{ nm}$  in the present scaling), the corresponding transmission spectra (not shown here) are drastically changed with respect to the clean case (see Fig. 5.5), as a result of the influence of the impurity potential on the transport through the device. The randomized potential landscape in the dot chain leads to a spatial deformation of the existing states and a breaking of the symmetries present in the clean system: The sharp Fano resonances are shifted due to the perturbation of the confined eigenstates in each dot, differently for each individual impurity configuration. The impurity potential also changes the energies of the leaking states, which results in modified conditions for their coupling to the leads, so that the broad transmission maxima are shifted, too. Additionally, new transmission peaks are introduced by leaking states that did not contribute in the clean case due to their symmetry [52]. For not too short impurity layer

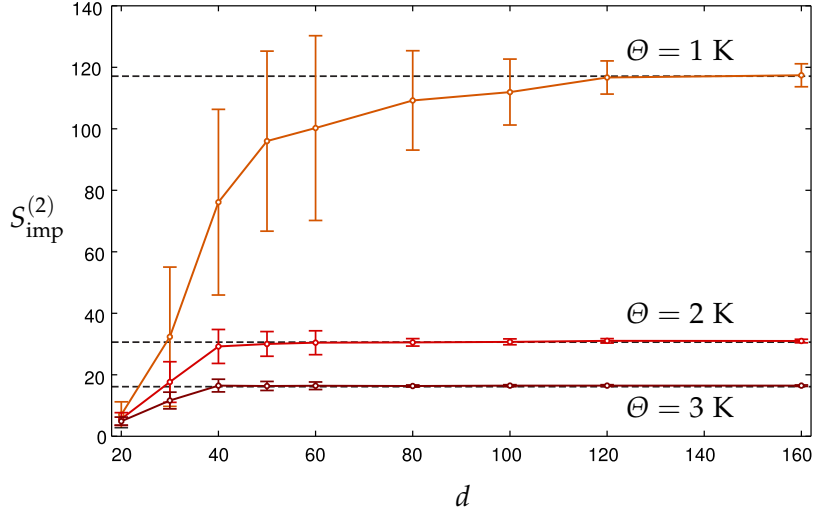


**Figure 5.11:** Mean value and standard deviation (for 27 impurity configurations) of the switching ratio  $S_{\text{imp}}^{(2)}(B = B_c)$  of two connected dots as a function of the impurity layer distance  $d$  at different temperatures. The dashed lines give the values  $S_c^{(2)}$  of the disorder free case.

distance  $d$  though, the described suppression valley in the conductance of the clean system is retained, still making valid the concept of magnetic conductance switching. As expected, the effects of disorder are enhanced as the impurity density is increased (not shown); in the present analysis we use a value of  $n_{\text{imp}} = 0.0025 \text{ nm}^{-2}$ . This rather high density of remote impurities is employed here in order to intensify their impact on transport in our simulations, whereas in practice cleaner samples are realizable for use in semiconductor nanostructures [21, 252].

In Fig. 5.11 the switching ratio in the presence of remote impurities  $S_{\text{imp}}^{(2)}(B = B_c)$  is shown as a function of the distance  $d$  from the impurity layer, for two connected ovals. The values of  $S_{\text{imp}}^{(2)}$  for each  $d$  are the average over 27 configurations of the randomly distributed impurities. When the impurity layer is closer to the 2D conducting structure, the average switching ratio is in general lower than its value in the clean system, the latter being practically reached for a distance  $d \gtrsim d_0(\Theta)$ , depending on the temperature. For  $\Theta \approx 1 \text{ K}$  we have  $d_0 \approx 100 \text{ nm}$ , corresponding to a transport mean free path  $l_e \approx 24 \mu\text{m}$  in the first Born approximation [75]. Nevertheless, the relatively large deviations from the mean indicate that, for each  $d \lesssim d_0(\Theta)$ , there are certain impurity configurations that provide a switching ratio much higher or lower than the average. This is due to the high sensitivity of  $G_{\text{off}}$  with respect to the potential pattern that is formed on the plane of the array. If the impurity configuration is, for example, such that a potential maximum is blocking the opening of a cavity to a lead, then  $G_{\text{off}}$  is suppressed, as the wave coming from the lead is strongly backscattered. This backscattering can be lifted when the magnetic field is turned on, leading to an overall increased switching ratio for this configuration. On the other hand, when the configuration of the impurities does not block the leads,  $G_{\text{off}}$  in the suppression valley is slightly higher compared to the clean case due to the additional resonances in the transmission, causing a reduced switching ratio. Thus, at distances where the potential on the 2DEG plane is not too strong to permit transmission at all, the randomly distributed impurities lie within a broad variation between the cases of blocking and non-blocking configurations, keeping the deviations from the mean high. When the impurities are put too close to the 2D structure ( $d \lesssim 30 \text{ nm}$ ), the shape specific suppression feature of the zero-field transmission is essentially lost, so that the overall conductance is practically unaffected by the field

strength, which thus minimizes the switching effect. For larger impurity layer distances the mean  $S_{\text{imp}}^{(2)}$  eventually saturates into the clean case value with decreasing deviations, as the potential becomes too weak to affect the transmittive states in the dots.

Using random impurity distributions to investigate the functionality of magnetic current switching in a more realistic environment, one can speak of a temperature dependent lower bound of the switching ratio (see Fig. 5.11) depending on the specific setup. This lower bound is increased as the influence of disorder is suppressed, that is, when a longer mean free path for the electrons is achieved. Technological progress actually makes it feasible to reach mean free paths in heterostructures comparable to the size of realizable nanoscale devices [21, 253, 254]. The almost ballistic nature of electron transport then allows for controllable conductance switching at low temperatures, in the sense that it is determined by the specific shape of the conducting device, the electron energy and the applied magnetic field.

## 5.6 Summary and conclusions

Having investigated the transmission properties of a linear array of equidistant identical oval shaped quantum dots, we demonstrated the functionality of such a structure as a magnetically controlled switching device in the deep quantum regime. The switching effect arises from the lifting of a deformation specific suppression in the transmission of the oval when a weak perpendicular field is turned on. The suppression valley in the transmission results from the destructive interference of states in the dots that are strongly coupled to the leads, and is specific to the elongated shape of the single billiard. This makes the effect relevant in systems of similarly shaped dots, e.g. elliptical. The switching ratio oscillates with the magnetic field strength, but as the effect is prominently present even at very weak fields, we have concentrated on its first peak. We have shown that the extension of the single dot into a chain of dots causes a much higher switching ratio, due to a stronger suppression of the zero-field conductance. However, we point out that almost optimal switching can be obtained by connecting only one more dot to the single one, giving a multiple value for the switching ratio while keeping the system size small. This could make the device practically advantageous but also favors quantum coherence itself, which is the principal requirement for the interference effects to take place.

The efficiency of switching is lowered with increasing temperature, as the desired shape specific characteristics of the transmission spectra are thermally washed out, which poses a limitation to low temperatures (up to about 2 Kelvin). In spite of the possibility to achieve mean free paths of the 2DEG much longer than the extent of the studied system, we have additionally investigated the robustness of the switching ratio in the presence of impurity scattering. The switching ratio acquires a higher or lower value than in the clean case depending, respectively, on whether the impurity configuration is blocking transport at zero magnetic field or not. Thus, for randomly distributed impurities a temperature dependent lower bound for the switching ratio of a sample can be set. The efficiency of magnetoconductance tuning then remains to be specified for the individual device.

Conclusively, it was demonstrated that electron billiards of specific elongated geometry and chains thereof can be used, due to interference-induced regularities in the suppression of their transmission, to design low temperature magnetoconductance.

---

# Current control in soft-wall electron billiards: energy-persistent scattering in the deep quantum regime

---

In this chapter we use ‘soft-wall’ boundary confinement, that is, a potential profile with finite slope, to induce charge current controllability in a two-terminal transport setup. In particular, the isolation of energetically persistent scattering pathways from the resonant manifold of an elongated electron billiard in the deep quantum regime is demonstrated. This in turn enables efficient conductance switching at varying temperature and Fermi velocity, using a weak magnetic field. The effect relies on the interplay between the elongated soft-wall confinement and magnetic focusing, which together rescale the scattering pathways and decouple quasi-bound states from the attached leads. The mechanism proves robust against billiard shape variations and qualifies as a nanoelectronic current control element. The results of this chapter are partially published in Ref. [255].

## 6.1 Persistent switching via geometric rescaling at low energies

In Chap. 5 it was shown how the elongated (oval) shape of a hard-wall open billiard may be utilized to switch conductance by means of quantum interference: quasi-degenerate, lead-coupled states were selectively brought into destructive output interference, thereby suppressing conductance, with a phase-modulating magnetic field causing high overall transmittivity. The effect was shown to be relatively robust with respect to small changes in shape deformation and weak disorder and requires only a very weak field. However, the fulfillment of the required interference conditions relies on the steepness of the wall boundaries and is naturally sensitive to small variations in the field strength. Furthermore, the geometrically induced suppression valley in conductance fixes the optimal switching Fermi energy to the center of the first propagation channel.

We will now demonstrate an alternative way to achieve conductance control by exploiting the orbital magnetism in a billiard with appropriately designed soft wall boundary: In contrast to the previous *phase*-dominated transport properties at low field strength, the magnetoconductance will now be controlled via *path*-dominated dynamics while remaining in the same energetic regime. Conceptually, we now pursue the separation of these two types of magnetotransport dynamics, phase- versus path-dominated, in a regime where they strongly overlap, corresponding to a suppression of quantum fluctuations in favor of directed pathways at wavelengths comparable to the system size—the ‘deep quantum regime’.

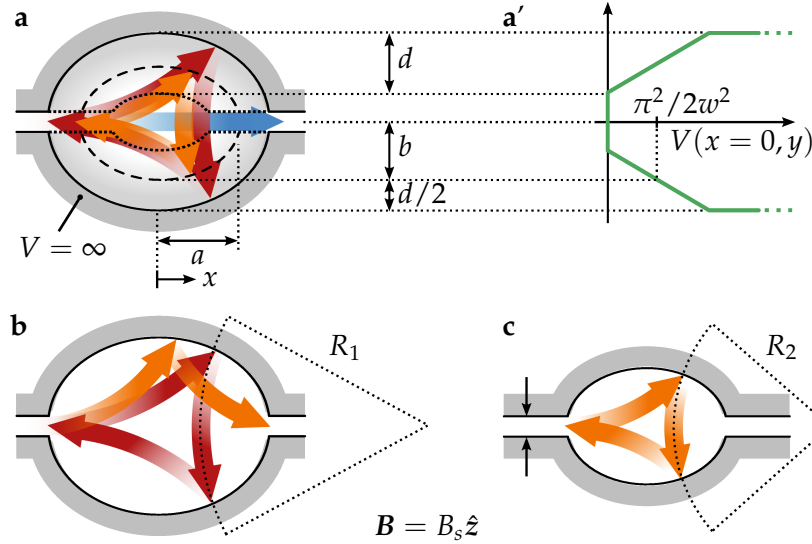


**Figure 6.1:** System setup and sketch of magnetically focused pathways. (a) Electron billiard defined by hard-wall confinement (solid line) and a soft-wall potential  $V(x,y)$  decreasing along elliptical contours to zero (dotted contour), with wall width  $d$  in the  $x$ - and  $y$ -directions. The wall opens up along  $y = 0$  to attached leads of width  $w$ , and its central contour (dashed) has semi-axes  $a$  and  $b$ . (a') Cross section at  $x = 0$  for linear wall potential, with central contour lying at the threshold of the first propagating channel. (b) Without the soft wall, a magnetically focused, backscattered pathway (with cyclotron radius  $R_1$ , red arrows) eventually turns into a transmitted pathway (with cyclotron radius  $R_2 < R_1$ , orange arrows) for sufficient decrease in energy, while (c) backscattering would be retained for a correspondingly smaller billiard. With appropriately chosen potential in (a), similar backscattered paths can persist with varying energy for a common field strength  $B_s$ , with forward propagation favored for  $B = 0$  (blue arrow). Note that the sketched arrows do not correspond to quantitative classical trajectories, but qualitatively indicate the background overall electronic motion.

From an experimental viewpoint, the magnetic field provides a unique macroscopic handle on those mesoscopic processes determining the conductance of the system, and the challenge is to find a way to control them under ‘comfortable’ conditions. In other words: How can a weak magnetic field switch the current flow through a sizable electron billiard at low bias and finite temperature, and over a broad Fermi level variation? The answer lies in identifying and designing transport mechanisms which respond reliably to changes in the field strength while remaining robust against variations in energy, and at the same time stay separated from omnipresent quantum fluctuations. The key feature in the observable response consists in a controllable background transmission, magnetically switched between its extrema, upon which only narrow interference-induced Fano resonances [35] are superimposed [12, 14, 36]. This requires energetically persistent scattering pathways that mediate transport or cause complete reflection, but couple only weakly to resonant states.

This scenario is realized in an open electron billiard with an elliptical soft-wall potential (see Fig. 6.1). The experimental setup in mind is a quantum dot with steep boundary potential [19, 20] supplied with additional peripheral gates [18] which further deplete the internal 2D electronic motion. With a perpendicular magnetic field  $\mathbf{B}$  piercing the dot, the combination of the elongated lateral shape with the soft wall enables an energy-invariant switching mechanism by isolating the required scattering pathways from the manifold of resonant levels. In short: For  $B = 0$ , the elliptic soft walls collimate the electronic motion into the longitudinal direction, causing high overall transmission. At a special ‘switching’ field strength  $B = B_s$ , the incoming electrons are focused [71] into a completely backscattered pathway, which becomes geometrically rescaled in the presence of the soft wall (as

sketched by the arrows in Fig. 6.1). In both cases, the crucial role of the soft wall is thus to create *energetically persistent* scattering pathways while decoupling localized resonant states from the openings. As a result, the setup enables efficient finite-temperature current switching for varying Fermi energy, by turning on a weak external magnetic field.<sup>1</sup>

It should be pointed out that, for the purely hard-wall billiard boundary (Figs. 6.1 (b), (c)), this type of geometrical rescaling of the magnetically focused path is not possible: At a given field strength, the electronic path is less deflected for lower energy (shown schematically by the orange path in (b)), and its specular reflection on the boundary eventually leads to complete or partial transmission of the electron. To keep the backscattering character of the focused wave, the hard-wall billiard (and in turn the scattered electron path) would have to be rescaled as shown in (c). For an appropriately chosen soft-wall potential profile, as shown quantitatively in the following, the penetration depth of the backscattered wave into the wall is reduced with decreasing energy, such that the boundary length is effectively reduced and focused trajectory retained (rescaled to smaller size) without modifying the dot confinement.

The chapter is structured as follows. In Sec. 6.2 we present the transmission spectrum of a chosen soft-wall billiard as a function of magnetic field and compare it to the one in absence of the soft-wall boundary, thus demonstrating the conductance switching efficiency of the proposed setup. The form of the transmission spectrum is analyzed in terms of the closed billiard eigenspectrum in Sec. 6.3. In Sec. 6.4 the persistent switching mechanism is elucidated by the spatial distribution of the scattering states and their current density. The alternative current switching properties of connected billiards are investigated in Sec. 6.5. Finally, Sec. 6.6 explores the modification and robustness of the switching efficiency in terms of variations in the billiard shape and soft-wall potential profile. Section 6.7 summarizes the chapter and concludes on the experimental functionality of the switching device.

## 6.2 Decoupling of resonances and controllable finite-temperature conductance

With decohering electrodes implemented by attached semi-infinite leads, the effective (energy dependent and non-Hermitian [127]) Hamiltonian of the open system is represented on a tight-binding lattice, and the transmission function  $T$  is computed via the extended (modular) recursive Green function scheme developed in Chap. 4. This allows for efficient and accurate transport calculations in a highly resolved parameter space for the considered low-energy regime. The conductance  $G$  at Fermi energy  $E_F$  and temperature  $\Theta$  is then obtained from  $T(E)$  within the Landauer-Büttiker framework presented in Chap. 2; specifically, we use the linear response formula, Eq. (2.46). As seen in Chaps. 3 and 4, upon an excitation in the leads, the appropriate parts of the Greenian further provide the local density of states  $\rho(\mathbf{r})$  as well as the scattering wave function which in turn yields the probability current density  $\mathbf{j}(\mathbf{r})$ , adapted here to the lattice model [80, 94]. The choice  $\hbar = e = m = a_0 \equiv 1$  fixes the units of energy  $E_0 = \hbar^2 / ma_0^2$  and magnetic field strength  $B_0 = \hbar / ea_0^2$  for given effective mass  $m$  and lattice constant  $a_0$ .

The transmission through the soft-wall billiard is shown in Fig. 6.2 (a) as function of field strength  $B$  for the scaled electronic momentum  $\kappa$  varying within the first propagating channel of the attached leads; we refer to this kind of plot as a ‘transmission map’. Qualitatively,

---

<sup>1</sup> Note that the switching here is the opposite to that of Chap. 5, where the zero-field conductance was suppressed and raised by the field: we here have the on-state of the switch in absence of the field, and the off-state for finite field strength.

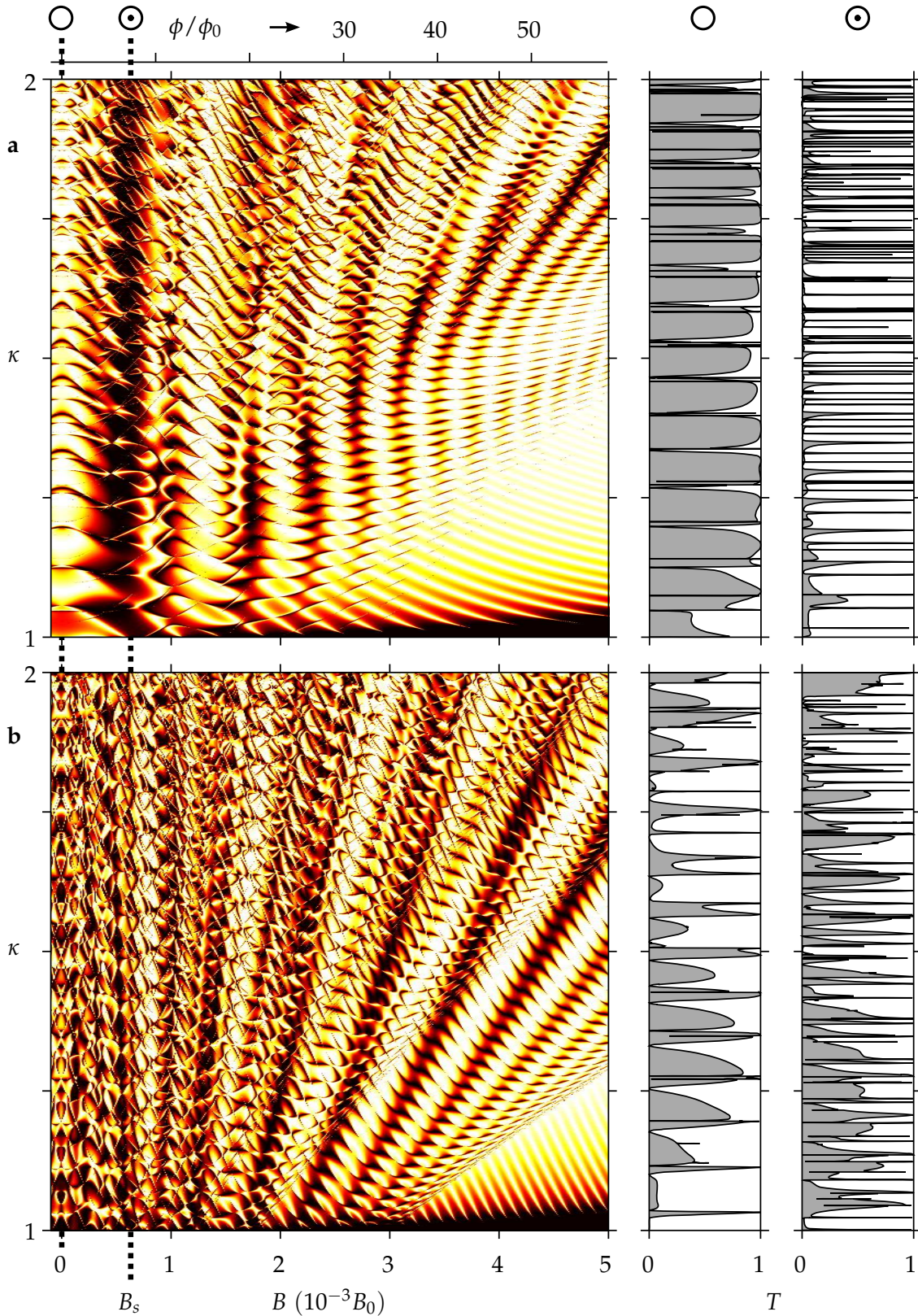


**Figure 6.2:** Transmission (from 0-black to 1-white) as a function of magnetic field strength  $B$  (or flux quanta  $\phi$ ) and scaled incoming momentum  $\kappa = p_{\text{in}}w/\pi$  within the first open channel  $1 < \kappa < 2$  of the attached leads, for (a) a billiard with the soft-wall potential of Fig. 6.1 (a') with  $(a, b, d, w) = (128, 84, 96, 32) a_0$ , and (b) the same billiard without soft wall. Right panels: cuts through the  $T(B, \kappa)$ -maps at zero field (marked  $\circ$ ) and at the switching field  $B_s = 0.63 \times 10^{-3} B_0$  (marked  $\odot$ ) or flux  $\phi_s = 7.32 \phi_0$  (where  $\phi_0 = h/e$  is the flux quantum). For a reference length unit  $a_0 = 2$  nm, the field strength unit is  $B_0 = \hbar/ea_0^2 = 164.55$  T.

the  $T(B, \kappa)$ -map for the soft-wall setup shares certain features with the corresponding map in absence of the soft wall, shown in Fig. 6.2 (b): At strong fields and sufficiently low energy (lower right corner of  $T(B, \kappa)$ -maps), transport is mediated by edge states which increasingly interfere with quasi-degenerate states [50] as energy increases (lower diagonal half). The slope of the resulting broad reflection and transmission stripes in the  $T(B, \kappa)$ -maps portray the formation of skipping orbits [71] in the billiard: Since their cyclotron radius scales like  $R \sim \sqrt{p_{\text{in}}^2 - 2V/B}$ , where  $p_{\text{in}}$  denotes the magnitude of the incoming electron momentum, the (approximate) commensurability between the skipping intervals and the (half) length of the hard-wall boundary is preserved along lines of positive slope in the  $B$ - $\kappa$ -plane, along which high reflection (transmission) occurs. This behavior is evident also for the soft-wall billiard at higher energies (upper right quadrant of Fig. 6.2 (a)), where its hard-wall character dominates. However, the stripes are now ‘bent’ outwards (to higher  $B$ ) at lower energies where the soft wall significantly influences the electron dynamics: Since the low-energy states are more confined by the soft wall, the billiard size effectively decreases, and consequently the transmission map features broaden along the  $B$ -axis (e.g., the isolated edge states in Fig. 6.2 (a) form at larger  $B$ -intervals), causing the interference stripes to bend. In other words, a stronger focusing field is generally needed to maintain the high or low  $T$  for increasing  $\kappa$  in the presence of the soft wall.

Both with and without soft wall, these stripes generally become less prominent and finally destroyed at weaker fields and higher energies (upper diagonal half of maps). This is because more billiard states become available above the bulk Landau levels (as seen in the closed billiard eigenspectrum discussed below in Sec. 6.3) which are spatially extended and whose multiple interference leads to broad but highly irregular resonant transmission features in both  $B$  and  $\kappa$ . In spite of the very complex dynamics in this regime, the presence of the soft wall induces a remarkable feature in the  $T(B, \kappa)$ -map (Fig. 6.2 (a)): At a relatively weak field  $B = B_s$ , backscattered states almost completely dominate the background transmission spectrum of the open billiard, forming a *vertical* and *broad* reflection stripe covering the whole channel, upon which only very narrow Fano resonances are superimposed. The inverse profile is acquired if the field is turned off: At  $B = 0$ , a highly transmitting background is perturbed only by very narrow resonant dips. Both features, the transmission and reflection stripes at  $B = 0$  and  $B = B_s$ , respectively, are absent without the soft wall (see Fig. 6.2 (b)). This is highlighted by the cuts through  $T(B, \kappa)$ -maps on the right of Fig. 6.2, where overall  $T(B = 0) \approx 1$  and  $T(B = 0) \approx 0$  for the soft-wall billiard while  $T(\kappa)$  shows strong oscillations and broad irregular resonances for the purely hard-wall billiard.

At finite temperature, the narrow resonant dips (peaks) at  $B = 0$  ( $B = B_s$ ) are effectively washed away by the thermal contribution of the highly transmitted (reflected) background states around the Fermi level. This is seen in Fig. 6.3 (a,b), where the normalized conductance is kept close to unity (zero) over a broad range in  $E_F$  even at considerable thermal width  $k_B\Theta$ . It is important to note that the efficiency of the effect is actually enhanced at finite temperature compared to the zero- $\Theta$  transmission spectra, in contrast to conductance control via resonant features which attenuate even at very low temperatures. In other words, although multiple sharp Fano resonances can be viewed as individual transmission switches (at different energies), they become inoperative as such for thermal widths comparable to the resonant widths. The smearing of sharp resonances is a desired ingredient for the type of control proposed here, where the whole background is uniformly switched between zero and maximum. The implemented soft wall potential thus enables a uniquely robust conductance switching effect, for a large quantum dot (i.e., accommodating a large number of resonant levels), and in a regime where quantum fluctuations typically dominate transport,

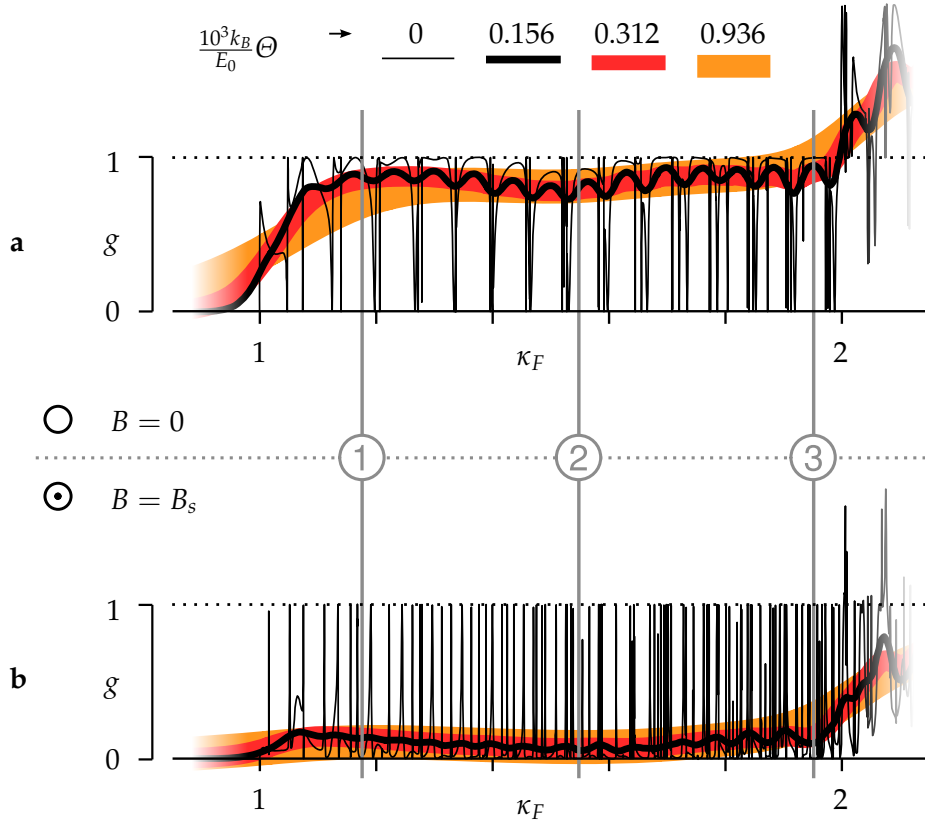


**Figure 6.3:** Dimensionless conductance  $g = G/G_0$  (with quantum  $G_0 = e^2/\pi\hbar$ ) in the first open channel (a) for  $B = 0$  and (b) for  $B = B_s$ , for the same billiard as in Fig. 6.2 (a), at different temperatures  $\Theta$ . With  $a_0 = 2$  nm and  $m = 0.069 m_e$  (transport at a GaAs/AlGaAs interface):  $E_0 = 276$  meV and  $\Theta = 0, 0.5, 1.0, 3.0$  K. Vertical lines indicate sample non-resonant momenta  $\kappa_{1,2,3}$  at which the LDOS and current density are shown in Fig. 6.5.

using a weak magnetic field.

### 6.3 Closed billiard eigenspectrum

The general characteristic features of the transmission maps  $T(B, \kappa)$  (which are common in the presence and absence of the soft-wall boundary) can be anticipated by comparison of the maps with the discrete eigenspectrum of the corresponding closed billiard, as shown in Fig. 6.4 for the soft-wall billiard, where the levels are plotted on top of its  $T(B, \kappa)$ -map. The scaled billiard eigenenergies as a function of magnetic field strength,  $\kappa_\nu(B)$ , constitute a generalization of the well known Darwin-Fock [256, 257] spectrum (obtained analytically for parabolic confinement) to arbitrary confining potential. In the present general case, the angular momentum is not conserved and generally avoided crossings occur between the different levels, upon which the anticrossing quasi-degenerate states exchange their character (that is, their spatial density distribution). However, the symmetry of the studied billiards implies the conservation of  $x$ - and  $y$ -parity. In variation of the single parameter  $B$ , states of opposite parity can become degenerate leading to exact crossings in the  $\kappa_\nu(B)$ -spectrum, since they remain uncoupled, while states of the same parity lead exclusively to avoided crossings [178, 258] (see also Ref. [259] for the case of a spatially periodic magnetic field).

The structure of the eigenspectrum has regular characteristics for large  $B$  and small  $\kappa$ :

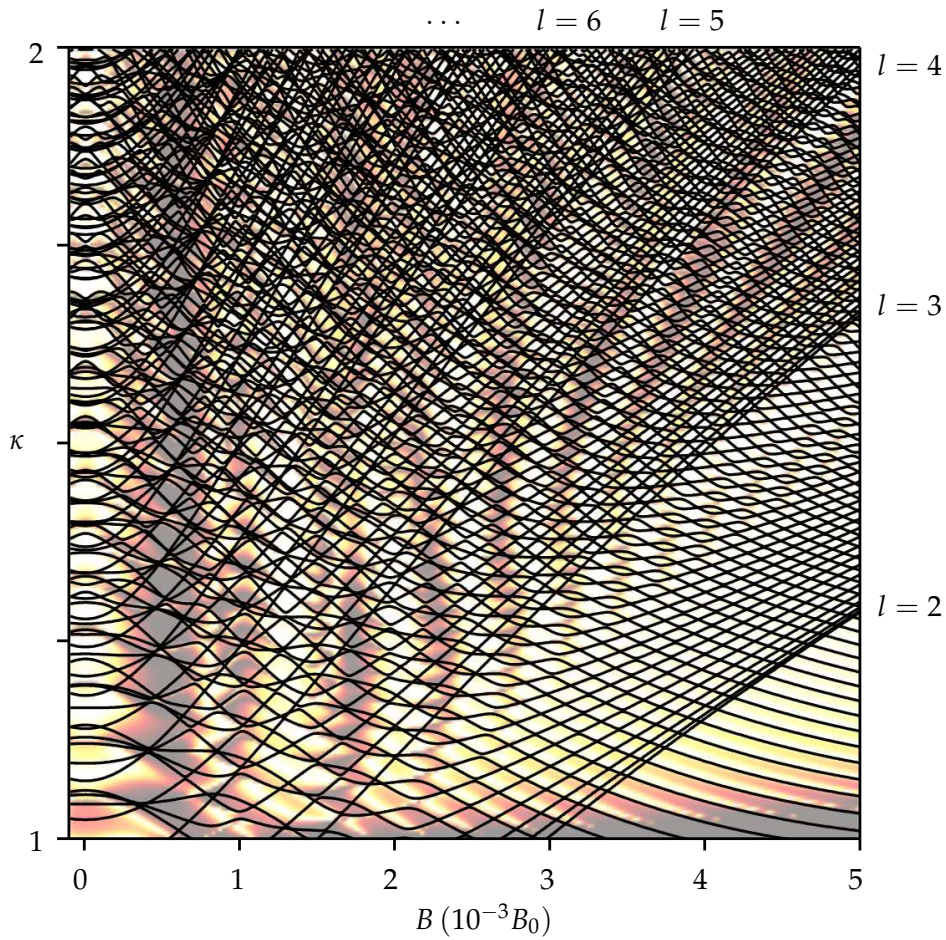


**Figure 6.4:** Energy levels  $\kappa_\nu$  of the closed soft-wall billiard (with the same potential as in Fig. 6.2 (a), but with the elliptic hard-wall boundary closing the lead openings) within the energy range of the first transport channel, for varying magnetic field strength  $B$ . For increasing  $B$ , the levels condense (asymptotically) into the bulk Landau levels (of the unconfined electron) indicated by their number  $l$ . The discrete spectrum is plotted on top of a faint copy of the  $T(B, \kappa)$ -map of Fig. 6.2 (a).

The energy levels are regularly spaced and gather together asymptotically for increasing  $B$  into bundles corresponding to the Landau levels  $l$  of the unconfined system (see Sec. 1.3).<sup>2</sup> Within the confining potential, these states become increasingly ‘condensed’ in the bulk of the billiard for increasing  $B$  and consequently their energy increases (positive slope in the  $\kappa_\nu(B)$  diagram); they are thus of ‘paramagnetic’ type, corresponding to classical cyclotron orbits (circulating anti-clockwise for positive  $B$ ). On the contrary, states which are delocalized and extend to the billiard boundary correspond to classical skipping orbits which form an inner arc of clockwise circulation (for positive  $B$ ) [260] when bouncing off the boundary and can be assigned a ‘diamagnetic’ type; their energy decreases with  $B$ , and for sufficiently large  $B$  and low  $\kappa$  they can be identified as edge states localized at the billiard boundary (negative slope in the  $\kappa_\nu(B)$  diagram). The above two types of states coexist in increasing number as the energy successively rises above the Landau level ‘caustics’ in the spectrum, and for low  $B$  and large  $\kappa$  (upper left corner of Fig. 6.4), their crossings and anticrossings form a complicated and irregular level structure [60].

<sup>2</sup> For the  $\kappa$ - and  $B$ -ranges plotted in Fig. 6.4, only the bundles demarcating the very lowest Landau levels are clearly discernible (e.g.  $l = 2, 3$ ); they become fainter with increasing  $\kappa$  at fixed low  $B$  because of the participation of an increasing number of crossing or anticrossing levels which obscure the structure of the spectrum (see, e.g.,  $l = 4, 5, 6$ ).

It is clear that the (diamagnetic) states localized closer to the boundary are the ones that dominate the overall transport in the open system, since they reach the lead openings with an increased amplitude. Their strong coupling to the leads causes their energy levels to broaden and shift significantly, so that the correspondence of eigenenergies and transmission peaks and dips is lost [15]; the transmission profile is rather determined by the *interference* of quasi-degenerate lead-coupled states. Indeed, we see that the characteristic broad transmission and reflection stripes in the  $T(B, \kappa)$ -map generally occur when level lines of negative slope become quasi-degenerate in the  $\kappa_v(B)$  diagram (see, e.g., the area between the  $l = 3$  and  $l = 4$  bundles); the fewer the lines that meet, the clearer the interference pattern in  $T$ . The condensed (paramagnetic) bulk states, on the other hand, correspond to narrow resonances in the transmission spectrum of the open billiard; their weak coupling to the leads leads to small shifts in resonant energy and the correspondence to closed billiard states is immediate. Indeed, level lines with large positive slope practically coincide with the sharp antiresonance lines in the  $T(B, \kappa)$ -map. Note that bulk states with small (or zero) slope are still extended enough to contribute to the interference in transmission; see, e.g., the area between the  $l = 2$  and  $l = 3$  bundles, where strongly coupled (large level repulsion at anticrossings) diamagnetic and paramagnetic states coincide with the formation (tails) of the reflection stripes in  $T$ .

It is finally remarked that, in terms of closed billiard eigenstates, the very distinct vertical reflection stripe around  $B = B_s$  in the  $T(B, \kappa)$ -map, allowing for energy-persistent conductance suppression, is not of the simple origin of the tilted stripes at larger  $B$ . Indeed, we now have a maximal number of interfering levels (even discarding the bulk-confined ones of positive slope) which, nevertheless, produce a well-defined backscattered amplitude whose spatial character persists in energy (to be analyzed in the next section). This behavior evidently originates from the impact of the soft wall: In the purely hard-wall billiard, although the level diagram is qualitatively similar, the multiple interference of low- $B$  extended states simply produces a complicated irregular transmission variation (see Fig. 6.2 around  $B = B_s$ ). Note that, in the lower half of the reflection stripe in Fig. 6.4, the large reflection can partially be attributed to the absence of available states between successive multilevel crossings.<sup>3</sup> The special impact of the soft wall is most striking in the upper half of the stripe where diamagnetic states cover the energy interval.

## 6.4 Switching between collimated and backscattered wave propagation

To understand the influence of the proposed type of soft wall potential along the transmission (reflection) stripes around  $B = 0$  ( $B = B_s$ ), and the induced mechanism underlying conductance control, let us analyze the electronic scattering states responsible for high (low) background transmission in the absence (presence) of the field. Fig. 6.5 (a,b) displays the local density of states (LDOS)  $\rho(x, y; \kappa)$  for electrons incident in the left lead of the billiard at sample non-resonant energies.

For  $B = 0$  (Fig. 6.5 (a)), we see that the effect of the finite potential is to direct the motion along the axis connecting the leads, thus enhancing transmission. This is achieved in a twofold way: (i) The special shape of the potential around the lead openings, forming a stub

---

<sup>3</sup> The level diagram here strongly resembles the original Darwin-Fock spectrum, since at such low energy the wave function poorly resolves the difference of the used confinement from a parabolic one. The resulting nearly exact multilevel crossings have been studied experimentally for two [261] and three [53] mixing levels which can coherently form a ‘dark’ state (complete cancellation of resonance amplitude).

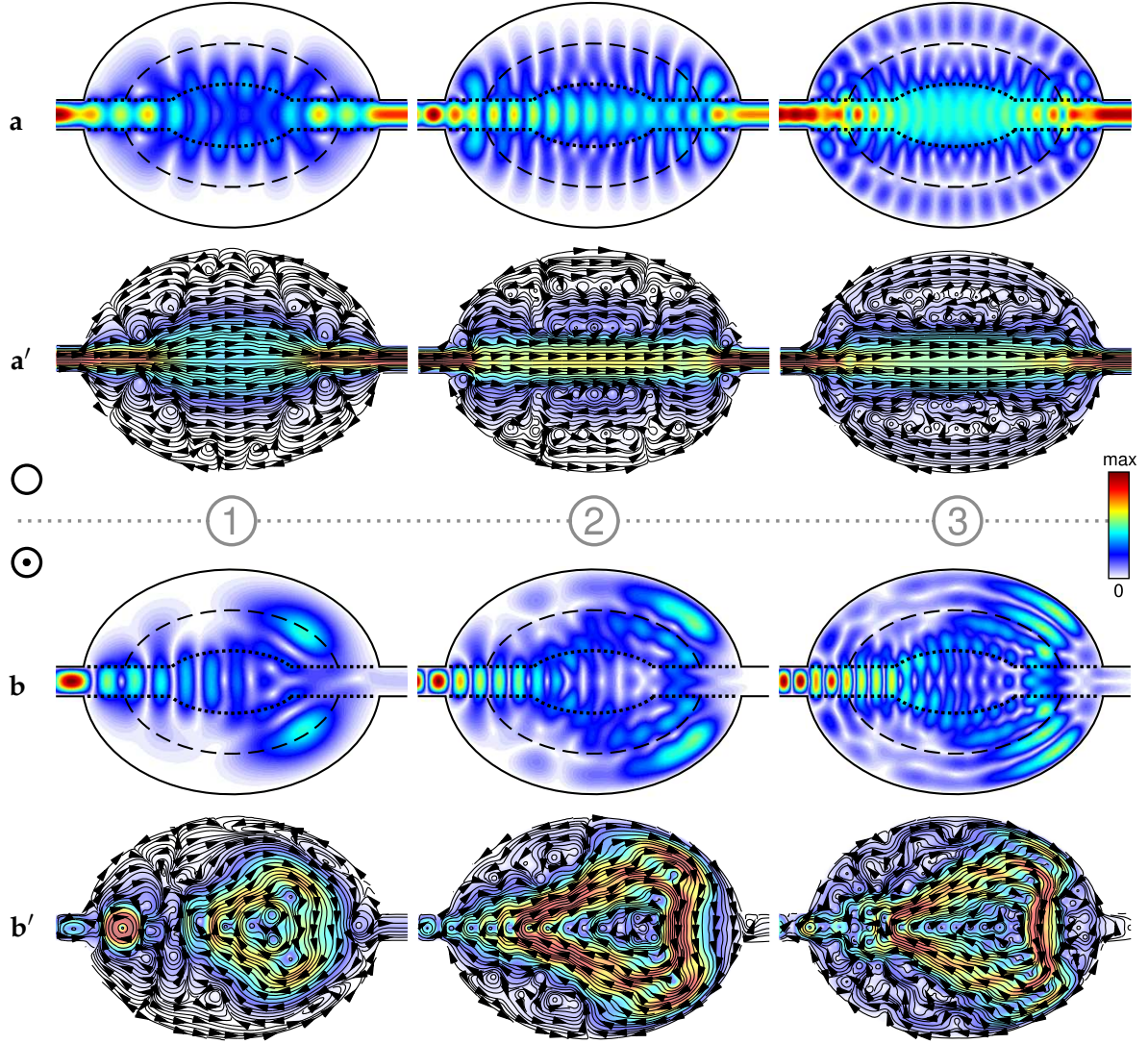


**Figure 6.5:** (a) Scaled LDOS  $\sqrt{\rho}$  and (a') scaled probability current density  $\sqrt{|j|}$  (the flow of  $j$  is depicted by directed streamlines) shown at momenta  $\kappa_{1,2,3}$  indicated by vertical lines in Fig. 6.3, for electrons incident in the left lead (colormap normalized to maximum value in each plot). (b,b') Same as above, but for  $B = B_s$ . The dashed (dotted) lines in (a,b) show the potential contour at  $V = \pi^2/2w^2$  ( $V = 0$ ).

of free motion into the billiard as a prolongation of each lead, suppresses the transversal component of the electronic local momentum, thereby collimating [94, 262] the motion in forward direction (in other words, the soft wall reduces the diffractive effect of the hard-wall lead openings). (ii) Owing to its elliptic contour, the soft wall depletes the scattering state along the billiard boundary and further confines it into an elongated profile leaking into both leads. For the same reason, states corresponding to distinct Fano resonances become well decoupled from the leads, and thus isolated from a significant (subtractive) contribution to the overall transport.

For  $B = B_s$  (Fig. 6.5 (b)), the scattering state profiles reveal the key role of the soft wall in energetically sustaining the backscattered pathways. Again, the mechanism is twofold: (i) States strongly coupled to the incoming lead are now magnetically focused onto the billiard boundary, so that the electron follows a pathway which is backscattered after ‘bouncing’ twice off the boundary [15, 51]. The soft wall here crucially comes to the aid of conductance

suppression by ‘rescaling’ the dynamics and thus keeping the non-resonant backscattered pathway energetically invariant: With increasing (decreasing) kinetic energy, the electron undergoes weaker (stronger) Lorentz deflection at constant  $B = B_s$ , but at the same time penetrates more (less) into the soft wall potential towards the boundary (compare outer lobes of  $\rho$  in Fig. 6.5 (b;1,2,3)). The soft wall thus effectively increases the billiard size with energy, and as a result, the magnetically focused, backscattered pathway persists over the whole channel. (ii) As in the field-free case, any long-lived resonant states are further confined away from both leads by the soft wall, rendering the corresponding Fano peaks extremely narrow.

The actual (stationary) electronic motion in the billiard is depicted in Fig. 6.5 (a’,b’)) through its probability current density  $j(x, y; \kappa)$ . With or without magnetic field, the wave nature of transport leads to multiple complex vortex structures covering the billiard, which change dramatically in energy. This detailed charge flow is, of course, totally different from that of classical particles moving in the billiard area. Nevertheless, we see that the parts of the flow with maximal density indeed favor motion along the above described pathways needed for conductance switching in varying  $E_F$ , that is, a forward collimated current for  $B = 0$  and a circulating backscattered current for  $B = B_s$ .

It should be pointed out that, although the soft wall succeeds in geometrically rescaling the low-field (two-bounce) backscattered pathway, the motion is in general drastically modified from that in a corresponding purely hard-wall billiard with spectral boundary reflection [54]. In the present case, the further into the soft wall the electron reaches, the more it is magnetically deflected due to its reduced (local) momentum, and the motion is further affected by continuous electrostatic refraction [263]. These effects are enhanced at stronger fields which localize the scattering states closer to the boundary over longer parts (unlike the two-bounce paths, which predominantly enter the wall radially). Therefore, such higher order (four-bounce, six-bounce, etc.) backscattered pathways [51, 264] cannot persist over large energy intervals for the same potential. Indeed, in Fig. 6.2 (a) vertical reflection stripes tend to form also at higher field strengths ( $B/B_0 \approx 1.8, 2.2$ , etc.), but are eventually tilted or destroyed as energy varies. Switching efficiency is thus restricted to smaller  $\kappa_F$ -range and lower  $\Theta$  at these fields.

### Mode-resolved higher channel transmission

A closer look at the higher energy backscattered state in Fig. 6.5 (b,3) reveals that its tail in the right lead belongs the second channel which is closed for propagation for  $\kappa < 2$ . The suppressed transmission of the state could thus be interpreted purely quantum mechanically (that is, disregarding that the multiply interfering billiard eigenlevels seen in Fig. 6.4 happen to produce a state qualitatively resembling a magnetically deflected classical trajectory) as the consequence of vanishing coupling to ground transversal mode of the outgoing lead due to opposite  $y$ -parity.

Indeed, this is confirmed by the mode-resolved transmission coefficients  $T_{mn}(\kappa)$  plotted in the first three channels in Fig. 6.6. We see that the lowest mode partial coefficient  $T_{11}$  (dark red), which is the only non-vanishing one in the first channel, largely continues its trend also in the second channel: the background (non-resonant)  $T_{11}$  is switched from practically one to zero over a large energy range. Now there are, however, contributions of scattering from ( $T_{m2}$ ) and to ( $T_{2n}$ ) the second mode in the leads as well.<sup>4</sup> In particular, there is a strong contribution of either of  $T_{21}$ ,  $T_{12}$  or  $T_{22}$  in different parts of the second channel for  $B = B_s$ ,

<sup>4</sup> Note that for  $B = 0$  only odd $\rightarrow$ odd or even $\rightarrow$ even mode transitions survive due to the conserved  $x$ -parity of the stationary scattering eigenstates (as evident, e.g., from Fig. 6.5 (a)).

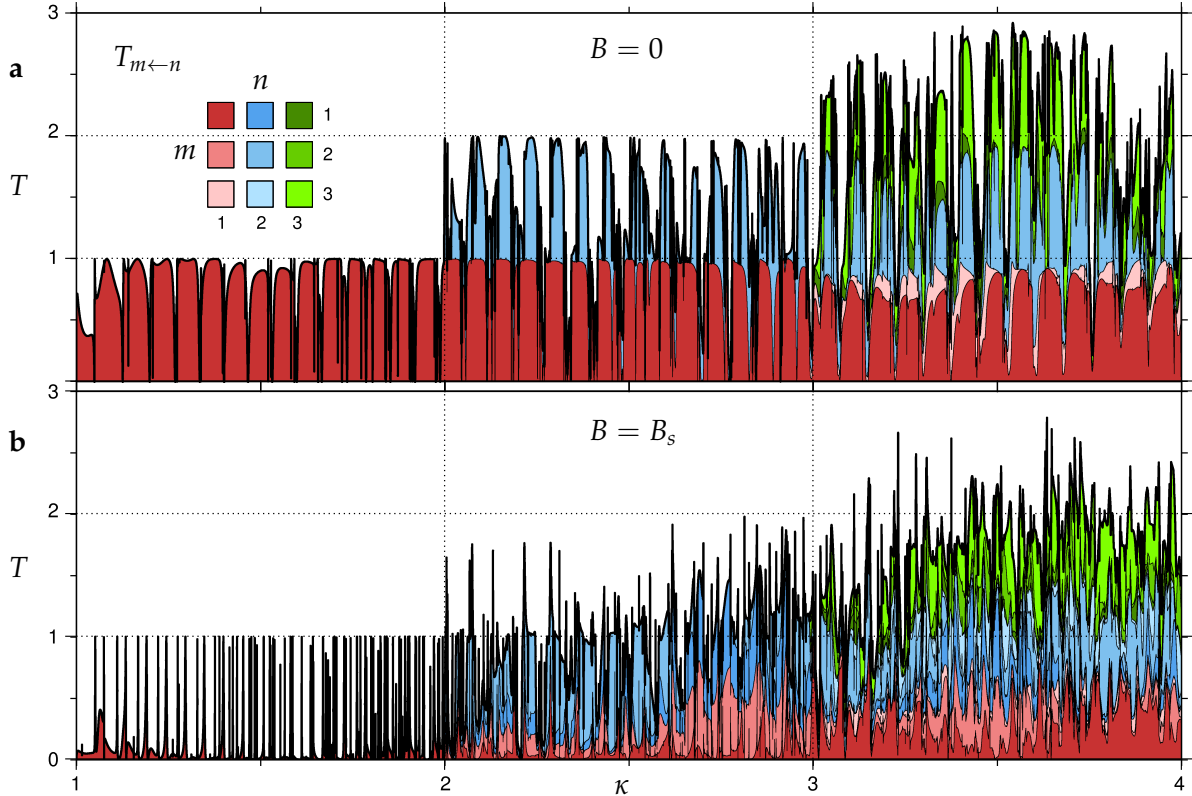


**Figure 6.6:** Mode-resolved transmission coefficients  $T_{mn}$  from transversal mode  $n$  to mode  $m$  of the attached leads within the first three channels of transport,  $1 \leq \kappa \leq 4$ , for (a)  $B = 0$  and (b)  $B = B_s$ . The individual coefficients are plotted cumulatively (on top of each other, with each  $T_{mn}$  offset to the previous one) with area colors for each mode pair  $(m, n)$  indicated in the inset of (a).

leading to an overall total  $T$  around unity. Although transmission for  $B = 0$  in the second channel is overall larger, one can clearly no longer speak of an efficient and energy-persistent conductance switching.

In the third channel transmission coefficients are even more dramatically altered with respect to the regularity in the first channel. Now the zero-field  $T_{11}$  component (dark red) is lowered from unity (in fact, performs a slow oscillation pattern in energy), and at  $B = B_s$  it no longer overall suppressed (it forms a slow oscillation opposite to the field-free case, with superimposed broad resonant features). The higher channel components are substantial at both  $B = 0$  and  $B = B_s$ , and the resulting total transmission (the sum of all partial coefficients) is of similar overall magnitude (the channel-averaged  $T$  is only slightly larger without the field), and so the switching functionality of this particular setup is evidently lost at this higher energy. We underline here the importance of the isolation of the classical-like collimated and backscattered electron paths in the deep quantum regime of the first channel from resonant contributions: Although the quantum-classical correspondence generically sets in at higher energies [12, 50], it is here achieved persistently—in the sense of spatially broad but still well defined wave propagation paths—in the very low energy regime.

## 6.5 Conductance switching in soft-wall billiard arrays

We now briefly investigate how the switching functionality of the soft-wall potential is altered when the electron billiards are connected into an  $N$ -dot array like in Chap. 5. In Fig. 6.7 the switching contrast  $\Delta g = g(B = 0) - g(B = B_s)$  of the single soft-wall billiard analyzed

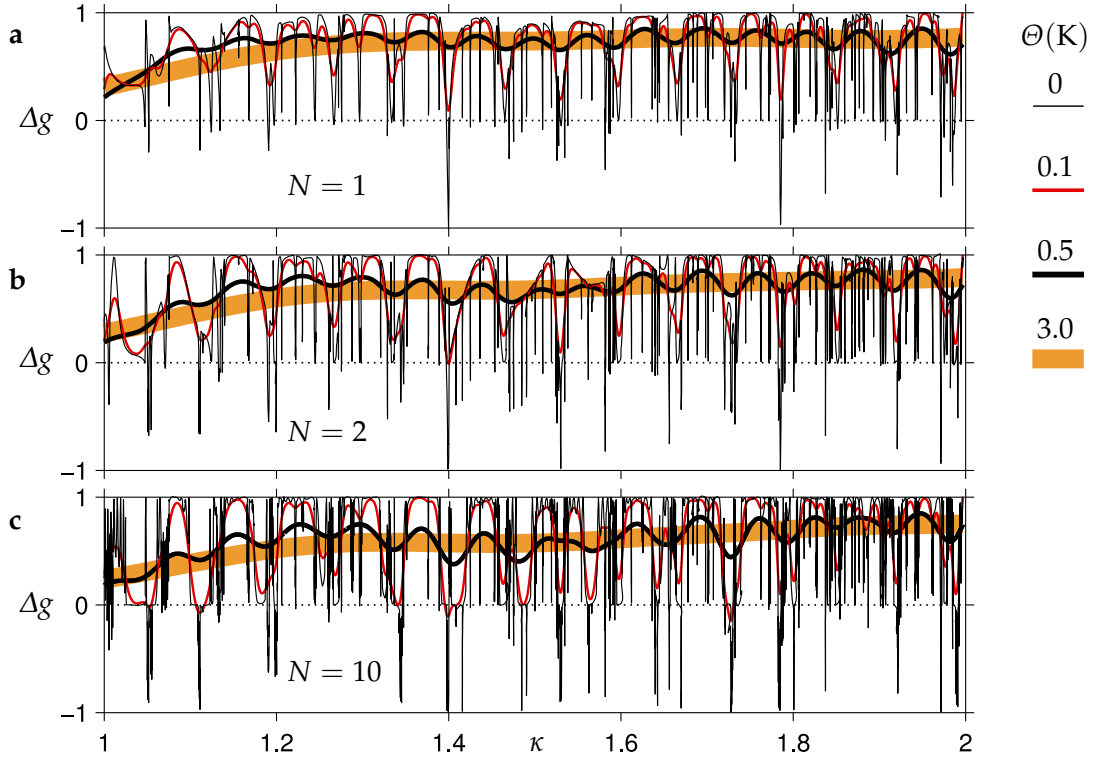


**Figure 6.7:** Conductance switching contrast  $\Delta g = g(B = 0) - g(B = B_s)$  in the first channel for (a) the single soft-wall billiard of Fig. 6.2, and for an array of (b)  $N = 2$  and (c)  $N = 10$  identical billiards connected via bridges (flat point contacts) aligned to the external leads and of common length  $d = w$ , at different temperatures  $\Theta$  (units defined by  $a_0 = 2 \text{ nm}$  and  $m = 0.069 m_e$ ).

so far is compared to a double-dot setup ( $N = 2$ ) and to a longer array of  $N = 10$  connected dots, in the first transport channel. Since  $g(B = B_s)$  is overall very close to zero for finite temperature, the switching contrast essentially coincides here with the field-free conductance,  $\Delta g \approx g(B = 0)$  over most part of the channel. Only in the pure transmission spectrum ( $g(\Theta = 0)$ , thin black line) the smooth background is perturbed by the narrow resonance features; these are in fact also the only energies at which we may have negative transmission switching  $\Delta g(\Theta = 0) < 0$ , while conductance switching is positive,  $\Delta g(\Theta > 0) > 0$ , practically everywhere for any considered temperature.

The connecting ‘bridges’ again consist of simple straight point contacts of zero potential and hard-wall boundaries, aligned with the outer leads and of equal width. As in the oval billiard array of the previous chapter, the dots now act as effective potential barriers of energy-dependent strength and extent. The common length of the bridges is chosen small, equal to their width, so that the induced shape (Breit-Wigner) resonances in the transmission spectrum of the double-dot setup have a large spacing and do not perturb severely the overall high single-dot transmission (recall the dependence of Breit-Wigner peak spacing on bridge length in Fig. 5.6). Indeed, let us concentrate on the  $\Theta = 0.1 \text{ K}$  profiles (red lines) in Fig. 6.7, which essentially show the field-free transmission without the very sharp Fano resonances. The profile for  $N = 1$  is retained in the  $N = 2$  case, with the difference that dips become occasionally deeper and, more importantly for switching, wide peaks now approach unity (corresponding to the bridge induced Breit-Wigner resonances). For the long array of  $N = 10$  dots the formation of bands with  $\Delta g \approx 1$  and gaps with  $\Delta g \approx 0$  is evident. This shows that, at very low temperature, the *maximal* switching contrast of unity can be achieved in the soft-wall billiard array, though restricted to specific and relatively *small* Fermi energy

ranges.

As the temperature is raised, the details of the  $\Delta g$  profiles wash out and the difference in energy variation between different  $N$  is diminished. Ultimately, the variation in  $\kappa$  saturates to a very smooth line for any  $N$  (here around the temperature  $\Theta = 3\text{K}$  for the parameters considered, thick orange lines); the *magnitude* of the line, however, is largest for the single-dot setup. In other words, the finite-temperature switching efficiency in the proposed billiard system does not rely on banded transmission induced by an array geometry (where *resonant* transmission is forced to unity by local periodicity [118]), but rather on the design of the single-dot confinement. This brings the experimental advantage that the transport device, which need only consist of a single dot, can be more easily fabricated at a size below the electronic coherence length (making the utilized coherent transport model more accurate) as well as the elastic mean free path (partly eliminating the need for impurity scattering in the description of the switching effect) for a given heterojunction setup.

## 6.6 Billiard geometry and soft-wall potential variations

Having demonstrated and explained the proposed mechanism for finite-temperature, energy-invariant conductance switching, including the modification of the effect for setups with connected electron billiards, we finally analyze the impact of variations in the shape of the confining potential as well as the soft-wall boundary profile. The shape of the billiard is altered by varying the semi-axes  $a$  and  $b$  of the elliptic boundary, and in order to present the changes in transport properties compactly we utilize the average transmission  $\bar{T} = \int_1^2 T(\kappa) d\kappa$  in the first channel (instead of the full transmission spectra) as a simple estimate of the overall transmittivity through the device.<sup>5</sup> This way we plot the single numbers  $\bar{T}$  for each shape parameter pair  $(a, b)$ , as done in Fig. 6.8(a) for  $B = 0$  and (a') for  $B = B_s$ . As we see, the field-free average transmittivity is largest for smaller  $b$  for any given  $a$ , where the billiard shape is more elongated along the  $x$ -axis and thus increasingly favors the desired forward collimation of the incoming electron wave. As discussed, the spectra in this region have a uniform background close to unity with superimposed sharp resonances of quasi-bound states decoupled from the leads. When  $b$  is increased, more and more billiard states leak into the leads and their multiple interference lead to an increasingly irregular transmission background; Fig. 6.8(a) shows that their channel average decreases almost uniformly in increasing  $b$ , with a global minimum for the largest billiard considered (both  $a$  and  $b$  maximal).

At the switching field  $B = B_s$ , the transmittivity has a global minimum for an intermediate degree of elongation of the billiard, for which the boundary shape combined with the soft wall supports backscattered states similar to the ones analyzed above. The appropriate shape range can here be roughly estimated by the commensurability of the bouncing pattern of classical orbits with a given cyclotron radius of deflection, where also the continuous diffraction of the paths within the wall potential has to be taken into account (see, e.g., classical trajectories computed in Ref. [51, 54]). We see that the global minimum in transmittivity is relatively broad in both  $a$  and  $b$ , meaning that the needed backscattered states are highly present, on average, for a substantial range of elongated shapes around

---

<sup>5</sup> This estimate gives a fairly accurate account of the transport properties relevant for switching for the billiard shape and soft-wall used so far, since the background transmission is practically constant at  $B = 0, B_s$ . This holds also in the immediate vicinity of this setup in parameter space. If the shape is drastically modified, however,  $\bar{T}$  is a rough estimate and the actual background variation in  $T(\kappa)$  (and the corresponding conductance) for every individual case should be considered to conclude on energy-dependent switching contrast; this is done here for sample soft-wall profiles.

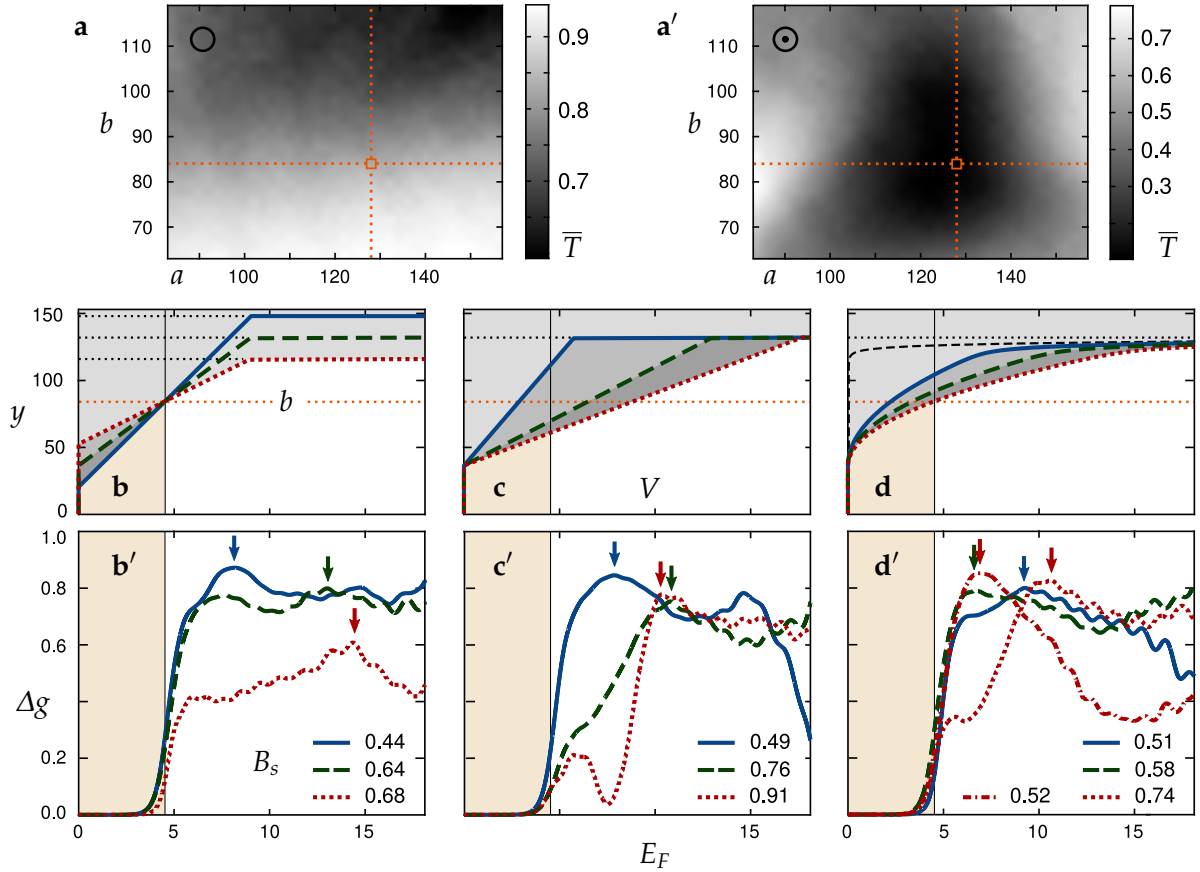


**Figure 6.8:** (a,a'): Mean transmission in the first channel,  $\bar{T}$ , for varying mid-wall semi-axes  $a$  and  $b$  of the billiard with the linear wall potential of Fig. 6.1 (a') with  $d = 96 a_0$ , at (a)  $B = 0$  and (a')  $B = B_s$ . The dotted lines indicate the geometry  $(a, b) = (128, 84) a_0$  chosen in Figs. 6.2, 6.3 and below. (b, c, d): Cross-section  $V(x = 0, y)$  for (b) varying wall width and (c) varying wall slope for a linear wall profile and (d) varying steepness for a parabolic soft wall profile with Wood-Saxon-type [265] boundary (thin dashed line). (b', c', d'): corresponding conductance change  $\Delta g = g_{B=0} - g_{B=B_s}$  at  $k_B \Theta / E_0 = 0.312 \times 10^{-3}$  for optimal switching field strengths  $B_s$  (shown in the legends in units of  $10^{-3} B_0$ ), within the first open channel (channel threshold indicated by vertical lines). Both dotted and dash-dotted lines in (d') correspond to the dotted potential profile in (d), but for different  $B_s$ . Arrows indicate the maximum of each curve. Lengths are in units of  $a_0$ . For  $a_0 = 2 \text{ nm}$  and  $m = 0.069 m_e$ :  $E_0 = 276 \text{ meV}$  and  $\Theta = 1.0 \text{ K}$ .

the one chosen here (indicated by the dotted lines in Fig. 6.8(a,a')). More importantly, this  $(a, b)$ -area of low  $\bar{T}$  at  $B = B_s$  has a large overlap with high  $\bar{T}$  areas at  $B = 0$ . This indicates a high degree of robustness of the conductance switching mechanism against alteration of the dot shape, which would be important in an experimental realization.

For the shape  $(a, b)$  chosen in the previous sections, Fig. 6.8(b', c', d') shows the switching contrast  $\Delta g$  at a reference thermal width  $k_B \Theta$  for the different soft wall profiles shown in Fig. 6.8(b, c, d) (as cross sections along  $y > 0$  at  $x = 0$ ), respectively, including smooth ones (d) that more closely simulate an experimentally fabricated device [18–20]. As expected from the complicated dynamics in the low- $B$  regime where switching is pursued, there is a substantial variability in switching efficiency among the various soft-wall profiles. We stress here that high switching efficiency is achieved for a broad variety of soft wall profiles at substantial thermal width, and relies on the enhanced  $g(B = 0)$  and suppressed  $g(B = B_s)$  of a *single* and relatively *large* billiard (of area  $\gg w^2$ ) containing *many* resonant

levels ( $> 130$  within the first channel at  $B = 0$ ) which become isolated from the leads.<sup>6</sup> The optimal switching field  $B_s$  generally increases with the steepness of the wall potential, in accordance with the stronger confinement of low-energy backscattered billiard states. Further, the various curves demonstrate that optimal switching (maximal  $\Delta g$ , see arrows in Fig. 6.8 (b', c', d')) can be adjusted to different  $E_F$  by changing the soft wall parameters. For certain setups (dotted line in (d)), energy-persistent backscattering (large  $\Delta g$ ) occurs for distinct  $B_s$ -values along separate parts of the channel, meaning that optimal  $E_F$  for switching can be magnetically tuned in this case; see dotted and dash-dotted lines in (d'), showing large  $\Delta g$  in the upper and lower channel half, respectively.

## 6.7 Summary and conclusions

In this chapter we demonstrated a simple way of isolating the magnetically controllable scattering continuum from the manifold of resonant levels of a many-level two-terminal electron billiard, persistently in energy. The underlying mechanism relies on the combined action of an elongated (elliptic) billiard boundary and a designed soft-wall potential, which together decouple quasi-bound states from the attached leads while simultaneously directing forward field-free transport or geometrically rescaling magnetically deflected, backscattered paths. This behavior enables efficient switching of transport over variable Fermi energy from a full conductance quantum (on-state) to practically zero (off-state) by turning on a weak magnetic field.

The experimental realization of the proposed switching device is feasible, e.g., in Ga[Al]As heterostructures by a combination of local oxidation techniques with optical or electron-beam lithography [18–20]. This provides a high precision in lateral dot shape with steep soft-wall potential corresponding to a depletion length  $\sim 15$  nm [19]. The quantum dot can be tuned by additional top or planar gates [18, 19], and large electron mean free paths are achievable at low temperature (e.g.,  $3\text{--}5$   $\mu\text{m}$  at 4.2 K [20]), which is important in order to maintain as high degree of ballisticity as possible [266]. Since the proposed switching device consists of a single dot, its fabrication is also facilitated below the electronic coherence length above  $\Theta \sim 1$  K [18, 71, 118]. Even in the presence of (weak) dephasing, though, the desired switching effect should in fact be enhanced, since it relies on the suppression of resonant interference: In similarity to the thermal averaging taken into account, dephasing would attenuate the Fano extrema [213] and thus contribute to the overall high versus low conductance needed for robust switching.

In conclusion, the proposed setup constitutes an efficient and robust conductance switching device operating at finite temperature, weak magnetic field and over broad Fermi level variation, and is realizable with current experimental techniques.

---

<sup>6</sup> In Ref. [51], a magnetoresistance resonance is caused by cascading of similar backscattered states in an array of smaller billiards (relative to lead openings) with a different kind of soft-wall potential; this resonant property occurs at very low temperature and is attributed to classical dynamics through a parabolic model potential. In Ref. [54], the same peak is attenuated for a single billiard, and another peak appears for  $B = 0$ , lowering switching efficiency. This is in contrast to the mechanism proposed here which relies on decoupling of resonances from an efficiently switchable, energetically robust scattering continuum of a single billiard.



---

# Directional magnetotransport control in multiterminal focusing quantum billiards

---

In this chapter we explore the four-terminal transmission of a semi-elliptic open quantum billiard in dependence of its geometry and an applied magnetic field, and show that a controllable switching of currents between the four terminals can be obtained. Depending on the eccentricity of the semi-ellipse and the width and placement of the leads, high transmittivity at zero magnetic field is reached either through states guided along the curved boundary or focused onto the straight boundary of the billiard. For small eccentricity, attachment of leads at the ellipse foci can yield optimized corresponding transmission, while departures from this behavior demonstrate the inapplicability of solely classical considerations in the deep quantum regime. The geometrically determined transmission is altered by the phase-modulating and deflecting effect of the magnetic field, which switches the pairs of leads connected by high transmittivity. It is shown that the elliptic boundary is responsible for these very special transport properties. At higher field strengths edge states form and the multiterminal transmission coefficients are determined by the topology of the billiard. The combination of magnetotransport with geometrically optimized transmission behavior leads to an efficient control of the current through the multiterminal structure. In particular, the electron flow can be directed from any input terminal to any output terminal at low temperature via the applied magnetic field, and at low field strength a current cross-junction is realizable. The results are partially published in Ref. [267].

## 7.1 From two-terminal to multiterminal conductance control: directional coupling by wave guiding and focusing

In the previous two chapters we demonstrated the ability to control the linear-response electronic current through billiard setups with two outer terminals connected to dephasing electrodes. This controllability was based on the separation of resonant billiard (confined) states weakly coupled to the leads from strongly coupled (leaking) ones through the design of the shape and potential profile of the billiard, and the tunability of the transmission background by a magnetic field (via phase modulation in Chap. 5 and magnetic focusing in Chap. 6). An implicit ingredient of the conductance switching efficiency was the symmetric attachment of the two outer leads on the device region. This way, stationary states at zero magnetic field are assured to be equally coupled to both leads by symmetry, thereby uniformly enhancing or diminishing their transport contribution. Specifically, an incoming

wave in the input lead populating a leaking state will also transmit well into the output lead, with the same terminal interference to energetically neighboring states. The coupling strength symmetry between the two terminals is then broken by the applied magnetic field, thus providing a handle on the conductance switching. Moreover, in two-terminal setups conservation of charge flux ensures that the conductance is symmetric between the terminals (that is, the current from left to right equals that from right to left at the same energy), regardless of the placement of the leads (which can be asymmetric in general) and the complex dynamics within the billiard (such as magnetically deflected paths which are completely different for left and right incoming waves).

This situation changes drastically when more than two leads are attached to the billiard. First of all, any state in the billiard (leaking or confined) will have a finite coupling to all attached leads. This poses a challenge already to the achievement of high transmission between two selected leads, let alone its switching, since in principle a portion of the incoming flux will always escape through the other leads. It is true that resonant states which happen to couple strongly to the chosen two leads will lead to high (though not reaching unity) transmission peaks. Such features do not survive thermal averaging, however, and large conductance relies on the continuous accessibility of states that are coupled to a selected lead pair and decoupled from the other leads. For a fixed billiard potential (that is, without applying localized gates which block lead openings at will), the coupling of the states to two selected leads is governed by the boundary geometry and lead placement which must be appropriately designed; the coupling strength can then be altered via the applied field.

The possibility to magnetically *switch* the current directionally from *any* input lead to *any* other output lead clearly becomes a highly demanding task. The billiard geometry now has to be such that (i) the applied field selectively induces strong coupling to a particular output lead while suppressing the coupling to the other output leads, for a given input lead, and (ii) enables this scheme for any chosen input lead. Apart from the key role of the form of billiard boundary geometry, an important role is here played by the geometrical symmetry of the device, by which the reciprocity relations for multiterminal conductance (see Eq. (2.62)) can be exploited.

We here investigate the transmission behavior of a 4-terminal semi-elliptic quantum billiard in dependence of its geometrical characteristics and examine how an injected wave can be directed selectively to a chosen output terminal using a magnetic field. For the sake of simplicity in recognizing the mechanisms responsible for the transport behavior, we here consider hard-wall boundary confinement. With the (semi-) elliptic geometry chosen, the classical dynamics of the closed billiard is regular, with ballistic particle trajectories divided into so called *librators* and *rotators*, which intersect its major axis at the segment between the foci and the segments between the foci and the boundary, respectively [247,268]. Librators and rotators correspond to quantum eigenmodes [269] localized about the minor semi-axis (also called 'bouncing ball modes') and along the elliptic boundary (also called 'whispering gallery modes' [270]), respectively. Attaching leads to the straight boundary of the semi-ellipse results in a generalized open mushroom [271] (Bunimovich) billiard with multiple stems of infinite length. The chaotic trajectories of the closed mushroom, entering its stems, escape into the leads in the open billiard and contribute to transmission. The crucial role of the convex billiard boundary in the quantum transmittivity of rotator states has been described in Ref. [270] for a 2-terminal semi-circular billiard. It is shown here that the zero-field multiterminal transport between leads attached to the billiard highly depends on the accessibility, through their coupling to these leads, of both liberator and rotator modes.

To analyze this dependence, we calculate the 4-terminal transmission coefficients for varying eccentricity of the semi-ellipse, exploring the dependence of the multilead trans-

mittivity on the curvature of the boundary. The crossover from librator to rotator modes being the dominant transmission mediators is revealed by altering the lead positions along the straight part of the billiard boundary. It is shown that an optimal transmittivity between both pairs of symmetrically placed leads can be achieved by an appropriate choice of eccentricity and lead positioning. This relies on the *guiding* and *focusing* effect of the semi-elliptic boundary on the rotator and librator modes, respectively. For small eccentricity, the placement of attached leads at the foci of the ellipse yields a high corresponding overall transmission coefficient, as would be expected classically. As a result of wave interference and diffraction, though, this condition does not apply for a generic setup, which implies a departure from solely classical considerations. The importance of the rotator and librator modes is further assessed by gradually perturbing the billiard with a circular disk placed on the curved boundary or in the interior.

With restrictions due to symmetry, the magnetic field changes each transmission coefficient differently; the question thus arises whether the multiterminal setup can function as a selective switch between the terminals by tuning the magnetic field, in the sense that transmission of an incoming particle is efficiently favored to specific leads and suppressed to others, as described above. Calculating the multiterminal transmission coefficients of selected setups for varying magnetic field, we show that such output controllability is indeed achieved: Highly efficient directional conductance for any input-output lead pair can be achieved at low temperature, as a consequence of the interplay between the magnetic deflection of electronic orbits, the geometrically induced effects on the scattering wave function, and the partial symmetry of the device.

The chapter is organized as follows. In Sec. 7.2 the geometrical setup of the 2D billiard is specified together with a brief reminder of the basic theoretical and computational framework for multiterminal quantum transport. Section 7.3 summarizes the consequences of the symmetries of the system with respect to the multiterminal transmission. In Sec. 7.4 the main features of the obtained multilead transmission spectra are discussed, along with a description of the underlying mechanisms.<sup>1</sup> This is followed by an analysis of the mean transmission components in dependence of the geometric properties of the billiard in Sec. 7.5. The impact of the magnetic field on transport is discussed in Sec. 7.6, concluding on the induced controllability of transmission to selected output leads. The necessity of the billiard properties for controllable combined output is demonstrated in Sec. 7.7 by comparison to a four-terminal setup of geometrically coupled quantum wires. Finally, the directional switching functionality of the semi-elliptic electron billiard is shown in Sec. 7.8 in terms of the linear conductance at finite temperature. Section 7.9 contains a brief summary and conclusions.

## 7.2 Setup and computational approach

The geometry of the 4-terminal hard-wall billiard is shown in Fig. 7.1. It consists of a semi-ellipse of eccentricity  $\epsilon = \sqrt{1 - b^2/a^2}$ , where  $a$  and  $b$  are the major and minor semi-axes respectively, on the straight border of which four vertical semi-infinite leads of equal width  $w < a/2$  are attached, symmetrically about the minor axis of the ellipse  $x = 0$ . The elliptic boundary is smoothly continued into the outer leads 1 and 2, between which the inner leads 3 and 4 are centered at distance  $l$  from the origin. Recall that the semi-infinite leads attached

---

<sup>1</sup> It is pointed out that the subject of this work are the quantum effects of transport through the four-terminal semiellipse; classical considerations, including the classical librator and rotator trajectories as well as the cyclotron radius of deflected orbits, provide a means of interpretation and comparison of limited validity, since we do not focus on the semiclassical regime.

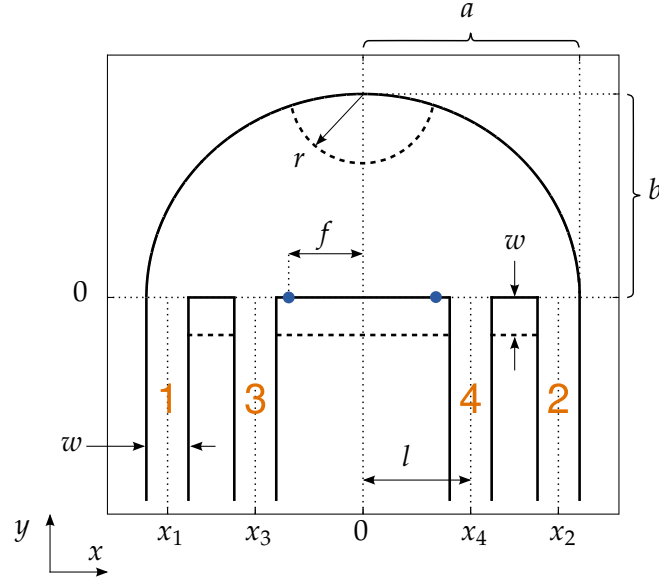


**Figure 7.1:** Geometry of the open billiard with indicated length parameters and lead labeling for eccentricity  $\epsilon = f/a = \sqrt{1 - b^2/a^2} = 0.35$ , lead width  $w = a/5$ , and inner lead positions  $\pm l = \pm a/2$ . The two dots at  $(x, y) = (\pm f, 0)$  are the foci of the (semi-) ellipse and the dashed lines correspond to alternative setups (see text).

to the closed billiard represent the coupling to particle reservoirs, from which there is no reflection back into the billiard.

To calculate the multi-terminal transmission coefficients of the system, Dirichlet boundary conditions are imposed on the scattering wave function along the boundary of the billiard, defined by a hard-wall potential  $V(\mathbf{r})$ .<sup>2</sup> Adapting to our natural units defined by  $\hbar = e = m = a_0 = 1$  (see App. E), the single-particle Hamiltonian is written  $\mathcal{H} = (-i\nabla + \mathbf{A})^2/2 + V(\mathbf{r})$  where the vector potential  $\mathbf{A}$  generates a magnetic field  $\mathbf{B} = \nabla \times \mathbf{A} = B\hat{z}$  which is perpendicular to the plane of the structure and homogeneous over the extent of the billiard area. The incoming electron wave is incident in one of the four leads with energy

$$E = \frac{\mathbf{k}^2}{2} = \frac{1}{2} \left[ (k_y^n)^2 + \left( \frac{n\pi}{w} \right)^2 \right] = \frac{1}{2} \left( \frac{\pi}{w} \right)^2 \kappa^2, \quad (7.1)$$

where  $n = 1, 2, \dots$  labels the subbands of the longitudinal momentum  $k_y^n$  along the unperturbed leads, generated by the transversal confinement to their common width  $w$ . The scaled momentum  $\kappa = kw/\pi = \sqrt{2E}w/\pi$  thus varies continuously in the interval  $n < \kappa < n + 1$  for motion in the  $n$ -th subband. As before, considering electronic transport at a GaAs/AlGaAs ( $m = 0.069 m_e$ ) interface and setting the lattice constant unit to  $a_0 = 2$  nm, the unit of energy becomes  $E_0 = \hbar^2/ma_0^2 = 276$  meV and the unit of field strength  $B_0 = \hbar/ea_0^2 = 164.55$  T; the lengths in the system are scaled by a reference ellipse major semi-axis  $a = 100 a_0 = 200$  nm.

The transmission coefficients  $T_{ij}(E)$  from lead  $j$  to lead  $i$  are given by the Greenian  $\mathcal{G}$  of the system via the multiterminal trace formula

$$T_{ij}(E) = \text{Tr}[\Gamma_i \mathcal{G} \Gamma_j \mathcal{G}^\dagger] \quad (i \neq j) \quad (7.2)$$

with  $\Gamma_i = i[\Sigma_i - \Sigma_i^\dagger]$ , where  $\Sigma_i$  is the partial self-energy due to the  $i$ -th attached lead. For

<sup>2</sup> We here concentrate on the geometric focusing effect of the boundary, separately from the effect of its softness in experimental realizations; the latter quantitatively modifies, but does not eliminate, the geometrically induced transport characteristics, and will not be considered here.

$i = j$ , the reflection coefficient of each lead  $j$ ,  $T_{jj} \equiv R_j$ , is given by the sum rule

$$n(E) = \sum_i T_{ji}(E) = \sum_i T_{ij}(E) = \sum_{i \neq j} T_{ij}(E) + R_j(E), \quad (7.3)$$

where  $n(E) = \text{int}[\kappa(E)]$  (integer part of  $\kappa(E)$ ) denotes here the number of open channels in the leads (of common width  $w$ ) at energy  $E$ , resulting from the unitarity of the scattering matrix of the system. Note that, in the presence of a magnetic field, the magnetoelectric subband thresholds raise in energy with increasing field strength  $B$ : in the bulk of the incoming leads, the energy must overcome the successive Landau levels, which bend upwards in energy when approaching the lead boundaries (see Sec. 1.3 and Fig. 1.5).

The relevant parts of the open system propagator  $\mathcal{G}$  are computed in the tight-binding approximation of the effective (non-Hermitian and energy dependent) Hamiltonian  $\mathcal{H}_{\text{eff}} = \mathcal{H} + \sum_{i=1}^4 \Sigma_i$  using the modular recursive Green function technique presented in Chap. 4. The considered setup is assembled using two types of modules: the semi-elliptic scatterer at constant magnetic field strength  $B$ , and a lead part of length  $30w$  where the magnetic field decreases linearly to zero (its length ensures that we effectively simulate a device in a homogeneous field; see Sec. 3.2.2). The modules are subsequently connected to form the complete setup (consisting of the semi-elliptic module and the four  $B$ -field adaptation modules), with the Green function of the connected modules obtained in each step by solving the associated matrix Dyson by means of the block-Gaussian elimination scheme developed in Sec. 4.5.

From lead-to-interior part of the propagator  $\mathcal{G}$  we also compute the partial local density of states (LDOS) as the diagonal elements of the partial spectral operator  $\mathcal{F}_i$ ,

$$\rho_i(\mathbf{r}, E) = \frac{1}{2\pi} \langle \mathbf{r} | \mathcal{F}_i | \mathbf{r} \rangle = \frac{1}{2\pi} \langle \mathbf{r} | \mathcal{G} \Gamma_i \mathcal{G}^\dagger | \mathbf{r} \rangle, \quad (7.4)$$

corresponding to the scattering probability density resulting from an incoming monochromatic wave of energy  $E$  in lead  $i$ .

### 7.3 Symmetries of the transmission coefficients

Before investigating the multiterminal transmission coefficients in varying geometry and field, we show how symmetries present in the system can be used to reduce the number of independent coefficients to be calculated. Time reversal symmetry (TRS) yields transpose scattering matrix under inversion of the magnetic field (see Sec. 2.2.2), implying for the transmission coefficients [127]:

$$T_{ij}(E; B) = T_{ji}(E; -B). \quad (7.5)$$

This reciprocity relation halves the number of independent transmission coefficients  $T_{i \neq j, j}$  when both field directions are considered. The reflection coefficients  $R_j = T_{i=j, j}$  are given by the sum rule Eq. (7.3) and remain the same under field reversal [cf. Eq. (7.5)], reducing the number of independent coefficients by the number of leads. For a 4-terminal billiard the  $4 \times 4 = 16$  coefficients are thus reduced to 6 independent ones.

In our billiard the spatial reflection symmetry about the  $y$ -axis introduces additional relations between symmetric pairs of leads. If leads  $i$  (at  $x_i$ ) and  $j$  (at  $x_j$ ) are placed symmetrically to leads  $i'$  (at  $-x_i$ ) and  $j'$  (at  $-x_j$ ), then

$$T_{ij}(E; B) = T_{i'j'}(E; -B), \quad (7.6)$$

$T_{ij}(B)$		input lead $j$			
		1	2	3	4
output lead $i$	1	$R_1(B)$	$T_{21}(-B)$	$T_{13}(B)$	$T_{32}(B)$
	2	$T_{21}(B)$	$R_2(B)$	$T_{32}(-B)$	$T_{13}(-B)$
	3	$T_{13}(-B)$	$T_{32}(B)$	$R_3(B)$	$T_{34}(B)$
	4	$T_{32}(-B)$	$T_{13}(B)$	$T_{34}(-B)$	$R_4(B)$

**Table 7.1:** Multiterminal transmission coefficients  $T_{ij}(B)$  from lead  $j$  (columns) to lead  $i$  (rows), deduced from the coefficients  $T_{21}$ ,  $T_{32}$ ,  $T_{13}$  and  $T_{34}$  at magnetic field strength  $B$  (see text). The surrounding boxes of the  $T_{i \neq j}$  correspond to the plotted line types in Figs. 7.3–7.9.

as the equations of motion for a (charged) particle are invariant under the transformation  $(x, B) \rightarrow (-x, -B)$  in the symmetric billiard. Explicitly, we get the two additional relations  $T_{24}(B) = T_{13}(-B)$  and  $T_{41}(B) = T_{32}(-B)$ , reducing the number of independent coefficients to 4 (if  $i' = j$  and  $j' = i$ , this reflection symmetry coincides with the TRS).

In the following, we will work explicitly with the coefficients  $T_{21}$ ,  $T_{32}$ ,  $T_{13}$  and  $T_{34}$  with input in each one of the four leads, because this set serves best for our discussion of the results. In Table 7.1 all transmission coefficients  $T_{ij}(B)$  are explicitly expressed in terms of these four.

## 7.4 Transmission spectra at zero magnetic field

The generic features of the zero-field multiterminal transmission spectra are presented for a geometric setup with relatively high overall transmission between inner leads, since this will prove to be a key property for the desired controllability of output terminal. The  $T_{ij}(\kappa)$  are shown in Fig. 7.2 (A) for  $\kappa$  within the first channel ( $n = 1$ ). All terminal combinations are represented, since their relations in Table 7.1 simplify accordingly for  $B = -B$ . Fig. 7.2 (B) shows the LDOS at selected energies for different leads of incident wave. Note that the presence of interference fringes in a lead signifies back-reflection into that lead.

As we see in  $T_{21}(\kappa)$ , transmission is overall close to unity between the outer leads. This results from rotator modes of the semi-elliptic billiard that would leak into finite stems at the outer lead positions, and therefore are strongly coupled to these leads in the open system. These leaking states constitute non-resonant pathways for transport, whose superposition leads to a high transmission background in  $T_{21}$  [see LDOS in Fig. 7.2 (B) (i,d)], smoothly varying in energy [52, 246].

States weakly coupled to the outer leads [see LDOS in Fig. 7.2 (B) (i,a) and (i,b)] constitute resonant pathways, whose interference with the non-resonant pathways leads to sharp resonances in  $T_{21}(\kappa)$  of width proportional to their coupling, which possess the characteristic Fano lineshape asymmetry [35–37]. In the case of a single non-resonant pathway, the asymmetry is caused by a transmission zero close to the resonant energy, owing to complete destructive interference between the resonant and non-resonant state. In our system each quasi-bound state (resonant pathway) in general couples to multiple multiterminal leaking

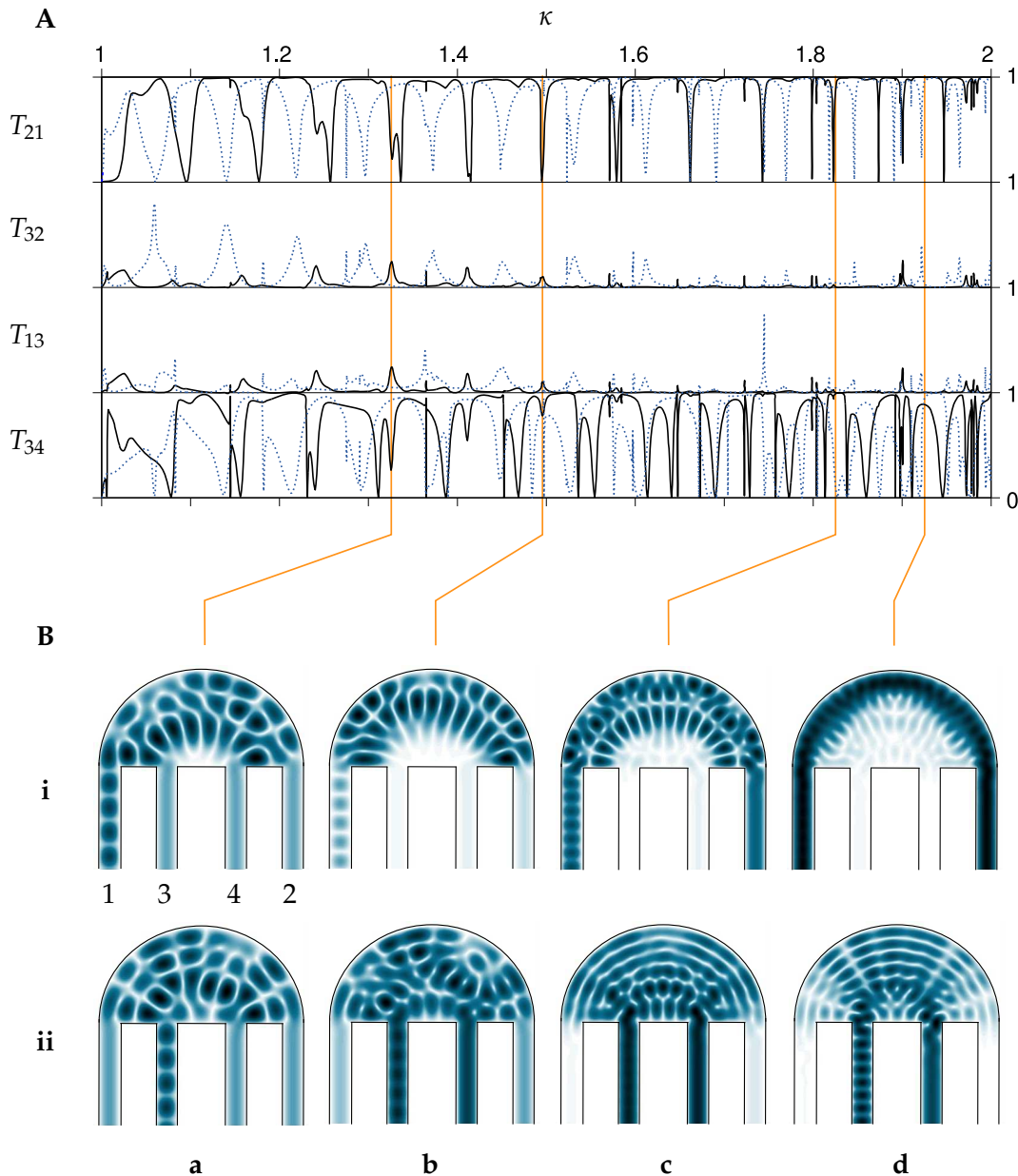


**Figure 7.2:** (A) The four independent transmission coefficients  $T_{ij}$  at zero magnetic field, as a function of the scaled energy  $\kappa = k \cdot w / \pi = \sqrt{2E} \cdot w / \pi$ , for the elliptic ( $\epsilon = \epsilon_3 = 0.35$ , black solid line) and circular (blue dotted line) billiard border, both with  $w = a/5$  and  $l = \epsilon_3 a$ . (B) LDOS for the semi-elliptic billiard at different energies (a), (b), (c), (d) indicated by the vertical lines in (A), with the particle incident in the (i) outer and (ii) inner left lead. The colormap scales with  $\sqrt{\rho(x, y)}$  from white ( $\rho = 0$ ) to black ( $\rho = \max$ ) and is normalized to its maximal value in each plot.

states (non-resonant pathways), which renders the total interference partially destructive and thus raises the minimum of the Fano resonance from zero [35]. Corresponding to the eigenstates of the closed semi-ellipse, the resonances superimposed on the transmission background appear in series of different quasi-periodicity in  $\kappa$ , determined by the quantization of the wave-number of the semi-elliptic modes (in analogy with the detailed description in Ref. [52] for the oval billiard).

The coefficient  $T_{34}$  is also overall high in the first channel for the chosen eccentricity and lead positioning, in this case resulting from the strong coupling mostly of libration modes to the inner leads. The convexity of the boundary plays a crucial role for this behavior, since

it focuses the scattering wave function, incident in an inner lead, around the middle of the straight boundary of the billiard [see Fig. 7.2 (B) (ii,c) at which energy  $T_{34}$  practically reaches unity]. Note that, since the leads in this setup are centered at the foci of the ellipse, classically both librators and rotators intersect the lead openings; quantum mechanically though, there is a larger number of eigenmodes of liblator type with maxima at the foci [269]. Due to interference between these modes, setting  $l = f = \epsilon a$  is not a necessity for the acquired high inner-lead transmission; it depends also on the chosen  $\epsilon$ , as will be shown in Sec. 7.5.

In  $T_{34}$  the sharp resonant dips in the high background are at the same positions as in  $T_{21}$  but generally of different width, arising from the same quasi-bound states coupling with different strength to the inner leads. Also, the Fano minima in  $T_{34}$  are of different height than in  $T_{21}$ , since different non-resonant transport paths are provided by the liblator modes, interfering with the resonant states. For some sharp resonances in  $T_{34}$  (e.g. at  $\kappa \approx 1.145$  and 1.365) the Fano asymmetry is more distinct, as they lie within a dip of the transmission background.

As a consequence of probability flux conservation [Eq. (7.3)], unit transmission in either  $T_{21} = T_{12}$  or  $T_{34} = T_{43}$  leads to vanishing transmission in both  $T_{32} = T_{23} = T_{41} = T_{14}$  and  $T_{13} = T_{31} = T_{24} = T_{42}$ . Thus, transmission between an outer and an inner lead, represented by the coefficients  $T_{32}$  and  $T_{13}$  in Fig. 7.2 (A), is almost zero over the whole channel for the chosen geometric parameters. It exhibits resonant peaks, coinciding with dips for the symmetric lead pairs, albeit of rather low amplitude, since the incoming wave is mostly reflected into the same lead [see Fig. 7.2 (B) (a)] or transmitted to the symmetrically placed lead [see Fig. 7.2 (B) (b)]. As each eigenstate of the semi-elliptic billiard is symmetric, it generically couples with different strength to inner and outer leads; desymmetrized lead positions then lead to lower transmittivity of the corresponding resonant states in the open system [270].

When the eccentricity of the billiard is slightly changed, the eigenstate wavelength in the elliptic coordinates is accordingly modified [269] and consequently the corresponding transmission resonances shift in  $\kappa$ . This is evident in Fig. 7.2 (A) for the semi-circular billiard (dotted cyan line): its area is slightly larger than the semi-ellipse, so that the resonances are shifted to lower  $\kappa$ . The dips in  $T_{21}$  and  $T_{34}$  (or peaks in  $T_{32}$  and  $T_{13}$ ) are overall broader for the semi-circular billiard, owing to the enhanced coupling of its eigenstates to both inner and outer leads. It also shows a pronounced imbalance between  $T_{32}$  and  $T_{13}$  at low energy: resonant transmission is larger from an outer lead to the inner lead which is closer to the opposite outer lead, where rotator modes can be accessed.

## 7.5 Geometry dependent mean transmission

Having presented the zero-field spectral features and their origins, we proceed to investigate the overall multiterminal transmittivity in dependence of the geometry of the setup by computing, for each set of parameters, the channel-integrated mean transmission coefficients

$$\bar{T}_{ij}^{(n)} = \int_{\kappa=n}^{\kappa=n+1} T_{ij}(\kappa) \quad (7.7)$$

of the  $n$ -th transversal subband, which constitute a measure of the overall response of the system upon an incoming wave in one of the leads.

In order to confirm the role of rotator and liblator modes in coupling symmetrically placed leads we first explore the effect of a perturbing disk on the mean transmission coefficients. In Fig. 7.3 the  $\bar{T}_{ij}^{(n=1)} \equiv \bar{T}_{ij}$  (the channel superscript is dropped for  $n = 1$ ) are shown as a function of varying radius of the disk, for three different eccentricities. In Fig. 7.3 (a)

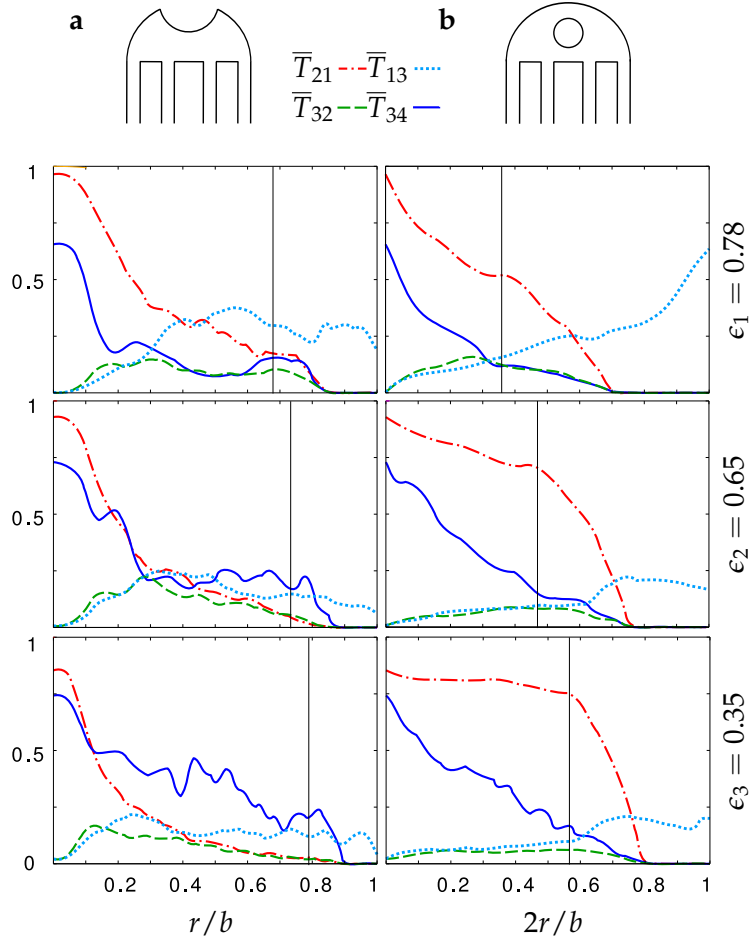


**Figure 7.3:** Zero-field channel-averaged transmission coefficients  $\bar{T}_{ij}$  between terminals  $(i, j) = (2, 1)$  (red dashed-dotted line),  $(3, 4)$  (blue solid line),  $(1, 3)$  (cyan dotted line),  $(3, 2)$  (green dashed line) with lead widths and positions as in Fig. 7.2 and eccentricities (from top to bottom row)  $\epsilon_1 = 0.78$ ,  $\epsilon_2 = 0.65$ ,  $\epsilon_3 = 0.35$ , for the semi-elliptic billiard with a disk inserted in the billiard (a) centered at  $(x, y) = (0, b)$  with radius  $r$  varying from 0 to  $b$  and (b) centered at  $(x, y) = (0, b/2)$  with  $r$  varying from 0 to  $b/2$ . The vertical lines denote the threshold radius  $r_t$  for tunneling within the first channel (see text).

the disk constitutes a circular recess of the elliptic boundary, and in Fig. 7.3 (b) it leaves the boundary of the billiard unperturbed, but partially blocks direct transport in its bulk.

In case (a) the rotator modes are gradually destroyed with increasing  $r$ , because incoming waves from an outer lead are deflected on the concave part of the boundary into the billiard interior (an analogous situation is presented in Ref. [270] for a fixed rectangular cut). Similarly, the librator modes are destroyed since they rely on the focusing ability, predominantly around the  $y$ -axis, of the convex boundary. As a result, the direct pathways between symmetric leads are depleted, leading to an abrupt decrease in  $\bar{T}_{21}(r)$  and  $\bar{T}_{34}(r)$  above a critical disk radius, which is about  $r_c \approx w/3$  for all  $\epsilon$  [note that the scaling  $r/b$  stretches the plots horizontally for larger  $\epsilon$ :  $r_c(\epsilon_1) \approx 0.10b$ ,  $r_c(\epsilon_2) \approx 0.08b$ ,  $r_c(\epsilon_3) \approx 0.06b$ ]. Below this critical disk radius, efficient guiding of rotator modes and focusing of librator modes can be considered robust to boundary perturbations.<sup>3</sup> For smaller  $\epsilon$ ,  $\bar{T}_{34}(r)$  remains

<sup>3</sup> The hard-wall disk barriers considered here represent drastic perturbations of the billiard geometry, constituting device imperfections that modify its transport properties. The more realistic case of disorder from impurity distributions was previously modeled in Chap. 5 and shown to allow for robustness of interference-induced magnetotransport up to a limiting disorder strength.

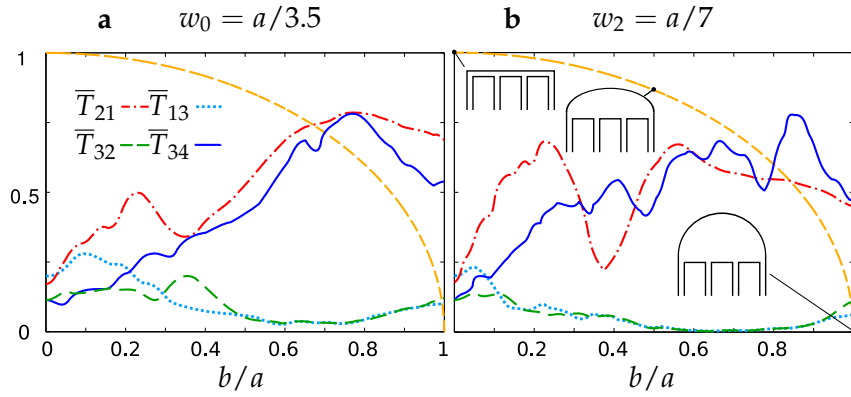


**Figure 7.4:**  $\bar{T}_{ij}$  for varying ratio  $b/a$ , with equidistantly attached leads of width (a)  $w_0 = a/3.5$  and (b)  $w_2 = a/7$ . The light (orange) dashed line shows the eccentricity  $\epsilon$ . The lower horizontal edge of the billiard here lies at  $y = -w$  (see Fig. 7.1), and the upper edge is varied from straight ( $b = 0$ ) to elliptic ( $0 < b < a$ ) to circular ( $b = a$ ), as illustrated by the inset pictures in (b).

substantial over larger  $r$ , since the larger billiard can support a larger number of direct scattering pathways between the inner leads. Deflection on the perturbed boundary enhances scattering to asymmetrically placed leads, leading to increased  $\bar{T}_{32}$  and  $\bar{T}_{13}$  from zero for  $r \neq 0$ .

In case (b) the librator modes are again rapidly destroyed by the disk, resulting in a decrease of  $\bar{T}_{34}(r)$  similar to that in (a). Rotator modes sufficiently localized along the elliptic boundary survive up to some disk size and still connect the outer leads; especially in (b,  $\epsilon_3$ ),  $\bar{T}_{21}(r)$  forms a characteristic high plateau until decreasing abruptly when the remaining free width between disk and boundary becomes smaller than the leadwidth  $w = a/5$ .

The latter condition is met above a threshold radius  $r_t$  given by (a)  $r_t/b = 1 - (5\sqrt{1 - \epsilon^2})^{-1}$  and (b)  $2r_t/b = 1 - 2(5\sqrt{1 - \epsilon^2})^{-1}$ , denoted by vertical lines in Fig. 7.3, at which the energy threshold for transport between opposite sides of the disk enters the first channel in the leads. When this threshold rises above  $\kappa = 2$  (for free width smaller than  $w/2$ ), only tunneling through the constrictions contributes to  $\bar{T}_{21}$ ,  $\bar{T}_{34}$  and  $\bar{T}_{32}$ , which then practically vanish; in contrast,  $\bar{T}_{13}$  is enhanced for large  $r$ , particularly in case (b,  $\epsilon_1$ ). Furthermore, larger number of accessible eigenstates causes more resonant features in the transmission spectra, leading to increased fluctuations of the  $\bar{T}_{ij}$  in continuously varying geometry for larger billiards (row  $\epsilon_3$ ).

Librator- and rotator-like eigenmodes of the billiard were shown to be necessary for high inner and outer lead transmission; nevertheless, their coupling to the leads further depends on the eccentricity of the unperturbed billiard for a given lead positioning. In Fig. 7.4 the  $\bar{T}_{ij}$  are plotted against the ratio  $b/a = \sqrt{1 - \epsilon^2}$  for different  $w$ . In order to access the limit of zero curvature ( $\epsilon = 1$ ), the straight edge of the billiard is lowered by one leadwidth (see dashed line in Fig. 7.1). For the true semi-elliptic setup the features in  $\bar{T}_{ij}(b/a)$  are shifted to larger  $b$  (and thus smaller  $\epsilon$ ), so that the change in size is compensated and the corresponding eigenmodes remain approximately at the same energies.  $\bar{T}_{21}$  and  $\bar{T}_{34}$  overall increase with  $b$ , as rotator- and librator-like modes start to form which couple outer and inner leads; in contrast,  $\bar{T}_{32}$  and  $\bar{T}_{13}$  overall decrease and possess a common broad minimum. For a certain eccentricity range a separation between inner and outer leads is thus possible, in the sense that cross-coupling between them (i.e. between an outer and an inner lead) is almost eliminated in zero magnetic field. Further, depending on  $\epsilon$ , rotator-like modes leaking into the outer leads can interfere into a suppressed transmission background, causing the characteristic wide dip in  $\bar{T}_{21}$  for  $b \approx a/3$ . By decreasing  $w$  the transversal subbands are

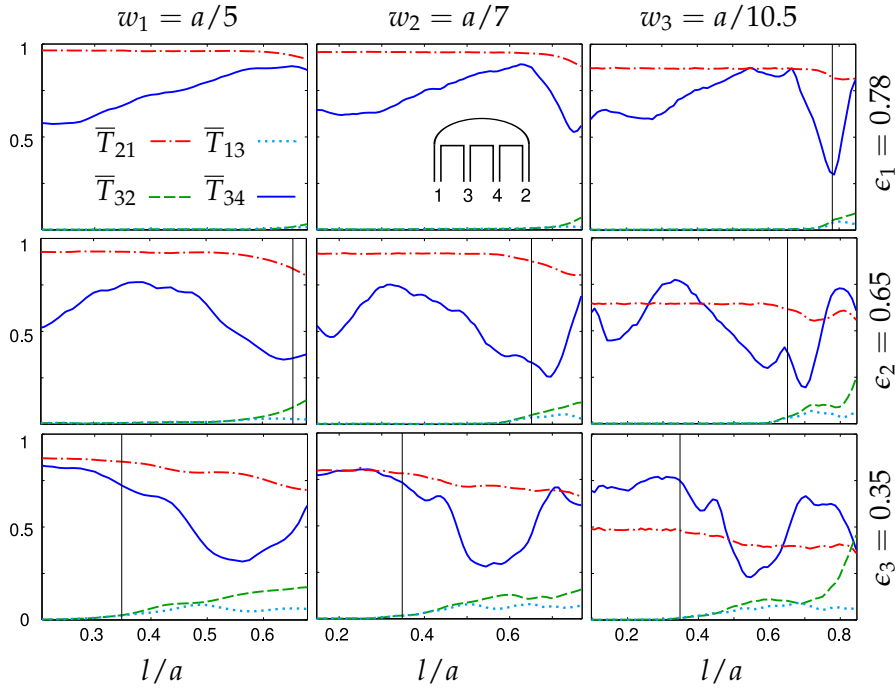


**Figure 7.5:**  $\bar{T}_{ij}$  in the unperturbed semi-elliptic billiard, for lead widths (left to right column)  $w_1 = a/5$ ,  $w_2 = a/7$ ,  $w_3 = a/10.5$  and eccentricities (top to bottom row)  $\epsilon_1 = 0.78$ ,  $\epsilon_2 = 0.65$ ,  $\epsilon_3 = 0.35$ , as a function of the displacement  $l$  of the inner leads from the origin. The vertical lines show the position of the focal points  $f/a = \epsilon$  for each setup.

shifted up in energy and the wavelength of the incoming particle decreases relatively to the billiard size, so that a larger number of eigenstates is spanned within the first channel. This leads to increased fluctuations of the  $\bar{T}_{ij}$  in Fig. 7.4 (b), similar to those in Fig. 7.3 (row  $\epsilon_3$ ).

Let us now investigate the overall transmission behavior in dependence of the placement of the inner leads, which determines their coupling to the different billiard eigenmodes. As the inner leads are moved away from the center, there is a gradual crossover of the direct transport paths from librator- to rotator-type states. The question arises whether it is sufficient, or even necessary, to place the inner leads at the ellipse foci in order to achieve high transmission between them, as shown in Fig. 7.2. In the classical picture the separation of librators and rotators by the focal points is sharp, and in the limit of zero leadwidth, all trajectories coming in from one focus are scattered directly (by only one reflection at the elliptic boundary) to the other, leading to unit transmission. For a finite leadwidth, a portion of the incoming trajectories is scattered onto the straight segments between the leads and eventually into an outer lead, so that the inner lead transmission is lowered from unity. In the quantum case, additionally, the spatial separation between librator and rotator modes is not sharp, especially at the low energies considered; thus, however narrow, the inner leads couple to both types of modes. Most importantly, though, the transmission coefficients highly depend on interference phenomena between the resonant states coupling to the leads. Even if the inner leads are placed close to the foci, where most eigenmodes possess a probability maximum [269], multiple destructive interference between them may lead to low overall transmission.

In Fig. 7.5 the variation of the mean transmission components with the inner lead displacement  $l$  is shown for different leadwidths and eccentricities. For large  $\epsilon$ ,  $\bar{T}_{34}(l)$  increases to maximum when the inner leads are next to the outer ones, though with transport dominated by librator modes since the foci lie within the outer lead openings ( $w_1, \epsilon_1$ ). This trend

is inverted for smaller  $\epsilon$ , where the foci come closer to the origin and allow for the coupling to rotator modes. Then  $(w_1, \epsilon_3)$   $\bar{T}_{34}(l)$  is maximal for the inner leads close to the origin and decreases to minimum for large  $l$ , as a result of destructive interference in combination with diffraction at the lead openings [101]. For narrower leads (columns  $w_2$  and  $w_3$ ) these features remain, with enhanced fluctuations like in Fig. 7.4.

We indeed see that placing the inner leads close to the foci does not necessarily lead to high overall transmission between these leads, demonstrating the departure from the classically expected behavior of our billiard in the deep quantum regime. Some of the setups, in particular of Fig. 7.5 ( $w_3, \epsilon_1$ ), even exhibit a wide minimum in  $\bar{T}_{34}$  around  $l = f$ .

$\bar{T}_{21}(l)$  overall increases with  $w$  and  $\epsilon$ , but remains largely unaffected by the variations in  $l$ . It decreases slightly only when  $l$  is large enough for the inner leads to couple to the same modes as the outer leads, which causes a corresponding increase in  $\bar{T}_{32}$  and  $\bar{T}_{13}$ .

For the magnetic control of multiterminal transmission, to be discussed in the following section, it is important to achieve high inner- and outer-lead zero-field transmission, while cross-coupling is suppressed; we see that these conditions are met in our setup by combining small  $l$  and  $\epsilon$  with relatively large  $w$ .

## 7.6 Transmission in a magnetic field

To understand how conductivity between terminals can be selectively manipulated with the magnetic field, we first analyze its impact on the transmission spectra and its interplay with the geometric properties. In the presence of the field the resonant states accordingly shift in energy [272], while its influence on their phase modifies their coupling to the leads and the interference with other states. Therefore, the widths of sharp Fano resonances generally change, and the non-resonant pathways interfere into a different transmission background. If the field is very weak, the spatial distribution of the eigenmodes remains practically unaffected, as does their individual coupling to the lead openings. A drastic change in the overall transmission in a weak field can still take place, though, when a small number of leaking modes interfere [52]. For a stronger magnetic field the spatial distribution of the states changes enough to generally yield a completely modified transmission spectrum. In the classical picture the charged particle moving in the billiard is deflected into circular orbits of cyclotron (Larmor) radius  $r_L = k/|B|$ , making the classification of trajectories into rotators and librators inapplicable. When the field strength is further increased,  $r_L$  eventually becomes so small that the particle moves along skipping trajectories at the billiard edges [71]. The corresponding quantum scattering wave function is localized into edge states [50], which enable almost reflectionless transport along the boundary.

In Fig. 7.6 (a) the transmission spectra at (i) zero, (ii - iii) intermediate and (iv) high magnetic field strength are shown for the unperturbed billiard. As in Sec. 7.4, the geometry is adjusted for high inner- and outer-lead zero-field transmission; in order to concentrate on magnetically induced spectral changes, even wider leads are used, avoiding increased fluctuations from multiple interference of billiard eigenmodes. The three first channels  $n = 1, 2, 3$  are addressed, showing the typical stepwise increase of (maximal) transmission with  $n$  and the effect of channel mode coupling.  $T_{21}$  and  $T_{34}$  are overall high in the first channel at  $B = 0$  [(a) (iii)], as previously discussed, but get modulated in the higher channels by increasingly wide dips and lowered background transmission caused by multimode interference. The field strength for (a) (ii) is chosen to suppress inner-lead transmission, which enables the control of multiterminal transport, as will be shown in Sec. 7.8. Waves coming in from lead 1 are deflected onto the curved boundary, which decouples them further from the inner leads, reducing the width of the dips in  $T_{21}$ .  $T_{34}$  is overall lowered, since waves

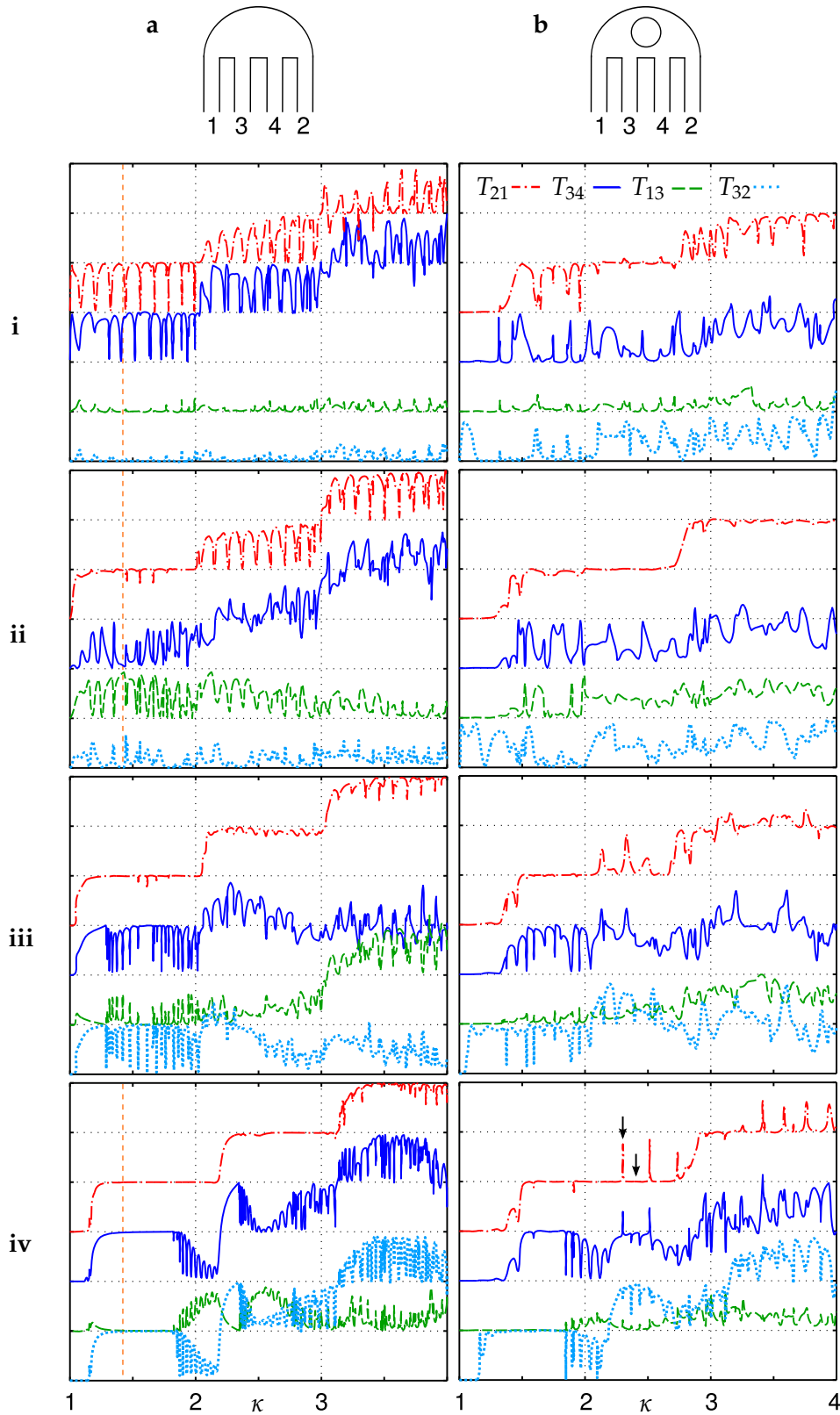


**Figure 7.6:** Transmission coefficients  $T_{21}$  (red),  $T_{34}$  (blue),  $T_{32}$  (green),  $T_{13}$  (cyan), with offsets 3, 2, 1, 0 respectively, as a function of  $\kappa$  within the first three transversal subbands  $n = 1, 2, 3$  of leads of width  $w = w_0 = a/3.5$ , attached equidistantly with  $l = (a - w/2)/3 = 0.84f$ , (a) for the unperturbed semi-ellipse billiard with  $\epsilon = 0.35$  and (b) for the same geometry with a disk of radius  $r = b/2 - 2w/3$  centered at  $(0, b/2)$ , at magnetic field (i)  $B = 0$ , (ii)  $B = 0.002$ , (iii)  $B = 0.005$ , (iv)  $B = 0.010$ , with  $B = B\hat{z}$ . Arrows and vertical dashed lines indicate  $\kappa$ -values at which the LDOS is shown in Figs. 7.7 and 7.10, respectively.



**Figure 7.7:** Partial LDOS corresponding to the  $\kappa$ -values indicated by the (a) left and (b) right arrow in Fig. 7.6 (b) (iv), for a wave incident in the leftmost ( $i = 1$ ) lead.

coming in from lead 4 (containing the right ellipse focus) are no longer focused into lead 3: the librator modes are destroyed in the presence of the deflecting field. On the contrary,  $T_{32} = T_{14}$  is drastically increased and  $T_{12}$  (not shown) is accordingly reduced: the Larmor radius at this field is, approximately, the one needed to deflect classical trajectories from lead 4 into lead 1 (or from lead 2 to lead 3) without reflection at the boundary, for energies in the first channel. This condition is not fulfilled anymore at the even higher field strength in (a) (iii), where edge states start to form. In the first channel, transmission is then favored to the next neighboring lead ( $T_{21}$ ,  $T_{34}$  and  $T_{13} = T_{42}$ ) and suppressed between other lead pairs. The complementarity between the multi-terminal coefficients is here clearly manifest in the coincidence of the dips in  $T_{34}$  and  $T_{13} = T_{42}$  with the peaks in  $T_{32} = T_{14}$ . These resonances appear when the nodal pattern of interfering edge states (or a multiple of the diameter of the classical skipping orbits) matches the distance of leads 2 and 3 instead of adjacent leads (this behavior is described in detail in Ref. [50] for a 2-terminal billiard). In the second and third channel, interference of a larger number of accessible modes enhances again fluctuations in the transmission background. At very high field strength [(a) (iv)] the edge states lie so far apart in energy (and classically  $r_L$  is so small) that plateaus of unit transmission to clockwise subsequent leads appear for energies in the lowest magnetoelectric (Landau) subband. When more edge states are energetically accessible we observe a difference between scattering at smooth and sharp lead openings. Diffraction at the sharp edges causes mixing and interference of the different edge states [50], leading to oscillations in  $T_{34}$ ,  $T_{32}$  and  $T_{13}$ . Only the  $T_{21}$  coefficient exhibits perfect transmission even at higher energy, since the edge states adiabatically follow the smooth elliptic boundary from lead 1 to 2. The stepwise increase of transmission with  $n$ , most pronounced in  $T_{21}$ , is shifted to higher  $\kappa$  with increasing field strength, following the threshold energies of the magnetic subbands.

To illustrate the effects of geometry in combination with the magnetic field on the scattering states, the LDOS at a chosen  $\kappa$  (vertical dashed lines in Fig. 7.6 (a)) is shown later in Fig. 7.10 in connection to directed multiterminal conductance.

As in Sec. 7.5, a disk inside the semi-elliptical billiard drastically changes its transmission properties by blocking direct transport paths between the leads. In Fig. 7.6 (b) the field dependent spectra are shown for this setup, with the disk leaving constrictions of minimal width  $2w/3$  with the boundary. The transmission threshold is then essentially shifted from  $n$  to  $3n/2$ , as can be seen by replacing  $w$  with  $2w/3$  in Eq. (7.1). Thus,  $T_{21}$ ,  $T_{34}$ , or  $T_{32} > n - 1$  below  $\kappa = 3n/2$  results from tunneling of the wave function through the constrictions. Distinct resonant tunneling peaks are seen below this threshold for  $n = 2$  (that is,  $1.5 < \kappa < 3$ ) in  $T_{21}$  and  $T_{34}$  at high field strength [Fig. 7.6 (b) (iii) and (iv)], mediated by edge states that are localized on the disk edges (similar to the states leading to sharp reflection resonances, due to different geometrical setup, in Ref. [106]). The LDOS for an incoming electron wave in the leftmost lead is shown in Fig. 7.7 for such a resonant state (a) and for a state between the resonances (b). The effective resonator length is, approximately, the mean periphery

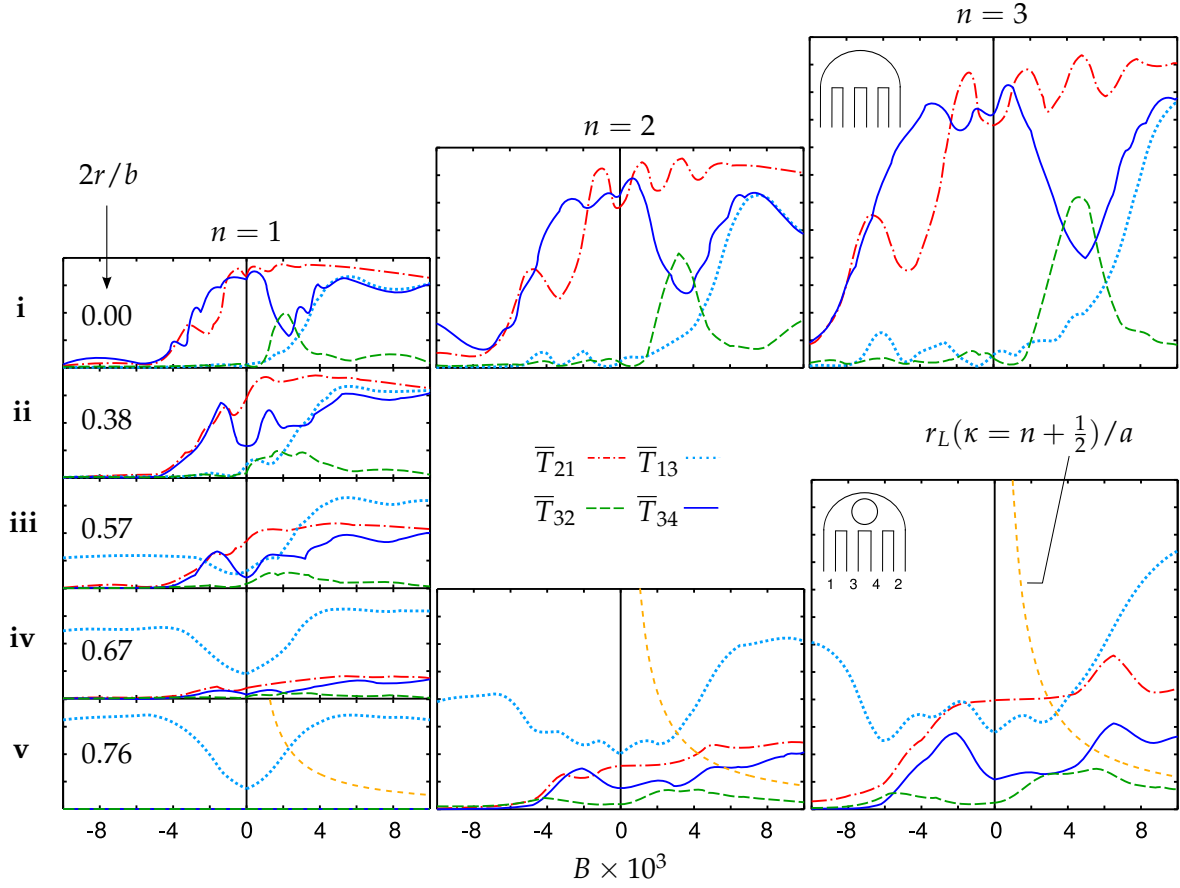


**Figure 7.8:** Mean transmission coefficients  $\bar{T}_{ij}$  as a function of the applied magnetic field  $B$  for the billiard of Fig. 7.6 with increasing disk radius  $r$  in the  $n = 1$  subband (top to bottom panels in left column); for zero and maximal  $r$  (top and bottom row, respectively) also the  $n = 2$  and  $n = 3$  subbands are shown. Each plot is of height  $\max[\bar{T}_{ij}^{(n)}] = n$ . The light (orange) dashed line in the bottom row panels shows the scaled Larmor radius  $r_L/a$  at the  $n$ -th channel's center  $\kappa = n + 1/2$ .

$2\pi(r + w/3)$ , leading to the observed peak spacing  $\Delta\kappa \approx 0.247$  in Fig. 7.6 (b) (iv). On the other hand, scattering upon the disk favors transmission between leads on the same side of it, so that  $\bar{T}_{13}$  overall increases and qualitatively approaches the unperturbed case for strong fields.

In Fig. 7.8 the four independent channel mean components  $\bar{T}_{ij}$  are plotted as a function of  $B$  for different radii  $r$  of the inserted disk [rows (i) to (v)]. The  $\bar{T}_{ij}^{(2)}$  and  $\bar{T}_{ij}^{(3)}$  are shown for  $r = 0$  (unperturbed billiard) and  $r = b/2 - w/3$  (almost divided billiard), where also the Larmor radius  $r_L(B) = \pi/w \cdot (n + \frac{1}{2})/|B|$  at each channel center is plotted to show the field impact on the classical trajectories. In absence of the disk [row (i)],  $\bar{T}_{21}$  is close to unity for  $B \geq 0$ , falling off slowly at large  $B$  as the magnetic threshold enters the channel [see Fig. 7.6 (a) (iv)]. For  $B < 0$  it decreases abruptly with field strength when  $r_L < a$ , since the incoming waves in lead 1 are deflected away from the elliptic boundary.  $\bar{T}_{34}$ , which is also large at  $B = 0$ , decreases to a prominent local minimum at  $B \approx +0.002$ , corresponding to the spectrum in Fig. 7.6 (a) (ii). At the minimum, a large portion of the wave coming from lead 4 is deflected into lead 1, leading to a corresponding maximum in  $\bar{T}_{14}$  [with  $\bar{T}_{14}(B) = \bar{T}_{41}(-B) = \bar{T}_{32}(B)$ , see Table 7.1], which is otherwise close to zero. It is this drastic change at the intermediate field strength  $B \approx +0.002$ , different for each mean transmission component, that will serve as a key property to enable multiterminal transport control for

the geometrical parameters used. At even stronger field the waves from lead 4 follow edge states directly into lead 3, so that  $\bar{T}_{34}$  increases again, while  $\bar{T}_{14} = \bar{T}_{32}$  decreases. For  $B < 0$ ,  $\bar{T}_{34}$  remains high over the local minimum of  $\bar{T}_{21}$  around  $B = -0.002$ , before it too falls off for stronger fields.  $\bar{T}_{13}$ , on the other hand, remains close to zero for all  $B < 0$ , increases with the field strength for  $B > 0$ , and finally follows  $\bar{T}_{34}$  in the edge state regime, where the pathways  $4 \rightarrow 3$  and  $3 \rightarrow 1$  are almost equivalent along the boundary: indeed, the  $T_{34}$  and  $T_{13}$  spectra practically coincide in Fig. 7.6 (a) (iv).

On all  $\bar{T}_{ij}(B)$  curves, though more visible in  $\bar{T}_{21}$  and  $\bar{T}_{34}$ , relatively small fluctuations in  $B$  are superimposed, which can be regarded as generalized collective AB oscillations from interference between spatially extended leaking states: the oscillations in  $T_{ij}(B)$  at each  $\kappa$  add up to a large-scale oscillation of the channel average. The characteristics of  $\bar{T}_{ij}$  remain qualitatively the same in the higher channels (with maximum =  $n$ ), mapped onto a larger  $B$ -scale: at higher energy larger field strength yields the same Larmor radius and similar variations as in  $\bar{T}_{ij}(B)$ . From the above we see that, depending on  $B$ , overall transmission is favored from each lead to certain other leads and suppressed to the rest. We will address this possibility for directed multiterminal transport in detail in Sec. 7.8.

The modification of the  $\bar{T}_{ij}(B)$  profiles by the perturbing disk is shown in Fig. 7.8 (i) to (v), where its radius  $r$  is increased so that transmission between leads on opposite sides is suppressed, as previously described [see Figs. 7.3 (b) and 7.6 (b)]. Thus  $\bar{T}_{21}(B)$ ,  $\bar{T}_{34}(B)$  and  $\bar{T}_{32}(B)$ , although retaining their trends, gradually decrease to zero for any  $B$  when the constrictions become narrower than the leads. In contrast,  $\bar{T}_{13}$  increases with  $r$  at  $B = 0$ , as seen also in Fig. 7.3 (b), and remains large at strong  $B > 0$ . Also at strong  $B < 0$ , though,  $\bar{T}_{13}$  increases with  $r$ , because the edge states (now clockwise deflected classical orbits) can guide the particle from lead 3 onto the disk edge and then onto the elliptic boundary to the left of the disk, which it follows into lead 1. Interestingly, for large enough disk [as in Fig. 7.8 (v), where the constriction width is  $w/3$ ] the 4-terminal billiard is effectively divided into two 2-terminal billiards for  $n = 1$ , so that transmission between leads on the same side of the disk becomes symmetric in  $B$ :  $\bar{T}_{13}(B) = \bar{T}_{13}(-B)$  and  $\bar{T}_{24}(B) = \bar{T}_{24}(-B)$ , as a consequence of the sum rule Eq. (7.3) and the symmetry relation Eq. (7.5) for the special case of a system with two leads [150]. This 2-terminal symmetry is not present in the higher channels [ $n = 2, 3$  in row (v)], where the smaller transversal wavelength enables transport through the constrictions.

Conclusively, the disk reduces the difference between the (independent)  $\bar{T}_{ij}(B)$ , thereby weakening the controllability of multiterminal transmission. Nevertheless, an appropriate disk-like blocking potential switches output from lead 2 to lead 3 (from lead 3 to lead 2) with input in lead 1 (in lead 4) at strong  $B > 0$ , which, in the context of directed transport, constitutes an additional (electric) switching mechanism based on the geometry-independent behavior of edge states.

## 7.7 Bent coupled wires

Magnetically induced directed transport in our setup was shown to rely on the convexity of its boundary, which enables highly transmissive pathways at low field strength by the formation of librator- and rotator-like modes. These coexist in the semi-ellipse, so in order to separately investigate the role of boundary-localized modes in the overall transmission, and the impact of their interference with gradually upcoming bulk modes, we consider the following setup: two circularly bent parallel quantum wires coupled through a smooth opening of adjustable width  $d$  at the bend [see sketch in Fig. 7.9 (a)]. The  $\bar{T}_{ij}(B)$  are plotted in Fig. 7.9 (a) without the opening (top) and for increasing opening width (second from top

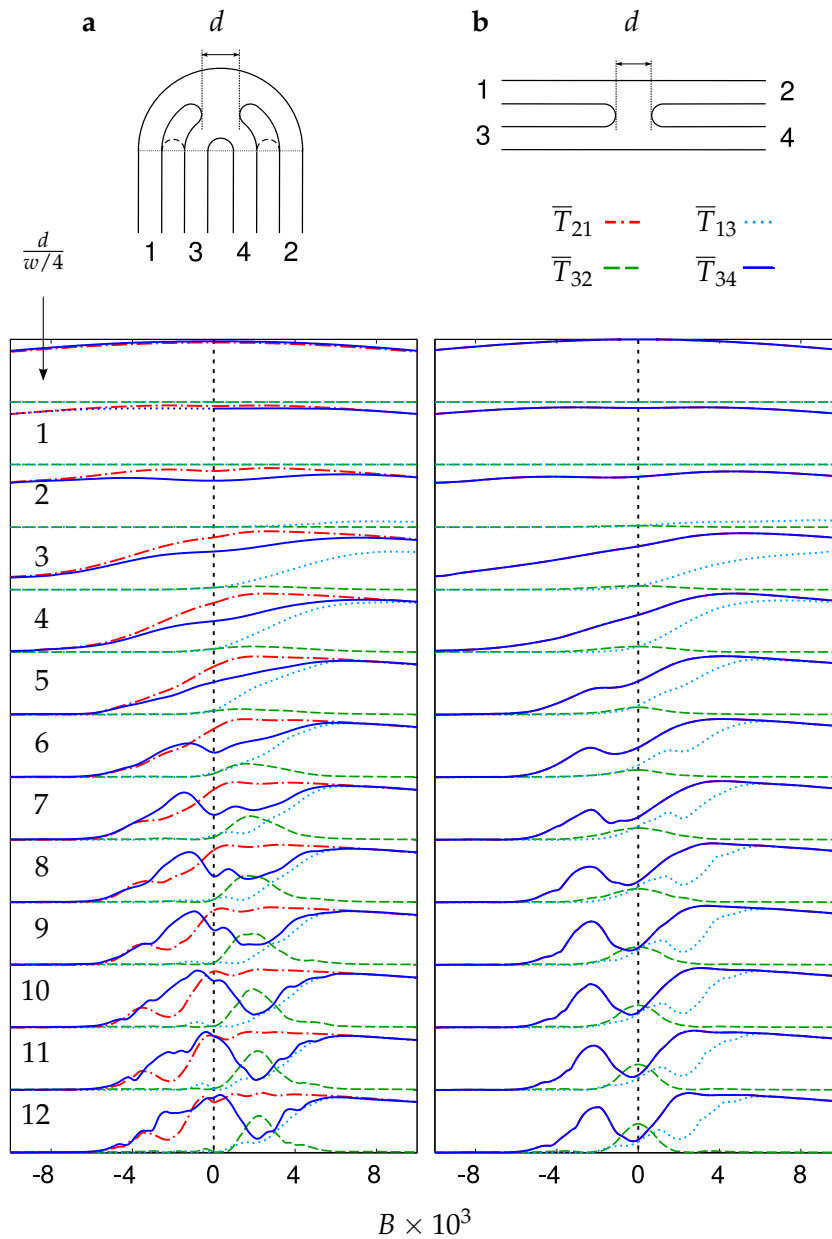


**Figure 7.9:**  $\bar{T}_{ij}(B)$  for two parallel wires at distance equal to their common width  $w = a/3.5$ , coupled by a smooth opening of width  $d$  and circular edges of radius  $w/2$ , (a) with the wires bent by an angle  $\pi$  across the coupling and (b) in straight configuration (parallel and equidistant to the  $x$ -axis). In the top plots there is no opening, and then the opening width is increased in steps of  $w/4$  from  $d = w/4$  to  $d = 3w$  (second from top to bottom, with transmission offsets decreasing by one), the latter yielding in (a) the semi-circular billiard with smooth lead openings.

to bottom), and are compared to the case of straight coupled wires [109, 273] in Fig. 7.9 (b), where curvature is absent and additional  $y$ -symmetry is present. With no opening the transmission in the two disconnected bent wires at  $B = 0$  is almost perfect:  $\bar{T}_{21}$  and  $\bar{T}_{34}$  depart from unity only due to narrow resonances caused by the curvature of the wires, which effectively induces an attractive potential [274].  $\bar{T}_{21}$  is slightly smaller than  $\bar{T}_{34}$ , because the resonances for the longer bent part lie closer in  $\kappa$ . Both slowly decrease at stronger fields, as the magnetoelectric subband threshold rises [like in Fig. 7.6 (a) (iv)]. A detailed study of transmission of similarly bent waveguides in uniform magnetic fields can be found in Ref. [275].

When the wires couple, the 2-terminal  $B$ -symmetry of the isolated wires is broken. As the opening is widened, the rotating modes connecting the outer and inner leads increasingly interfere with states that extend into the opening, leading to enhanced back-scattering dips in the corresponding transmission coefficients and a following decrease in  $\bar{T}_{21}$  and  $\bar{T}_{34}$ . The role of rotator- and libration-like modes is here manifest in the inner-lead transmission as  $d$  is varied at  $B \approx 0$ .  $\bar{T}_{34}$  is high for  $d \approx 0$ , where transport is dominated by rotator-like modes, decreases at intermediate  $d$ , where the rotators are destroyed by the opening in the inner convex boundary, and increases again for large  $d$  ( $\gtrsim 6w/4$ ), where the outer convex boundary focuses the wave function into libration-like modes. At appropriate strength, the magnetic field favors transport between terminals on either side of opening by deflection of the particle orbits.  $\bar{T}_{32}$  increases to a local maximum at intermediate  $B > 0$ , which rises for larger  $d$ .  $\bar{T}_{13}$ , on the other hand, rises significantly only at high  $B > 0$  where the particle is guided by edge states.

For maximal opening  $d = 3w$  the setup becomes the 4-terminal semi-circular billiard, now with smooth lead openings. Controllability of output terminal, as described in Sec. 7.6, then becomes optimal, and the  $\bar{T}_{ij}(B)$  profiles are very similar to the ones in Fig. 7.8 (i). This shows that the smoothness of the lead openings, as well as the small change in eccentricity and size, although clearly affecting the dynamics in the scattering system and thereby the detailed spectral features, leave the overall field dependence qualitatively unchanged.

In Fig. 7.9 (b) the strong field asymptotics of the  $\bar{T}_{ij}(B)$  for the straight coupled wires coincide with those of the bent wires, since transport through edge states is rather affected by the topology, and not by the geometry, of the scatterer. The first obvious difference here is that the additional reflection symmetry about the  $x$ -axis renders the components  $\bar{T}_{21}$  and  $\bar{T}_{34}$ , whose difference was central in the discussion so far, identical. That is, regardless of the field strength, high transmission between the outer leads can never be combined with low transmission between the inner leads, as it can for the bent wires. Also due to spatial symmetry,  $\bar{T}_{32}$  must now be symmetric in  $B$ , and its broad peak around  $B = +0.002$  for the bent wires is shifted to  $B = 0$ . As a result, crossed-lead transmission (between leads 2, 3 or 1, 4) can no longer be switched from high to low by inverting the field. At weak fields,  $\bar{T}_{34}(B)$  varies similarly for bent and straight wires for small  $d \lesssim 6w/4$ ; for large  $d$  though, the straight wires, unlike the bent wires, yield low  $\bar{T}_{34} = \bar{T}_{21}$  around  $B = 0$ , because of the absence of modes that are focused at the lead openings or guide the incoming wave along the boundary. We conclude that the increased symmetry of the straight leads and the absence of the convex boundary reduce the possible combinations of magnetically induced transport directions between the terminals.

## 7.8 Directed conductance

In the discussion so far we have utilized the channel-integrated mean transmission [Eq. (7.7)] as a tool to compactly describe the average response of the transmission to parameter changes. The actual measurable conductance coefficients  $g_{ij}$  connecting the current flowing inwards at terminal  $i$  with the voltage differences to all other terminals  $j$  are, in the linear response regime at temperature  $\Theta$ , given by the multiterminal Landauer-Büttiker formula (see Eq. (2.59)) in units of the (spin-degenerate) conductance quantum  $G_0 = e^2/\pi\hbar$ ,

$$g_{ij}(\Theta; E_F) = \int_{-\infty}^{+\infty} T_{ij}(E) F(\Theta, E_F; E) dE, \quad (7.8)$$

where  $F(\Theta, E_F; E)$  is the thermal broadening function in the form given in Eq. (5.7). Thus,  $g_{ij}$  essentially equals the thermally averaged multiterminal transmission around the electron

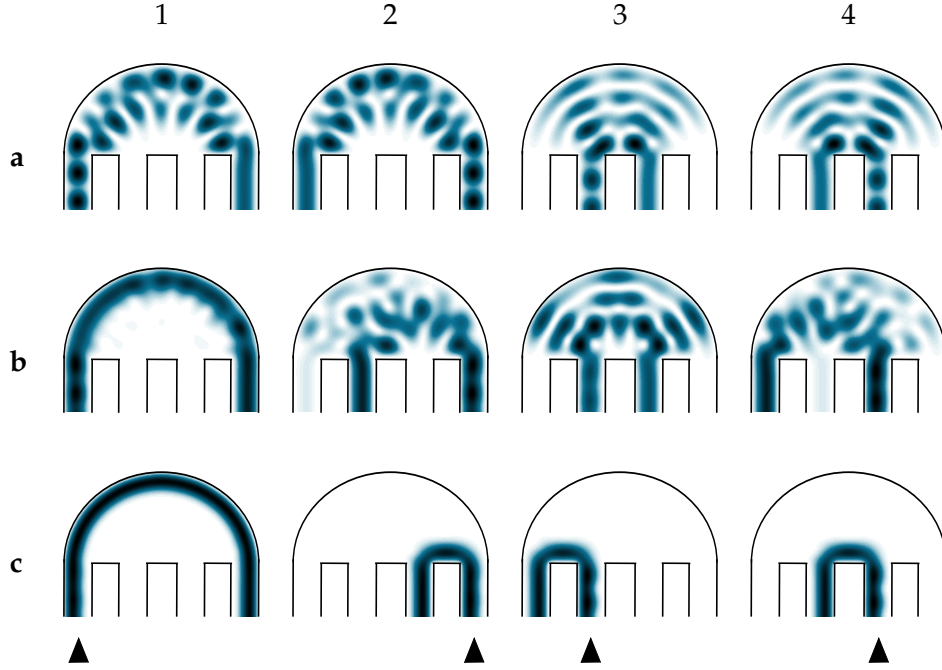


**Figure 7.10:** Partial LDOS for incoming wave in lead  $i = 1, 2, 3, 4$  (indicated by  $\blacktriangle$ ) for (a)  $B = 0$ , (b)  $B = 0.002$ , and (c)  $B = 0.010$  n.u., corresponding to the vertical lines at  $\kappa = 1.425$  in Fig. 7.6 (a) (i), (ii), and (iv), respectively, for the same billiard geometry.

Fermi energy, with a width proportional to  $\Theta$ , and coincides with  $T_{ij}$  at  $\Theta = 0$ .

The output controllability described in Sec. 7.6 can be enhanced in terms of the conductance at low temperature and low Fermi energy, where transmission features are resolved in a smaller  $\kappa$ -range than the whole channel. While the local maxima (minima) of  $\bar{T}_{32}$  and  $\bar{T}_{34}$  in Fig. 7.8 (i) suggest a maximal efficiency for magnetically directed transport of about 50% in the unperturbed elliptic setup, adjusting temperature and Fermi energy appropriately can yield corresponding conductance maxima (minima) close to unity (zero) at these field strengths. To provide an example, we choose the Fermi energy corresponding to  $\kappa = \kappa_F = \sqrt{2E_F} \cdot w / \pi = 1.425$ , indicated by dashed vertical lines in the transmission spectra of Fig. 7.6 (a) (i), (ii), and (iv). The LDOS profiles for electrons incident in each terminal at the corresponding field strengths are shown in Fig. 7.10, revealing the variable directional coupling of the scattering states between the terminals. Note the contribution of rotator- and libration-like states at zero field in Fig. 7.10 (a), the magnetically deflected states at moderate field in (b), and the edge states at strong field in (c). At a temperature  $\Theta = 100$  mK, the resulting conductance coefficients for the same field strengths are shown in Fig. 7.11 as grayscale cells for the individual  $g_{ij}$  ordered like in Table 7.1. The diagonal elements  $g_{ii}$  following from Eq. (7.8) do not contribute to calculated currents, but indicate the degree of reflectance for ballistic transport and show the depart from unity of the sum of conductances from or to the other ( $\neq i$ ) terminals. For the chosen parameters the conductance coefficients practically reach unity (black cells) for specific terminal combinations  $i \rightarrow j$  and practically vanish for the rest (white cells), depending on the direction and strength of the field. In particular, for each input lead  $i$ , the output can be switched selectively to any lead  $j \neq i$  by appropriately tuning  $B$  (as indicated by the sketched arrows in the lower panels of Fig. 7.11). This relies on the above discussed interplay of geometry and magnetic field effects. For large  $|B|$  (see  $B = \pm 0.010$  blocks in Fig. 7.11) edge states form and conductance is determined by the topology of the boundary (in general directed edge state transport can also be implemented, but with finite potential barriers [71, 113, 115] at the lead openings).

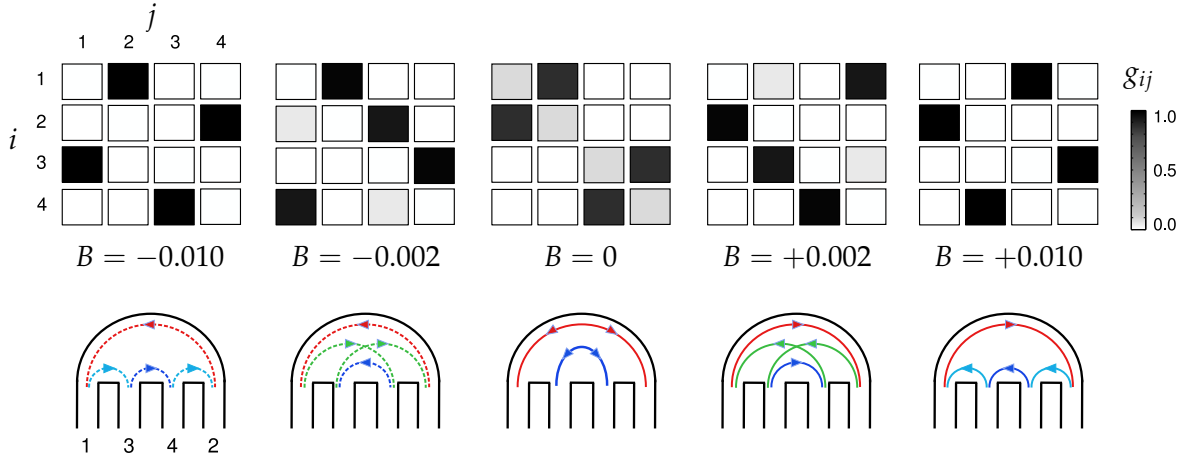


**Figure 7.11:** Multiterminal conductance coefficients  $g_{ij}$  at scaled Fermi energy  $\kappa_F = w/\pi \cdot \sqrt{2E_F} = 1.425$  and temperature  $\Theta = 100$  mK, for  $B = 0$ ,  $B = \pm 0.002$  and  $B = \pm 0.010$ . In each  $4 \times 4$  block, row  $i$  labels the input and column  $j$  the output current terminal. The sketched arrows in the lower panel indicate the directional coupling of electron flow (not trajectories) between the terminals in the billiard (opposite direction to the charge current).

At zero and intermediate  $|B|$  the output is governed by interference of spatially extended scattering states leading, for this billiard, to overall high transmittivity between certain non-neighboring terminals, as seen in the  $B = 0$  and  $B = \pm 0.002$  blocks in Fig. 7.11.

This shows that the current can be efficiently directed from a given input to a selected output terminal. Especially for zero and intermediate magnetic field strength it is even possible to construct a controllable cross-junction for the currents: choosing, e.g., leads 1 and 3 as input terminals and leads 2 and 4 as output, current is flowing from lead 1 to 2 and from lead 3 to 4 for  $B = 0$ . For  $B = +0.002$  current is flowing mostly from lead 1 to lead 4 and from lead 3 to lead 2, thus exchanging the directed connections between the terminals with applied magnetic field.

For higher  $\Theta$  the  $g_{ij}(\Theta; E_F)$  in Fig. 7.11 are generally shifted to more intermediate values, because  $F(\Theta, E_F; E)$  is broadened and additional spectral features are included in the integration around  $E_F$  in Eq. (7.8). On the other hand, for very low  $\Theta$  the transmission spectrum is highly resolved by  $F(\Theta, E_F; E)$  and the  $g_{ij}$  become sensitive to small changes in  $E_F$ . These dependencies are not present in the channel means  $\bar{T}_{ij}^{(n)}$ , which therefore serve to estimate the field strength values suitable for directed transport in a given billiard; with adjusted temperature and Fermi energy, the effect can then be optimized by slightly modifying the transmission features through fine-tuning of  $B$ , in order to controllably obtain maximal and minimal  $g_{ij}$ .

## 7.9 Summary and conclusions

We have investigated the ballistic transport properties and low-temperature magnetoconductance of a 4-terminal semi-elliptic quantum billiard. Analyzing the strong dependency of the transmission on the magnetic field and geometrical parameters like eccentricity of the semi-ellipse and placement and width of the leads, we have shown how electrons can effectively and controllably be guided from one input lead to any other output lead, including the cross-switching of output from combined input.

At zero field strength electrons are guided between the two outer or the two inner leads by modes corresponding to classical rotator or librator trajectories, respectively. The role

of rotator and libration modes has been clarified by introducing a perturbing disk, thereby destroying modes selectively. In this context we have shown that the transmission is robust under small perturbations and that the disk offers additional possibilities of transmission control. The efficiency of the selective transmission has been optimized with respect to the geometric parameters. Here it turns out that the optimal position of the inner leads deviates from the classically expected one at the focal points of the ellipse and that an eccentricity of about 0.35 for equidistant terminals is optimal.

The application of the magnetic field allows to controllably change the conductance coefficients: at appropriate field strengths electrons coming from one input lead can be guided to any other output lead. This results from the deflecting effect of the field at intermediate strength. Further, by increasing the field strength to the edge state regime, conductance is mostly determined by the topology of the billiard. In this regime sharp edges cause mixing and interference of multiple edge states, leading to oscillations in the transmission spectra, while a smooth boundary guides the individual edge states without mixing.

To further examine the role of the elliptic boundary, i.e. of the existence of rotator and libration modes, we have investigated the transmission through a pair of bent coupled quantum wires and compared it to the topological equivalent setup of two straight coupled wires. The bent wires show a degree of control superior to the straight setup, but the semi-ellipse allows for the highest degree of conductance control. While the channel-averaged transmission clearly shows the possibility of directed transport, very high switching efficiency is achieved at low but realistic temperatures and appropriate values of the Fermi energy. The semi-ellipse qualifies as a magnetically controllable cross-junction for ballistic quantum transport.



---

# Summary, conclusions, and perspectives

---

In this thesis the magnetotransport through electronic billiard devices was studied in dependence of the characteristics of the confining potential. Focusing on the interplay between the geometry of the setups and the effects of the magnetic field, it was demonstrated that special non-universal features in the transmission spectra arise which enable the efficient control of conductance by different underlying mechanisms.

## **Review of coherent quantum transport theory of electronic billiard systems**

We started with a top-bottom presentation of the employed theoretical approach to coherent transport in two-dimensional nanoelectronic structures: In Chap. 1 the concepts and methods of band engineering as well as the approximations used to arrive at the two-dimensional electron gas were reviewed, together with the consequences of reduced dimensionality for quantum states. In Chap. 2 we introduced the Landauer-Büttiker picture of transport and the identification of transmission as the main component of conductance, discussing also the associated conceptual issues of modeling attached electrodes and the low-temperature and -bias limits of the theory. In Chap. 3 the treatment of the resulting scattering problem in the Green function framework was selectively reproduced in its general form, highlighting the implications of multiterminal setups with generic asymptotic lead confinement. This gave us the opportunity to discuss the main types of interference-induced phenomena inherent in magnetotransport, namely Fano resonances and Aharonov-Bohm (AB) oscillations, from the viewpoint of billiard systems. We closed this theoretical part with a note on scattering in locally symmetric structures, developed recently for one-dimensional systems.

## **Modular Green function method for multiterminal, multiply connected structures**

The actual numerical method developed for the computation of the system propagator, pertaining to all quantities of interest, was presented in Chap. 4 within the tight-binding approach. We here showed how an extended version of the recursive Green function technique, in which subsystems are inter- and intra-connected into a composite structure, can be formulated uniformly in terms of a block-Gaussian elimination scheme enabling efficient assembly of setups of arbitrary topology. A low-level reordered block-Gaussian elimination scheme was further developed for the core computation of single multiterminal subsystems of arbitrary geometry, with selective output of global quantities (scattering matrix and transmission) as opposed to local ones (wave function and state and current densities). The method is tailor-made for efficient transport computations of planar connected structures

of complex geometry and topology in a highly resolved parameter space. As example setups we studied a three-terminal elliptic billiard and its multiple connection into a looped composite billiard structure. This setup features complex combinations of Fano and AB interference in the resulting multiterminal transmission maps (as a function of energy and magnetic field) as well as characteristic local density patterns.

### **Conductance control by geometric state separation and magnetic phase modulation in quantum billiard arrays**

In Chap. 5 we showed that efficient switching of magnetoconductance in the linear response regime can be achieved with two-terminal linear arrays of oval quantum billiards. The switching effect relies on the property of the single oval to separate confined states from states leaking into the attached leads. The leaking states interfere destructively over a broad energy range causing a suppressed transmission which becomes maximal by the phase modulating effect of a very weak magnetic field. In the array setup Breit-Wigner peaks were distinguished from Fano resonances and analyzed in terms of the local density. The formation of bands in the transmission spectra were shown to enhance the switching ratio which is large already for the double-dot system. The robustness of the conductance control functionality was examined in the presence of weak disorder, showing a temperature dependent lower bound of the switching ratio.

### **Soft-wall billiards as robust and efficient current switching elements at varying Fermi energy and temperature**

In Chap. 6 we supplied a similarly elongated billiard with soft wall boundaries whose appropriate design leads to a very efficient control of the electronic current over the whole first transport channel of the leads. Here the electron flow is forwardly collimated for zero field and backscattered at a certain switching field, persistently in energy. The role of the soft wall is to isolate the resonant manifold of quasi-bound states of the billiard from the scattering continuum and simultaneously to rescale the magnetically deflected path-like states which retain their backscattering character. The mechanism enables enhanced switching contrast at varying temperature and Fermi energy and proves robust against billiard shape and soft-wall variations.

### **Directional quantum magnetotransport by geometric focusing and guiding in multiterminal billiards**

In Chap. 7 we undertook the challenging task of multiterminal conductance control using a hard-wall semi-elliptic billiard with four leads attached to the straight edge, showing that magnetically controllable current switching between the terminals can be obtained. High field-free transmission is here reached via guiding or focusing by the curved billiard boundary which couples rotator and librator modes to the outer and inner leads, respectively. A thorough investigation of this behavior in terms of the geometry parameters and lead positioning was performed concluding on optimal combinations. The lead pairs connected by maximal transmission coefficients are switched by the deflecting effect of the magnetic field. Including the field-free operating state of the device, the electronic flow can be selectively directed from any input terminal to any output terminal. In particular, the device realizes a directional current cross-junction switched by a weak field at low temperatures.

---

In conclusion, it has been demonstrated that efficient and robust electronic current control may be achieved with appropriately designed quantum billiards through the interplay between confinement-induced transmission properties and the effects of applied magnetic fields—from the phase-modulating via the Lorentz-deflecting to the edge-state regime of magnetotransport. The proposed two- or four-terminal conductance switching nanoelectronic elements are of relatively simple geometric form and can be realized with current technologies. In particular, fabrication of such devices should be feasible in GaAs/AlGaAs heterostructures by combining local oxidation techniques with optical or electron-beam lithography [18–21] which enable precise lateral dot shape and steep boundaries, with the shape tuned by additional top or planar gates [18,19] and with size well below the electronic mean free path [20,21]. The work finally gives the message that wave propagation can be tamed into deterministic and tunable transport features even in the deep quantum regime by selectively suppressing universal fluctuation features in favor of desired non-universal behavior.

## Outlook

---

An immediate and promising extension of the present work is to consider combinations of the elements investigated in terms of current control in new types of structures. In particular, the remarkable efficiency of switching induced by certain soft wall profiles in the two-terminal elongated dot makes it tempting to apply a similar soft boundary to the multiterminal setup studied (along its convex boundary) to see if it may stabilize and enhance the cross-junction functionality. Another variation would be to add finite potential barriers or tunable constrictions—which are also easily realizable—to the lead openings in order to investigate alternative aspects of controllability. Indeed, the mechanisms pertaining to conductance control were seen to rely partially on the specific decoupling of billiard states from the leads, and this effect would be enhanced by such modifications. Along these lines, a perspective opened is to explore the occurrence of the very special interference-induced current suppression in the hard-wall oval billiard also for other geometries and potentials: Similar systematic degeneracies of opposite- or equal-parity states might exist for different billiard shapes and lead to tunable regularities in transport. Earlier work by Drouvelis *et al.* [276] here comes to the aid of mapping closed billiard spectra to their shapes.

Keeping the two-dimensional billiard type confinement and multiterminal topology, a departure to qualitatively different effects is possible by adding ‘ingredients’ to the computational method: One of the advantages of the Green function method in its tight-binding form is the straightforward generalization and/or modification to alternative Hamiltonians. For example, the electronic spin can be included essentially by substituting the matrix elements with spinor blocks, opening the perspective to study spin-dependent transport and its possible controllability. Apart from the Zeeman coupling to applied magnetic fields, the different types of states (confined and leaking, bulk- or boundary-localized) seen in the elongated billiards may lead to non-trivial alterations in transport caused by spin-orbit coupling [136,137]. In a similar manner, hybrid structures with superconducting elements and partial Andreev reflection processes [277,278] may be effectively studied in the light of confinement-induced transport control by implementing a Bogoliubov-de Gennes Hamiltonian [279]. Another easy modification of the square lattice Hamiltonian is to appropriately delete on-site and modify hopping elements to transform it to a simple tight-binding honeycomb lattice Hamiltonian to study similar billiards defined on graphene [123,280,281] (the

mathematical grid used so far now becomes a simple approximation to the atomic lattice itself). A more advanced modification would even be to incorporate a Floquet Hamiltonian into the real space one, following the recent work in Ref. [282], to simulate periodically driven (irradiated) billiards. Apart from the above extensions on the level of the system Hamiltonian, a promising perspective would finally be to investigate current controllability and the underlying mechanisms beyond the linear response regime utilizing the full non-equilibrium Green function formalism [3,4,191–193] in a multiterminal setting.

Returning to the presently developed computational tools, and in particular the inter- and intra-connection technique of the extended Green function scheme proposed in Chap. 4, appealing mesoscopic setups to study are multiply dot-connected double quantum wire systems: two straight quantum wires coupled via multiple short lead stubs containing embedded quantum dots. This would implement an array of coupled AB ring-like building blocks [59,283] with four outer terminals, alternatively seen as a nanoelectronic ‘ladder’ setup [111,284], though with nodes and arms of non-trivial geometric structure. The setup would give the opportunity to study the interrelation between Fano and AB interference by modifying the confining potential of the embedded dots (e.g., to separate leaking from confined states, as was done here for a single dot) in multiply connected topologies. An alternative two-terminal looped setup is the electronic Mach-Zehnder interferometer [285] which could be coupled to peripheral quantum dots (thus realizing a Mach-Zehnder-Fano interferometer [286]) in the form of billiards of designed geometries to tune the interference-induced output.

Finally, we recall that the main advantage of the developed inter- and intra-connection Green function method is the ability to connect a large number of few types of arbitrary blocks into multiply connected structures. An interesting perspective would therefore be to explore the (magneto-) transport properties of larger networks of connected quantum dots (or antidot superlattices [227]) with dots of individual internal structure. This type of system reveals the present method as an ideal applicational tool to accompany the intended generalization of the newly developed theory of local symmetries, briefly outlined in Sec. 3.5, to two-dimensional systems. Typical locally symmetric setups would be, e. g., quantum dot lattices with distributed defects in terms of deformed dots or clusters of different dot types. Together with further development of the local symmetry concepts and formalism, such systems may be described and understood from a novel viewpoint and trigger further explorations of complex structures.



# Green functions of leads

In this appendix the spatially represented Green functions of an infinite and semi-infinite ideal lead (quantum wire) are derived, which are used in Secs. 3.2.2 and 4.3.1, respectively.

## A.1 Green function of an infinite Q1D wire

We consider an infinite wire parallel to the  $x$ -direction, described by a confining potential  $V_w(x, y) = V_w(y)$  (in zero magnetic field). Motion along the wire is separated from that in the transversal direction, and the solutions of the stationary Schrödinger equation can be written in the form

$$\Phi_{n,k}(x, y) = \chi_n(y)e^{ikx}, \quad (\text{A.1})$$

where the transversal wave functions  $\chi_n(y)$  are orthonormal solutions of

$$\left[ -\frac{1}{2m} \frac{\partial^2}{\partial y^2} + V_w(z) \right] \chi_n(y) = E_n \chi_n(y), \quad (\text{A.2})$$

and  $k$  is a continuous wave number yielding energy eigenvalues

$$E_{n,k} = E_n + \frac{\hbar^2}{2m} k^2 \quad (\text{A.3})$$

for the total Hamiltonian  $\mathcal{H}_w$ . The transversal potential can be of arbitrary profile, but we assume that it supports bound states along  $y$  and choose the  $\chi_n$  to be real; for the hard-wall leads we will consider, they are given by Eq. (1.27).

The retarded Green function

$$\mathcal{G}^+(\mathbf{r}, \mathbf{r}'; E) = \lim_{\eta \rightarrow 0} \langle \mathbf{r} | \mathcal{G}(E + i\eta) | \mathbf{r}' \rangle \quad (\text{A.4})$$

is given through the spectral representation of  $\mathcal{G}$  in the eigenbasis  $\{\Phi_{n,k}\}$ ,

$$\langle \mathbf{r} | \mathcal{G}(E + i\eta) | \mathbf{r}' \rangle = \sum_{n,k} \frac{\langle \mathbf{r} | \Phi_{n,k} \rangle \langle \Phi_{n,k} | \mathbf{r}' \rangle}{E - \mathcal{H}_w + i\eta} = \sum_{n,k} \frac{\Phi_{n,k}(\mathbf{r}) \Phi_{n,k}^*(\mathbf{r}')}{E - E_{n,k} + i\eta}. \quad (\text{A.5})$$

Inserting Eq. (A.1) into Eq. (A.2) and replacing the sum over continuous  $k$ -values by an integral weighted by the 1D density of states in  $k$ -space, we have

$$\mathcal{G}_{\text{qw}}^+(x, y, x', y'; E) = \lim_{\eta \rightarrow 0} \sum_n \int_{-\infty}^{+\infty} \frac{dk}{2\pi} \chi_n(y) \chi_n(y') \frac{e^{ik(x-x')}}{E - E_n - \hbar^2 k^2 / 2m + i\eta}, \quad (\text{A.6})$$

$$= -\frac{m}{\pi \hbar^2} \lim_{\zeta \rightarrow 0} \sum_n \chi_n(y) \chi_n(y') \int_{-\infty}^{+\infty} dk \frac{e^{ik(x-x')}}{k^2 - k_n^2 (1 + i\zeta)}, \quad (\text{A.7})$$

for the quantum wire, where

$$\frac{\hbar^2}{2m}k_n^2 = E - E_n = \frac{\eta}{\zeta} \quad (\text{A.8})$$

and the integrand has two poles at

$$k_\zeta^\pm = \pm k_n \sqrt{1 + i\zeta} \approx \pm k_n \left(1 + i\frac{\zeta}{2}\right), \quad \zeta \rightarrow 0 \quad (\text{A.9})$$

which are located in the upper (+) and lower (−) half plane.

The integral can now be solved by contour integration: For  $x > x'$  ( $x < x'$ ), the integrand is bounded in the upper (lower) half plane since  $e^{ik(x-x')} \propto e^{\mp \text{Im}k|x-x'|}$  with  $\text{Im}k > 0$  ( $\text{Im}k < 0$ ), and we define a semicircular anticlockwise (clockwise) integration contour which encloses the pole at  $k_\zeta^+$  ( $k_\zeta^-$ ) with the straight segment on the real  $k$ -axis. With the contribution from the semicircular arcs vanishing at  $|k| \rightarrow \infty$ , the integral evaluates, from the residues  $R^\pm$  of the poles at  $k_\zeta^\pm$ , respectively, to

$$\pm 2\pi i R^\pm = \pm 2\pi i \lim_{k \rightarrow k_\zeta^\pm} (k - k_\zeta^\pm) \frac{e^{ik(x-x')}}{(k - k_\zeta^+)(k - k_\zeta^-)} = \pm 2\pi i \frac{e^{ik_\zeta^\pm(x-x')}}{k_\zeta^\pm - k_\zeta^\mp}, \quad x \gtrless x' \quad (\text{A.10})$$

$$= \frac{2\pi i}{2k_n \sqrt{1 + i\zeta}} e^{ik_n \sqrt{1 + i\zeta} |x-x'|} \xrightarrow{\zeta \rightarrow 0} \frac{i\pi}{k_n} e^{ik_n |x-x'|} \quad \forall x, x', \quad (\text{A.11})$$

where in the end the limit required in Eq. (A.4) is taken. We thus finally obtain

$$\mathcal{G}_{\text{qw}}^\pm(x, y, x', y'; E) = \pm \sum_n \frac{1}{i\hbar v_n} \chi_n(y) \chi_n(y') e^{\pm ik_n |x-x'|}, \quad (\text{A.12})$$

where  $v_n = \hbar k_n / m = \sqrt{2(E - E_n) / m}$  is the longitudinal velocity in the  $n$ -th channel. Here also the advanced Green function has been included through the reciprocity relation  $\mathcal{G}^- = [\mathcal{G}^+]^*$ , where we notice the symmetry in  $\mathbf{r} \leftrightarrow \mathbf{r}'$  for each  $\mathcal{G}_{\text{qw}}^\pm$ .

For a given position  $x'$  of the initial point relative to the position  $x$  of the final point along the wire,  $\mathcal{G}_{\text{qw}}^+$  in Eq. (A.12) can be viewed as an  $(x, y)$ -dependent wave function expanded in the eigenstates  $\Phi_{n,k}(x, y)$  of the wire, with  $(x', y')$ -dependent expansion coefficients [124]; or vice versa for  $\mathcal{G}_{\text{qw}}^-$ . Considering, for definiteness, the retarded Greenian, we have

$$\mathcal{G}_{\text{qw}}^+(x, y, x', y'; E) = \sum_n \Phi_{n,s}(x, y) c_{n,-s}(x', y'), \quad (\text{A.13})$$

where

$$c_{n,s}(x', y') = \frac{\Phi_{n,s}(x', y')}{i\hbar v_n}, \quad s = \begin{cases} +, & x > x' \\ -, & x < x' \end{cases}, \quad (\text{A.14})$$

with  $\Phi_{n,\pm} = \Phi_{n,\pm k_n}$ . In view of the general discussion on Green functions, this superposition of wire eigenstates is the response of the system at  $(x, y)$  to a  $\delta$ -like excitation at  $(x', y')$  at energy  $E$ . If these partial waves, while generated at  $(x', y')$ , are additionally transmitted through or reflected by some obstacle, then their total amplitudes upon reaching  $(x, y)$  will be modified by corresponding transmission or reflection amplitudes. This is the case for the  $S$ -matrix elements entering Eq. (3.38).

## A.2 Interface Green function of a semi-infinite Q1D wire

For a semi-infinite quantum wire in the positive  $x$ -direction starting at  $x = 0$ , like the leads attached to the scatterer domain in modeling a transport device, we theoretically assume  $V(x < 0, y) = \infty$  so that the wave function vanishes for  $x < 0$  and thus obeys the Dirichlet boundary condition  $\Phi(x = 0, y) = 0$ .

The stationary Schrödinger equation now has eigensolutions

$$\Phi_{n,k}(x, y) = \chi_n(y) \sin(kx), \quad (\text{A.15})$$

where the transversal wave functions  $\chi_n(y)$  form an orthonormal set, like in the infinite wire, and are chosen real in the absence of a magnetic field. Considering hard-wall leads of width  $w$ , the transversal modes are given by Eq. (1.27). In practice, however, we will set the origin  $y = 0$  at the lead boundary (the right boundary when viewed in the  $x$ -direction) so that the modes are phase shifted into

$$\chi_n(y) = \sqrt{\frac{2}{w}} \sin(k_{y,n}y), \quad k_{y,n} = \frac{n\pi}{w}. \quad (\text{A.16})$$

The retarded Green function is thus given by

$$\mathcal{G}_{\text{sqw}}^+(x, y, x', y'; E) = \lim_{\eta \rightarrow 0} \sum_n \int_0^{+\infty} \frac{dk}{\pi} \chi_n(y) \chi_n(y') \frac{\sin(kx) \sin(kx')}{E - E_n - \hbar^2 k^2 / 2m + i\eta}, \quad (\text{A.17})$$

where two counter-propagating waves with wavenumbers  $\pm k$  have been taken into account for the standing wave along the wire.

Since we aim at the interface part of the lattice Greenian only (at sites adjacent to the surface sites of the scatterer domain) which is used for the self-energy in Sec. 4.3.1, we set  $x = x' > 0$  [127] (the value is specified shortly). This  $x$ -local part can then be written

$$\mathcal{G}_{\text{sqw}}^+(x, y, x, y'; E) = \lim_{\eta \rightarrow 0} \sum_n \int_{-\infty}^{+\infty} \frac{dk}{\pi} \chi_n(y) \chi_n(y') \frac{1 - e^{2ikx}}{E - E_n - \hbar^2 k^2 / 2m + i\eta} \quad (\text{A.18})$$

$$= -\frac{m}{4\pi\hbar^2} \lim_{\varsigma \rightarrow 0} \sum_n \chi_n(y) \chi_n(y') \int_{-\infty}^{+\infty} dk \frac{1 - e^{2ikx}}{k^2 - k_n^2(1 + i\varsigma)}, \quad (\text{A.19})$$

with the substitution  $\hbar^2 k_n^2 / 2m = E - E_n = \eta / \varsigma$ , where the identity

$$2i \sin(kx) = e^{ikx} - e^{-ikx} \Rightarrow 4 \sin^2(kx) = 1 - e^{2ikx} + 1 - e^{-2ikx} \quad (\text{A.20})$$

and the symmetry of  $\sin^2(kx)$  in  $k$  have been used.

The integral has the same poles  $k_{\varsigma}^{\pm} = \pm k_n \sqrt{1 + i\varsigma}$  as for the infinite wire, but now  $x > 0$  so the contour integration is performed only in the upper half of the complex  $k$ -plane. In similarity to the calculation in Eqs. (A.10) and (A.11), the residue theorem yields

$$\mathcal{G}_{\text{sqw}}^+(x, y, x, y'; E) = -\sum_n \frac{2}{\hbar v_n} \chi_n(y) e^{ik_n x} \chi_n(y') \quad (\text{A.21})$$

after rewriting  $1 - e^{2ik_n x} = e^{ik_n x} (e^{-ik_n x} - e^{ik_n x}) = 2ie^{ik_n x} \sin(k_n x)$ .

On the tight-binding lattice, the gridpoints along the edge of the semi-infinite lead (at the interface to the scatterer) are located at  $x = a_0$  [127], that is, one lattice constant away from where the grid-represented wave function (A.15), with the Q1D energy dispersion (4.26), is set to zero (at the first gridpoints outside the lead, which coincide with the last gridpoints

of the attached scatterer). Taking into account also the mode velocity  $v_n = 2ta_0 \sin(k_n a_0) / \hbar$  (see Eq. (4.27)), the retarded and advanced semi-infinite lead Green functions along the lead edge become

$$\mathcal{G}_{\text{sqw}}^{\pm}(a_0, y, a_0, y'; E) = -\frac{1}{ta_0} \sum_n \chi_n(y, E) e^{\pm i k_n(E) a_0} \chi_n(y', E) \equiv g^{\pm}(y, y', E), \quad (\text{A.22})$$

or, in the matrix element notation of Chap. 4,

$$\mathbf{g}_{\alpha\beta}^{\pm} = -\frac{1}{t} \sum_n \chi_{n;\alpha} e^{\pm i k_n a_0} \chi_{n;\beta} \quad (\text{A.23})$$

for (any) sites  $\alpha, \beta$  along the edge, where the lattice constant  $a_0$  has been absorbed in the matrix  $\mathbf{g}^{\pm}$  on the uniform grid.

---

# Block-matrix inversion and Schur complement

---

In this appendix we derive the inverse of a general block matrix in terms of its individual blocks, a tool of matrix algebra appearing recurrently in the computation of lattice Greenians of composite systems. The application to a general decomposition of a lattice Hamiltonian matrix is included for clarity.

## B.1 Inversion by block-Gaussian elimination

Consider a square  $N \times N$  matrix  $\mathbf{M}$  which has the block structure

$$\mathbf{M} = \begin{pmatrix} \mathbf{A} & \mathbf{B} \\ \mathbf{C} & \mathbf{D} \end{pmatrix} \quad (\text{B.1})$$

where  $\mathbf{A}$  is an  $(N - n) \times (N - n)$  matrix and  $\mathbf{D}$  is an  $n \times n$  matrix.

If existent, the inverse  $\mathbf{M}^{-1}$  of  $\mathbf{M}$ , with  $\mathbf{M}\mathbf{M}^{-1} = \mathbf{M}^{-1}\mathbf{M} = \mathbf{I}_N$ , where  $\mathbf{I}_N$  is the  $N \times N$  identity matrix, can be found by block-Gaussian elimination which is equivalent to multiplying the equation

$$\begin{pmatrix} \mathbf{A} & \mathbf{B} \\ \mathbf{C} & \mathbf{D} \end{pmatrix} \mathbf{M}^{-1} = \begin{pmatrix} \mathbf{I}_{N-n} & \mathbf{0} \\ \mathbf{0} & \mathbf{I}_n \end{pmatrix} \quad (\text{B.2})$$

from the left by suitable matrices depending on whether the lower block of the first block-column or the upper block of the second block-column is to be eliminated initially. We call these procedures ‘lower-major’ and ‘upper-major’ elimination, respectively.

### Lower-major elimination

For lower-major elimination, we multiply Eq. (B.2) from the left by the matrix product

$$\mathbf{P}_B \mathbf{P}_D \mathbf{P}_C \mathbf{P}_A, \quad (\text{B.3})$$

with

$$\mathbf{P}_A = \begin{pmatrix} \mathbf{A}^{-1} & \mathbf{0} \\ \mathbf{0} & \mathbf{I}_n \end{pmatrix}, \quad \mathbf{P}_B = \begin{pmatrix} \mathbf{I}_{N-n} & -\mathbf{A}^{-1}\mathbf{B} \\ \mathbf{0} & \mathbf{I}_n \end{pmatrix} \quad (\text{B.4})$$

$$\mathbf{P}_C = \begin{pmatrix} \mathbf{I}_{N-n} & \mathbf{0} \\ -\mathbf{C} & \mathbf{I}_n \end{pmatrix}, \quad \mathbf{P}_D = \begin{pmatrix} \mathbf{I}_{N-n} & \mathbf{0} \\ \mathbf{0} & \mathbf{S}_A^{-1} \end{pmatrix},$$

where

$$\mathbf{S}_A = \mathbf{D} - \mathbf{C}\mathbf{A}^{-1}\mathbf{B} \quad (\text{B.5})$$

is the Schur complement [243] of the block  $\mathbf{A}$  in  $\mathbf{M}$ . Consecutive multiplication from the left by the matrices  $\mathbf{P}_A, \mathbf{P}_C, \mathbf{P}_D, \mathbf{P}_B$  introduces blocks  $\mathbf{I}_{N-n}, \mathbf{0}, \mathbf{I}_n, \mathbf{0}$  in the positions  $\mathbf{A}, \mathbf{C}, \mathbf{D}, \mathbf{B}$  of the original matrix  $\mathbf{M}$ , respectively, thus constituting the block-Gaussian elimination procedure starting with the left block-column. Provided that  $\mathbf{A}$  and  $\mathbf{S}_A$  are invertible, the result is

$$\mathbf{M}^{-1} = \mathbf{P}_B \mathbf{P}_D \mathbf{P}_C \mathbf{P}_A = \begin{pmatrix} \mathbf{A}^{-1} + \mathbf{A}^{-1} \mathbf{B} \mathbf{S}_A^{-1} \mathbf{C} \mathbf{A}^{-1} & -\mathbf{A}^{-1} \mathbf{B} \mathbf{S}_A^{-1} \\ -\mathbf{S}_A^{-1} \mathbf{C} \mathbf{A}^{-1} & \mathbf{S}_A^{-1} \end{pmatrix}, \quad (\text{B.6})$$

showing that the lower diagonal block of the inverse matrix equals the inverse of the Schur complement of the upper diagonal block of the original matrix.

The first three steps of the *full* lower-major elimination, multiplying by  $\mathbf{P}_D \mathbf{P}_C \mathbf{P}_A$ , requires two matrix inversions  $\mathbf{A}^{-1}$  and  $\mathbf{S}_A^{-1}$  and constitutes a *forward elimination* which brings  $\mathbf{M}$  to an upper-triangular form. The last step of multiplying by  $\mathbf{P}_B$  is called *backward substitution* and consists in substituting the already computed outcome of the forward elimination into the final inverse  $\mathbf{M}^{-1}$ , which requires matrix multiplications but no further matrix inversion.

### Upper-major elimination

For upper-major elimination, we multiply Eq.(B.2) from the left by the matrix product

$$\mathbf{P}'_C \mathbf{P}'_A \mathbf{P}'_B \mathbf{P}'_D, \quad (\text{B.7})$$

with

$$\mathbf{P}'_A = \begin{pmatrix} \mathbf{S}_A^{-1} & \mathbf{0} \\ \mathbf{0} & \mathbf{I}_n \end{pmatrix}, \quad \mathbf{P}'_B = \begin{pmatrix} \mathbf{I}_{N-n} & -\mathbf{B} \\ \mathbf{0} & \mathbf{I}_n \end{pmatrix} \quad (\text{B.8})$$

$$\mathbf{P}'_C = \begin{pmatrix} \mathbf{I}_{N-n} & \mathbf{0} \\ -\mathbf{D}^{-1} \mathbf{C} & \mathbf{I}_n \end{pmatrix}, \quad \mathbf{P}'_D = \begin{pmatrix} \mathbf{I}_{N-n} & \mathbf{0} \\ \mathbf{0} & \mathbf{D}^{-1} \end{pmatrix},$$

where

$$\mathbf{S}_D = \mathbf{A} - \mathbf{B} \mathbf{D}^{-1} \mathbf{C} \quad (\text{B.9})$$

is the Schur complement of the block  $\mathbf{D}$  in  $\mathbf{M}$ . Consecutive multiplication from the left by the matrices  $\mathbf{P}'_D, \mathbf{P}'_B, \mathbf{P}'_A, \mathbf{P}'_C$  introduces blocks  $\mathbf{I}_n, \mathbf{0}, \mathbf{I}_{N-n}, \mathbf{0}$  in the positions  $\mathbf{D}, \mathbf{B}, \mathbf{A}, \mathbf{C}$  of the original matrix  $\mathbf{M}$ , respectively, thus constituting the block-Gaussian elimination procedure starting with the right block-column. Provided that  $\mathbf{D}$  and  $\mathbf{S}_D$  are invertible, the result is

$$\mathbf{M}^{-1} = \mathbf{P}'_C \mathbf{P}'_A \mathbf{P}'_B \mathbf{P}'_D = \begin{pmatrix} \mathbf{S}_D^{-1} & -\mathbf{S}_D^{-1} \mathbf{B} \mathbf{D}^{-1} \\ -\mathbf{D}^{-1} \mathbf{C} \mathbf{S}_D^{-1} & \mathbf{D}^{-1} + \mathbf{D}^{-1} \mathbf{C} \mathbf{S}_D^{-1} \mathbf{B} \mathbf{D}^{-1} \end{pmatrix}, \quad (\text{B.10})$$

showing that the upper diagonal block of the inverse matrix equals the inverse of the Schur complement of the lower diagonal block of the original matrix.

The first three steps of the *full* upper-major elimination, multiplying by  $\mathbf{P}'_A \mathbf{P}'_B \mathbf{P}'_D$ , requires two matrix inversions  $\mathbf{D}^{-1}$  and  $\mathbf{S}_D^{-1}$  and constitutes a *backward elimination* which brings  $\mathbf{M}$  to a lower-triangular form. The last step of multiplying by  $\mathbf{P}'_C$  is called *forward substitution* and consists in substituting the already computed outcome of the backward elimination into the final inverse  $\mathbf{M}^{-1}$ , which requires matrix multiplications but no further matrix inversion.

### Relation between Schur complements

The two alternative routes of block-Gaussian elimination above lead to an evident symmetry in the block-structure of the inverse  $\mathbf{M}^{-1}$ : The results in Eqs.(B.6) and (B.10) are mapped

to each other by simultaneously exchanging  $\mathbf{A} \leftrightarrow \mathbf{D}$ ,  $\mathbf{B} \leftrightarrow \mathbf{C}$  and (upper  $\leftrightarrow$  lower) block-rows, (left  $\leftrightarrow$  right) block-columns. In particular, Eqs. (B.6) and (B.10) yield the block-matrix identities

$$\mathbf{S}_D^{-1} = \mathbf{A}^{-1} + \mathbf{A}^{-1}\mathbf{B}\mathbf{S}_A^{-1}\mathbf{C}\mathbf{A}^{-1}, \quad (\text{B.11})$$

$$\mathbf{S}_A^{-1} = \mathbf{D}^{-1} + \mathbf{D}^{-1}\mathbf{C}\mathbf{S}_D^{-1}\mathbf{B}\mathbf{A}^{-1} \quad (\text{B.12})$$

and

$$\mathbf{S}_D^{-1}\mathbf{B}\mathbf{D}^{-1} = \mathbf{A}^{-1}\mathbf{B}\mathbf{S}_A^{-1}, \quad (\text{B.13})$$

$$\mathbf{D}^{-1}\mathbf{C}\mathbf{S}_D^{-1} = \mathbf{S}_A^{-1}\mathbf{C}\mathbf{A}^{-1}, \quad (\text{B.14})$$

which relate the two Schur complements via the blocks of  $\mathbf{M}$ .

## B.2 Application to block-partitioned lattice Hamiltonian

The above general matrix-algebraic manipulations acquire physical meaning in the context of Greenians if we identify the block matrix  $\mathbf{M}$  as the matrix  $E\mathbf{I} - \tilde{\mathbf{H}} = \mathbf{\Delta}$  in the lattice Green equation

$$\mathbf{\Delta}\tilde{\mathbf{G}} = \mathbf{I} \Rightarrow \begin{pmatrix} E\mathbf{I}_{N-n} - \tilde{\mathbf{H}}_{11} & -\tilde{\mathbf{H}}_{12} \\ -\tilde{\mathbf{H}}_{21} & E\mathbf{I}_n - \tilde{\mathbf{H}}_{22} \end{pmatrix} \tilde{\mathbf{G}} = \begin{pmatrix} \mathbf{I}_{N-n} & \mathbf{0} \\ \mathbf{0} & \mathbf{I}_n \end{pmatrix}, \quad (\text{B.15})$$

with the Hamiltonian matrix

$$\tilde{\mathbf{H}} = \begin{pmatrix} \tilde{\mathbf{H}}_{11} & \tilde{\mathbf{H}}_{12} \\ \tilde{\mathbf{H}}_{21} & \tilde{\mathbf{H}}_{22} \end{pmatrix} \quad (\text{B.16})$$

$$\equiv \mathbf{H} + \mathbf{W} = \begin{pmatrix} \mathbf{H}_1 & \mathbf{0} \\ \mathbf{0} & \mathbf{H}_2 \end{pmatrix} + \begin{pmatrix} \mathbf{0} & \mathbf{W}_{12} \\ \mathbf{W}_{21} & \mathbf{0} \end{pmatrix} = \begin{pmatrix} \mathbf{H}_1 & \mathbf{W}_{12} \\ \mathbf{W}_{21} & \mathbf{H}_2 \end{pmatrix} \quad (\text{B.17})$$

describing a discretized system of size  $N$  (number of sites) decomposed into two domains  $\mathbb{D}_1$  of size  $N - n$  (described by  $\mathbf{H}_1$  when isolated), and  $\mathbb{D}_2$  of size  $n$  (described by  $\mathbf{H}_2$  when isolated) whose sites are coupled via the block-antidiagonal matrix  $\mathbf{W}$ .

The blocks  $\mathbf{B}$  and  $\mathbf{C}$  of App. B.1 thus become the coupling matrices between the domains, while the inverses of the blocks  $\mathbf{A}$  and  $\mathbf{D}$  are the Greenians of the isolated domains,

$$\mathbf{G}_1 = \mathbf{\Delta}_1^{-1} = (E\mathbf{I}_{N-n} - \mathbf{H}_1)^{-1}, \quad \mathbf{G}_2 = \mathbf{\Delta}_2^{-1} = (E\mathbf{I}_n - \mathbf{H}_2)^{-1}, \quad (\text{B.18})$$

which are assumed existent; either because the energy  $E$  does not coincide with real poles of the  $\mathbf{G}_{1,2}$ , or because the  $\mathbf{G}_{1,2}$  have only complex poles (i. e., away from the real  $E$ -axis) due to non-hermiticity of  $\mathbf{H}_{1,2}$  (caused, e. g., by coupling to an open boundary).

Although the domains  $\mathbb{D}_1$  and  $\mathbb{D}_2$  can in principle be treated in a symmetric manner, the order in which to perform the block-Gaussian elimination to obtain  $\tilde{\mathbf{G}}$  is now dictated, in practice, by the relative size of the domains: Assuming  $n < N$ , is it computationally preferable to perform (direct) inversion of the smaller matrix  $\mathbf{\Delta}_2$ , following the upper-major elimination route of App. B.1. The analogue of Eq. (B.10) then yields

$$\tilde{\mathbf{G}} = \begin{pmatrix} \tilde{\mathbf{G}}_{11} & \tilde{\mathbf{G}}_{12} \\ \tilde{\mathbf{G}}_{21} & \tilde{\mathbf{G}}_{22} \end{pmatrix} = \begin{pmatrix} \tilde{\mathbf{G}}_{11} & \tilde{\mathbf{G}}_{11}\mathbf{W}_{12}\mathbf{G}_2 \\ \mathbf{G}_2\mathbf{W}_{21}\tilde{\mathbf{G}}_{11} & \mathbf{G}_2 + \mathbf{G}_2\mathbf{W}_{21}\tilde{\mathbf{G}}_{11}\mathbf{W}_{12}\mathbf{G}_2 \end{pmatrix}, \quad (\text{B.19})$$

where

$$\tilde{\mathbf{G}}_{11} = (E\mathbf{I}_{N-n} - \mathbf{H}_1 - \mathbf{W}_{12}\mathbf{G}_2\mathbf{W}_{21})^{-1} \quad (\text{B.20})$$

is the inverse of the Schur complement of the block  $E\mathbf{I}_n - \mathbf{H}_2$  in  $\mathbf{\Delta}$ .

### Self-energy from subsystem

We recognize that the Hamiltonian for subsystem 1 is effectively modified by the (non-hermitian and energy dependent) self-energy

$$\boldsymbol{\Sigma}_1 \equiv \mathbf{W}_{12} \mathbf{G}_2 \mathbf{W}_{21} \quad (\text{B.21})$$

due to the coupling to subsystem 2, with resolvent

$$\tilde{\mathbf{G}}_{11} = [E\mathbf{I}_{N-n} - (\tilde{\mathbf{H}}_1 + \boldsymbol{\Sigma}_1)]^{-1} \quad (\text{B.22})$$

in the coupled system.

In the case where subsystem 2 is a semi-infinite lead, we thus recover the (grid-represented) formulation of an open scatterer in Secs. 3.3 and 4.3. The Greenian of subsystem 2 is then given analytically, so that no inversion needs to be computed to obtain it. If  $\mathbb{D}_2$  is a slice to be added to an existing domain during assembly of the grid-represented scatterer, then  $\mathbf{G}_2$  requires the inversion of a relatively small matrix. On the other hand, if  $\mathbb{D}_1$  and  $\mathbb{D}_2$  are extended domains whose isolated propagators have already been computed, then the order of block-Gaussian elimination does not matter.

### Relation to Dyson equation

The propagator from sites in  $\mathbb{D}_1$  to sites in  $\mathbb{D}_2$  is given by

$$\tilde{\mathbf{G}}_{21} = \mathbf{G}_2 \mathbf{W}_{21} \tilde{\mathbf{G}}_{11} = \mathbf{G}_2 \mathbf{W}_{21} (\mathbf{G}_1^{-1} - \boldsymbol{\Sigma}_1)^{-1} \quad (\text{B.23})$$

$$= \mathbf{G}_2 \mathbf{W}_{21} (\mathbf{I}_{N-n} - \mathbf{G}_1 \boldsymbol{\Sigma}_1)^{-1} \mathbf{G}_1, \quad (\text{B.24})$$

and the identities (B.11) and (B.14), which become

$$\tilde{\mathbf{G}}_{11} = \mathbf{G}_1 + \mathbf{G}_1 \mathbf{W}_{12} \tilde{\mathbf{G}}_{22} \mathbf{W}_{21} \mathbf{G}_1 \quad (\text{B.25})$$

and

$$\mathbf{G}_2 \mathbf{W}_{21} \tilde{\mathbf{G}}_{11} = \tilde{\mathbf{G}}_{22} \mathbf{W}_{21} \mathbf{G}_1, \quad (\text{B.26})$$

respectively, yield the propagator between sites in  $\mathbb{D}_1$ ,

$$\tilde{\mathbf{G}}_{11} = \mathbf{G}_1 + \mathbf{G}_1 \boldsymbol{\Sigma}_1 \tilde{\mathbf{G}}_{11} \quad (\text{B.27})$$

$$= \mathbf{G}_1 + \mathbf{G}_1 \boldsymbol{\Sigma}_1 (\mathbf{I}_{N-n} - \mathbf{G}_1 \boldsymbol{\Sigma}_1)^{-1} \mathbf{G}_1. \quad (\text{B.28})$$

Similarly, we find the propagators

$$\tilde{\mathbf{G}}_{12} = \mathbf{G}_1 (\mathbf{I}_{N-n} - \boldsymbol{\Sigma}_1 \mathbf{G}_1)^{-1} \mathbf{W}_{12} \mathbf{G}_2 \quad (\text{B.29})$$

and

$$\tilde{\mathbf{G}}_{22} = \mathbf{G}_2 + \mathbf{G}_2 \mathbf{W}_{21} \mathbf{G}_1 (\mathbf{I}_{N-n} - \boldsymbol{\Sigma}_1 \mathbf{G}_1)^{-1} \mathbf{W}_{12} \mathbf{G}_2. \quad (\text{B.30})$$

We have thus shown that the block-Gaussian elimination scheme applied on the block Hamiltonian matrix of two connected domains  $\mathbb{D}_1$  and  $\mathbb{D}_2$  is equivalent to solving the corresponding Dyson equation (4.63) of Sec. 4.4.1.



# Inter- and intra-connection of modules

In this appendix we apply the block-Gaussian elimination scheme of App. B to solve the tight-binding matrix Dyson equation for two the total Greenian of two inter-connected modules (subsystems of the total systems) and of a module intra-connected to itself.

## C.1 Inter-connection between two modules

Assuming that the Greenians  $\mathbf{G}_1$  and  $\mathbf{G}_2$  of two separate modules 1 and 2 have already been computed as solutions of the uncoupled Green equation

$$\mathbf{G}(\mathbf{E} - \mathbf{H}) = (\mathbf{E} - \mathbf{H})\mathbf{G} = \mathbf{I}, \quad (\text{C.1})$$

where

$$\mathbf{H} = \begin{pmatrix} \mathbf{H}_1 & \mathbf{0} \\ \mathbf{0} & \mathbf{H}_2 \end{pmatrix} = \tilde{\mathbf{H}}_{(\mathbf{W}=\mathbf{0})} = \text{diag} \left[ \begin{pmatrix} \mathbf{H}_1^{uu} & \mathbf{H}_1^{uc} \\ \mathbf{H}_1^{cu} & \mathbf{H}_1^{cc} \end{pmatrix}, \begin{pmatrix} \mathbf{H}_2^{uu} & \mathbf{H}_2^{uc} \\ \mathbf{H}_2^{cu} & \mathbf{H}_2^{cc} \end{pmatrix} \right], \quad (\text{C.2})$$

$$\mathbf{G} = \begin{pmatrix} \mathbf{G}_1 & \mathbf{0} \\ \mathbf{0} & \mathbf{G}_2 \end{pmatrix} = \begin{pmatrix} \Delta_1^{-1} & \mathbf{0} \\ \mathbf{0} & \Delta_2^{-1} \end{pmatrix} = \text{diag} \left[ \begin{pmatrix} \mathbf{G}_1^{uu} & \mathbf{G}_1^{uc} \\ \mathbf{G}_1^{cu} & \mathbf{G}_1^{cc} \end{pmatrix}, \begin{pmatrix} \mathbf{G}_2^{uu} & \mathbf{G}_2^{uc} \\ \mathbf{G}_2^{cu} & \mathbf{G}_2^{cc} \end{pmatrix} \right] \quad (\text{C.3})$$

the Greenian  $\tilde{\mathbf{G}}$  of the connected system is expressed in terms of  $\mathbf{G}_1$ ,  $\mathbf{G}_2$  and the coupling  $\mathbf{W}$  between them by solving the associated matrix Dyson equation (4.63) (the dimension of  $\mathbf{I}$ ,  $\mathbf{E} = E\mathbf{I}$  and  $\mathbf{0}$  at different instances is here to be understood from the respective block matrix structure). As discussed in Sec. 4.4.1 and App. B.2, this is equivalent to perform a block-Gaussian elimination on the large-scale partitioned matrix Green equation

$$(\mathbf{E} - \tilde{\mathbf{H}})\tilde{\mathbf{G}} = \mathbf{I} \quad (\text{C.4})$$

with the connected system Hamiltonian

$$\tilde{\mathbf{H}} = \mathbf{H} + \mathbf{W} = \left( \begin{array}{cc|cc} \mathbf{H}_1^{uu} & \mathbf{H}_1^{uc} & \mathbf{0} & \mathbf{0} \\ \mathbf{H}_1^{cu} & \mathbf{H}_1^{cc} & \mathbf{0} & \mathbf{W}_{12}^{cc} \\ \hline \mathbf{0} & \mathbf{0} & \mathbf{H}_2^{uu} & \mathbf{H}_2^{uc} \\ \mathbf{0} & \mathbf{W}_{21}^{cc} & \mathbf{H}_2^{cu} & \mathbf{H}_2^{cc} \end{array} \right), \quad (\text{C.5})$$

where  $c$  and  $u$  denote the sections of the corresponding module to be connected and to remain unconnected, respectively, with the Hermitian matrix

$$\mathbf{W} = \begin{pmatrix} \mathbf{0} & \mathbf{W}_{12} \\ \mathbf{W}_{21} & \mathbf{0} \end{pmatrix} = \text{antidiag} \left[ \begin{pmatrix} \mathbf{0} & \mathbf{0} \\ \mathbf{0} & \mathbf{W}_{12}^{cc} \end{pmatrix}, \begin{pmatrix} \mathbf{0} & \mathbf{0} \\ \mathbf{0} & \mathbf{W}_{21}^{cc} \end{pmatrix} \right] \quad (\text{C.6})$$

coupling the  $c$ -sections. The blocks  $\mathbf{W}_{12}^{cc}$  and  $\mathbf{W}_{21}^{cc}$  are square matrices of dimension equal to the (common) number of sites in each module to be connected.

Since both  $\mathbf{G}_1$  and  $\mathbf{G}_2$  are known, we use an alternative route essentially combining the lower- and upper-major elimination orders of App. B, by first multiplying Eq. (C.4) from the left by  $\mathbf{G}$ , which allows us to exploit the sparsity and block-symmetry of the matrix

$$\mathbf{G}\tilde{\Delta} = \mathbf{G}(\mathbf{E} - \tilde{\mathbf{H}}) = \left( \begin{array}{cc|cc} \mathbf{I} & \mathbf{0} & \mathbf{0} & \mathbf{p}_{12}^{uc} \\ \mathbf{0} & \mathbf{I} & \mathbf{0} & \mathbf{p}_{12}^{cc} \\ \hline \mathbf{0} & \mathbf{p}_{21}^{uc} & \mathbf{I} & \mathbf{0} \\ \mathbf{0} & \mathbf{p}_{21}^{cc} & \mathbf{0} & \mathbf{I} \end{array} \right), \quad (\text{C.7})$$

where

$$\mathbf{p}_{21}^{uc} = -\mathbf{G}_2^{uc}\mathbf{W}_{21}^{cc}, \quad \mathbf{p}_{21}^{cc} = -\mathbf{G}_2^{cc}\mathbf{W}_{21}^{cc}, \quad \mathbf{p}_{12}^{cc} = -\mathbf{G}_1^{cc}\mathbf{W}_{12}^{cc}, \quad \mathbf{p}_{12}^{uc} = -\mathbf{G}_1^{uc}\mathbf{W}_2^{cc}. \quad (\text{C.8})$$

To proceed with the block-elimination, the equation

$$\mathbf{G}(\mathbf{E} - \tilde{\mathbf{H}})\tilde{\mathbf{G}} = \mathbf{G} \quad (\text{C.9})$$

is now acted upon from the left with the product

$$\mathbf{P} = \mathbf{P}_{12}^{uc} \mathbf{P}_{12}^{cc} \mathbf{R} \mathbf{P}_{21}^{cc} \mathbf{P}_{21}^{uc}, \quad (\text{C.10})$$

containing the row-operator matrices

$$\begin{aligned} \mathbf{P}_{21}^{uc} &= \begin{pmatrix} \mathbf{I} & \mathbf{0} & \mathbf{0} & \mathbf{0} \\ \mathbf{0} & \mathbf{I} & \mathbf{0} & \mathbf{0} \\ \mathbf{0} & -\mathbf{p}_{21}^{uc} & \mathbf{I} & \mathbf{0} \\ \mathbf{0} & \mathbf{0} & \mathbf{0} & \mathbf{I} \end{pmatrix}, & \mathbf{P}_{21}^{cc} &= \begin{pmatrix} \mathbf{I} & \mathbf{0} & \mathbf{0} & \mathbf{0} \\ \mathbf{0} & \mathbf{I} & \mathbf{0} & \mathbf{0} \\ \mathbf{0} & \mathbf{0} & \mathbf{I} & \mathbf{0} \\ \mathbf{0} & -\mathbf{p}_{21}^{cc} & \mathbf{0} & \mathbf{I} \end{pmatrix} \\ \mathbf{P}_{12}^{cc} &= \begin{pmatrix} \mathbf{I} & \mathbf{0} & \mathbf{0} & \mathbf{0} \\ \mathbf{0} & \mathbf{I} & \mathbf{0} & -\mathbf{p}_{12}^{cc} \\ \mathbf{0} & \mathbf{0} & \mathbf{I} & \mathbf{0} \\ \mathbf{0} & \mathbf{0} & \mathbf{0} & \mathbf{I} \end{pmatrix}, & \mathbf{P}_{12}^{uc} &= \begin{pmatrix} \mathbf{I} & \mathbf{0} & \mathbf{0} & -\mathbf{p}_{12}^{uc} \\ \mathbf{0} & \mathbf{I} & \mathbf{0} & \mathbf{0} \\ \mathbf{0} & \mathbf{0} & \mathbf{I} & \mathbf{0} \\ \mathbf{0} & \mathbf{0} & \mathbf{0} & \mathbf{I} \end{pmatrix}, \end{aligned} \quad (\text{C.11})$$

which eliminate the blocks  $\mathbf{p}_{21}^{uc}$ ,  $\mathbf{p}_{21}^{cc}$ ,  $\mathbf{p}_{12}^{cc}$ ,  $\mathbf{p}_{12}^{uc}$  of  $\mathbf{G}\tilde{\Delta}$ , respectively. The block-diagonal central matrix

$$\mathbf{R} = \text{diag} \left[ \begin{pmatrix} \mathbf{I} & \mathbf{0} \\ \mathbf{0} & \mathbf{I} \end{pmatrix}, \begin{pmatrix} \mathbf{I} & -\mathbf{G}_2^{uc}\sigma_2\gamma \\ \mathbf{0} & \gamma \end{pmatrix} \right], \quad (\text{C.12})$$

which is the one providing the inverse Schur complement of  $\mathbf{H}_1$ , contains the self-energy

$$\sigma_2 = \mathbf{W}_{21}^{cc}\mathbf{G}_1^{cc}\mathbf{W}_{12}^{cc} \quad (\text{C.13})$$

of module 2 due to the coupling to module 1 as well as the inverse

$$\gamma = (\mathbf{I}^{cc} - \mathbf{G}_2^{cc}\sigma_2)^{-1} \quad (\text{C.14})$$

of the size of the connection interface. The propagator for the connected system is finally given by

$$\tilde{\mathbf{G}} = \mathbf{P}\mathbf{G} = \left( \begin{array}{cc|cc} \tilde{\mathbf{G}}_{11}^{uu} & \tilde{\mathbf{G}}_{11}^{uc} & \tilde{\mathbf{G}}_{12}^{uu} & \tilde{\mathbf{G}}_{12}^{uc} \\ \tilde{\mathbf{G}}_{11}^{cu} & \tilde{\mathbf{G}}_{11}^{cc} & \tilde{\mathbf{G}}_{12}^{cu} & \tilde{\mathbf{G}}_{12}^{cc} \\ \hline \tilde{\mathbf{G}}_{21}^{uu} & \tilde{\mathbf{G}}_{21}^{uc} & \tilde{\mathbf{G}}_{22}^{uu} & \tilde{\mathbf{G}}_{22}^{uc} \\ \tilde{\mathbf{G}}_{21}^{cu} & \tilde{\mathbf{G}}_{21}^{cc} & \tilde{\mathbf{G}}_{22}^{cu} & \tilde{\mathbf{G}}_{22}^{cc} \end{array} \right) = \quad (\text{C.15})$$

$$\left( \begin{array}{cc|cc} \mathbf{G}_1^{uu} + \mathbf{G}_1^{uc} \tilde{\sigma}_1 \mathbf{G}_1^{cu} & \mathbf{G}_1^{uc} + \mathbf{G}_1^{uc} \tilde{\sigma}_1 \mathbf{G}_1^{cc} & \mathbf{G}_1^{uc} \mathbf{W}_{12}^{cc} \tilde{\mathbf{G}}_{22}^{cu} & \mathbf{G}_1^{uc} \mathbf{W}_{12}^{cc} \tilde{\mathbf{G}}_{22}^{cc} \\ \mathbf{G}_1^{cu} + \mathbf{G}_1^{cc} \tilde{\sigma}_1 \mathbf{G}_1^{cu} & \mathbf{G}_1^{cc} + \mathbf{G}_1^{cc} \tilde{\sigma}_1 \mathbf{G}_1^{cc} & \mathbf{G}_1^{cc} \mathbf{W}_{12}^{cc} \tilde{\mathbf{G}}_{22}^{cu} & \mathbf{G}_1^{cc} \mathbf{W}_{12}^{cc} \tilde{\mathbf{G}}_{22}^{cc} \\ \hline \tilde{\mathbf{G}}_{22}^{uc} \mathbf{W}_{21}^{cc} \mathbf{G}_1^{cu} & \tilde{\mathbf{G}}_{22}^{uc} \mathbf{W}_{21}^{cc} \mathbf{G}_1^{cc} & \mathbf{G}_2^{uu} + \mathbf{G}_2^{uc} \sigma_2 \tilde{\mathbf{G}}_{22}^{cu} & \mathbf{G}_2^{uc} + \mathbf{G}_2^{uc} \sigma_2 \tilde{\mathbf{G}}_{22}^{cc} \\ \tilde{\mathbf{G}}_{22}^{cc} \mathbf{W}_{21}^{cc} \mathbf{G}_1^{cu} & \tilde{\mathbf{G}}_{22}^{cc} \mathbf{W}_{21}^{cc} \mathbf{G}_1^{cc} & \gamma \mathbf{G}_2^{cu} & \gamma \mathbf{G}_2^{cc} \end{array} \right), \quad (\text{C.16})$$

where

$$\tilde{\sigma}_1 = \mathbf{W}_{12}^{cc} \tilde{\mathbf{G}}_{22}^{cc} \mathbf{W}_{21}^{cc} = \mathbf{W}_{12}^{cc} \gamma \mathbf{G}_2^{cc} \mathbf{W}_{21}^{cc} \quad (\text{C.17})$$

is a modified form of self-energy of module 1 due to its coupling to module 2.

## C.2 Intra-connection of a module

For the intra-connection between two (equally sized) boundary sections  $c_1$  and  $c_2$  (with the sites of the one being pairwise nearest neighbors to the sites of the other) of a single module, we apply the same concept as for the inter-connection but with the block-partitioning

$$\mathbf{H} = \begin{pmatrix} \mathbf{H}^{uu} & \mathbf{H}^{uc_1} & \mathbf{H}^{uc_2} \\ \mathbf{H}^{c_1u} & \mathbf{H}^{c_1c_1} & \mathbf{0} \\ \mathbf{H}^{c_2u} & \mathbf{0} & \mathbf{H}^{c_2c_2} \end{pmatrix}, \quad (\text{C.18})$$

$$\mathbf{G} = \begin{pmatrix} \mathbf{G}^{uu} & \mathbf{G}^{uc_1} & \mathbf{G}^{uc_2} \\ \mathbf{G}^{c_1u} & \mathbf{G}^{c_1c_1} & \mathbf{G}^{c_1c_2} \\ \mathbf{G}^{c_2u} & \mathbf{G}^{c_2c_1} & \mathbf{G}^{c_2c_2} \end{pmatrix} \quad (\text{C.19})$$

for the disconnected module, where  $u$  denotes the part of the module to remain unconnected (all sites except for the  $c_1$ - and  $c_2$ -sites of the connection interface). Note that  $\mathbf{G}$  is here already a full matrix, since propagation between the sections  $c_1$  and  $c_2$  occurs, of course, via the interior  $u$  of one and the same module.

The tight-binding matrix Dyson equation (4.63) is now solved for the Greenian  $\tilde{\mathbf{G}}$  of the connected system in terms of the blocks of  $\mathbf{G}$  and of the coupling matrix

$$\mathbf{W} = \begin{pmatrix} \mathbf{0} & \mathbf{0} & \mathbf{0} \\ \mathbf{0} & \mathbf{0} & \mathbf{W}^{c_1c_2} \\ \mathbf{0} & \mathbf{W}^{c_2c_1} & \mathbf{0} \end{pmatrix}, \quad (\text{C.20})$$

where again  $\mathbf{W}_{12}^{cc}$  and  $\mathbf{W}_{21}^{cc}$  are square matrices of the dimension of the connection interface which couple sections  $c_1$  and  $c_2$ .

We thus solve the Dyson equation by performing block-Gaussian elimination on the partitioned Green equation  $(\mathbf{E} - \tilde{\mathbf{H}})\tilde{\mathbf{G}} = \mathbf{I}$  with the connected system Hamiltonian

$$\tilde{\mathbf{H}} = \mathbf{H} + \mathbf{W} = \left( \begin{array}{c|cc} \mathbf{H}^{uu} & \mathbf{H}^{uc_1} & \mathbf{H}^{uc_2} \\ \hline \mathbf{H}^{c_1u} & \mathbf{H}^{c_1c_1} & \mathbf{W}^{c_1c_2} \\ \mathbf{H}^{c_2u} & \mathbf{W}^{c_2c_1} & \mathbf{H}^{c_2c_2} \end{array} \right) \equiv \left( \begin{array}{c|cc} \mathbf{H}^{uu} & \mathbf{H}^{u1} & \mathbf{H}^{u2} \\ \hline \mathbf{H}^{1u} & \mathbf{H}^{11} & \mathbf{W}^{12} \\ \mathbf{H}^{2u} & \mathbf{W}^{21} & \mathbf{H}^{22} \end{array} \right), \quad (\text{C.21})$$

where we have replaced the connected section superscripts as

$$c_1 \rightarrow 1, \quad c_2 \rightarrow 2 \quad (\text{C.22})$$

to simplify notation in the expressions to follow.

We first multiply Eq. (C.4) from the left with  $\mathbf{G}$  which already eliminates the first block-column of  $\tilde{\mathbf{A}} = \mathbf{E} - \tilde{\mathbf{H}}$ ,

$$\mathbf{G}\tilde{\mathbf{A}} = \mathbf{G}(\mathbf{E} - \tilde{\mathbf{H}}) = \left( \begin{array}{c|cc} \mathbf{I} & \mathbf{p}^{u1} & \mathbf{p}^{u1} \\ \hline \mathbf{0} & \mathbf{p}^{11} & \mathbf{p}^{12} \\ \mathbf{0} & \mathbf{p}^{21} & \mathbf{p}^{22} \end{array} \right), \quad (\text{C.23})$$

where

$$\begin{aligned} \mathbf{p}^{u1} &= -\mathbf{G}^{u2}\mathbf{W}^{21}, & \mathbf{p}^{u2} &= -\mathbf{G}^{u1}\mathbf{W}^{12}, \\ \mathbf{p}^{11} &= \mathbf{I} - \mathbf{G}^{12}\mathbf{W}^{21}, & \mathbf{p}^{12} &= -\mathbf{G}^{11}\mathbf{W}^{12}, \\ \mathbf{p}^{21} &= -\mathbf{G}^{22}\mathbf{W}^{21}, & \mathbf{p}^{22} &= \mathbf{I} - \mathbf{G}^{21}\mathbf{W}^{12}. \end{aligned} \quad (\text{C.24})$$

The equation  $\mathbf{G}(\mathbf{E} - \tilde{\mathbf{H}})\tilde{\mathbf{G}} = \mathbf{G}$  is then acted upon from the left with the product

$$\mathbf{P} = \mathbf{P}^{u1} \mathbf{P}^{u2} \mathbf{P}^{12} \mathbf{\Lambda} \mathbf{P}^{21} \mathbf{\Theta}, \quad (\text{C.25})$$

where the row-operator matrices

$$\mathbf{P}^{21} = \left( \begin{array}{ccc} \mathbf{I} & \mathbf{0} & \mathbf{0} \\ \mathbf{0} & \mathbf{I} & \mathbf{0} \\ \mathbf{0} & -\mathbf{p}^{21} & \mathbf{I} \end{array} \right), \quad \mathbf{P}^{12} = \left( \begin{array}{ccc} \mathbf{I} & \mathbf{0} & \mathbf{0} \\ \mathbf{0} & \mathbf{I} & -\mathbf{p}^{12} \\ \mathbf{0} & \mathbf{0} & \mathbf{I} \end{array} \right), \quad (\text{C.26})$$

$$\mathbf{P}^{u2} = \left( \begin{array}{ccc} \mathbf{I} & \mathbf{0} & -\mathbf{p}^{u2} \\ \mathbf{0} & \mathbf{I} & \mathbf{0} \\ \mathbf{0} & \mathbf{0} & \mathbf{I} \end{array} \right), \quad \mathbf{P}^{u1} = \left( \begin{array}{ccc} \mathbf{I} & -\mathbf{p}^{21} & \mathbf{0} \\ \mathbf{0} & \mathbf{I} & \mathbf{0} \\ \mathbf{0} & \mathbf{0} & \mathbf{I} \end{array} \right),$$

eliminate the offdiagonal blocks  $\mathbf{p}^{21}$ ,  $\mathbf{p}^{12}$ ,  $\mathbf{p}^{u2}$ ,  $\mathbf{p}^{u1}$  of  $\mathbf{G}\tilde{\mathbf{A}}$ , respectively. The block-diagonal matrices

$$\mathbf{\Theta} = \left( \begin{array}{ccc} \mathbf{I} & \mathbf{0} & \mathbf{0} \\ \mathbf{0} & \mathbf{\theta} & \mathbf{0} \\ \mathbf{0} & \mathbf{0} & \mathbf{I} \end{array} \right), \quad \mathbf{\Lambda} = \left( \begin{array}{ccc} \mathbf{I} & \mathbf{0} & \mathbf{0} \\ \mathbf{0} & \mathbf{I} & \mathbf{0} \\ \mathbf{0} & \mathbf{0} & \mathbf{\lambda} \end{array} \right) \quad (\text{C.27})$$

contain the inverses

$$\mathbf{\theta} = [\mathbf{p}^{11}]^{-1} = [\mathbf{I} - \mathbf{G}^{12}\mathbf{W}^{21}]^{-1}, \quad (\text{C.28})$$

$$\mathbf{\lambda} = [\mathbf{p}^{22} - \mathbf{p}^{21}\mathbf{\theta}\mathbf{p}^{12}]^{-1} = [\mathbf{I} - \mathbf{G}^{21}\mathbf{W}^{12} - \mathbf{G}^{22}\mathbf{W}^{21}\mathbf{\theta}\mathbf{G}^{11}\mathbf{W}^{12}]^{-1} \quad (\text{C.29})$$

of the size of the connection interface. The propagator for the connected module is then given by

$$\tilde{\mathbf{G}} = \mathbf{P}\mathbf{G} = \left( \begin{array}{c|cc} \tilde{\mathbf{G}}^{uu} & \tilde{\mathbf{G}}^{u1} & \tilde{\mathbf{G}}^{u2} \\ \hline \tilde{\mathbf{G}}^{1u} & \tilde{\mathbf{G}}^{11} & \tilde{\mathbf{G}}^{12} \\ \tilde{\mathbf{G}}^{2u} & \tilde{\mathbf{G}}^{21} & \tilde{\mathbf{G}}^{22} \end{array} \right) = \quad (\text{C.30})$$

$$\left( \begin{array}{c|cc} \mathbf{G}^{uu} + \tilde{\mathbf{G}}_{\mathbf{W}}^{uu} & \mathbf{G}^{u1} + \tilde{\mathbf{G}}_{\mathbf{W}}^{u1} & \mathbf{G}^{u2} + \tilde{\mathbf{G}}_{\mathbf{W}}^{u2} \\ \hline \theta(\mathbf{G}^{1u} + \mathbf{G}^{11}\mathbf{W}^{12}\tilde{\mathbf{G}}^{2u}) & \theta(\mathbf{G}^{11} + \mathbf{G}^{11}\mathbf{W}^{12}\tilde{\mathbf{G}}^{21}) & \theta(\mathbf{G}^{12} + \mathbf{G}^{11}\mathbf{W}^{12}\tilde{\mathbf{G}}^{22}) \\ \lambda(\mathbf{G}^{2u} + \mathbf{G}^{22}\mathbf{W}^{21}\theta\mathbf{G}^{1u}) & \lambda(\mathbf{G}^{21} + \mathbf{G}^{22}\mathbf{W}^{21}\theta\mathbf{G}^{11}) & \lambda(\mathbf{G}^{22} + \mathbf{G}^{22}\mathbf{W}^{21}\theta\mathbf{G}^{12}) \end{array} \right), \quad (\text{C.31})$$

where the shorthand notation

$$\tilde{\mathbf{G}}_{\mathbf{W}}^{uz} = \mathbf{G}^{u1}\mathbf{W}^{12}\tilde{\mathbf{G}}^{2z} + \mathbf{G}^{u2}\mathbf{W}^{21}\tilde{\mathbf{G}}^{1z} \quad (z = 1, 2, u) \quad (\text{C.32})$$

has been used for the upper block-row.



# Gauge transformation of the Greenian

In this appendix we show how the Green function is gauge transformed between two given axial gauges and derive the general generating function for the transformation of the Green function of a module into the gauge of another module, as used in the inter-connection scheme presented in Sec. 4.5.

## D.1 Gauge transformation of the Green function between two different axial gauges

Observable quantities in quantum theory, such as probability densities, should be independent of gauge transformations of the electromagnetic potential, and therefore the wavefunction under such a transformation acquires at most a phase factor. Specifically, in the stationary picture used, if the magnetic vector potential is transformed via a scalar generating function  $\Lambda(\mathbf{r})$  of space as

$$\mathbf{A}(\mathbf{r}) \longrightarrow \mathbf{A}'(\mathbf{r}) = \mathbf{A}(\mathbf{r}) + \nabla\Lambda(\mathbf{r}), \quad (\text{D.1})$$

then the wave function is transformed as [148]

$$\psi(\mathbf{r}) \longrightarrow \psi'(\mathbf{r}) = \psi(\mathbf{r}) \exp \left[ i \frac{e}{\hbar} \Lambda(\mathbf{r}) \right]. \quad (\text{D.2})$$

From the general eigenstate expansion of the Green function propagating from point  $\mathbf{r}_\beta$  to point  $\mathbf{r}_\alpha$

$$\mathcal{G}(\mathbf{r}_\alpha, \mathbf{r}_\beta; E) = \sum_n \frac{\psi_n(\mathbf{r}_\alpha) \psi_n^*(\mathbf{r}_\beta)}{E - E_n \pm i\eta}, \quad (\eta \rightarrow 0), \quad (\text{D.3})$$

the corresponding gauge transformation of the Green function is

$$\mathcal{G}(\mathbf{r}_\alpha, \mathbf{r}_\beta; E) \longrightarrow \mathcal{G}'(\mathbf{r}_\alpha, \mathbf{r}_\beta; E) = \exp \left[ i \frac{e}{\hbar} \Lambda(\mathbf{r}_\alpha) \right] \mathcal{G}(\mathbf{r}_\alpha, \mathbf{r}_\beta; E) \exp \left[ -i \frac{e}{\hbar} \Lambda(\mathbf{r}_\beta) \right]. \quad (\text{D.4})$$

For the rectangular grid on which the Hamiltonian is discretized, it is convenient to use an axial gauge

$$\mathbf{A}(\mathbf{r}) = \begin{pmatrix} A_x \\ A_y \\ A_z \end{pmatrix} = \begin{pmatrix} -\nu B y \\ (1 - \nu) B x \\ 0 \end{pmatrix} \quad (\text{D.5})$$

for the vector potential, where the real parameter  $\nu$  is freely chosen. Upon a gauge transformation of the vector potential from a gauge  $\mathbf{A}(\mathbf{r})$  with parameter  $\nu$  to another gauge  $\mathbf{A}'(\mathbf{r})$

with parameter  $\nu'$ , we imply that their difference is the gradient of a generating function  $\Lambda(\mathbf{r})$ ,

$$\mathbf{A}'(\mathbf{r}) - \mathbf{A}(\mathbf{r}) = \begin{pmatrix} (\nu - \nu')By \\ (\nu - \nu')Bx \\ 0 \end{pmatrix} = \nabla\Lambda(\mathbf{r}). \quad (\text{D.6})$$

The simplest choice for the generating function is then

$$\Lambda(\mathbf{r}) = (\nu - \nu')Bxy, \quad (\text{D.7})$$

which leads to the following explicit gauge transformation for the Green function:

$$\mathcal{G}'(\mathbf{r}_\alpha, \mathbf{r}_\beta; E) = \exp \left[ i\frac{e}{\hbar}(\nu - \nu')Bx_\alpha y_\alpha \right] \mathcal{G}(\mathbf{r}_\alpha, \mathbf{r}_\beta; E) \exp \left[ -i\frac{e}{\hbar}(\nu - \nu')Bx_\beta y_\beta \right]. \quad (\text{D.8})$$

Note that the coordinate system here is common for the two axial gauges. Next, we will derive the generating function for a gauge transformation following an initial coordinate transformation.

## D.2 Gauge transformation for the inter-connection of two modules

In the modular version of the computational method, the propagator of each module is computed in its own coordinate system. It is preferably aligned so that the vertical extent is smaller on average (since it corresponds to the size of internal slice block-matrices to be inverted), and the origin is conventionally set to the center of the computational box containing the module. When a module is inter-connected to another module, it is thus in general necessary to shift and rotate the coordinates of the first module to match the coordinates of the second module at the connection (equivalently, the second module could be rotated and shifted, or both; we choose to transform the first module by convention). The rotation and shift of the coordinate system,  $\mathbf{r} \rightarrow \mathbf{r}'$ , introduces a new effective gauge in the first module,  $\mathbf{A}(\mathbf{r}) \rightarrow \mathbf{A}'(\mathbf{r}')$  (which is not necessarily of the axial form (D.5); see below). In order to connect the shifted and rotated first module to the second, this new effective gauge has to be transformed to match the gauge  $\mathbf{A}''(\mathbf{r}')$  (with gauge parameter  $\nu''$ ) of the second module in the common coordinate system  $\mathbf{r}'$ . We will now determine a complete generating function  $\Lambda(\mathbf{r})$  for this gauge transformation.

The coordinate transformation of the first module generally consists of a rotation by an angle  $\vartheta$  and an additional shift  $\mathbf{d}$ ,

$$\begin{pmatrix} x \\ y \end{pmatrix} \longrightarrow \begin{pmatrix} x' \\ y' \end{pmatrix} = \begin{pmatrix} c & -s \\ s & c \end{pmatrix} \begin{pmatrix} x \\ y \end{pmatrix} + \begin{pmatrix} d_x \\ d_y \end{pmatrix} \quad (\text{D.9})$$

where we use the shorthands  $c \equiv \cos(\vartheta)$ ,  $s \equiv \sin(\vartheta)$ . The z-coordinate is omitted in the following since we do not consider in-plane magnetic fields and thereby set  $A_z(\mathbf{r}) \equiv 0$ . The vector potential in the new coordinates in terms of the old one is

$$\mathbf{A}'(\mathbf{r}') = \begin{pmatrix} A'_x(x', y') \\ A'_y(x', y') \end{pmatrix} = \begin{pmatrix} c & -s \\ s & c \end{pmatrix} \begin{pmatrix} A_x(\mathbf{r}(x', y')) \\ A_y(\mathbf{r}(x', y')) \end{pmatrix}, \quad (\text{D.10})$$

which, when choosing the initial axial gauge (D.5), takes the explicit form

$$\begin{aligned} \mathbf{A}'(\mathbf{r}') &= B \begin{pmatrix} sc(2\nu - 1) & -\nu' \\ 1 - \nu' & -sc(2\nu - 1) \end{pmatrix} \begin{pmatrix} x' - d_x \\ y' - d_y \end{pmatrix} \\ &= B \begin{pmatrix} -\nu'(y' - d_y) \\ (1 - \nu')(x' - d_x) \end{pmatrix} + Bsc(2\nu - 1) \begin{pmatrix} x' - d_x \\ -(y' - d_y) \end{pmatrix}, \end{aligned} \quad (\text{D.11})$$

where a new gauge parameter

$$v' \equiv s^2 - v(s^2 - c^2) \quad (\text{D.12})$$

has been defined. As we see, because of the rotation, the new gauge is generally not of the axial form in the shifted coordinates, but has an additional term (second term in Eq. (D.11)) depending on the original gauge parameter  $v$ . Only the axial term (first term in Eq. (D.11)) generates the magnetic field  $B$ , but the additional term introduces a gauge transformation to the wavefunction. Note that for a symmetric initial gauge,  $v = v' = 1/2$ , the additional term vanishes for any rotation angle and the gauge remains axial. The non-axial term also vanishes for arbitrary  $v$  if we rotate by multiples of  $\pi/2$ , as will indeed be the case for the square lattice.

We now consider the connection of the shifted and rotated first module to a second module in an axial gauge with parameter  $v''$  in the new coordinate system,

$$A''(\mathbf{r}') = B \begin{pmatrix} -v''y' \\ (1-v'')x' \end{pmatrix}, \quad (\text{D.13})$$

which differs from the general transformed vector potential of the first module by

$$A''(\mathbf{r}') - A'(\mathbf{r}') = \nabla_{\mathbf{r}'} \Lambda(\mathbf{r}') \quad (\text{D.14})$$

$$= B(v' - v'') \begin{pmatrix} y' \\ x' \end{pmatrix} + B \begin{pmatrix} -v'd_y \\ (1-v')d_x \end{pmatrix} + B_{sc}(2v - 1) \begin{pmatrix} -(x' - d_x) \\ y' - d_y \end{pmatrix}. \quad (\text{D.15})$$

The generating function for arbitrary rotation angle can thus be chosen as

$$\begin{aligned} \Lambda(x', y') = & B(v' - v'')x'y' + B[-v'd_yx' + (1-v')d_xy'] \\ & + B_{sc}(2v - 1) \left( d_x x' - d_y y' - \frac{x'^2 - y'^2}{2} \right), \end{aligned} \quad (\text{D.16})$$

to be used in the general transformation (D.4) of the Green function of the first module into module into new coordinates and gauge.

On the square grid with vertical or horizontal connection interfaces we will only have rotation angles of  $0$ ,  $\pi/2$ ,  $\pi$ , or  $3\pi/2$  radians, in which case the last terms including  $sc$  above vanish. Taking also into account the values of  $v'$  from Eq. (D.12) in terms of the original parameter  $v$  (which are invariant under rotations by  $\pi$ ), the explicit form of the generating function for these four rotation angles simplifies to:

$$\Lambda_{\theta=0}(x', y') = \Lambda_{\theta=\pi}(x', y') = B[(v - v'')x'y' - v d_y x' + (1 - v) d_x y'], \quad (\text{D.17})$$

$$\Lambda_{\theta=\frac{\pi}{2}}(x', y') = \Lambda_{\theta=\frac{3\pi}{2}}(x', y') = B[(1 - v - v'')x'y' + (v - 1) d_y x' + v d_x y']. \quad (\text{D.18})$$

Note finally that, for the inter-connection of multiple modules, the 'first' module in a connection is an already assembled module which has obtained its origin and gauge parameter  $v$  from the last connected module.



## Natural units

This appendix provides reference tables with relevant quantities (Table E.1), conversion factors to SI units (Table E.2), as well as physical constants (Table E.3), for the system of natural units (n.u.) used in the text. These are obtained by setting

$$\hbar = m = e = a_0 \equiv 1 \quad (\text{E.1})$$

for Planck's constant ( $\hbar$ ), the electronic effective mass in the medium considered ( $m$ ), the elementary charge ( $e$ ), and the lattice constant ( $a_0$ ) of the square computational grid, and choosing an appropriate value for  $a_0$ .

Quantity	n.u.	SI
Length	$a_0$	m
Mass	$m$	kg
Action	$\hbar$	$\text{J s} = \frac{\text{kg m}^2}{\text{s}}$
Charge	$e$	C
Time	$\frac{ma_0^2}{\hbar}$	s
Energy	$\frac{\hbar^2}{ma_0^2}$	$\text{J} = \frac{\text{kg m}^2}{\text{s}^2}$
Magnetic flux density	$\frac{\hbar}{ea_0^2}$	$\text{T} = \frac{\text{J s}}{\text{C m}^2}$
Charge current	$\frac{e\hbar}{ma_0^2}$	$\text{A} = \frac{\text{C}}{\text{s}}$

**Table E.1:** Natural units of commonly used quantities based on setting  $\hbar = m = e = a_0 \equiv 1$ , and their equivalent in the International System (SI) of units.

Quantity	n.u	SI
Length	1 [ $a_0$ ]	$2 \cdot 10^{-9}$ m
Mass	1 [ $m$ ]	$6.28556 \cdot 10^{-32}$ kg
Time	1 $\left[ \frac{ma_0^2}{\hbar} \right]$	$2.38405 \cdot 10^{-15}$ s
Energy	1 $\left[ \frac{\hbar^2}{ma_0^2} \right]$	$4.42356 \cdot 10^{-20}$ J = 0.27609 meV
Magnetic flux density	1 $\left[ \frac{\hbar}{ea_0^2} \right]$	164.555 T
Charge current	1 $\left[ \frac{e\hbar}{ma_0^2} \right]$	$6.72044 \cdot 10^{-5}$ A

**Table E.2:** Conversion factors from our natural units to SI units for the choice  $a_0 = 2$  nm and  $m = 0.069 m_e$  (GaAs/AlGaAs interface).

Physical constant	n.u	SI
Elementary charge $e$	1	$1.6022 \cdot 10^{-19}$ C
Planck constant $\hbar$	1	$1.0546 \cdot 10^{-34}$ kg
Magnetic flux quantum $h/e$	$2\pi$	$4.13567 \cdot 10^{-15}$ Wb
Boltzmann constant $k_B$	$3.12124 \text{ K}^{-1}$	$1.3807 \cdot 10^{-23} \text{ J K}^{-1}$ = $8.6175 \cdot 10^{-5} \text{ eV K}^{-1}$
Speed of light $c$	357.36025	$2.99792 \cdot 10^8 \text{ m s}^{-1}$

**Table E.3:** Physical constants in natural units, independent of  $a_0$  and  $m$  ( $e$ ,  $\hbar$ ,  $h/e$ ) or determined by the choice  $a_0 = 2$  nm,  $m = 0.069 m_e$  ( $k_B$ ,  $c$ ), and their corresponding value in SI units.

# Bibliography

---

- [1] R. Landauer, *Electrical resistance of disordered one-dimensional lattices*, *Phil. Mag.* **21**(172) (1970).
- [2] M. Büttiker, *Four-Terminal Phase-Coherent Conductance*, *Phys. Rev. Lett.* **57**(14), 1761 (1986).
- [3] S. Datta, *Steady-state quantum kinetic equation*, *Phys. Rev. B* **40**(8), 5830 (1989).
- [4] S. Datta, *A simple kinetic equation for steady-state quantum transport*, *J. Phys.: Cond. Mat.* **2**(40), 8023 (1990).
- [5] D. A. Wharam, T. J. Thornton, R. Newbury, M. Pepper, H. Ahmed, J. E. F. Frost, D. G. Hasko, D. C. Peacock, D. A. Ritchie, G. a. C. Jones, *One-dimensional transport and the quantisation of the ballistic resistance*, *J. Phys. C: Solid State Phys.* **21**(8), L209 (1988).
- [6] B. J. van Wees, L. P. Kouwenhoven, E. M. M. Willems, C. J. P. M. Harmans, J. E. Mooij, H. van Houten, C. W. J. Beenakker, J. G. Williamson, C. T. Foxon, *Quantum ballistic and adiabatic electron transport studied with quantum point contacts*, *Phys. Rev. B* **43**(15), 12431 (1991).
- [7] J. C. Chen, Y. Lin, K. T. Lin, T. Ueda, S. Komiyama, *Effects of impurity scattering on the quantized conductance of a quasi-one-dimensional quantum wire*, *Appl. Phys. Lett.* **94**(1), 012105 (2009).
- [8] J. A. Nixon, J. H. Davies, H. U. Baranger, *Breakdown of quantized conductance in point contacts calculated using realistic potentials*, *Phys. Rev. B* **43**(15), 12638 (1991).
- [9] I. V. Zozoulenko, K. Berggren, *Quantum scattering, resonant states, and conductance fluctuations in an open square electron billiard*, *Phys. Rev. B* **56**(11), 6931 (1997).
- [10] R. G. Nazmitdinov, K. N. Pichugin, I. Rotter, P. Šeba, *Conductance of open quantum billiards and classical trajectories*, *Phys. Rev. B* **66**(8), 085322 (2002).
- [11] J. P. Bird, R. Akis, D. K. Ferry, A. P. S. d. Moura, Y. Lai, K. M. Indlekofer, *Interference and interactions in open quantum dots*, *Rep. Prog. Phys.* **66**, 583 (2003).
- [12] B. Weingartner, S. Rotter, J. Burgdörfer, *Simulation of electron transport through a quantum dot with soft walls*, *Phys. Rev. B* **72**(11), 115342 (2005).
- [13] A. F. Sadreev, E. N. Bulgakov, I. Rotter, *Bound states in the continuum in open quantum billiards with a variable shape*, *Phys. Rev. B* **73**(23), 235342 (2006).
- [14] E. R. Racec, U. Wulf, P. N. Racec, *Fano regime of transport through open quantum dots*, *Phys. Rev. B* **82**(8), 085313 (2010).

- [15] D. K. Ferry, A. M. Burke, R. Akis, R. Brunner, T. E. Day, R. Meisels, F. Kuchar, J. P. Bird, B. R. Bennett, *Open quantum dots—probing the quantum to classical transition*, *Semicond. Sci. Technol.* **26**(4), 043001 (2011).
- [16] M. C. Gutzwiller, *Chaos in Classical and Quantum Mechanics* (Springer, New York) (1990).
- [17] R. de Picciotto, H. L. Stormer, A. Yacoby, L. N. Pfeiffer, K. W. Baldwin, K. W. West, *2D-1D Coupling in Cleaved Edge Overgrowth*, *Phys. Rev. Lett.* **85**(8), 1730 (2000).
- [18] A. Fuhrer, S. Lüscher, T. Heinzel, K. Ensslin, W. Wegscheider, M. Bichler, *Transport properties of quantum dots with steep walls*, *Phys. Rev. B* **63**(12), 125309 (2001).
- [19] T. Heinzel, R. Held, S. Lüscher, K. Ensslin, W. Wegscheider, M. Bichler, *Electronic properties of nanostructures defined in Ga[Al]As heterostructures by local oxidation*, *Physica E* **9**(1), 84 (2001).
- [20] V. I. Borisov, V. G. Lapin, V. E. Sizov, A. G. Temiryazev, *Transistor structures with controlled potential profile in one-dimensional quantum channel*, *Tech. Phys. Lett.* **37**(2), 136 (2011).
- [21] S. S. Buchholz, S. F. Fischer, U. Kunze, D. Reuter, A. D. Wieck, *Nonlocal Aharonov–Bohm conductance oscillations in an asymmetric quantum ring*, *Appl. Phys. Lett.* **94**(2), 022107 (2009).
- [22] R. C. Ashoori, *Electrons in artificial atoms*, *Nature* **379**(6564), 413 (1996).
- [23] H. Schomerus, J. Tworzydło, *Quantum-to-Classical Crossover of Quasibound States in Open Quantum Systems*, *Phys. Rev. Lett.* **93**(15), 154102 (2004).
- [24] E. J. Heller, *Bound-State Eigenfunctions of Classically Chaotic Hamiltonian Systems: Scars of Periodic Orbits*, *Phys. Rev. Lett.* **53**(16), 1515 (1984).
- [25] T. Takami, *Semiclassical interpretation of avoided crossings for classically nonintegrable systems*, *Phys. Rev. Lett.* **68**(23), 3371 (1992).
- [26] R. Akis, D. K. Ferry, J. P. Bird, *Wave Function Scarring Effects in Open Stadium Shaped Quantum Dots*, *Phys. Rev. Lett.* **79**(1), 123 (1997).
- [27] S. Rotter, F. Aigner, J. Burgdorfer, *Statistics of transmission eigenvalues in two-dimensional quantum cavities: Ballistic versus stochastic scattering*, *Phys. Rev. B* **75**(12), 125312 (2007).
- [28] A. F. Sadreev, *Current statistics for transport through rectangular and circular billiards*, *Phys. Rev. E* **70**(1), 016208 (2004).
- [29] F. Aigner, S. Rotter, J. Burgdörfer, *Shot Noise in the Chaotic-to-Regular Crossover Regime*, *Phys. Rev. Lett.* **94**(21), 216801 (2005).
- [30] C. M. Marcus, A. J. Rimberg, R. M. Westervelt, P. F. Hopkins, A. C. Gossard, *Conductance fluctuations and chaotic scattering in ballistic microstructures*, *Phys. Rev. Lett.* **69**(3), 506 (1992).
- [31] K. Berggren, A. F. Sadreev, A. A. Starikov, *Crossover from regular to irregular behavior in current flow through open billiards*, *Phys. Rev. E* **66**(1), 016218 (2002).

- 
- [32] P. Jacquod, R. S. Whitney, *Semiclassical theory of quantum chaotic transport: Phase-space splitting, coherent backscattering, and weak localization*, Phys. Rev. B **73**(19), 195115 (2006).
- [33] K. Richter, M. Sieber, *Semiclassical Theory of Chaotic Quantum Transport*, Phys. Rev. Lett. **89**(20), 206801 (2002).
- [34] L. Wirtz, C. Stampfer, S. Rotter, J. Burgdörfer, *Semiclassical theory for transmission through open billiards: Convergence towards quantum transport*, Phys. Rev. E **67**(1), 016206 (2003).
- [35] U. Fano, *Effects of Configuration Interaction on Intensities and Phase Shifts*, Phys. Rev. **124**(6), 1866 (1961).
- [36] A. E. Miroschnichenko, S. Flach, Y. S. Kivshar, *Fano resonances in nanoscale structures*, Rev. Mod. Phys. **82**(3), 2257 (2010).
- [37] J. U. Nöckel, A. D. Stone, *Resonance line shapes in quasi-one-dimensional scattering*, Phys. Rev. B **50**(23), 17415 (1994).
- [38] J. Göres, D. Goldhaber-Gordon, S. Heemeyer, M. A. Kastner, H. Shtrikman, D. Mahalu, U. Meirav, *Fano resonances in electronic transport through a single-electron transistor*, Phys. Rev. B **62**(3), 2188 (2000).
- [39] S. Rotter, F. Libisch, J. Burgdörfer, U. Kuhl, H. Stöckmann, *Tunable Fano resonances in transport through microwave billiards*, Phys. Rev. E **69**(4), 046208 (2004).
- [40] M. Mendoza, P. A. Schulz, R. O. Vallejos, C. H. Lewenkopf, *Fano resonances in the conductance of quantum dots with mixed dynamics*, Phys. Rev. B **77**(15), 155307 (2008).
- [41] S. Klaiman, N. Moiseyev, H. R. Sadeghpour, *Interpretation of the Fano lineshape reversal in quantum waveguides*, Phys. Rev. B **75**(11), 113305 (2007).
- [42] J. Fransson, M. Kang, Y. Yoon, S. Xiao, Y. Ochiai, J. Reno, N. Aoki, J. P. Bird, *Tuning the Fano Resonance with an Intruder Continuum*, Nano Lett. (2014).
- [43] E. Persson, K. Pichugin, I. Rotter, P. Šeba, *Interfering resonances in a quantum billiard*, Phys. Rev. E **58**(6), 8001 (1998).
- [44] A. I. Magunov, I. Rotter, S. I. Strakhova, *Fano resonances in the overlapping regime*, Phys. Rev. B **68**(24), 245305 (2003).
- [45] E. Persson, I. Rotter, H. Stöckmann, M. Barth, *Observation of Resonance Trapping in an Open Microwave Cavity*, Phys. Rev. Lett. **85**(12), 2478 (2000).
- [46] P. Seba, I. Rotter, M. Müller, E. Persson, K. Pichugin, *Open microwave cavities*, Physica E **9**(3), 484 (2001).
- [47] P. Šeba, I. Rotter, M. Müller, E. Persson, K. Pichugin, *Collective modes in an open microwave billiard*, Phys. Rev. E **61**(1), 66 (2000).
- [48] I. Rotter, *A non-Hermitian Hamilton operator and the physics of open quantum systems*, J. Phys. A: Math. Theor. **42**(15), 153001 (51pp) (2009).
- [49] I. V. Zozoulenko, A. S. Sachrajda, C. Gould, K. Berggren, P. Zawadzki, Y. Feng, Z. Wasilewski, *Few-electron open dots: Single level transport*, Phys. Rev. Lett. **83**(9), 1838 (1999).
-

- [50] S. Rotter, B. Weingartner, N. Rohringer, J. Burgdörfer, *Ballistic quantum transport at high energies and high magnetic fields*, Phys. Rev. B **68**(16), 165302 (2003).
- [51] R. Brunner, R. Meisels, F. Kuchar, R. Akis, D. K. Ferry, J. P. Bird, *Draining of the Sea of Chaos: Role of Resonant Transmission and Reflection in an Array of Billiards*, Phys. Rev. Lett. **98**(20), 204101 (2007).
- [52] D. Buchholz, P. Drouvelis, P. Schmelcher, *Tunable transmission via quantum state evolution in oval quantum dots*, Europhys. Lett. **81**(3), 37001 (2008).
- [53] C. Payette, G. Yu, J. A. Gupta, D. G. Austing, S. V. Nair, B. Partoens, S. Amaha, S. Tarucha, *Coherent Three-Level Mixing in an Electronic Quantum Dot*, Phys. Rev. Lett. **102**(2), 026808 (2009).
- [54] N. Aoki, R. Brunner, A. M. Burke, R. Akis, R. Meisels, D. K. Ferry, Y. Ochiai, *Direct Imaging of Electron States in Open Quantum Dots*, Phys. Rev. Lett. **108**(13), 136804 (2012).
- [55] V. Kotimäki, E. Räsänen, H. Hennig, E. J. Heller, *Fractal dynamics in chaotic quantum transport*, Phys. Rev. E **88**(2), 022913 (2013).
- [56] Y. Aharonov, D. Bohm, *Significance of Electromagnetic Potentials in the Quantum Theory*, Phys. Rev. **115**(3), 485 (1959).
- [57] G. Timp, A. M. Chang, J. E. Cunningham, T. Y. Chang, P. Mankiewich, R. Behringer, R. E. Howard, *Observation of the Aharonov-Bohm effect for  $\omega_c\tau > 1$* , Phys. Rev. Lett. **58**(26), 2814 (1987).
- [58] D. Frustaglia, M. Hentschel, K. Richter, *Quantum Transport in Nonuniform Magnetic Fields: Aharonov-Bohm Ring as a Spin Switch*, Phys. Rev. Lett. **87**(25), 256602 (2001).
- [59] O. Kalman, P. Foldi, M. G. Benedict, F. M. Peeters, *Magnetoconductance of rectangular arrays of quantum rings*, Phys. Rev. B **78**(12), 125306 (2008).
- [60] U. Sivan, Y. Imry, C. Hartzstein, *Aharonov-Bohm and quantum Hall effects in singly connected quantum dots*, Phys. Rev. B **39**(2), 1242 (1989).
- [61] Y. Wang, J. Wang, H. Guo, *Magnetoconductance of a stadium-shaped quantum dot: A finite-element-method approach*, Phys. Rev. B **49**(3), 1928 (1994).
- [62] K. Kobayashi, H. Aikawa, S. Katsumoto, Y. Iye, *Tuning of the Fano Effect through a Quantum Dot in an Aharonov-Bohm Interferometer*, Phys. Rev. Lett. **88**(25), 256806 (2002).
- [63] Z. Y. Zeng, F. Claro, A. Pérez, *Fano resonances and Aharonov-Bohm effects in transport through a square quantum dot molecule*, Phys. Rev. B **65**(8), 085308 (2002).
- [64] K. Kobayashi, H. Aikawa, A. Sano, S. Katsumoto, Y. Iye, *Fano resonance in a quantum wire with a side-coupled quantum dot*, Phys. Rev. B **70**(3), 035319 (2004).
- [65] T. Nakanishi, K. Terakura, T. Ando, *Theory of Fano effects in an Aharonov-Bohm ring with a quantum dot*, Phys. Rev. B **69**(11), 115307 (2004).
- [66] S. Jana, A. Chakrabarti, *Aharonov-Bohm ring with a side-coupled atomic cluster: Magneto-transport and the selective switching effect*, Phys. Rev. B **77**(15), 155310 (2008).
- [67] B. Szafran, F. M. Peeters, *Lorentz-force-induced asymmetry in the Aharonov-Bohm effect in a three-terminal semiconductor quantum ring*, Europhys. Lett. **70**(6), 810 (2005).

- 
- [68] M. R. Poniedziłek, B. Szafran, *Multisubband transport and magnetic deflection of Fermi electron trajectories in three terminal junctions and rings*, J. Phys.: Cond. Mat. **24**(8), 085801 (2012).
- [69] M. R. Poniedziłek, B. Szafran, *Magnetic forces and localized resonances in electron transfer through quantum rings*, J. Phys.: Cond. Mat. **22**(46), 465801 (2010).
- [70] L. Onsager, *Reciprocal Relations in Irreversible Processes. I.*, Phys. Rev. **37**(4), 405 (1931).
- [71] C. W. J. Beenakker, H. van Houten, *Quantum Transport in Semiconductor Nanostructures*, Solid State Phys. **44**, 1 (1991).
- [72] K. v. Klitzing, G. Dorda, M. Pepper, *New Method for High-Accuracy Determination of the Fine-Structure Constant Based on Quantized Hall Resistance*, Phys. Rev. Lett. **45**(6), 494 (1980).
- [73] R. B. Laughlin, *Quantized Hall conductivity in two dimensions*, Phys. Rev. B **23**(10), 5632 (1981).
- [74] I. Žutić, J. Fabian, S. Das Sarma, *Spintronics: Fundamentals and applications*, Rev. Mod. Phys. **76**(2), 323 (2004).
- [75] J. H. Davies, *The Physics Of Low-Dimensional Semiconductors, An Introduction* (Cambridge University Press, Cambridge, UK) (1997).
- [76] P. Drouvelis, G. Fagas, P. Schmelcher, *Magnetically controlled current flow in coupled-dot arrays*, J. Phys.: Cond. Mat. **19**(32), 326209 (2007).
- [77] M. Elhassan, R. Akis, J. P. Bird, D. K. Ferry, T. Ida, K. Ishibashi, *Magnetically induced Bragg scattering of electrons in quantum-dot crystals*, Phys. Rev. B **70**(20), 205341 (2004).
- [78] R. Brunner, R. Akis, D. K. Ferry, F. Kuchar, R. Meisels, *Coupling-Induced Bipartite Pointer States in Arrays of Electron Billiards: Quantum Darwinism in Action?*, Phys. Rev. Lett. **101**(2), 024102 (2008).
- [79] M. Elhassan, J. P. Bird, A. Shailos, C. Prasad, R. Akis, D. K. Ferry, Y. Takagaki, L. Lin, N. Aoki, Y. Ochiai, K. Ishibashi, Y. Aoyagi, *Coupling-driven transition from multiple to single-dot interference in open quantum-dot arrays*, Phys. Rev. B **64**(8), 085325 (2001).
- [80] I. V. Zozoulenko, F. A. Maaø, E. H. Hauge, *Coherent magnetotransport in confined arrays of antidots. I. Dispersion relations and current densities*, Phys. Rev. B **53**(12), 7975 (1996).
- [81] I. V. Zozoulenko, F. A. Maaø, E. H. Hauge, *Coherent magnetotransport in confined arrays of antidots. II. Two-terminal conductance*, Phys. Rev. B **53**(12), 7987 (1996).
- [82] B. L. Johnson, C. Barnes, G. Kirczenow, *Theory of the Hall effect in two-dimensional quantum-dot arrays*, Phys. Rev. B **46**(23), 15302 (1992).
- [83] G. Kirczenow, *Theory of two-dimensional quantum-dot arrays in magnetic fields: Electronic structure and lateral quantum transport*, Phys. Rev. B **46**(3), 1439 (1992).
- [84] G. Chen, G. Klimeck, S. Datta, G. Chen, W. A. Goddard, *Resonant tunneling through quantum-dot arrays*, Phys. Rev. B **50**(11), 8035 (1994).
- [85] J. Cai, G. D. Mahan, *Energy bands of quantum dot arrays*, Phys. Rev. B **76**(20), 205116 (2007).
-

- [86] J. Dempsey, N. F. Johnson, L. Brey, B. I. Halperin, *Collective modes in quantum-dot arrays in magnetic fields*, Phys. Rev. B **42**(18), 11708 (1990).
- [87] D. S. Golubev, A. D. Zaikin, *Transport of interacting electrons in arrays of quantum dots and diffusive wires*, Phys. Rev. B **70**(16), 165423 (2004).
- [88] C. A. Büsser, A. Moreo, E. Dagotto, *Conductance dip in the Kondo regime of linear arrays of quantum dots*, Phys. Rev. B **70**(3), 035402 (2004).
- [89] R. A. Jalabert, A. D. Stone, Y. Alhassid, *Statistical theory of Coulomb blockade oscillations: Quantum chaos in quantum dots*, Phys. Rev. Lett. **68**(23), 3468 (1992).
- [90] K. A. Matveev, L. I. Glazman, H. U. Baranger, *Coulomb blockade of tunneling through a double quantum dot*, Phys. Rev. B **54**(8), 5637 (1996).
- [91] M. J. McLennan, Y. Lee, S. Datta, *Voltage drop in mesoscopic systems: A numerical study using a quantum kinetic equation*, Phys. Rev. B **43**(17), 13846 (1991).
- [92] S. Datta, *Exclusion principle and the Landauer-Büttiker formalism*, Phys. Rev. B **45**(3), 1347 (1992).
- [93] H. Oliveira, C. Manchein, M. Beims, *Soft wall effects on interacting particles in billiards*, Phys. Rev. E **78**(4) (2008).
- [94] H. U. Baranger, D. P. DiVincenzo, R. A. Jalabert, A. D. Stone, *Classical and quantum ballistic-transport anomalies in microjunctions*, Phys. Rev. B **44**(19), 10637 (1991).
- [95] R. Brunner, R. Meisels, F. Kuchar, M. ElHassan, J. Bird, K. Ishibashi, *Investigations of backscattering peaks and of the nature of the confining potential in open quantum dots*, Physica E **21**(2–4), 491 (2004).
- [96] P. A. Lee, A. D. Stone, *Universal Conductance Fluctuations in Metals*, Phys. Rev. Lett. **55**(15), 1622 (1985).
- [97] P. A. Lee, D. S. Fisher, *Anderson Localization in Two Dimensions*, Phys. Rev. Lett. **47**(12), 882 (1981).
- [98] G. Bergmann, *Weak localization in thin films: a time-of-flight experiment with conduction electrons*, Phys. Rep. **107**(1), 1 (1984).
- [99] H. U. Baranger, R. A. Jalabert, A. D. Stone, *Weak localization and integrability in ballistic cavities*, Phys. Rev. Lett. **70**(25), 3876 (1993).
- [100] R. A. Jalabert, H. U. Baranger, A. D. Stone, *Conductance fluctuations in the ballistic regime: A probe of quantum chaos?*, Phys. Rev. Lett. **65**(19), 2442 (1990).
- [101] I. Brezinova, C. Stampfer, L. Wirtz, S. Rotter, J. Burgdorfer, *Diffraction paths for weak localization in quantum billiards*, Phys. Rev. B **77**(16), 165321 (2008).
- [102] P. W. Brouwer, A. Altland, *Anderson localization from classical trajectories*, Phys. Rev. B **78**(7), 075304 (2008).
- [103] C. W. J. Beenakker, *Random-matrix theory of quantum transport*, Rev. Mod. Phys. **69**(3), 731 (1997).
- [104] Y. Alhassid, *The statistical theory of quantum dots*, Rev. Mod. Phys. **72**(4), 895 (2000).

- 
- [105] M. Mendoza, P. A. Schulz, *Imaging and switching of Fano resonances in open quantum cavities*, Phys. Rev. B **71**(24), 245303 (2005).
- [106] B. Szafran, M. R. Poniedziłek, *Tuning Fano resonances by magnetic forces for electron transport through a quantum wire side coupled to a quantum ring*, Phys. Rev. B **82**(7), 075320 (2010).
- [107] L. Burgnies, O. Vanbésien, D. Lippens, *An analysis of wave patterns in multiport quantum waveguide structures*, J. Phys. D: Appl. Phys. **32**(6), 706 (1999).
- [108] E. Polizzi, N. B. Abdallah, O. Vanbésien, D. Lippens, *Space lateral transfer and negative differential conductance regimes in quantum waveguide junctions*, J. Appl. Phys. **87**(12), 8700 (2000).
- [109] A. Bertoni, P. Bordone, R. Brunetti, C. Jacoboni, S. Reggiani, *Quantum Logic Gates based on Coherent Electron Transport in Quantum Wires*, Phys. Rev. Lett. **84**(25), 5912 (2000).
- [110] M. Governale, M. Macucci, B. Pellegrini, *Shape of the tunneling conductance peaks for coupled electron waveguides*, Phys. Rev. B **62**(7), 4557 (2000).
- [111] O. Vanbésien, D. Lippens, *Directional coupling in dual-branch electron-waveguide junctions*, Phys. Rev. B **52**(7), 5144 (1995).
- [112] W. Sheng, H. Xu, *Transport characteristics of a window-coupled quantum-wire system in nonuniform magnetic fields*, J. Appl. Phys. **84**(4), 2146 (1998).
- [113] W. Sheng, B. Gu, J. Wang, J. Xia, *Tunneling transmission in two quantum wires coupled by a magnetically defined barrier*, J. Appl. Phys. **82**(12), 6083 (1997).
- [114] J. Harris, R. Akis, D. K. Ferry, *Magnetically switched quantum waveguide qubit*, Appl. Phys. Lett. **79**(14), 2214 (2001).
- [115] X. Yue-E, C. Yuan-Ping, Y. Xiao-Hong, *Magnetotransport in a dual waveguide coupled by a finite barrier: Energy filter and directional coupler*, Chin. Phys. **16**(10), 3087 (2007).
- [116] O. A. Tkachenko, V. A. Tkachenko, Z. D. Kvon, A. L. Aseev, J. Portal, *Quantum inter-fereential Y-junction switch*, Nanotechnology **23**(9), 095202 (2012).
- [117] S. Rotter, P. Ambichl, F. Libisch, *Generating Particlelike Scattering States in Wave Transport*, Phys. Rev. Lett. **106**(12), 120602 (2011).
- [118] D. Ferry, S. M. Goodnick, *Transport in Nanostructures* (Cambridge University Press, Cambridge, UK) (1997).
- [119] D. J. Thouless, S. Kirkpatrick, *Conductivity of the disordered linear chain*, J. Phys. C: Solid State Phys. **14**(3), 235 (1981).
- [120] A. MacKinnon, *The calculation of transport properties and density of states of disordered solids*, Z. Phys. B **59**(4), 385 (1985).
- [121] F. Sols, M. Macucci, U. Ravaioli, K. Hess, *Theory for a quantum modulated transistor*, J. Appl. Phys. **66**(8), 3892 (1989).
- [122] S. Rotter, J. Tang, L. Wirtz, J. Trost, J. Burgdörfer, *Modular recursive Green's function method for ballistic quantum transport*, Phys. Rev. B **62**(3), 1950 (2000).
-

- [123] K. Kazymyrenko, X. Waintal, *Knitting algorithm for calculating Green functions in quantum systems*, Phys. Rev. B **77**(11), 115119 (2008).
- [124] C. Jacoboni, *Theory of Electron Transport in Semiconductors, Springer Series in Solid-State Sciences*, volume 165 (Springer, Berlin) (2010).
- [125] J. R. Chelikowsky, M. L. Cohen, *Nonlocal pseudopotential calculations for the electronic structure of eleven diamond and zinc-blende semiconductors*, Phys. Rev. B **14**(2), 556 (1976).
- [126] S. M. Sze, M. Lee, *Semiconductor Devices: Physics and Technology* (Wiley, New York) (2012).
- [127] S. Datta, *Electronic Transport in Mesoscopic Systems* (Cambridge University Press, Cambridge, UK) (1995).
- [128] P. Mello, N. Kumar, *Quantum transport in mesoscopic systems : complexity and statistical fluctuations, a maximum-entropy viewpoint* (Oxford University Press, New York) (2004).
- [129] O. Bohigas, M. J. Giannoni, C. Schmit, *Characterization of Chaotic Quantum Spectra and Universality of Level Fluctuation Laws*, Phys. Rev. Lett. **52**(1), 1 (1984).
- [130] R. Winkler, *Spin-orbit Coupling Effects in Two-Dimensional Electron and Hole Systems* (Springer, Berlin) (2003).
- [131] T. Ihn, *Electronic quantum transport in mesoscopic semiconductor structures* (Springer, New York) (2004).
- [132] R. Landau, *Quantum mechanics II : a second course in quantum theory* (Wiley, New York) (1996).
- [133] L. M. Roth, B. Lax, S. Zwerdling, *Theory of Optical Magneto-Absorption Effects in Semiconductors*, Phys. Rev. **114**(1), 90 (1959).
- [134] Y. A. Bychkov, E. I. Rashba, *Oscillatory effects and the magnetic susceptibility of carriers in inversion layers*, J. Phys. C: Solid State Phys. **17**(33), 6039 (1984).
- [135] S. J. Papadakis, E. P. D. Poortere, H. C. Manoharan, M. Shayegan, R. Winkler, *The Effect of Spin Splitting on the Metallic Behavior of a Two-Dimensional System*, Science **283**(5410), 2056 (1999).
- [136] D. Sánchez, L. Serra, *Fano-Rashba effect in a quantum wire*, Phys. Rev. B **74**(15), 153313 (2006).
- [137] O. Zaitsev, D. Frustaglia, K. Richter, *Role of Orbital Dynamics in Spin Relaxation and Weak Antilocalization in Quantum Dots*, Phys. Rev. Lett. **94**(2), 026809 (2005).
- [138] A. A. Burkov, A. S. Núñez, A. H. MacDonald, *Theory of spin-charge-coupled transport in a two-dimensional electron gas with Rashba spin-orbit interactions*, Phys. Rev. B **70**(15), 155308 (2004).
- [139] T. Koga, J. Nitta, T. Akazaki, H. Takayanagi, *Rashba Spin-Orbit Coupling Probed by the Weak Antilocalization Analysis in InAlAs/InGaAs/InAlAs Quantum Wells as a Function of Quantum Well Asymmetry*, Phys. Rev. Lett. **89**(4), 046801 (2002).

- 
- [140] J. Wunderlich, B. Kaestner, J. Sinova, T. Jungwirth, *Experimental Observation of the Spin-Hall Effect in a Two-Dimensional Spin-Orbit Coupled Semiconductor System*, Phys. Rev. Lett. **94**(4), 047204 (2005).
- [141] M. Abramowitz, I. A. Stegun, *Handbook of Mathematical Functions: With Formulas, Graphs, and Mathematical Tables* (Dover, New York) (1972).
- [142] S. B. Kaplan, A. C. Warren, *Magnetoconductance oscillations of a quasi-one-dimensional electron gas in a parabolic transverse potential*, Phys. Rev. B **34**(2), 1346 (1986).
- [143] K. Berggren, *Characterization of very narrow quasi-one-dimensional quantum channels*, Phys. Rev. B **37**(17), 10118 (1988).
- [144] A. M. Kriman, N. C. Kluksdahl, D. K. Ferry, *Scattering states and distribution functions for microstructures*, Phys. Rev. B **36**(11), 5953 (1987).
- [145] F. Sols, *Scattering, dissipation, and transport in mesoscopic systems*, Ann. Phys. **214**(2), 386 (1992).
- [146] P. Roman, *Advanced Quantum Theory* (Addison-Wesley, Reading) (1965).
- [147] E. Merzbacher, *Quantum mechanics* (Wiley, New York) (1970).
- [148] K. Gottfried, T. Yan, *Quantum Mechanics: Fundamentals* (Springer, New York) (2003).
- [149] A. Messiah, *Quantum mechanics* (North-Holland Pub. Co., Amsterdam) (1962).
- [150] M. Büttiker, *Symmetry of Electrical Conduction*, IBM J. Res. Dev. **32**(3), 317 (1988).
- [151] H. B. G. Casimir, *On Onsager's Principle of Microscopic Reversibility*, Rev. Mod. Phys. **17**(2-3), 343 (1945).
- [152] R. Kalina, B. Szafran, S. Bednarek, F. M. Peeters, *Magnetic-Field Asymmetry of Electron Wave Packet Transmission in Bent Channels Capacitively Coupled to a Metal Gate*, Phys. Rev. Lett. **102**(6), 066807 (2009).
- [153] P. F. Bagwell, T. P. Orlando, *Landauer's conductance formula and its generalization to finite voltages*, Phys. Rev. B **40**(3), 1456 (1989).
- [154] H. v. Houten, C. Beenakker, *Quantum Point Contacts*, Physics Today **49**(7), 22 (2008).
- [155] Y. Imry, *Introduction to Mesoscopic Physics* (Oxford University Press, New York) (2008).
- [156] L. Onsager, *Reciprocal Relations in Irreversible Processes. II.*, Phys. Rev. **38**(12), 2265 (1931).
- [157] R. Golizadeh-Mojarad, S. Datta, *Nonequilibrium Green's function based models for dephasing in quantum transport*, Phys. Rev. B **75**(8), 081301 (2007).
- [158] P. A. Kalozoumis, C. Morfonios, F. K. Diakonov, P. Schmelcher, *Invariants of Broken Discrete Symmetries*, Phys. Rev. Lett. **113**(5), 050403 (2014).
- [159] S. Datta, *Quantum Transport: Atom to Transistor* (Cambridge University Press, Cambridge, UK) (2005).
- [160] S. E. Laux, D. J. Frank, F. Stern, *Quasi-one-dimensional electron states in a split-gate GaAs/AlGaAs heterostructure*, Surf. Sci. **196**(1-3), 101 (1988).

- [161] J. A. Nixon, J. H. Davies, H. U. Baranger, *Conductance of quantum point contacts calculated using realistic potentials*, *Superlatt. Microstruct.* **9**(2), 187 (1991).
- [162] E. N. Economou, *Green's Functions in Quantum Physics* (Springer, Berlin) (2006).
- [163] H. Haug, A. Jauho, *Quantum Kinetics in Transport and Optics of Semiconductors* (Springer, Berlin) (2007).
- [164] P. M. Morse, H. Feshbach, *Methods of theoretical physics* (McGraw-Hill, New York) (1953).
- [165] A. D. Stone, A. Szafer, *What is measured when you measure a resistance? The Landauer formula revisited*, *IBM J. Res. Dev.* **32**(3), 384 (1988).
- [166] D. S. Fisher, P. A. Lee, *Relation between conductivity and transmission matrix*, *Phys. Rev. B* **23**(12), 6851 (1981).
- [167] H. U. Baranger, A. D. Stone, *Electrical linear-response theory in an arbitrary magnetic field: A new Fermi-surface formation*, *Phys. Rev. B* **40**(12), 8169 (1989).
- [168] F. M. Peeters, J. De Boeck, *Chapter 7 - Hybrid magnetic-semiconductor nanostructures*, in H. S. Nalwa (Ed.), *Handbook of Nanostructured Materials and Nanotechnology*, pp. 345–426 (Academic Press, Burlington) (2000).
- [169] H. A. Carmona, A. K. Geim, A. Nogaret, P. C. Main, T. J. Foster, M. Henini, S. P. Beaumont, M. G. Blamire, *Two Dimensional Electrons in a Lateral Magnetic Superlattice*, *Phys. Rev. Lett.* **74**(15), 3009 (1995).
- [170] P. D. Ye, D. Weiss, R. R. Gerhardt, M. Seeger, K. von Klitzing, K. Eberl, H. Nickel, *Electrons in a Periodic Magnetic Field Induced by a Regular Array of Micromagnets*, *Phys. Rev. Lett.* **74**(15), 3013 (1995).
- [171] A. Nogaret, S. J. Bending, M. Henini, *Resistance Resonance Effects through Magnetic Edge States*, *Phys. Rev. Lett.* **84**(10), 2231 (2000).
- [172] M. Di Ventra, *Electrical Transport in Nanoscale Systems* (Cambridge University Press, Cambridge, UK) (2008).
- [173] J. M. Ziman, *Elements of Advanced Quantum Theory* (Cambridge University Press, Cambridge, UK) (1969).
- [174] B. A. Lippmann, J. Schwinger, *Variational Principles for Scattering Processes. I*, *Phys. Rev.* **79**(3), 469 (1950).
- [175] R. H. Landau, *Quantum mechanics II: a second course in quantum theory*. (Wiley, New York) (2004).
- [176] M. Born, *Zur Quantenmechanik der Stoßvorgänge*, *Z. Phys.* **37**(12), 863 (1926).
- [177] J. R. Taylor, *Scattering theory: the quantum theory on nonrelativistic collisions* (Wiley, New York) (1972).
- [178] L. Reichl, *The Transition to Chaos: Conservative Classical Systems and Quantum Manifestations* (Springer, Berlin) (2004).

- 
- [179] A. M. Lane, R. G. Thomas, *R-Matrix Theory of Nuclear Reactions*, Rev. Mod. Phys. **30**(2), 257 (1958).
- [180] E. P. Wigner, L. Eisenbud, *Higher Angular Momenta and Long Range Interaction in Resonance Reactions*, Phys. Rev. **72**(1), 29 (1947).
- [181] G. Akguc, L. E. Reichl, *Effect of evanescent modes and chaos on deterministic scattering in electron waveguides*, Phys. Rev. E **64**(5), 056221 (2001).
- [182] G. B. Akguc, L. E. Reichl, *Direct scattering processes and signatures of chaos in quantum waveguides*, Phys. Rev. E **67**(4), 046202 (2003).
- [183] H. Schanz, *Reaction matrix for Dirichlet billiards with attached waveguides*, Physica E **18**(4), 429 (2003).
- [184] B. Farid, *Ground and Low-Lying Excited States of Interacting Electron Systems; A Survey and Some Critical Analyses*, in *Electron Correlation in the Solid State*, p. 103 (World Scientific Publishing) (1999).
- [185] B. Farid, *A Luttinger's theorem revisited*, Phil. Mag. B **79**(8), 1097 (1999).
- [186] G. Onida, L. Reining, A. Rubio, *Electronic excitations: density-functional versus many-body Green's-function approaches*, Rev. Mod. Phys. **74**(2), 601 (2002).
- [187] W. v. Haeringen, B. Farid, D. Lenstra, *On the Many Body Theory of the Energy Gap in Semiconductors*, Phys. Scr. **1987**(T19A), 282 (1987).
- [188] H. Bruus, K. Flensberg, *Many-Body Quantum Theory in Condensed Matter Physics: An Introduction* (Oxford University Press, Oxford, UK) (2004).
- [189] L. V. Keldysh, *Diagram technique for nonequilibrium processes*, Sov. Phys. JETP **20**, 1018 (1965).
- [190] L. P. Kadanoff, G. Baym, *Quantum statistical mechanics: Green's function methods in equilibrium and nonequilibrium problems* (W.A. Benjamin, New York) (1962).
- [191] S. Datta, *Nanoscale device modeling: the Green's function method*, Superlatt. Microstruct. **28**(4), 253 (2000).
- [192] R. Lake, S. Datta, *Nonequilibrium Green's-function method applied to double-barrier resonant-tunneling diodes*, Phys. Rev. B **45**(12), 6670 (1992).
- [193] R. Lake, G. Klimeck, R. C. Bowen, D. Jovanovic, *Single and multiband modeling of quantum electron transport through layered semiconductor devices*, J. Appl. Phys. **81**(12), 7845 (1997).
- [194] J. Taylor, H. Guo, J. Wang, *Ab initio modeling of quantum transport properties of molecular electronic devices*, Phys. Rev. B **63**(24), 245407 (2001).
- [195] M. Galperin, M. A. Ratner, A. Nitzan, *Molecular transport junctions: vibrational effects*, J. Phys.: Cond. Mat. **19**(10), 103201 (2007).
- [196] A. Jauho, N. S. Wingreen, Y. Meir, *Time-dependent transport in interacting and noninteracting resonant-tunneling systems*, Phys. Rev. B **50**(8), 5528 (1994).
-

- [197] N. S. Wingreen, A. Jauho, Y. Meir, *Time-dependent transport through a mesoscopic structure*, Phys. Rev. B **48**(11), 8487 (1993).
- [198] M. P. Anantram, S. Datta, *Effect of phase breaking on the ac response of mesoscopic systems*, Phys. Rev. B **51**(12), 7632 (1995).
- [199] B. Wang, J. Wang, H. Guo, *Current Partition: A Nonequilibrium Green's Function Approach*, Phys. Rev. Lett. **82**(2), 398 (1999).
- [200] B. Gaury, J. Weston, M. Santin, M. Houzet, C. Groth, X. Waintal, *Numerical simulations of time-resolved quantum electronics*, Phys. Rep. **534**(1), 1 (2014).
- [201] O. Shevtsov, X. Waintal, *Numerical toolkit for electronic quantum transport at finite frequency*, Phys. Rev. B **87**(8), 085304 (2013).
- [202] M. P. Anantram, M. Lundstrom, D. Nikonov, *Modeling of Nanoscale Devices*, Proc. IEEE **96**(9), 1511 (2008).
- [203] Y. Meir, N. S. Wingreen, *Landauer formula for the current through an interacting electron region*, Phys. Rev. Lett. **68**(16), 2512 (1992).
- [204] C. Caroli, R. Combescot, P. Nozieres, D. Saint-James, *Direct calculation of the tunneling current*, J. Phys. C: Solid State Phys. **4**(8), 916 (1971).
- [205] U. Fano, *Sullo spettro di assorbimento dei gas nobili presso il limite dello spettro d'arco*, Nuovo Cimento **12**(3), 154 (1935).
- [206] U. Fano, G. Pupillo, A. Zannoni, C. Clark, *On the absorption spectrum of noble gases at the arc spectrum limit*, J. Res. Natl. Inst. Stan. Technol. **110**(6), 583 (2005).
- [207] H. Feshbach, *Unified theory of nuclear reactions*, Ann. Phys. **5**(4), 357 (1958).
- [208] E. Majorana, *Teoria dei tripletti P' Incompleti*, Nuovo Cimento **8**(1), 107 (1931).
- [209] G. Bassani, S. I. d. Fisica, *Ettore Majorana: Scientific Papers* (Springer, Berlin) (2007).
- [210] A. Vittorini-Orgeas, A. Bianconi, *From Majorana Theory of Atomic Autoionization to Feshbach Resonances in High Temperature Superconductors*, J. Supercond. **22**(3), 215 (2009).
- [211] K. Sasada, N. Hatano, G. Ordóñez, *Resonant Spectrum Analysis of the Conductance of an Open Quantum System and Three Types of Fano Parameter*, J. Phys. Soc. Jpn. **80**(10), 104707 (2011).
- [212] A. A. Clerk, X. Waintal, P. W. Brouwer, *Fano Resonances as a Probe of Phase Coherence in Quantum Dots*, Phys. Rev. Lett. **86**(20), 4636 (2001).
- [213] A. Bärnthaler, S. Rotter, F. Libisch, J. Burgdörfer, S. Gehler, U. Kuhl, H. Stöckmann, *Probing Decoherence through Fano Resonances*, Phys. Rev. Lett. **105**(5), 056801 (2010).
- [214] Y. Aharonov, D. Bohm, *Further Considerations on Electromagnetic Potentials in the Quantum Theory*, Phys. Rev. **123**(4), 1511 (1961).
- [215] R. G. Chambers, *Shift of an Electron Interference Pattern by Enclosed Magnetic Flux*, Phys. Rev. Lett. **5**(1), 3 (1960).

- 
- [216] A. Tonomura, T. Matsuda, R. Suzuki, A. Fukuhara, N. Osakabe, H. Umezaki, J. Endo, K. Shinagawa, Y. Sugita, H. Fujiwara, *Observation of Aharonov-Bohm Effect by Electron Holography*, Phys. Rev. Lett. **48**(21), 1443 (1982).
- [217] L. P. Kouwenhoven, C. M. Marcus, P. L. McEuen, S. Tarucha, R. M. Westervelt, N. S. Wingreen, *Electron Transport in Quantum Dots*, in L. L. Sohn, L. P. Kouwenhoven, G. Schön (Eds.), *Mesoscopic Electron Transport*, number 345 in NATO ASI Series, pp. 105–214 (Springer Netherlands) (1997).
- [218] Y. Gefen, Y. Imry, M. Y. Azbel, *Quantum Oscillations and the Aharonov-Bohm Effect for Parallel Resistors*, Phys. Rev. Lett. **52**(2), 129 (1984).
- [219] S. Chakravarty, A. Schmid, *Weak localization: The quasiclassical theory of electrons in a random potential*, Phys. Rep. **140**(4), 193 (1986).
- [220] P. A. Kalozoumis, C. Morfonios, F. K. Diakonov, P. Schmelcher, *Local symmetries in one-dimensional quantum scattering*, Phys. Rev. A **87**(3), 032113 (2013).
- [221] P. A. Kalozoumis, C. Morfonios, N. Palaiodimopoulos, F. K. Diakonov, P. Schmelcher, *Local symmetries and perfect transmission in aperiodic photonic multilayers*, Phys. Rev. A **88**(3), 033857 (2013).
- [222] C. Morfonios, P. Schmelcher, P. A. Kalozoumis, F. K. Diakonov, *Local symmetry dynamics in one-dimensional aperiodic lattices: a numerical study*, Nonlinear Dyn. **78**(1) (2014), in press.
- [223] A. Cresti, R. Farchioni, G. Grosso, G. P. Parravicini, *Keldysh-Green function formalism for current profiles in mesoscopic systems*, Phys. Rev. B **68**(7), 075306 (2003).
- [224] G. Metalidis, P. Bruno, *Green's function technique for studying electron flow in two-dimensional mesoscopic samples*, Phys. Rev. B **72**(23), 235304 (2005).
- [225] S. Sanvito, C. J. Lambert, J. H. Jefferson, A. M. Bratkovsky, *General Green's-function formalism for transport calculations with spd Hamiltonians and giant magnetoresistance in Co- and Ni-based magnetic multilayers*, Phys. Rev. B **59**(18), 11936 (1999).
- [226] A. Svizhenko, M. P. Anantram, T. R. Govindan, B. Biegel, R. Venugopal, *Two-dimensional quantum mechanical modeling of nanotransistors*, J. Appl. Phys. **91**(4), 2343 (2002).
- [227] P. Rotter, U. Rössler, H. Silberbauer, M. Suhrke, *Antidot-superlattices: minibands and magnetotransport*, Physica B **212**(3), 231 (1995).
- [228] F. A. Maaø, I. V. Zozulenko, E. H. Hauge, *Quantum point contacts with smooth geometries: Exact versus approximate results*, Phys. Rev. B **50**(23), 17320 (1994).
- [229] R. Venugopal, S. Goasguen, S. Datta, M. S. Lundstrom, *Quantum mechanical analysis of channel access geometry and series resistance in nanoscale transistors*, J. Appl. Phys. **95**(1), 292 (2004).
- [230] P. S. Drouvelis, P. Schmelcher, P. Bastian, *Parallel implementation of the recursive Green's function method*, J. Comp. Phys. **215**(2), 741 (2006).
-

- [231] M. Luisier, G. Klimeck, A. Schenk, W. Fichtner, T. B. Boykin, *A Parallel Sparse Linear Solver for Nearest-Neighbor Tight-Binding Problems*, in E. Luque, T. Margalef, D. Benítez (Eds.), *Euro-Par 2008 – Parallel Processing*, number 5168 in Lecture Notes in Computer Science, pp. 790–800 (Springer, Berlin) (2008).
- [232] A. Kuzmin, M. Luisier, O. Schenk, *Fast Methods for Computing Selected Elements of the Green’s Function in Massively Parallel Nanoelectronic Device Simulations*, in F. Wolf, B. Mohr, D. a. Mey (Eds.), *Euro-Par 2013 Parallel Processing*, number 8097 in Lecture Notes in Computer Science, pp. 533–544 (Springer, Berlin) (2013).
- [233] D. Guan, U. Ravaioli, R. W. Giannetta, M. Hannan, I. Adesida, M. R. Melloch, *Nonequilibrium Green’s function method for a quantum Hall device in a magnetic field*, Phys. Rev. B **67**(20), 205328 (2003).
- [234] D. Mamaluy, M. Sabathil, P. Vogl, *Efficient method for the calculation of ballistic quantum transport*, J. Appl. Phys. **93**(8), 4628 (2003).
- [235] D. Mamaluy, D. Vasileska, M. Sabathil, T. Zibold, P. Vogl, *Contact block reduction method for ballistic transport and carrier densities of open nanostructures*, Phys. Rev. B **71**(24), 245321 (2005).
- [236] M. Wimmer, K. Richter, *Optimal block-tridiagonalization of matrices for coherent charge transport*, J. Comp. Phys. **228**(23), 8548 (2009).
- [237] G. Thorgilsson, G. Viktorsson, S. I. Erlingsson, *Recursive Green’s function method for multi-terminal nanostructures*, J. Comp. Phys. (2014).
- [238] P. Vogl, H. P. Hjalmarson, J. D. Dow, *A Semi-empirical tight-binding theory of the electronic structure of semiconductors*, J. Phys. Chem. Sol. **44**(5), 365 (1983).
- [239] T. B. Boykin, *Exact representation of  $\exp(iq \cdot r)$  in the empirical tight-binding method and its application to electromagnetic interactions*, Phys. Rev. B **60**(23), 15810 (1999).
- [240] R. Peierls, *Zur Theorie des Diamagnetismus von Leitungselektronen*, Z. Phys. **80**(11-12), 763 (1933).
- [241] T. B. Boykin, R. C. Bowen, G. Klimeck, *Electromagnetic coupling and gauge invariance in the empirical tight-binding method*, Phys. Rev. B **63**(24), 245314 (2001).
- [242] G. H. Golub, C. F. V. Loan, *Matrix Computations* (John Hopkins University Press, Baltimore) (1996).
- [243] D. S. Watkins, *Fundamentals of Matrix Computations* (Wiley, New York) (2010).
- [244] T. B. Boykin, M. Luisier, G. Klimeck, *Current density and continuity in discretized models*, Eur. J. Phys. **31**(5), 1077 (2010).
- [245] E. Anderson, Z. Bai, C. Bischof, L. Blackford, J. Demmel, J. Dongarra, J. Du Croz, A. Greenbaum, S. Hammarling, A. McKenney, D. Sorensen, *LAPACK Users’ Guide* (Soc. Ind. Appl. Math.) (1999).
- [246] C. Morfonios, D. Buchholz, P. Schmelcher, *Magnetoconductance switching in an array of oval quantum dots*, Phys. Rev. B **80**(3), 035301 (2009).
- [247] M. V. Berry, *Regularity and chaos in classical mechanics, illustrated by three deformations of a circular ‘billiard’*, Eur. J. Phys. **2**(2), 91 (1981).

- 
- [248] H. Makino, T. Harayama, Y. Aizawa, *Effects of bifurcations on the energy level statistics for oval billiards*, Phys. Rev. E **59**(4), 4026 (1999).
- [249] M. Büttiker, Y. Imry, M. Y. Azbel, *Quantum oscillations in one-dimensional normal-metal rings*, Phys. Rev. A **30**(4), 1982 (1984).
- [250] W. Zhe-Xian, M. Yi, D. Ze-Jun, *Electronic transport through an open elliptic cavity*, Chin. Phys. **16**(11), 3507 (2007).
- [251] R. Lehoucq, D. Sorensen, C. Yang, *ARPACK Users' Guide* (Soc. Ind. Appl. Math.) (1998).
- [252] K. Friedland, R. Hey, H. Kostial, R. Klann, K. Ploog, *New Concept for the Reduction of Impurity Scattering in Remotely Doped GaAs Quantum Wells*, Phys. Rev. Lett. **77**(22), 4616 (1996).
- [253] D. Reuter, D. Kahler, U. Kunze, A. D. Wieck, *Layer-compensated selectively doped Al<sub>x</sub>Ga<sub>1-x</sub>As/GaAs heterostructures as a base material for nanolithography*, Semicond. Sci. Technol. **16**(7), 603 (2001).
- [254] M. Knop, M. Richter, R. Massmann, U. Wieser, U. Kunze, D. Reuter, C. Riedesel, A. D. Wieck, *Preparation of electron waveguide devices on GaAs/AlGaAs using negative-tone resist calixarene*, Semicond. Sci. Technol. **20**(8), 814 (2005).
- [255] C. Morfonios, P. Schmelcher, *Current Control by Resonance Decoupling and Magnetic Focusing in Soft-Wall Billiards*, Phys. Rev. Lett. **113**(8), 086802 (2014).
- [256] V. Fock, *Bemerkung zur Quantelung des harmonischen Oszillators im Magnetfeld*, Z. Phys. **47**(5-6), 446 (1928).
- [257] C. G. Darwin, *The Diamagnetism of the Free Electron*, Proc. Cambridge Philos. Soc. **27**(01), 86 (1931).
- [258] H. Stöckmann, *Quantum Chaos: An Introduction* (Cambridge University Press, Cambridge, UK) (1999).
- [259] D. Buchholz, P. S. Drouvelis, P. Schmelcher, *Single electron quantum dot in a spatially periodic magnetic field*, Phys. Rev. B **73**(23), 235346 (2006).
- [260] C. S. Lent, *Edge states in a circular quantum dot*, Phys. Rev. B **43**(5), 4179 (1991).
- [261] C. Payette, D. Austing, G. Yu, J. Gupta, S. Nair, B. Partoens, S. Amaha, S. Tarucha, *Two-level anti-crossings high up in the single-particle energy spectrum of a quantum dot*, Physica E **40**(6), 1807 (2008).
- [262] L. W. Molenkamp, A. A. M. Staring, C. W. J. Beenakker, R. Eppenga, C. E. Timmering, J. G. Williamson, C. J. P. M. Harmans, C. T. Foxon, *Electron-beam collimation with a quantum point contact*, Phys. Rev. B **41**(2), 1274 (1990).
- [263] J. Repp, G. Meyer, K. Rieder, *Snell's Law for Surface Electrons: Refraction of an Electron Gas Imaged in Real Space*, Phys. Rev. Lett. **92**(3), 036803 (2004).
- [264] R. Brunner, D. K. Ferry, R. Akis, R. Meisels, F. Kuchar, A. M. Burke, J. P. Bird, *Open quantum dots: II. Probing the classical to quantum transition*, J. Phys.: Cond. Mat. **24**(34), 343202 (2012).
-

- [265] F. J. Betancur, I. D. Mikhailov, L. E. Oliveira, *Shallow donor states in GaAs-(Ga, Al)As quantum dots with different potential shapes*, J. Phys. D: Appl. Phys. **31**(23), 3391 (1998).
- [266] A. M. See, I. Pilgrim, B. C. Scannell, R. D. Montgomery, O. Klochan, A. M. Burke, M. Aagesen, P. E. Lindelof, I. Farrer, D. A. Ritchie, R. P. Taylor, A. R. Hamilton, A. P. Micolich, *Impact of Small-Angle Scattering on Ballistic Transport in Quantum Dots*, Phys. Rev. Lett. **108**(19) (2012).
- [267] C. Morfonios, D. Buchholz, P. Schmelcher, *Magnetic field-induced control of transport in multiterminal focusing quantum billiards*, Phys. Rev. B **83**(20), 205316 (2011).
- [268] F. Lenz, F. K. Diakonov, P. Schmelcher, *Scattering dynamics of driven closed billiards*, Europhys. Lett. **79**(2), 20002 (2007).
- [269] H. Waalkens, J. Wiersig, H. R. Dullin, *Elliptic Quantum Billiard*, Ann. Phys. **260**(1), 50 (1997).
- [270] R. G. Nazmitdinov, K. N. Pichugin, I. Rotter, P. Šeba, *Whispering gallery modes in open quantum billiards*, Phys. Rev. E **64**(5), 056214 (2001).
- [271] L. A. Bunimovich, *Mushrooms and other billiards with divided phase space*, Chaos **11**(4), 802 (2001).
- [272] J. U. Nöckel, *Resonances in quantum-dot transport*, Phys. Rev. B **46**(23), 15348 (1992).
- [273] Y. Hirayama, A. D. Wieck, T. Bever, K. von Klitzing, K. Ploog, *Parallel in-plane-gated wires coupled by a ballistic window*, Phys. Rev. B **46**(7), 4035 (1992).
- [274] Y. Nagaoka, M. Ikegami, *Quantum Mechanics of an Electron on a Curved Surface*, in P. H. Fukuyama, P. T. Ando (Eds.), *Transport Phenomena in Mesoscopic Systems*, number 109 in Springer Series in Solid-State Sciences, pp. 167–173 (Springer, Berlin) (1992).
- [275] O. Olendski, L. Mikhailovska, *Curved quantum waveguides in uniform magnetic fields*, Phys. Rev. B **72**(23), 235314 (2005).
- [276] P. S. Drouvelis, P. Schmelcher, F. K. Diakonov, *Probing the shape of quantum dots with magnetic fields*, Phys. Rev. B **69**(15), 155312 (2004).
- [277] R. Fazio, R. Raimondi, *Resonant Andreev Tunneling in Strongly Interacting Quantum Dots*, Phys. Rev. Lett. **80**(13), 2913 (1998).
- [278] N. G. Fytas, F. K. Diakonov, P. Schmelcher, M. Scheid, A. Lassel, K. Richter, G. Fagas, *Magnetic-field dependence of transport in normal and Andreev billiards: A classical interpretation of the averaged quantum behavior*, Phys. Rev. B **72**(8), 085336 (2005).
- [279] Q. Han, *A method of studying the Bogoliubov–de Gennes equations for the superconducting vortex lattice state*, J. Phys.: Cond. Mat. **22**(3), 035702 (2010).
- [280] J. H. Bardarson, M. Titov, P. W. Brouwer, *Electrostatic Confinement of Electrons in an Integrable Graphene Quantum Dot*, Phys. Rev. Lett. **102**(22), 226803 (2009).
- [281] J. Güttinger, F. Molitor, C. Stampfer, S. Schnez, A. Jacobsen, S. Dröscher, T. Ihn, K. Ensslin, *Transport through graphene quantum dots*, Rep. Prog. Phys. **75**(12), 126502 (2012).
- [282] A. Gómez-León, G. Platero, *Floquet-Bloch Theory and Topology in Periodically Driven Lattices*, Phys. Rev. Lett. **110**(20), 200403 (2013).

- [283] P. Földi, O. Kálmán, M. G. Benedict, F. M. Peeters, *Networks of Quantum Nanorings: Programmable Spintronic Devices*, *Nano Lett.* **8**(8), 2556 (2008).
- [284] P. Földi, V. Szaszko-Bogár, F. M. Peeters, *High-temperature conductance of a two-dimensional superlattice controlled by spin-orbit interaction*, *Phys. Rev. B* **83**(11), 115313 (2011).
- [285] Y. Ji, Y. Chung, D. Sprinzak, M. Heiblum, D. Mahalu, H. Shtrikman, *An electronic Mach–Zehnder interferometer*, *Nature* **422**(6930), 415 (2003).
- [286] Y. Xu, A. E. Miroshnichenko, *Manipulation of the resonance interaction in Mach-Zehnder-Fano interferometers*, *Phys. Rev. A* **84**(3), 033828 (2011).



# Acknowledgements

---

*Knowledge is in the end based on acknowledgement.*

— Ludwig Wittgenstein

As most activities in life, this thesis must be seen as an emergence of the interactions with the surrounding people. Unable to acknowledge all, I will here restrict myself to the ‘nearest neighbors’...

First of all I warmly thank my doctoral advisor Prof. Peter Schmelcher for introducing me to the world of mesoscopic quantum transport and for providing an excellent scientific and cooperative framework for research. His sharp mind, broad experience and true fascination for unconventional aspects and directions have been a continuous source of inspiration and motivation.

I am deeply thankful to Prof. Fotis Diakonou, my first mentor and later collaborator, whose contagious passion for physics brought me onto the path of research and still pervades our communication. His deep insight, alternative thinking and sheer curiosity, as well as his openness to any kind of problem have been invaluable.

Let me also express my gratitude to Daniel Buchholz for his enduring and openhanded guidance during the first steps of the research. His knowledge on the topic and programming expertise have always served as a scientific compass.

Heartily thanks go to my friend and collaborator Panagiotis Kalozoumis for his great scientific input and for all the fruitful discussions.

I am indebted to my friends and colleagues Alexandra Zampetaki and Simos Mistakidis for their support and for patiently proofreading the thesis.

Along this journey I had the luck to meet my dear companions Ioannis Brouzos and Panagiotis Giannakeas, each of them an extraordinary mind and personality. Iannis’ incomparable creativity and passionate talent and Panos’ analytic thinking and steady wisdom have been true lessons for life. I will never forget our endless discussions, on physics or not, as well as their enlightening and encouraging presence in any moment.

Many thanks go to my first close friend in Heidelberg, Marios Tsatsos, whose enthusiasm and sense of adventure always triggered new activities beyond the office. I also thank Alexandros Karlis, Emmerich Tempfli, my office mate Matthis Eroms as well as flat mates Johannes Lampel and Angelo Mangia, together with all other friends who made the stay in Heidelberg unforgettable.

Within our research group, I am truly grateful for getting to know a series of bright minds and great characters who have made life at the institute a pleasure; among others, Christoph Petri, Florian Lenz, Bernd Hezel, Michael Mayle, and Stephan Middelkamp in the Heidelberg team, and Evangelos Karamatskos, Lushuai Cao, Jan Stockhofe, Sven Krönke, Benno Liebchen, Markus Kurz, Benjamin Hess, Thomas Wulf, Andrea Klumpp, Valentin Bolsinger, Johannes Schurer, and Antonio Negretti in the Hamburg team.

I also thank the developers of Etanercept for making my life easier.

To my parents and to my sister I will always be grateful for being there for me and never stopping to believe in what I set out to do. Without their care and heroic courage this thesis would not have been possible.

Last but not least, although words come up short, I would like to thank Monika for her endless reservoirs of patience, love and support, and our daughter Elina for all the moments of pure joy.